Long-term evolution of normal fault systems: Controls on the development and evolution of extensional structures in the neotectonic Kenyan Rift, East Africa

Jonathan P. Dunningham B.A., MSci

I declare that this thesis has been composed by myself and has not been submitted in association with any other degree. The work reported within was undertaken by myself, except where outside contributions have been stated and duly acknowledged.

Jonathan Paul Dunningham
Edinburgh, 2004

Abstract

Knowledge of the long-term behaviour of extensional fault networks is essential to the understanding of many aspects of geology, such as sedimentary basin formation and seismic hazard analysis. Although a number of models of fault evolution have been proposed, there is, as yet, a scarcity of quantitative field data to test their geological validity.

The South Kenya Rift presents an unparalleled opportunity to investigate the early (0-2Myr) geological development of a normal fault system in an extensional rift setting. The advantage of this region is that the floor of the rift is dissected by a network of well-exposed faults that were active prior to, and contemporaneously with, the last two million years of rift volcanism. The fault blocks are typically no more than a few kilometres in length, with a maximum of 100-200m of vertical displacement. In many localities, trachytic and basaltic lava flows onlap against pre-existing fault blocks and have been rotated or cross-cut during later phases of fault activity. These continental rift lavas, which are rich in potassium, act as dateable marker horizons that can be used to reconstruct the quantitative growth-history of extensional faulting.

Differential GPS, which can provide a positional accuracy of ±4cm in terms of latitude and longitude and ±8cm in terms of fault elevation, was used to survey the dimensions of normal fault blocks in the field. In general, positional data were collected every metre along the crest and base of each fault scarp and, where possible, along lava flow contacts. Such data, when combined with $^{40}Ar/^{39}Ar$ ages determined from the syn-tectonic lava flows, were used to build up a detailed, quantitative, growth-history of faulting in four field localities; two at the centre and two at the eastern margin of the Kenya Rift.

Extensional faulting in the South Kenya Rift appears to have been a very episodic process, expressed as: i) growth of small (2-3km long) 'bell-shaped' fault segments that had relatively large fault displacement/length (d/L) ratios (~0.06-0.10) and were in some cases characterised by high vertical displacement rates (up to ~12mmyr^{-1}), prior to, ii) a phase of linkage between the pre-existing fault segments to form a single fault with a lowered d/L value (~0.01-0.02).

Vertical displacement rates during this linkage phase (0.1-0.3mmyr^{-1}) were sometimes significantly lower than those recorded during the initial period of fault growth. Where appropriate data are available, the approximate ratio of footwall uplift to hangingwall subsidence for fault displacements over a timescale of several hundred kyr is 1:1.4 to 1:2.

The observed reduction in fault displacement rates and d/L values may result from down-dip fault interaction with vertical strength contrasts in the volcanic lava pile or, on a more fundamental scale, the base of the effective elastic thickness (T_e). Fault development is also likely to be influenced by the effects of magmatism, since periods of increased fault activity often occur subsequent to renewed phases of rift volcanism and possible dyke emplacement. Episodic fault-growth could therefore be explained by tectono-magmatic cycling within the South Kenya Rift. On a large scale, there is evidence for a progressive migration of strain towards the centre of the rift over the past 2Myr.

Acknowledgements

Table of Contents

Chapter 1: Scientific Rationale and Background

1.1 Rationale

The growth and evolution of normal faults and normal fault networks has been a particularly active area of scientific research over the past 15 years. The driving force behind this area of study comes from a number of sources. Faults and fault arrays govern the formation of extensional basins and hence, understanding their development is of great interest to the hydrocarbon industry. Fault blocks form important structural traps for oilfields and as fractures in the rock, they have an influence on fluid and hydrocarbon migration. Topographic lows generated in fault hangingwalls also form ideal locations for syn-rift sedimentary depocentres and kitchen areas from which hydrocarbons are expelled. As fault arrays grow and evolve they will also control sediment dispersal pathways and hence influence hydrocarbon reservoir potential. Petroleum reservoir characterisation in a heavily faulted region requires a detailed understanding of all the faults in order to understand how they may influence reservoir compartmentalisation. Detailed understanding of the development of fault networks is similarly required for assisting in the problem of long-term radioactive waste disposal, where faults may act as unwanted conduits for radioactive fluids. Knowledge of fault behaviour is important in the fields of civil engineering, where faults may act as zones of weakness and cause instability and subsidence. This is even more critical in seismically active regions.

Analytical, numerical and fieldwork-based studies have all attempted to understand how individual faults grow (e.g. Watterson, 1986; Walsh and Watterson, 1987, 1988; Peacock and Sanderson, 1991; Cowie and Scholz, 1992a,b; Dawers *et al.*, 1993; Trudgill and Cartwright, 1994; Willemse *et al.*, 1996; Willemse 1997; Jackson *et al.*, 2002a,b) and more recently how arrays and networks of extensional faults evolve over geological timescales. (Cowie *et al.*, 2000; Meyer *et al.*, 2002; Gawthorpe *et al.*, 2003). There is now an extensive database of work concentrating on the growth of solitary normal faults, the interaction and linkage of fault arrays and now the evolution of, and feedback between, normal fault networks. Most studies attempt to produce fault growth models by analysing morphological data, such as fault displacements and lengths, from fault populations. These data offer a snapshot of fault systems at the present-day,

but provide no definitive understanding of their growth history. Analysis of faults in subsurface seismic data, tied to a number of dated stratigraphic horizons, has helped to elucidate both the growth histories of large, mature, rift-bounding normal faults (e.g. Contreras *et al.*, 2000) but also smaller scale structures within fault networks (e.g. McLeod *et al.*, 2002; Meyer *et al.*, 2002; Gawthorpe *et al.*, 2003). Cosmogenic dating of uplifted fault rocks has similarly been employed to provide information on the rate of lateral fault growth (Jackson *et al.*, 2002b) and fault segment linkage (Gupta *et al.*, 2003).

The primary objectives of this study have been to analyse and quantify the growth of normal faults, as part of a fault network. Important questions that have been investigated as part of the study were:

1. Do faults grow at a constant rate over geological timescales, or is their growth a more episodic process?

2. Do all faults within a population grow at a similar rate, independent of size, or are some faults more active than others?

3. Do some faults within a population become inactive as strain is localised across the fault network?

Existing models propose a number of endmembers for fault growth, ranging from simple, elliptical-shaped growth morphologies of independent normal faults (e.g. Walsh and Watterson, 1987) through to more complex growth patterns resulting from the interaction and linkage of fault segments (e.g. Trudgill and Cartwright, 1994; Ferrill *et al.*, 1999; Cowie *et al.*, 2000; McLeod *et al.*, 2000). Studies of fault arrays in subsurface data have, to some extent, made it possible to quantify rates of growth. Similarly, recent numerical modelling and observations from subsurface seismic data suggest that strain becomes progressively localised across areally extensive fault populations (Cowie *et al.*, 2000; Meyer *et al.*, 2002). However, there are still few field-based studies to test the results of numerical outputs or to study fault data close to, or below, the limits of seismic resolution (Gawthorpe *et al.*, 2003). The results presented in this thesis are an attempt to address this issue and to fill an important gap in current understanding of how normal faults evolve.

The South Kenya Rift is an ideal region in which to study the development of normal fault populations. The floor of the rift is dissected by a network of kilometre-scale normal faults that have been active during Neogene and Quaternary times and are coeval with a phase of regional volcanism. As such, pre-existing fault blocks are often onlapped by regional volcanic flows and then reactivated such that lavas are rotated onto the back of footwall blocks or are preserved as a series of narrow lava ledges along the fault scarp. $^{40}Ar/^{39}Ar$ radiometric dating of the lava flows hence offers the opportunity to quantify the growth of a small-scale normal fault network at a better resolution than is available with subsurface data. Understanding the development of these structures provides a useful analogue model for early, syn-rift basin development.

1.2. Review of Extensional Fault Studies

1.2.1 Fault scaling relationships

Present understanding of the mechanics of continental extension has derived from studies based both upon numerical modelling and fieldwork at a variety of scales. Large, basin scale numerical models (e.g. McKenzie, 1978; Lin and Parmentier, 1990; England, 1983) have sought to view the mechanics of rift formation as the result of deformation of an homogeneous continuum. At the other end of the spectrum, studies have been made in order to establish a mechanism for the growth and evolution of brittle fault arrays that are inherently part of the mechanics of continental extension (Watterson, 1986; Walsh and Watterson, 1988; Cowie and Scholz, 1992a,b). Early numerical modelling (Cowie and Scholz, 1992a) and field-based research (Watterson, 1986; Walsh and Watterson, 1987, 1988) has been dedicated to understanding the distribution of displacement along isolated faults and to fixing a scaling relation between fault length and displacement. Such relations are important because they provide not only constraints on the mechanisms of fault growth, but can also allow an estimation of extension on faults that are below the limits of analytical resolution (Cowie and Scholz, 1992a,b). Without information on the latter it would be impossible to make any inferences about the total amount of extension within a rift setting.

A number of scaling relations have been proposed. Elliot (1976) gives a linear correlation between fault displacement (D) and length (L) such that;

$$D=0.007L \tag{1.1}$$

Walsh and Watterson (1987, 1988) studied the displacement on sets of normal faults occurring in British coalfields and combined this with data from other regions (e.g. Icelandic faults, mid-ocean ridge faults and Texan oilfield faults) to infer a new empirical law that incorporates a factor, P, which depends on the rock properties;

$$D=L^2/P \tag{1.2}$$

Combining fault displacement-length datasets in this way has been considered to be a method of generating generic fault scaling relationships that apply to faults ranging over three orders of magnitude in length (Marret and Allmendinger, 1991; Gillespie *et al.*, 1992). There is, however, no complete consensus as to the nature of any generic fault scaling relation. Cowie and Scholz (1992a) have numerically modelled the growth of an isolated fault within a thin elastic sheet so as to give a linear fault displacement-length relationship. They criticise the use of combined fault datasets such as those of Walsh and Watterson (1988) on the grounds that the scaling factor will depend to a large extent on rock properties (Cowie and Scholz, 1992b). More recently, Dawers *et al.* (1993) have collected displacement-length data from isolated normal faults ranging over three orders of magnitude in length, located within a single lithology, the Quaternary Bishop Tuff, in Northern Owens Valley, California. Their data also appears to suggest a linear relationship between displacement and fault length. The apparent best-fit to the global fault dataset (figure 1.1) has now been calculated as:

$$D_{max}=0.03L^{1.06} \tag{1.3}$$

(after Schlische *et al.*, 1996)

1.2.2 Effects of rock stratigraphy on fault morphology

Vertical variations in rheology, which would be expected in a layered sedimentary or volcano-sedimentary sequence, also have a strong influence on the distribution of displacement along a fault plane (Muraoka and Kamata, 1983; Dawers *et al.*, 1993; Mansfield and Cartwright, 1996; Nicol *et al.*, 1996). In their study of faulting within the Volcanic Tablelands, Dawers *et al.* (1993) recognise two distinct patterns of displacement along the length of the fault scarps; elliptical (for faults less than 200m in length) and flat-topped (trapezoidal – for faults greater than several hundred metres in length) (figure 1.2). They relate this change in the characteristic displacement-length profile to the size at which the fault is able to break through the ~150m thick Bishop Tuff ash flow sheet and begin to interact with the underlying poorly consolidated unit. Small faults, which are contained entirely within the tuff, propagate as circular cracks and hence will have an elliptical displacement-length profile. The more flat-topped profiles will be generated when the faults break through the base of the brittle sheet and are restricted by the underlying lithology.

Muraoka and Kamata (1983) have studied the effect of rock lithology on the behaviour of faults in a layered sequence of Quaternary sandstones and mudstones in Japan. Fault displacement is observed to be largest in the sandstone members, which behave in a brittle fashion, and dies out in the more ductile mudrock units where deformation becomes more distributed.

Analysis of faulting from 3D seismic data and coal mine plans has revealed the influence of horizontal lithological layering on fault tip-lines in three dimensions (Mansfield and Cartwright, 1996; Nicol *et al.*, 1996). Nicol *et al.* (1996) suggest that layering can have a strong influence on the form of the fault tip-line where "the thicknesses of the lithological layers are large relative to the fault dimension or where the contrast in layer properties is particularly marked". In this situation, downward propagation of the fault tip-line (e.g. across the transition from a brittle horizon into an underlying ductile member) may be restricted such that the tip-line loses its characteristic elliptical profile and becomes more rectangular in shape (Nicol *et al.*, 1996). Fault displacement-length profiles, as measured in the field, are expressions of a fault tip-line at a free surface (i.e. the ground surface). Such profiles would, therefore, be expected to be more

elongate in shape than the typical elliptical displacement–length profiles expected for isolated faults within a thick, homogeneous, lithology. Recently, in their field-based study of normal fault growth in layered sedimentary rocks, Wilkins and Gross (2002) also describe how faults with tips restricted by lithological boundaries develop anomalously large D_{max}/L ratios.

Perhaps the largest mechanical boundary to influence vertical fault propagation is the base of the brittle, seismogenic upper crust. Cowie and Scholz (1992b) suggest that, within global fault datasets, small faults (with lengths less than 10km) have lower D_{max}/L values than larger faults. They ascribe this observation to a crossover between small faults, which are entirely contained within the upper crust, and large faults that are vertically restricted by the base of the seismogenic layer. However, Wilkins and Gross (2002) suggest that the effective mechanical layer thickness that controls fault restriction, and hence D_{max}/L ratios, is important at all scales and thus, the base of the seismogenic layer should not be regarded as a special case.
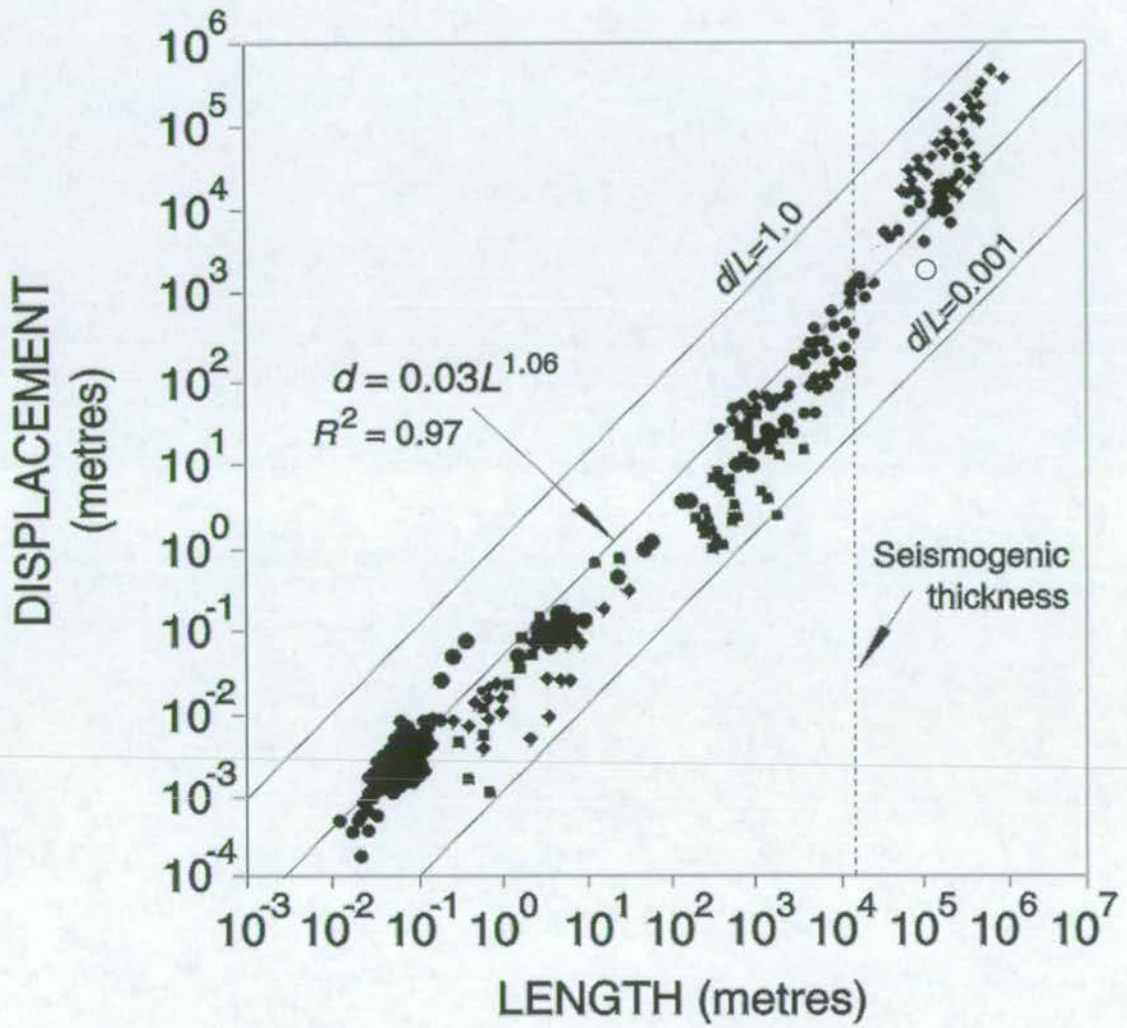
Figure 1.1 Log-log plot of displacement (D) versus length for various published fault populations. Open circle: Strathspey-Brent-Statfjord fault (McLeod *et al.*, 2000). The best-fit curve of Schlische *et al.* (1996) (d=0.03L$^{1.06}$) is indicated. Also shown by the vertical dashed line is the thickness of the seismogenic layer (see section 1.2.2). (modified after Morewood and Roberts, 2002).
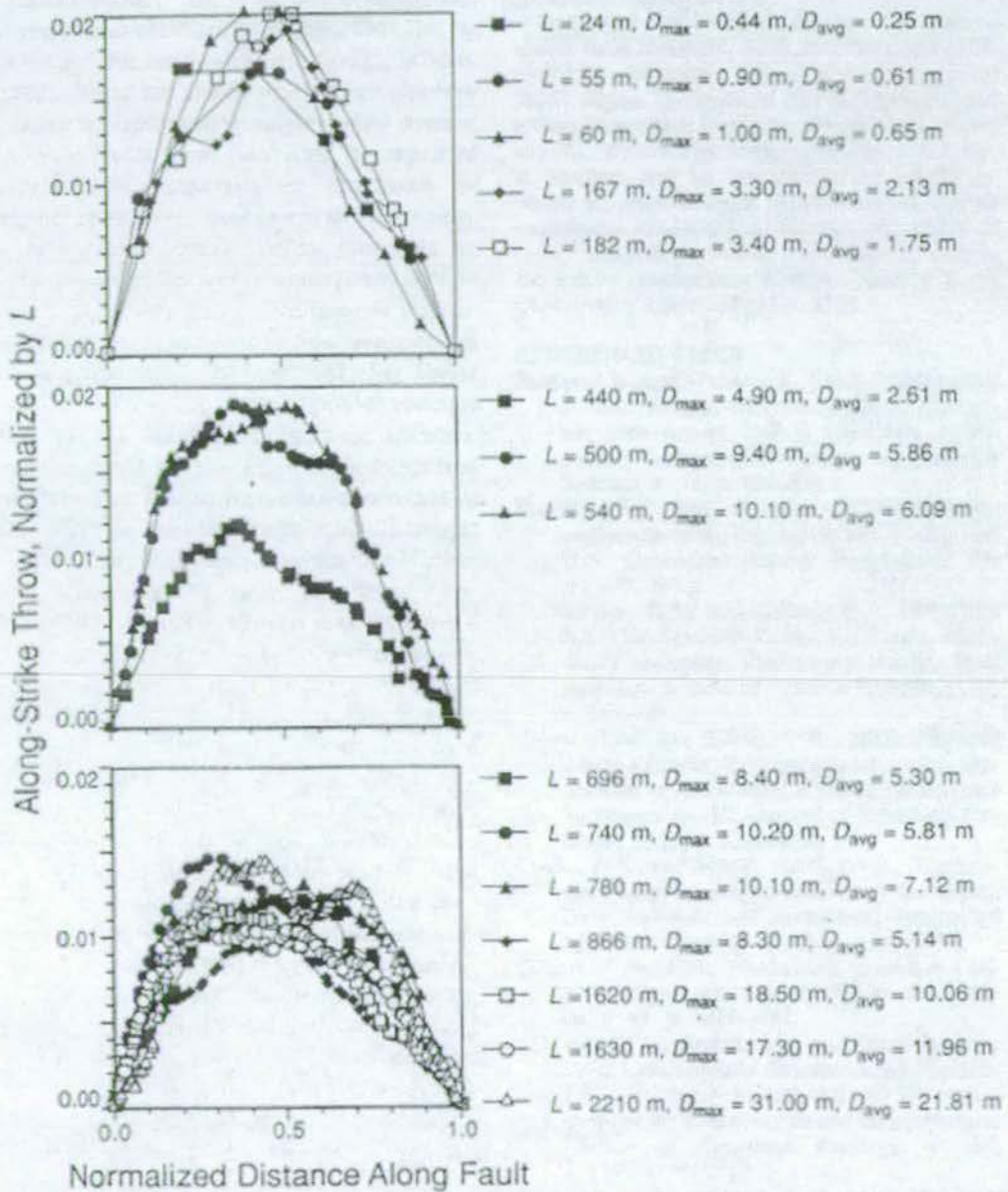
Figure 1.2 Throw distributions normalised for length (L) for 15 faults in the Volcanic Tableland, California. The faults have been separated into three classes according to profile shape and maximum displacement (D_{max}) to L ratios. Upper panel: faults with L<200m characterised by peaked profiles with D_{max}/L ~0.018. Middle panel: unclassified profiles. Lower panel: faults with L>600m; trapezoidal profiles with D_{max}/L ~0.012. (from Dawers *et al.*, 1993)

1.2.3 Fault Interaction and Linkage

As well as being ascribed to variations in rock lithology, deviations from the idealised scaling relations are also believed to reflect the influence of interactions between active neighbouring faults. Much of the work on scaling relations in isolated faults (Watterson, 1986; Walsh and Watterson, 1987, 1988; Cowie and Scholz, 1992a,b) suggests that fault segments should grow in such a way as to form circular-to elliptical-shaped displacement-length profiles (figure 1.3). The linear displacement-length relationship of Cowie and Scholz (1992a) and Dawers *et al.* (1993) suggests that faults should grow in a self-similar fashion while the studies of Watterson (1986) and Walsh and Watterson (1987, 1988) suggest that fault displacement should increase more rapidly than fault length. Walsh and Watterson (1987) imagined that the form of a recent fault scarp could be modelled as the sum of a number of slip events that are circular in form (figure 1.3).

Idealised circular to elliptical fault displacement-length profiles, where the position of maximum slip (D_{max}) is located at the centre of the fault, are only valid for isolated faults. Peacock and Sanderson (1991), in their study of centimetre-scale normal faults in the Lower Jurassic limestones and mudrocks of Kilve, Somerset, document migration in the position of D_{max} away from the centre of the fault and towards the fault tips. They suggest that these asymmetric displacement-length profiles are generated as a result of interaction between closely spaced, neighbouring faults (figure 1.4).
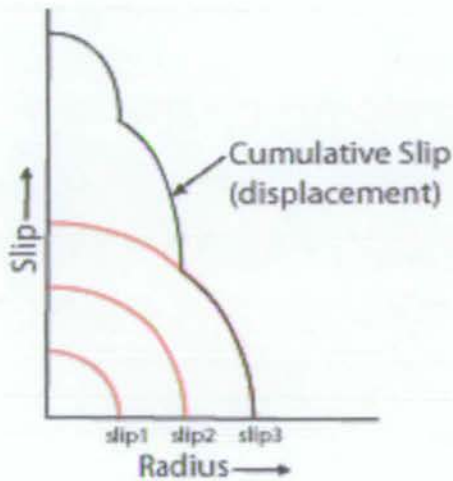
Figure 1.3 Illustration of slip in three successive events on a growing, isolated fault (redrawn from Walsh and Watterson, 1987).

a)

b)
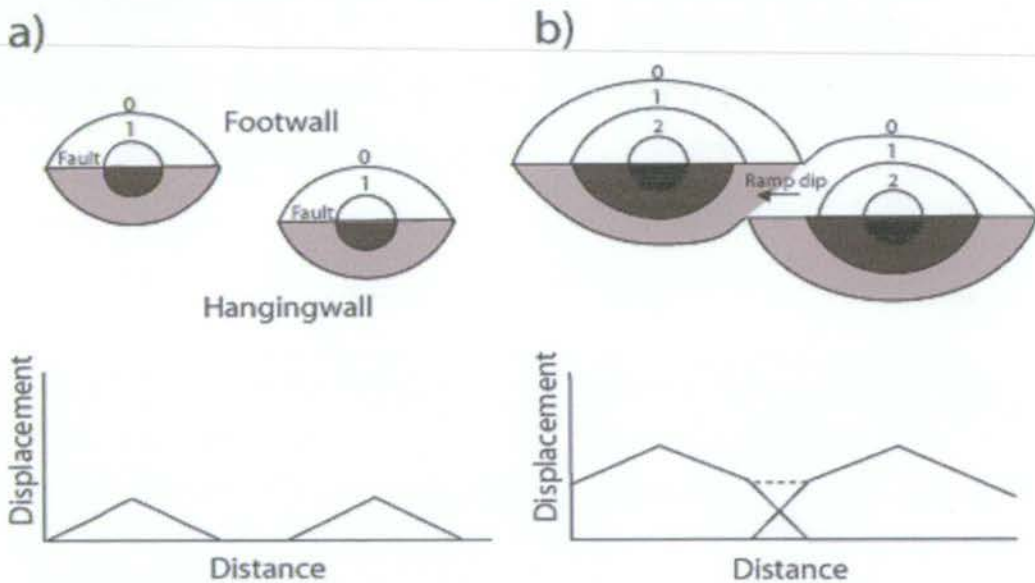
Figure 1.4 Schematic diagram showing the development of active normal fault segments (shading on downthrown side). a) The segments do not interact, so the displacement-length profiles (below) are characteristic of isolated faults. b) The segments begin to overlap and interact. Displacement is transferred to the region between the segments by the rotation of the intervening relay ramp. The overlap is marked by steep displacement gradients and a displacement minimum on the faults (redrawn from Peacock and Sanderson, 1991).

Many later field studies have also emphasised the asymmetric nature of fault displacement-length profiles, which are often observed to be skewed towards neighbouring fault segments (Dawers and Anders, 1995; Cartwright *et al.*, 1995; Gupta and Scholz, 2000). The displacement gradients of the fault tips have been shown to be higher when faults are interacting than when they are isolated (Peacock and Sanderson, 1991; Dawers and Anders, 1995). Interacting faults may be underlapping or overlapping depending on the stage of growth. Zones of fault overlap are variously known as relay ramps (Larsen, 1988), accommodation zones (Bosworth, 1985), fault bridges (Ramsay and Huber, 1987) or strain transfer zones (Morley *et al.*, 1990) and are often characterised by diffuse faulting and local bending of the land surface. Relay ramps can act as important conduits for sediment transport and hydrocarbon movement across fault zones (Morley *et al.*, 1990; Peacock and Sanderson, 1994). Eventual linkage of the faults within an array may occur by breaching of the 'relay ramps' (Trudgill and Cartwright, 1994). Linkage may be "soft", where the ramps deform by tilting, folding and small scale faulting, or "hard" where continued interaction of fault segments leads to breaching of the relay and formation of a continuous through-going fault (figure 1.5).
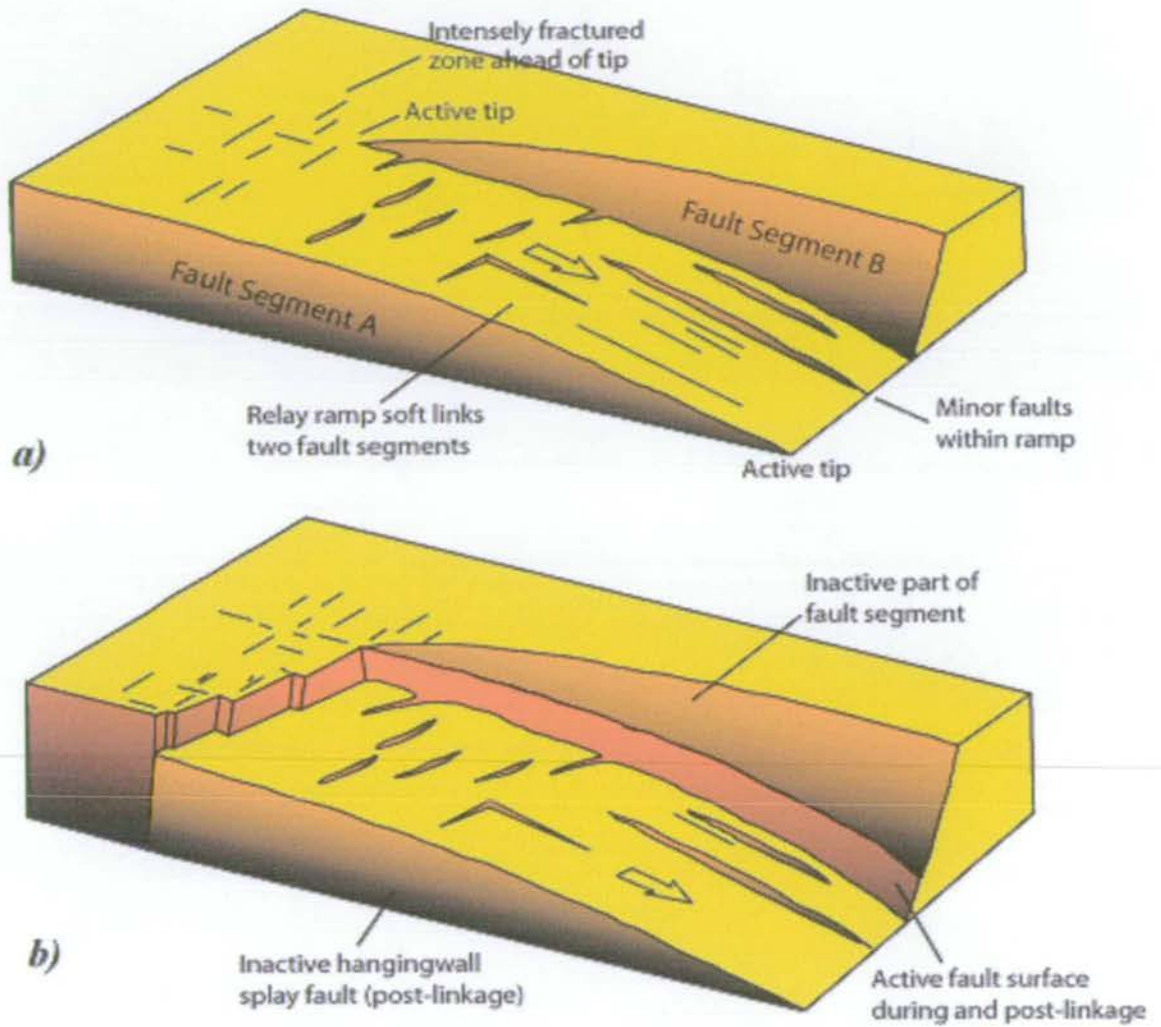
Figure 1.5 'Soft' and 'Hard' linked faults. a) Prior to breaching, Fault segments A and B are soft-linked by a relay ramp. b) Hard linkage of the fault segments and breaching of the relay ramp. (redrawn from Trudgill and Cartwright, 1994)

Once linked, these composite faults develop a displacement length profile that is comparable to that expected for a single, isolated fault, provided all the distributed deformation associated with the breached relay (tilting, folding etc) is taken into account (Dawers and Anders, 1995). However, it is still unclear as to whether most of the displacement on the through-going fault occurs prior to, or post linkage. The latter case would generate faults that are initially underdisplaced with respect to their length, together with large, shallow, hangingwall depocentres. These faults could later re-equilibrate towards the expected d-L profile of an isolated fault by increasing their displacement while maintaining constant length (e.g. Cartwright *et al.*, 1995). The former case would instead generate a 'saw-tooth' displacement-length profile and relatively deep, isolated, depocentres associated with each fault segment that would later coalesce during fault linkage. A consequence of having distributed deformation at sites of segment linkage is that the footwall profile of the linked fault will retain small displacement minima at the positions of linkage. Similarly, within hangingwall depocentres, transverse anticlines (Anders and Schlische, 1994; Schlische, 1995; McLeod *et al.*, 2000; Jackson *et al.*, 2002a) and release faults (Destro, 1995; Destro *et al.*, 2003) are often seen close to the main basin bounding faults. These intrabasin highs separate the primary depocentre into subbasins and have been interpreted as the positions of palaeo relay-ramps. Interpretation of 3D seismic volumes from the Northern North Sea has revealed how fault segment interaction and linkage can, in this way, control hangingwall depocentre evolution (Davies *et al.*, 2000; Dawers and Underhill, 2000; McLeod *et al.*, 2000).

Numerical modelling has also been usefully applied to understanding the development of linked fault arrays. Willemse *et al.* (1996) (figure 1.6) have used boundary element modelling to describe the effect of interaction between circular to elliptical fault surfaces with different fault aspect ratios (ratio of horizontal fault length to down-dip fault width) and have demonstrated the similarity between the displacement-length profiles of linked fault arrays and the elliptical shaped profiles expected for isolated faults.
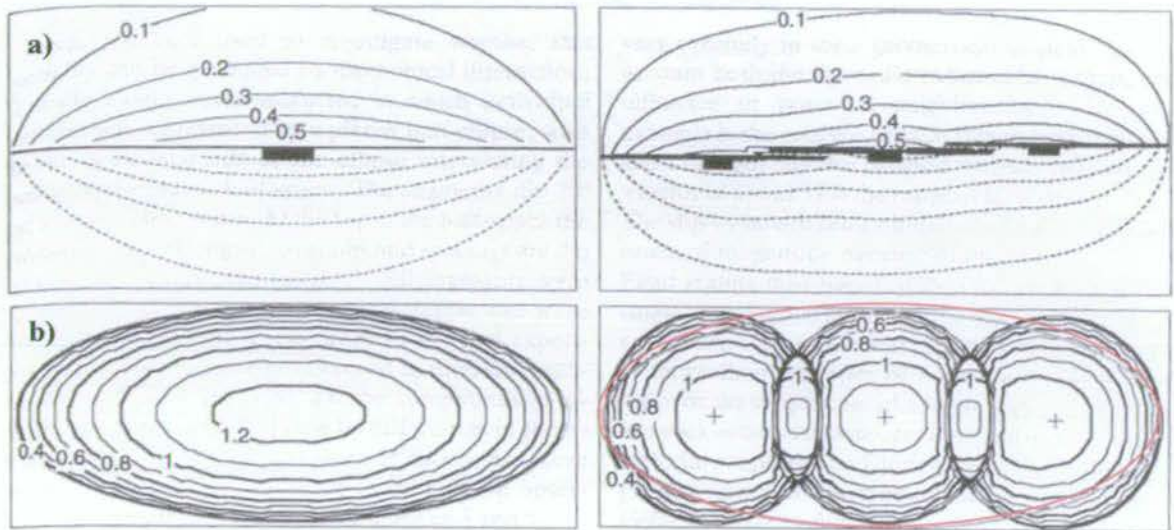
Figure 1.6 Comparison between a single elliptical fault (left) and a fault array of the same length (right) generated from boundary element modelling. a) Plan view of fault geometry showing contours of vertical displacement on a horizontal plane through the centre of the fault(s). b) Contours of normalised slip. For the fault array, the contours delineate total slip accommodated across the array, which is obtained by summing the slip on the individual segments. The red ellipse on the right shows the tip-line shape of the elliptical fault shown on the left (modified after Willemse *et al.*, 1996).

Recent and ongoing work now aims to quantitatively document the growth, interaction and linkage of fault arrays and hence, understand the impact on fault morphology, sediment dispersal patterns and fluvial pathways. Subsurface seismic data has been employed to study fault development over lengthscales ranging from a few kilometres (e.g. Meyer *et al.*, 2002) through to tens of kilometres (Contreras *et al.*, 2000; McLeod *et al.*, 2000; Young *et al.*, 2001). Essentially the methods of study are all very similar and involve correlating synrift sedimentary packages across fault-generated hangingwall depocentres with the aid of biostratigraphic or radiometric age constraints. Dawers and Underhill (2000) and McLeod *et al.* (2000) have demonstrated that formation of the >100km long Strathspey-Brent-Statfjord fault in the northern North Sea resulted from the coalescence of a number of 3-6km long, early syn-rift fault segments. Following linkage, there appears to have been only a partial re-equilibration of the overall fault system, since the observed maximum fault displacement is low (~2.3km), compared with that predicted from the displacement-length scaling relationship of $D_{max}=0.03L^{1.06}$ assumed by Schlische *et al.* (1996) (see figure 1.1). McLeod *et al.* (2000) believe this is due to a cessation of extensional tectonics before the fault could achieve a displacement-length relationship characteristic of the global fault dataset. Contreras *et al.* (2000) use temporally constrained 2D seismic data to document the growth and evolution of three interacting fault segments that bound the Lake Malawi basin in East Africa. The authors describe variation in the activity of the segments such that the location of maximum displacement does not remain fixed in time or space. Like McLeod *et al.* (2000) they suggest that irregularities in the overall displacement-length profile for the three segments may result from a lack of time for fault re-equilibration. Unlike the North Sea studies, however, Contreras *et al.* (2000) observe a considerable increase in fault segment displacement gradients prior to linkage. The Malawi fault appears to be developing by late linkage of fault segments (c.f. Dawers and Anders, 1995; Peacock and Sanderson, 1991) while the Strathspey-Brent-Statfjord fault of the North Sea appears to have formed from early linkage of fault segments followed by some degree of displacement re-equilibration (c.f. Cartwright *et al.*, 1995).

The precise relationship between relay ramps and fault morphology at depth is still a subject of current debate (Walsh *et al.*, 2003). Field-based studies can, in general, only offer a two-dimensional perspective. Studies of coal-mine plans and seismic reflection data have revealed faults that, though appearing to consist of an array of isolated segments in one plane of observation, actually link to form a single, through-going, structure when viewed in 3D. In such

a case, relay ramps may form as a result of fault bifurcation or soft-linked fault-stepping during fault tip-propagation due to the presence of some irregularity or asperity at the growing fault tip line (Childs *et al.*, 1995, 1996; Huggins *et al.*, 1995; Walsh *et al.*, 2003). Fault segments documented in field-based studies may therefore share a common fault plane at depth and grow as kinematically related structures from inception. Walsh *et al.* (2003) argue that such a mechanism would explain the often observed similarity between the aggregate displacement along a segmented fault array and that of an individual, isolated fault. Since the fault segments have *always* been part of the same fault structure at depth, the overall displacement-length profile would be expected to mirror that of the underlying fault. Therefore, it is suggested that the key to differentiating between faults that have evolved from an array of kinematically related structures, as opposed to from an array of initially isolated structures, requires a detailed analysis of aggregate fault displacements, taking into account both localised and distributed deformation. Fault arrays that show displacement deficits at the sites of segment linkage must have grown as a consequence of interaction between initially isolated segments, whereas those with an overall displacement-length profile similar to that of a single fault *could* have formed from the growth of a kinematically related fault system (Walsh *et al.*, 2003).

Meyer *et al.* (2002) studied the development of a population of mainly Pliocene and Pleistocene syn-sedimentary normal faults of the Timor Sea, offshore NW Australia, using 3D seismic reflection data. Faulting was initiated approximately 6Ma and early fault development was characterised by rapid lateral propagation, possibly as faults were reacting to, deeper, Tertiary normal fault lineaments. Following this initial 1-2Myr period, faults began to accrue displacement at a constant rate while their lengths remained relatively unchanged. This work challenges traditional notions that faults grow self-similarly by a systematic increase in both displacement and length with time.

Studies based on the analysis of seismic data are to some extent limited by the vertical seismic resolution, which is often not better than ~25m. Fieldwork has attempted to improve the temporal resolution of data that records the early synrift phase of fault growth and linkage. Fault evolution in the Suez rift has been extensively documented by a number of authors (Gawthorpe *et al.*, 1997, 2003; Gupta *et al.*, 1999; Sharp *et al.*, 2000; Jackson *et al.*, 2002a). Jackson *et al.* (2002a) combine a detailed analysis of syn-rift stratigraphy (chronology, thickness changes, facies variations and onlap patterns) with more traditional structural analyses (e.g. d-L data) to

provide a 6.4Myr growth history for the East Tanka fault zone, Suez Rift. During the initial 2.4Myrs of rifting, this fault was composed of two, 1-1.5km long, isolated fault segments that eventually hard linked to form a single fault zone some 3.5km in length. Expanding on this work, Gawthorpe *et al.* (2003) describe the temporal evolution of a normal fault population from a 500km^2 area of the Hammam Faraun fault block, Suez rift over a 24Myr period from Oligocene to the present day. Thickness variations, facies distributions and onlap/truncation patterns within the synrift sedimentary sequence preserved in hangingwall depocentres were analysed in order to define the location of fault tips, fault segment lengths and locus of fault activity for different periods in the rift history. Additionally, ages for the five synrift formations and other key stratal surfaces established by means of biostratigraphic, magnetostratigraphic and $^{87}Sr/^{86}Sr$ radiometric determinations have allowed a quantitative reconstruction of the fault development in this region (Sharp *et al.*, 2000; Gawthorpe *et al.*, 2003). In support of the observations of Meyer *et al.* (2002), many of the fault segments in this region appear to have achieved their final trace length very early, within the initial 2.5Myrs of rifting. Subsequently faults accumulated displacement but showed little lateral propagation.

Cosmogenic dating of uplifted fault blocks is another relatively new technique being used to constrain the earliest phases of fault segment growth and linkage (Jackson *et al.*, 2002b; Gupta *et al.*, 2003). Gupta *et al.*, 2003 dated well exposed windgap surfaces along the footwall crest of a 4.5km long fault array in the Canyonlands, Utah using ^{10}Be surface exposure dating. Windgaps are erosional nickpoints observed along scarp crests that result from previous fluvial incision. It is suggested that windgaps develop as streams are diverted away from their original pathways by a rapid increase in fault displacement rate, such that the rate of fluvial incision into the scarp cannot keep pace with uplift (Jackson *et al.*, 1996; Morewood and Roberts, 1999, 2002; Gilpin *et al.*, 2001; Gupta *et al.*, 2003). Gupta *et al.* (2003) demonstrate that the oldest ^{10}Be ages in the Canyonlands study correspond to the central fault segment of the array, which has the greatest tectonic offset, while the youngest ages are associated with an adjacent fault overlap zone. They also imply that high displacement rates in the overlap zone may be due to mechanical interaction of the overlapping segments. Jackson *et al.* (2002b) have used ^{10}Be measurements in quartzites to study the growth and lateral propagation of a late Quaternary anticline forming above a blind reverse fault in Central Otago, New Zealand.

1.2.4 Fault-length cumulative-frequency distributions

Many studies of fault populations have attempted to classify the cumulative frequency distributions of fault lengths according to a statistical law. To some extent, such a law would be able to define the spatial and temporal development of fault arrays and allow some prediction to be made regarding the physical parameters governing fault growth and propagation. Essentially, the majority of fault arrays described in the published literature have been characterised by one of two distributions: 1) an exponential law of the form,

$$N(L) = N_T e^{-\lambda L} \tag{1.4}$$

Where: N is the total number of faults with dimensions greater than or equal to some length (L), N_T is the total number of measurements and λ is a scaling parameter that is the inverse of the characteristic fault length.

Or, 2) a power law of the form,

$$N(L) = \alpha L^{-C} \tag{1.5}$$

Where: α is a constant related to the total number of measurements and C is the power-law exponent (Clifton *et al.*, 2000).

Fault populations that obey an exponential length-frequency distribution are generally observed either 1) in the early stages of evolution, when the extensional terrain has only undergone a small amount of strain, and where the nucleation of new faults exceeds the growth of existing faults (Cowie *et al.*, 1995; Gupta and Scholz, 2000) or 2) after the largest structures have exceeded the thickness of the brittle layer containing the faults (Ackermann and Schlische, 1997). Power-law distributions appear to represent fault populations in regions that have undergone an intermediate amount of crustal extension. In this situation fault arrays behave in a manner governed by the power law exponent, ν. The larger the value of the exponent the greater the influence of the small faults on the overall population. Some authors have suggested that the power law exponent of fault populations may decrease through time as more of the extensional deformation becomes localised onto a few through-going structures (Sornette *et al.*, 1990;

Cowie *et al.*, 1995; Cladaunos and Marrett, 1996). Wojtal (1994) has described 'facetted' length-frequency distributions for various scales of reverse faults found in thrust duplexes. He suggests that the observed distribution reflects the fact that the faults are not behaving as a single population but rather the majority of the regional strain is taken up on a few large faults bounding fault duplexes, which can be regarded as a single fault population, as distinct from the smaller, intra-duplex structures which take up comparatively little deformation. Similarly, in their study of centimetre-scale normal faulting within the Mesozoic Danville rift, USA, Ackermann and Schlische (1997) have described two sub-populations of faults; those that have exceeded the thickness of the mechanical layer containing the faults and those that are contained entirely within that unit (figure 1.7). Such multifractal fault length-frequency distributions suggest that it may not be possible to characterise a fault array by a single statistical law and that cumulative frequency distributions may change with time (Wojtal, 1994; Cowie *et al.*, 1995).
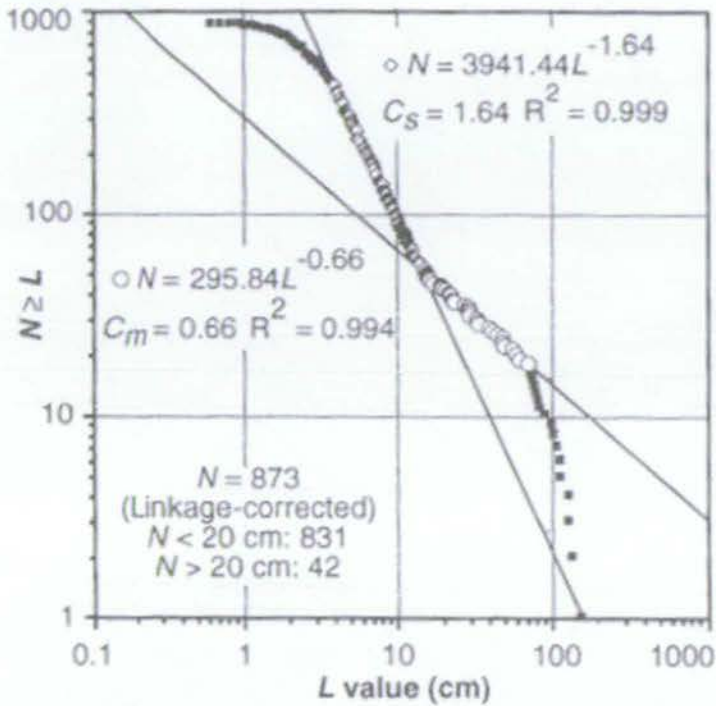
Figure 1.7 'Facetted' cumulative frequency distribution for fault lengths within the Danville rift. Note two distinct segments, suggesting two subsets of faults having slopes that differ by a value of ~1.0. Subscripts of m and s are for master faults and small faults, respectively. C is the power-law exponent. (from Ackermann and Schlische, 1997).
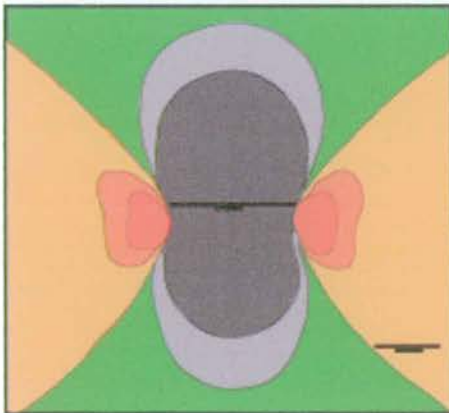
Figure 1.8 Diagram showing the Coulomb Failure Function due to slip on a dipping normal fault. Areas of stress enhancement are indicated in red. Optimally orientated structures are located parallel and along strike from the ruptured fault, as indicated. Regions of stress shadow are located next to the centre of the rutured fault, here contoured in grey. (redrawn from Cowie, 1998)

1.2.5 Models of rift development

The Coulomb Failure Function (CFF) can be used to explain growth, interaction and linkage of neighbouring fault segments (Cowie, 1998). This provides a mechanism of positive feedback (stress loading) that encourages underlapping faults to grow together, and ultimately link, while slowing propagation of an overlapping fault tip entering the 'stress shadow' of a neighbouring fault segment (figure 1.8).

A number of workers have applied this mechanism to understand growth and evolution of a two-dimensional fault array as a product of fault segment growth and linkage (Cowie, 1998; Cowie *et al.*, 1993, 1995, 2000). The authors use numerical methods to simulate shear deformation of an elastic plate using a 2D square lattice. A constant velocity is applied along one edge of the plate while the other is kept fixed. At random, each lattice element is prescribed a certain stress threshold value, above which, the element will rupture. Cowie *et al.* (1995) applied this model to investigate the earliest phase of rupture development and how the fault pattern emerges and evolves with increasing strain. The inherently random nature of the stress threshold values means that, with application of stress, the plate initially ruptures diffusely with the nucleation of small faults across the entire surface. Some of these faults continue to accumulate displacement and grow laterally by breaking previously unruptured elements and by interaction and linkage with neighbouring structures, while the majority show little evolution through time and eventually become inactive. Hence the general progression through time is that the number of active faults decreases while the size and displacement of a few faults gradually increases. The implications for the growth of large sedimentary depocentres as a result of the formation of these late, throughgoing, faults are considered by Cowie *et al.* (2000) and is summarised in figure 1.9. They recognize four distinct stages in fault array evolution:

i) *Early rift initiation:* This is characterised by diffuse, small scale faulting and associated numerous isolated depocentres. There is only a weak interaction between faults at this stage.

ii) *Mid-rift initiation:* During this phase isolated fault segments continue to nucleate but interaction between neighbouring structures becomes progressively more important, leading to the onset of more numerous linkage events. Fault associated depocentres not only enlarge and coalesce but are also calculated to shift laterally as fault activity migrates between segments along strike.

iii)   *Late rift initiation:* Extensive fault interaction and linkage leads to the generation of large faults and major depocentres. Smaller, isolated fault segments become inactive as they enter the stress shadows cast by the larger structures when they propagate and link laterally. The fault population is characterised by the presence of several large, linked faults, and numerous early-formed minor faults that are relict from stages i) and ii).

iv)   *Rift initiation-rift climax transition:* The active fault population during this final phase is dominated by a few large, through-going structures. Many smaller faults in footwall and hangingwall areas have since become inactive. Major depocentres are associated with the large, active faults and the pattern of subsidence along strike is more uniform than that observed during phase ii).

The 2D nature of this thin-plate model restricts its application to faults that are large compared to the assumed length of the lattice elements. This assumed length can be varied according to the scale of the rift setting under consideration (e.g. Cowie *et al.*, 1995; Cowie *et al.*, 2000).

Conclusions drawn from numerical modelling of fault network evolution have been tested and to some extent confirmed by independent analytical and fieldwork studies. Nicol *et al.* (1997) calculated long-term displacement rates, averaged over time intervals of 1 to 40 Myr, along 86 synsedimentary normal faults. The data were for normal faults from offshore (via 2D and 3D seismic analysis) and onshore extensional terrains. The authors observed that the displacement rates on faults within a single fault system were generally stable over time scales greater than ~1Myr and that the rates depend strongly on the relative size of the fault. They suggest that faults become large relative to nearby faults by having higher displacement rates, even when small, rather than being active for longer. According to this model, initial size differences between faults were established during the nucleation and early growth of the fault system (i.e. within a period less than the 1Myr time resolution).

(1) Early Rift Initiation: Onset of fault nucleation and segment growth in relative isolation

Isolated depocentre develops adjacent to bilaterally propagating segment

- Initiation and growth of numerous small isolated depocentres adjacent to early formed faults

(2) Mid-rift Initiation: Continued nucleation, and onset of segment interaction and linkage

w, x, y, z: enhanced

- Abrupt enlargement of early formed depocentres by linkage of adjacent fault segments.
- Major depocentres established in hangingwall of longer segments.

(3) Late Rift Initiation: Dominant fault segment interaction and linkage

w, x : inactive
y, z : enhanced

Major depocentre develops as large fault array grows by linkage

- Growth of major depocentres by coalescence of smaller depocentres as deformation localises on major fault segments. Maximum subsidence rates at segment centres
- Depocentres adjacent to inactive fault segments cease to subside

(4) Rift Initiation – Rift Climax Transition: Full linkage of fault segments to produce a through-going fault system

w, x : inactive
y, z : enhanced

- Single large depocentre develops adjacent to the major linked fault
- More uniform subsidence rate along strike

Figure 1.9 Tectono-stratigraphic model for synrift depocentre evolution in response to fault array development (from Cowie *et al.*, 2000).

In their analysis of a Tertiary syn-sedimentary normal fault population identified from 3D seismic reflection data, Meyer *et al.* (2002) demonstrate a progressive concentration of strain onto fewer and larger faults through time. Lengths and displacement rates of individual faults were established early in the rift episode and were generally constant through time, with larger faults moving faster than smaller ones. This suggests that the length-frequency distribution of the faults remained constant and there was little, if any, linkage between neighbouring fault segments. Essentially, the hierarchy of faults in the array developed early in the history of faulting.

McLeod *et al.* (2000; 2002) have observed small, kilometre scale, faults in the hangingwall to the Strathspey-Brent-Statfjord fault of the Northern North Sea that appear to represent early, now inactive extensional structures. These early structures, which control the distribution of the Middle Jurassic Tarbert Formation (Davies *et al.*, 2000), were active during the initial 3-4Myr of the rift event as part of a diffuse fault population, but later died as strain became localised and the basin developed a graben-like geometry.

Faults in the Gulf of Suez appear to have evolved from a diffuse network of numerous, weakly interacting fault segments to a situation where deformation was localised on to a few main border faults (Gupta *et al.*, 1998; Sharp *et al.*, 2000; Gawthorpe *et al.*, 2003). Fault localisation would be expected to produce a progression from many isolated subbasins to a much larger half-graben structure with many of the early, ultimately inactive, faults preserved in its hangingwall and footwall. Such early depocentres have been inferred in the field from the distribution of the early synrift Nukhul Formation on the footwall to the Miocene Suez Rift (Gupta *et al.*, 1998). Similarly Sharp *et al.* (2000) have described examples of small fault controlled basins of Oligo-Miocene age on the eastern flanks of the same rift. Like the fault populations described in Nicol *et al.* (1997) and Meyer *et al.* (2002), there is evidence, in Suez, for the progressive localisation of strain and death of small faults through time, though unlike these studies there is evidence for segment linkage following early fault propagation. Hence, there is no early fault hierarchy within this population.

Analogue modelling has also provided useful information on the development of extensional fault populations (Ackermann *et al.*, 2001; Mansfield and Cartwright; 2001). Mansfield and

Cartwright (2001) describe growth of faults as a result of the gravitational collapse of a two-layer plaster/mud sequence. They observe fault segment growth, overlap and linkage over a wide range of scales across the fault population.

1.2.6 Relevance of this study to previous work

While a lot of work has attempted to describe the mechanisms of fault growth and evolution, in practice it has been difficult to quantify such processes. Dawers and Anders (1995) note that most models of fault growth (e.g. Peacock and Sanderson, 1991) assume that "the final displacement profile is a proxy for the growth history of the fault". In other words, the location of maximum displacement must represent the point of fault nucleation. Furthermore, this suggests that faults with symmetric profiles propagated equi-dimensionally from the nucleation point, while other faults with steep displacement gradients and asymmetric profiles were influenced by fault interaction. However, these studies cannot unequivocally establish and accurately define a fault growth history over geological time scales.

Attempts have been made to understand the temporal evolution of several large normal fault zones (Anders and Schlische, 1994; Contreras *et al.*, 2000; Dawers and Underhill, 2000; McLeod *et al.*, 2000) using dated stratigraphic horizons to constrain the temporal and spatial pattern of footwall uplift and hangingwall subsidence. Analysis of subsurface data from the Timor Sea provides evidence for progressive strain localisation within a normal fault network (Meyer *et al.*, 2002). Gawthorpe *et al.* (2003) have undertaken an important fieldbased study documenting the development of fault populations and further evidence for strain localisation. Such studies have a higher resolution than subsurface data, and are essential if we are to test numerical rifting models such as that of Cowie *et al.* (2000), which imply early, diffuse faulting developing towards localisation onto large, through-going structures. However, there is still no consensus between qualitative self-similar fault growth models (e.g. Peacock and Sanderson, 1991; Dawers and Anders, 1995) and models based on temporal constraints from syn-rift stratigraphy that suggest early fault propagation followed by later accumulation of displacement (e.g. Meyer *et al.*, 2002; Gawthorpe *et al.*, 2003). It is also still equivocal as to whether fault length hierarchies are established early during basin evolution (e.g. Nicol *et al.*, 1997; Meyer *et al.*, 2002) or if faults begin life as small features with low displacement rates that later interact and link to form much larger fault blocks (Cowie *et al.*, 2000; Gawthorpe *et al.*, 2003). There

are still too few studies focused on quantifying the earliest syn-rift phase of basin evolution to be sure which of these models are more reasonable.

The Southern Kenya Rift offers an opportunity to ground-truth ideas of fault development. Extensive flows of Pleistocene trachyte and basalt blanket the floor of the rift in the vicinity of Lake Magadi. During and subsequent to regional volcanic activity, a network of normal faults (locally known as *'grid faults'*) broke the floor of the valley into ribbon-like horst-and-graben features (Baker and Mitchell, 1976; Crossley, 1976, 1979). Faulting ranges from several hundred metres to tens of kilometres in length and shows evidence for fault segmentation, interaction and linkage. The competent nature of the rocks in this region and the lack of significant erosion have ensured excellent preservation of the original fault generated saw-tooth topography of the rift valley floor. A major advantage of the Magadi area is that the rift floor faults w ere a ctive *p rior t o, a nd c ontemporaneously with*, d atable p hases o f v olcanism i n t he region. Evidence for t his c omes from field observations of trachytic and basaltic l ava flows resting unconformably on tilted fault blocks and onlapping against and around pre-existing fault blocks. In such areas it is possible to establish a chronology of individual fault growth and fault network evolution. This will be considered further in chapters 2 and 3.

Chapter 2: Introduction to the Geology and Structure of the South Kenya Rift

2.1 The East African Rift System

2.1.1 Introduction

The African Rift System is a 3,500km long curvilinear depression that runs from the Gulf of Suez in the north, to Namibia in the south. The East African sector of the system is composed of two tectonically distinct rift trends known as the Eastern and the Western rift branches, which are separated by Lake Nyanza (Victoria) (figure 2.1). Although both rift arms are tectonically active, the Western Rift is characterised by a greater number of large magnitude seismic events (e.g. Foster and Jackson, 1998) than the Eastern Rift, where earthquakes are generally small and shallow (see figure 2.2 and 2.3, table 2.1). However, microseismicity has been recorded at a number of locations along the length of the Eastern Rift (Young *et al.*, 1991; Hollnack and Stangl, 1998; Ibs-von Seht *et al.*, 2001, see also section 2.4.5).

The Western Rift is characterised by a narrow (maximum width of 50km) system of elongate extensional basins, many of which are covered by extensive, deep, lakes: Mobutu, Edward, Kivu, Tanganyika, Rukwa, and Malawi. Basin fills imaged in 2D seismic data indicate maximum sedimentary thicknesses of 7-8km (Morley *et al.*, 1999). Extension in the Eastern (Gregory) Rift was initiated in the Late Oligocene, prior to development of the western branch (Morley *et al.*, 1999). However, the rift basins of the eastern branch are filled, and in places overlapped, by extensive Miocene-Recent flood lava flows. With the exception of Lake Turkana, the lakes of the Eastern Rift are generally small and shallow. Morley *et al.* (1999) suggest that, in general, the Western Rift can be regarded as a good model for a young continental rift while the eastern branch is more representative of a mature continental rift system that has failed to produce oceanic crust.
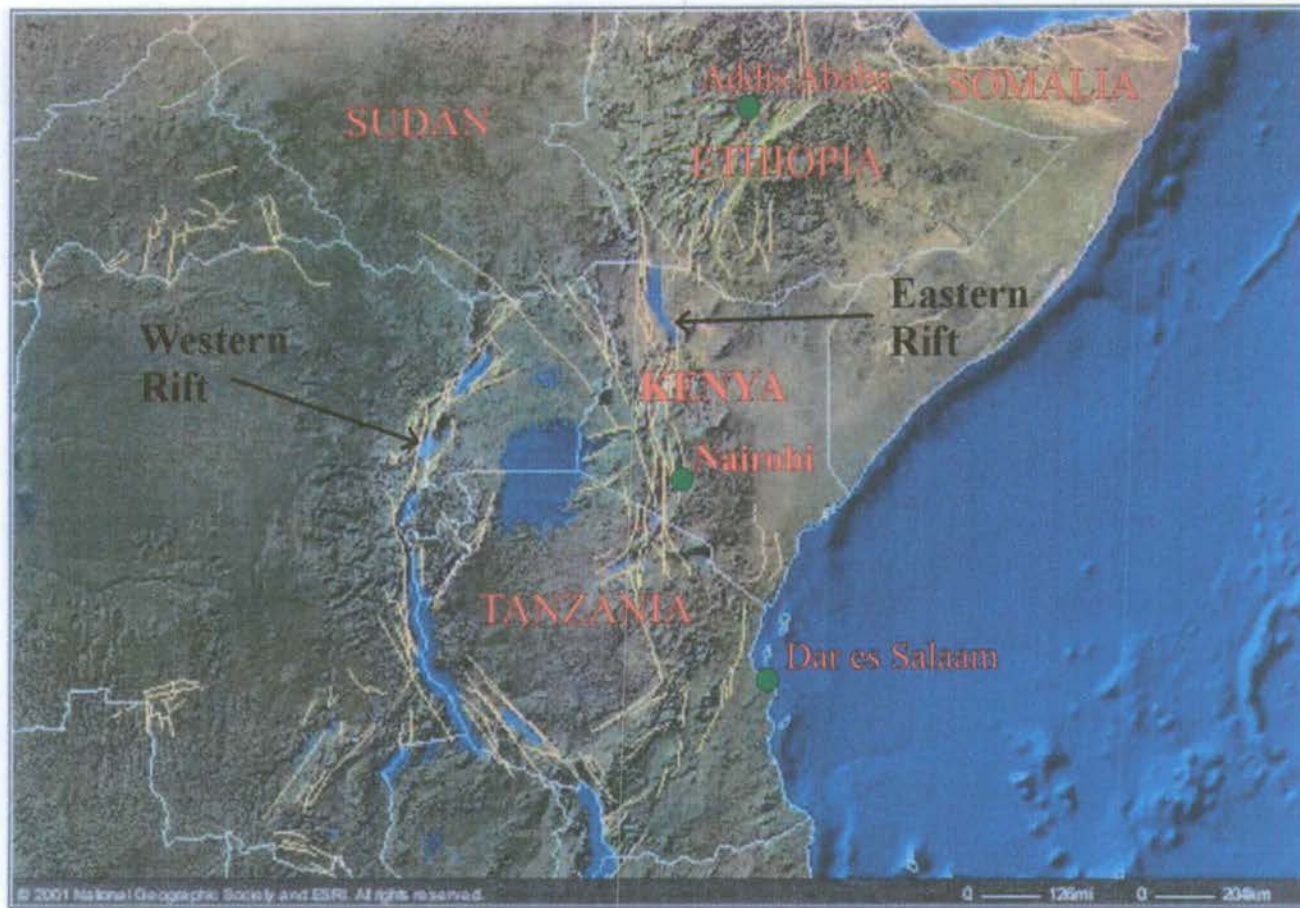
Figure 2.2 Map showing the onshore topography and offshore bathymetry of the East African Region. The two principal arms of the East African Rift System are identified from the concentrations of fault lines (marked in yellow). Also apparent are the main rift valley lakes, which occupy topographic depressions along both rift axes (from National Geographic and ESRI, 2002).

Event Magnitude Map
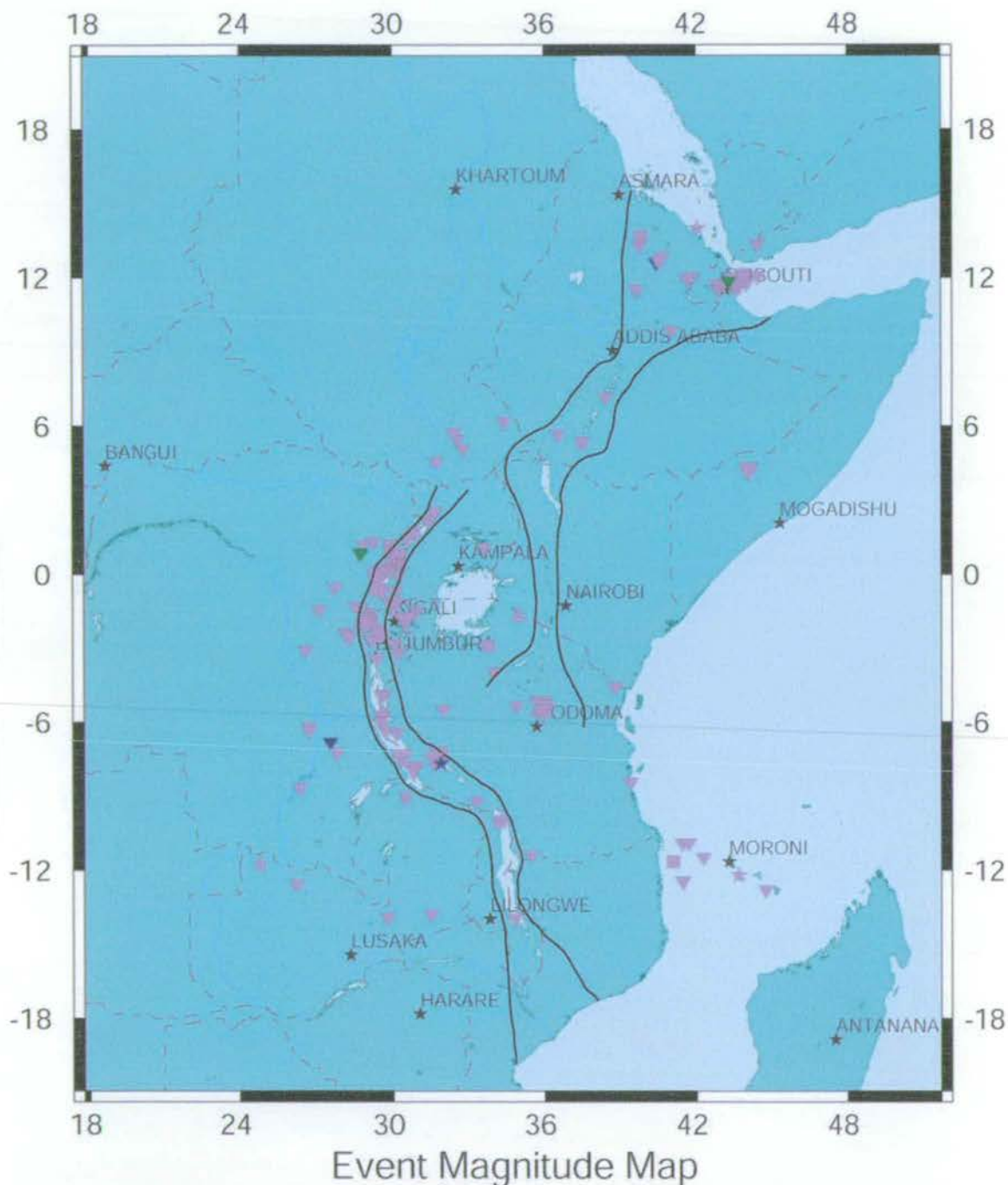
Figure 2.3 Map of East Africa showing the locations of large earthquakes (M=5-8) occurring during the period 7/8/1993-7/8/2003. The depth of earthquake nucleation is indicated by the colour bar in Table 2.1. For each event, the shape of the symbol indicates the seismic catalogue used for epicentre location. The majority of events can be located to the crust of the Western Rift arm. Map generated using Incorporated Research Institutions for Seismology (IRIS) (2003).

Event Magnitude Map
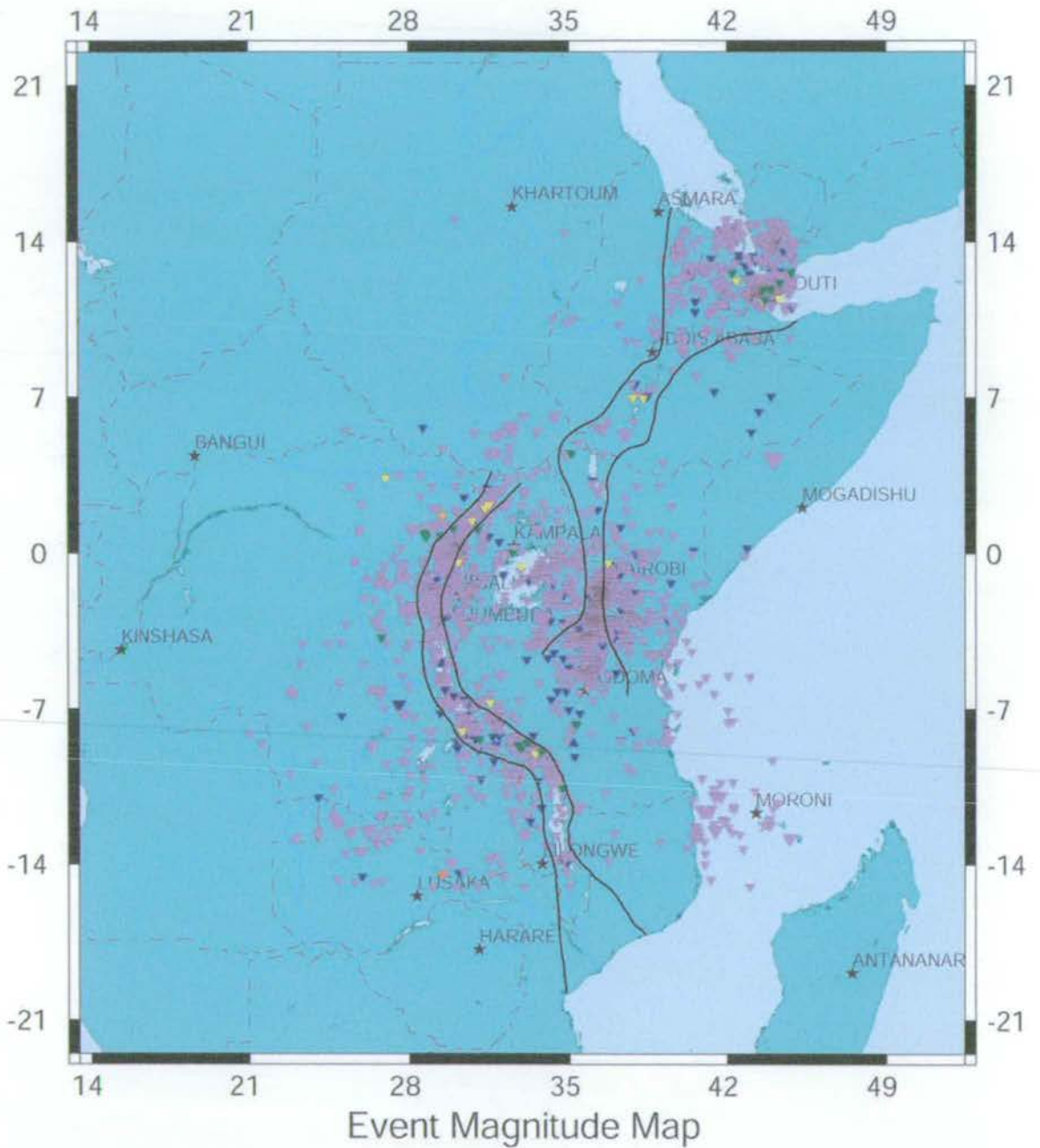
Figure 2.3 Map showing epicentre locations for all earthquake events occurring in East Africa during the period 7/8/1993-7/8/2003. A key to symbols is given in Table 2.1. The image was generated using Incorporated Research Institutions for Seismology (IRIS) (2003).
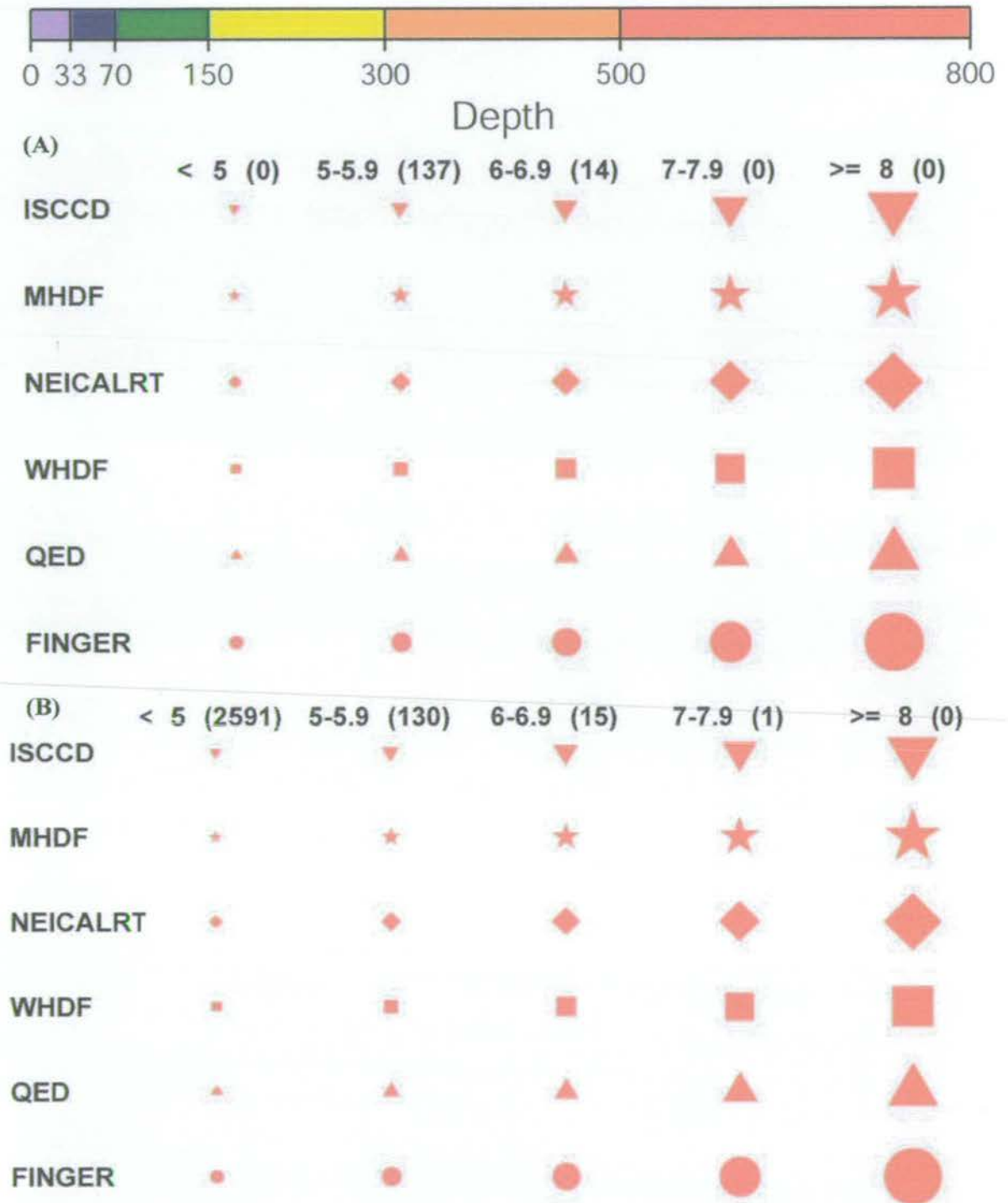
Table 2.1 Key to accompany: (A) figure 2.2 and (B) figure 2.3. Colour bar indicates earthquake depths. List of earthquake catalogues: ISCCD: International seismological centre list, MHDF: Monthly Hypocentre Data File, NEICALRT and FINGER: lists distributed by the USGS National Earthquake Information Service (NEIC), WHDF: Weekly Hypocentre Data File, QED: Quick Epicentre Determinations. Columns are groupings of earthquake magnitude (number of events in parentheses) (from Incorporated Research Institutions for Seismology (IRIS), 2003).

2.1.2 Rift basin development

Through the analysis of 2D seismic and bathymetric data recorded on Lake Tanganyika, Rosendahl and his co-workers (e.g. Rosendahl *et al.*, 1986) were the first researchers to recognise some of the major structural features of the East African Rift Valley. They showed that the rift floor beneath Lake Tanganyika is composed of a series of opposite-facing asymmetric half-grabens, separated by high ridges of basement rocks, termed accommodation or transfer zones. Further studies based on this groundbreaking work have identified similar structures in other regions of the rift valley. Morley (1999a) has documented a number of trends in rift basin evolution through the analysis of syn-tectonic sedimentary sequences revealed on 2D seismic data. He suggests that rifts develop initially as a series of along-strike synformal depressions characterised by a random mixture of fault dips. As extension continues, some faults grow by linkage while many others cease activity, as strain becomes concentrated onto fewer, larger faults. At this large scale, it appears as though individual basins of the East African Rift may have developed by means of a mechanism of strain localisation, as predicted by numerical modelling (see section 1.2.5). During the later stages of rift development, all the extension may become localised onto a basin-bounding fault, hence forming a half-graben geometry.

The nature of the inter-basinal transfer zones depends to a large extent on the polarity of the basin-bounding normal faults (figure 2.4). Adjacent basins with the same polarity, i.e. the bounding fault is on the same side in both basins, may, with time, merge due to soft-linkage of a relay ramp between the faults. These are classified as synthetic transfer zones (Morley *et al.*, 1990). Conjugate transfer zones exist where the neighbouring basins have opposite polarities and, in that case, the structure of the transfer zone may be much more complex (Morley, 1999b). Though the majority of extension is localised on the basin-bounding faults deformation is also commonly taken up on synthetic minor faults, located parallel to the major structures. Where there is an along-strike change in the polarity of the basin bounding faults, there will be a concomitant switch in the polarities of the minor structures, most often through soft linkage transfer of displacement on interfingering sets of faults (Morley, 1999b) (figure 2.5). As rifting proceeds, one of the border faults may change polarity such that the conjugate transfer zone changes to a synthetic type and the rift basins merge to become a single entity. Such a switch in polarity will involve a complex reorganisation of the

associated minor, synthetic faulting, as has been recorded in the Paleogene-Recent Turkana Basin and the Late Cretaceous–Paleogene of the Anza Graben (Morley, 1999b).
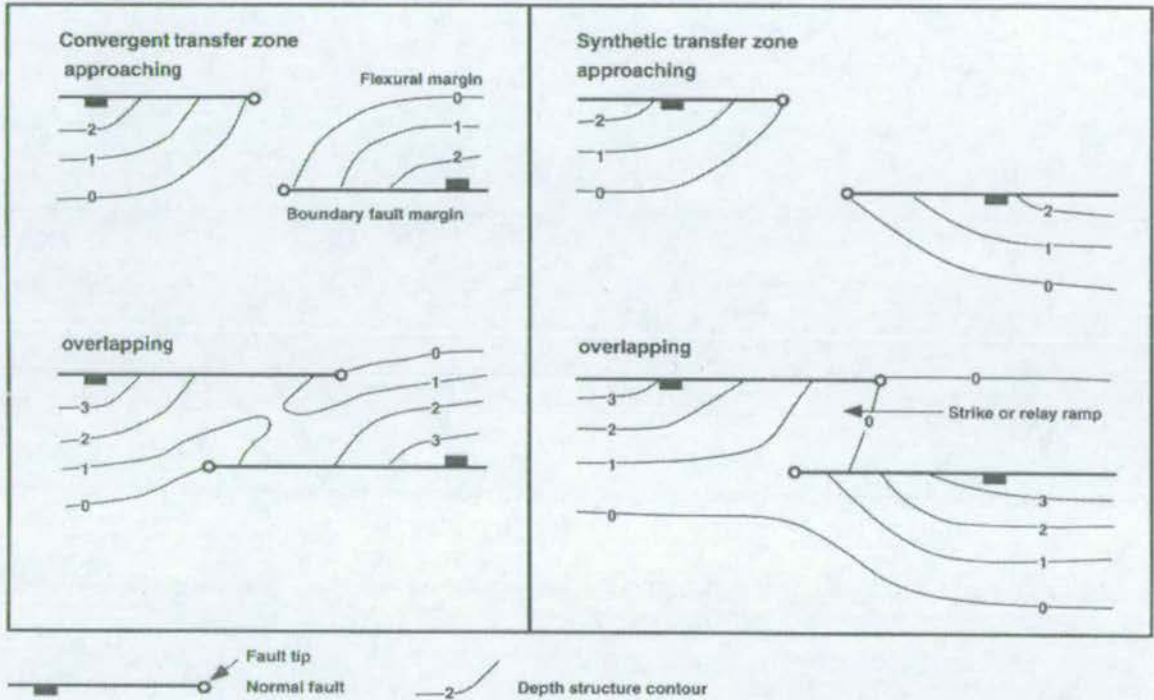
Figure 2.4 Diagram showing the development of transfer zone geometries during the growth of two faults of opposite polarity (left – 'convergent transfer zone') and identical polarity (right – 'synthetic transfer zone') (from Morley, 1999b).

Figure 2.5 Idealised map showing the complex interfingering of minor fault sets within a convergent transfer zone. (redrawn from Morley, 1999b)

2.2 The Kenya Rift

2.2.1 Introduction

The Kenya Rift forms the central and most southerly portions of the eastern branch of the East African rift system and extends for some 900km from the Turkana depression, along the Kenya-Ethiopia border, in the north, to the Northern Tanzanian divergence in the south (figure 2.6). The rift roughly follows the location of the suture between the Tanzanian Archean Craton in the west and the Mozambique Mobile Belt in the East. The rocks of the Mozambique Mobile Belt were emplaced on top of the Tanzanian cratonic mass during the Late Proterozoic (850-720Ma) as a series of nappes transported from the north and northeast. Following the initial emplacement, a phase of sinistral transcurrent deformation, between 635Ma and 550Ma, overprinted the suture zone with a pervasive stretching fabric. The final phase of collision established a series of NW-SE trending, upright, ductile/brittle shear zones that cut, and locally reactivate, pre-existing structures.

2.2.2 Influence of basement heterogenities on rift development

The multiple deformation events associated with the Proterozoic orogenesis produced three important mechanical anisotropies that have influenced the location of subsequent deformation within the East African continental crust. (Smith and Mosley, 1993; Morley, 1999c). Perhaps the most important of these is the boundary between the Archean Craton and the Mozambique Belt. This represents an important thermal and mechanical heterogenity within the lithosphere, which as mentioned above, is believed to have directly influenced the position and style of Mesozoic and Cenozoic rifting in East Africa. Of secondary importance are the continental-scale, NW-SE trending, shear zones (termed discrete fabrics by Morley, 1999c) that cut both the craton and the mobile belt and which appear to affect rift orientations and the location of rift transfer zones (Smith and Mosley, 1993). These shear zones effectively represent regions of weakness that may be reactivated in preference to the creation of new fractures in the intact country rock, provided the fabric is in the correct orientation with respect to the principal stress axes.

The pre-existing NW-SE trending shear fabrics appear to have had an important influence on the development of the East African Rift. Smith and Mosley (1993) have subdivided the Kenyan Rift into three structural provinces, separated by two major NW-SE trending fault zones; the Kerio-Borgoria-Marmanet transfer zone in the north, and the Engorika-Magadi-Lembolos transfer zone in the south (figure 2.6). Both fault zones appear to have a profound influence on rift fault morphology over a variety of scales. Within the provinces fault orientation is largely N-S, as a direct response to the E-W regional extension direction, and there is little influence from pre-existing basement lineaments. It can be regarded as 'extensional deformation associated with a homogeneous substratum' (Le Turdu *et al.*, 1999). Elsewhere, interaction of the regional N-S fault trend with basement heterogenities that are orientated at an oblique angle to the rift axis results in unusual fault geometries. Studies of fault morphology, based on a combination of SPOT remote sensing data and fieldwork, in the Baringo-Borgoria Region of the Central Kenya Rift have revealed zig-zag fault patterns and en echelon, sigmoidal, horst and graben structures (Grimaud *et al.*, 1994; Le Turdu *et al.*, 1995, 1999). This unusual style of faulting has been interpreted to result from interference between regional N-S grid faulting and a number of N140-160° trending discrete basement heterogenities that form part of the Aswa Shear Zone (a major NW-SE orientated mylonite lineament that represents a remnant of the Proterozoic collisional event and is believed to underlie the Kerio-Borgoria-Marmanet transfer zone (shown in figure 2.6)).

Another region in which to study unusual fault morphologies is the South Kenya Rift. The Magadi Region of that part of the rift is largely dominated by N-S orientated fault swarms (see also section 2.3). However, in a region west of Lake Magadi, N-S trending faults of all length scales either stop, or curve, into an oblique trend of N150-160°. This zone, termed the Magadi Transverse Zone, is believed to result from fault interaction with a basement lineament (Le Turdu *et al.*, 1999; Morley, 1999c) and is characterised by a series of almond-shaped horsts and grabens (figure 2.7).

A feature common to all oblique fault zones in the Kenya rift is that they rarely form a continuous fault system. Hence, they are passive features and do not appear to function as regional oblique slip or strike-slip transfer faults (Grimaud *et al.*, 1994; Morley, 1999c) (figure 2.8).

EXPLANATION

▭	Precambrian Basement
▭	Kenya Rift Zone
▭	Lakes
▭	Other Areas
/	Major normal fault
⁄	Basement lineament
T R Z	Turkana Rift Zone
G R Z	Gregory Rift Zone
N R Z	Nyanza Rift Zone
Ba	Lake Baringo
Bo	Lake Borgoria
Na	Lake Naivasha
M	Lake Magadi
N	Lake Natron
Mn	Lake Manyara
Ey	Lake Eyasi
S	Suswa Volcano
K B M	Kerio-Borgoria-Marmanet fault zone
E M L	Engorika-Magadi-Lembolos fault zone

Figure 2.6 Structure of the Kenya Rift (modified after Smith and Mosley, 1993). Black rectangle indicates location of figure 2.9.
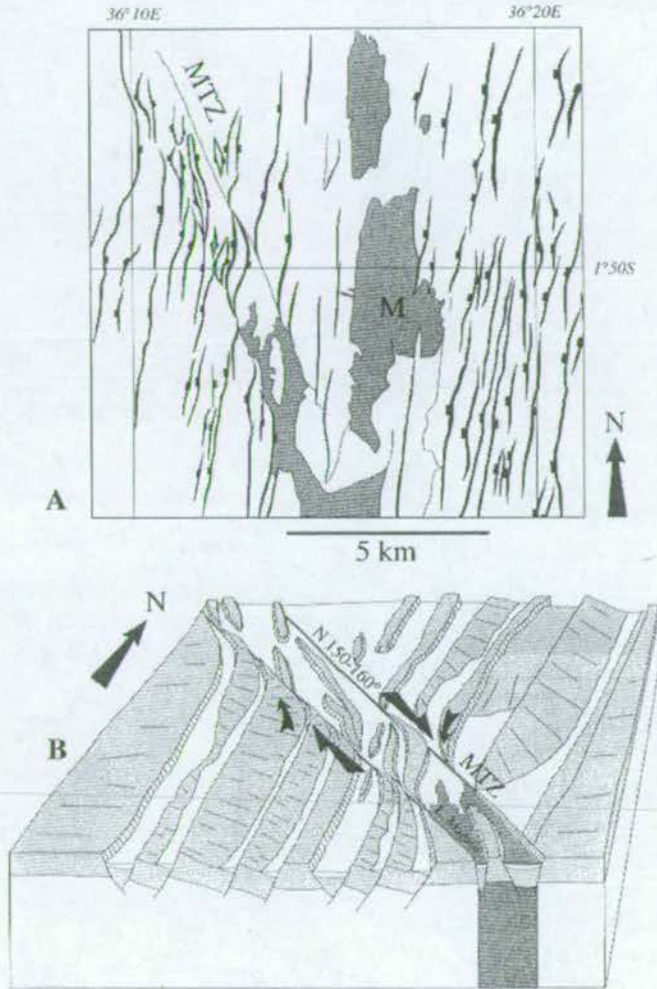
Figure 2.7 Fault structure associated with the Magadi Transverse Zone (MTZ).

A) Structural interpretation of the Magadi Basin from SPOT data where, M = Lake Magadi; MTZ = Magadi Transverse Zone.

B) 3D model of the same region showing curved normal fault blocks interpreted to result from an element of right-lateral movement along a 150-160° trending basement heterogenity (from Le Turdu *et al.*, 1999).
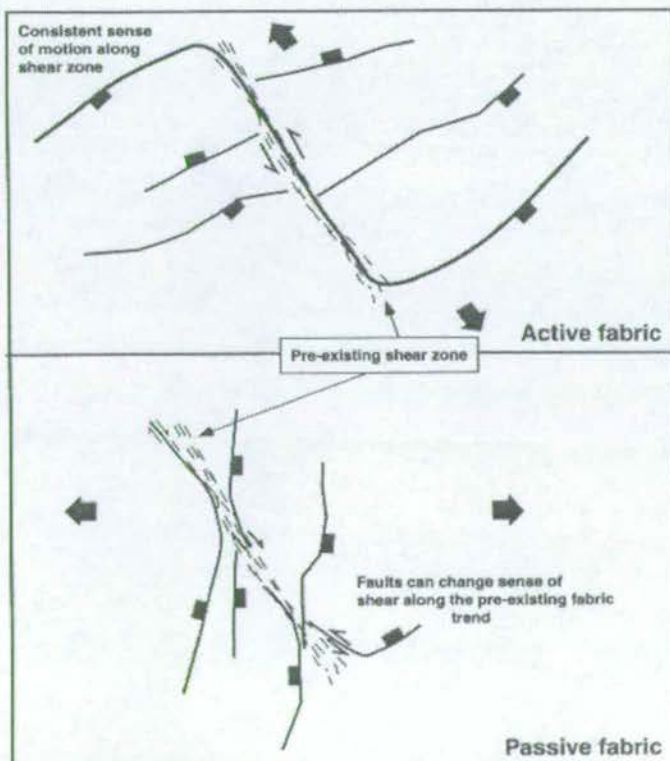
Figure 2.8 Idealised diagrams showing the principal differences between active (above) and passive (below) structural fabrics developed above basement heterogenities (from Morley, 1999c).

2.3 The South Kenya Rift

The South Kenya Rift extends for some 120km between Mount Suswa, in the north, to the Tanzanian border, in the south (figure 2.9). In this region, the rift valley has an asymmetric graben morphology, bounded to the west by a major border fault (the Sonjo-Naitiami fault) that began uplifting the 100km long Nguruman Escarpment between 12Ma and 7Ma (Baker, 1958; Baker *et al.*, 1978). The escarpment has a maximum elevation of 2000m, which descends to approximately 600m at the centre of the rift valley. Intense fluvial erosion has strongly influenced development of the upper rift flank by exposing and deeply dissecting the Archean Basement System rocks to form the Loita Hills. The Ngong-Turoka fault bounds the eastern flank of the rift valley. This structure is antithetic to the Sonjo-Naitiami fault and moved between 3.6 and 1.4Ma (Fairhead *et al.*, 1972), converting the South Kenya Rift from a half-graben to a graben geometry. Asymmetric grabens such as this are typical of many regions of the East African Rift Valley (e.g. Rosendahl *et al.*, 1986; Hayward and Ebinger, 1996; Morley *et al.*, 1999).

The floor of the rift valley is covered by extensive flows of trachyte, basalt and benmoreite lavas (Baker, 1958,1963; Crossley, 1979) that are believed to have been erupted over the past 12Ma from fissures or from numerous small volcanic centres (Fairhead *et al.*, 1972). This lava pile has since been broken-up by extensional faulting (locally known as 'grid' faulting; Baker, 1958, 1963), such that the valley floor has developed a saw-toothed topography (figures 2.10 and 2.11).

EXPLANATION
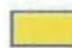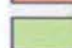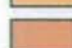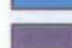
Lacustrine sediments, alluvium and volcanic ash	Upper Pliocene Limuru Trachytes
Mau ashes of the Naivasha region (not mentioned)	Upper Pliocene Singaraini Basalts
Suswa volcanics	Miocene-Pliocene central volcanoes
Pleistocene Plateau Trachytes	Miocene -Pliocene Lengitoto Trachytes and Kirikiti Basalts
Ol Tepesi Basalts and North Kordjya Trachyte	Miocene pre-rift volcanics
Upper Pliocene Kordjya Basalt	Precambrian metamorphic rocks

Figure 2.9 Geology of the South Kenya Rift (modified after Baker and Mitchell, 1976). Black rectangle demarcates the region around Lake Magadi, as covered by figure 2.11. Oblique line indicates the approximate location of the diagrammatic cross-sections shown in figure 2.12

Figure 2.10 Aerial photograph looking south toward Lake Magadi. Note the steep scarps, generated by 'grid' faulting, in the foreground. (from Brunner Mond, 2001)

Figure 2.11 Landsat 7 image of Lake Magadi and the surrounding area. Note the pervasive faulting across the region.

Individual faults range from several hundred metres to tens of kilometres in length and metres to tens of metres in displacement (Baker, 1958, 1963) and generally trend slightly east of north. Fairhead *et al.*, (1972) have broadly constrained the age of extension within the Plateau Trachyte, at the centre of the rift, to between 0.8 and 0.4Ma (Middle Pleistocene), the lower limit being determined from pumice and fossil evidence in lake beds apparently unaffected by faulting. Further studies have shown that in areas on the rift margin, such as the Kedong-Olorgesalie Region (Baker and Mitchell, 1976), successive volcanic beds have been cut by a number of episodes of faulting that occurred between 0.7Ma to 0.4Ma (figure 2.12).

The general N-S trend of the grid fault network suggests an approximate E-W extensional stress orientation for this region during the fault episode. Atmaoui and Hollnack (2003) have analysed fault patterns from remote sensing data (SPOT images (1:125,000) (figure 2.13) and aerial photographs (1:76,000)) and neotectonic joint orientations in the High Magadi Beds on the shores of Lake Magadi. The authors recognise principal structural orientations of N015°E and N015°W, the latter of which is consistent with the southern segment of the Kenya Rift. When combined with focal mechanism solutions obtained from microseismic activity around the Magadi Region, these data indicate an E-W to ESE-WNW normal faulting extension direction.

Importantly, the low rainfall and generally arid conditions in the South Kenya Rift means that the rocks and the original fault-generated topography have been little affected by erosional processes. Although alluvial sediment accumulation is common in the hangingwalls to many of the faults in this region, the deposits are generally superficial in nature and, where uplifted and incised by fluvial erosion, are seen to be no more than ~20m in thickness. Hence, the South Kenya Rift provides excellent exposure of kilometre-scale faulting.
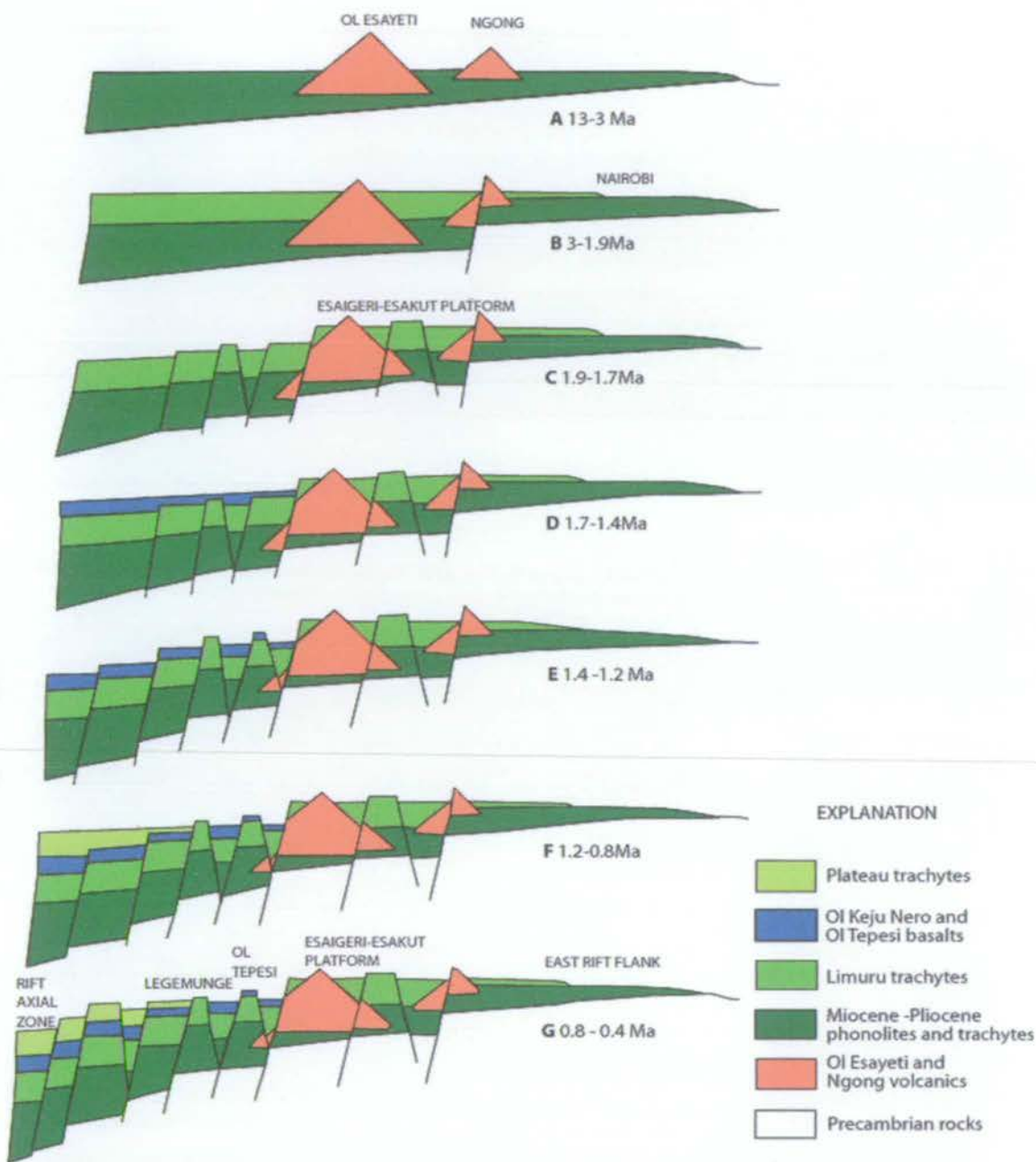
Figure 2.12 Diagrammatic sections showing the evolution of the eastern margin of the South Kenya Rift (modified after Baker and Mitchell, 1976).

Figure 2.13 Rose diagram showing the principal orientations of faults measured from 1: 125,000 scale SPOT images (N = 1635) (from Atmaoui and Hollnack, 2003).

2.4 Geology of the South Kenya Rift

A geological map of the South Kenya Rift, showing the principal lava flows of the area, is shown in figure 2.9. The regional stratigraphy of the formations will now be described in chronological order based on work by Baker (1958, 1963), Baker and Mitchell (1976), Baker *et al.*, (1978, 1988) and Crossley (1979). The structural and stratigraphic development of the rift is summarised in figure 2.14.

2.4.1 Metamorphic rocks – Basement System (Archean)

The extensive Miocene to Recent volcanism associated with formation of the South Kenya Rift rests on a Precambrian metamorphic basement comprising schists, gneisses and quartzites of the Mozambique Mobile Belt (Baker, 1958; Crossley, 1979; Smith and Mosley, 1993; Simiyu and Keller, 1998). Exposures of these rocks are confined to the upper slopes of the Nguruman Escarpment, on the west flank of the rift (Baker, 1958; Crossley, 1979).

2.4.2 Prerift stratigraphy (Mid Miocene)

The earliest volcanism in the region of the Kenya Rift consists of phonolites, nephelinites and trachytes erupted directly onto metamorphic basement topography. The volcanics were extruded from central volcanoes and fissures at the core of a wide, downwarped, trough that formed as a precursor to the present narrow rift (King, 1978; Crossley, 1979). Lava flows and agglomerates (dated to between 12.0 and 15.2Ma; Crossley, 1979) are preserved in patches to the immediate west of the Nguruman Escarpment, in areas where erosion has not exhumed Precambrian rocks. Areally extensive flows of phonolite (dated to 13Ma) are similarly exposed on the eastern rift flank (Fairhead *et al.*, 1972; Baker *et al.*, 1978).
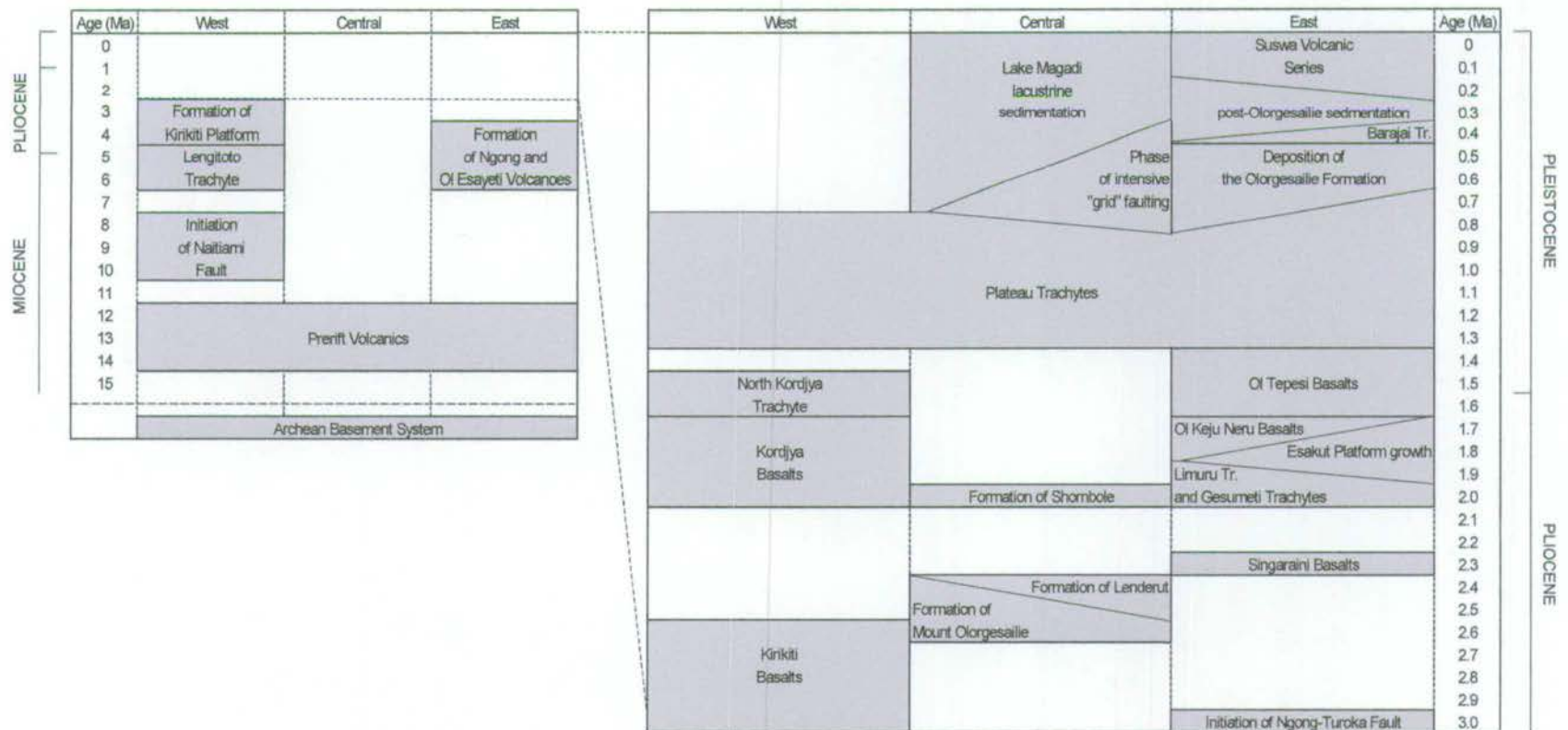
Figure 2.14 Chronostratigraphic diagram for the South Kenya Rift. Columns separate the stratigraphy and structural events into three regions according to their approximate geographic location within the rift; where two events occur contemporaneously within the same region, they are divided by a diagonal line that slopes in a direction determined by their relative locations (e.g. the Barajai Trachytes lie immediately to the east of the post-Olorgesailie sediments within the eastern rift sector and are therefore divided by a line sloping towards the left). (From Baker (1958, 1963), Baker and Mitchell (1976), Baker *et al.*, (1978, 1988) and Crossley (1979))

2.4.3 Rift Phase (Late Miocene-Recent)

a) Lengitoto Trachyte (Late Miocene)

This pale, greenish-grey, volcanic rock, containing sparse phenocrysts of anorthoclase and sanidine, is exposed as a narrow ledge on the crest of the Lengitoto Plateau, along the western margin of the rift valley, and onlaps onto the base of a pre-existing escarpment formed by movement on the Naitiami fault. $^{40}K/^{39}Ar$ determinations provide ages of 6.9-5.0Ma for the Lengitoto Trachyte, suggesting that faulting initiated along the western rift margin sometime between 12Ma and 7Ma (Crossley, 1979). This represents the earliest phase of tectonic activity associated with Kenyan rifting and it resulted in the formation of an asymmetric half-graben as a result of 550m of displacement accumulation on the Naitiami fault, prior to deposition of the Lengitoto Trachyte (Baker *et al.*, 1978).

b) Kirikiti Basalts (Pliocene)

The Kirikiti Basalts (3.1-2.5Ma) are a series of dark grey olivine basalts, in places interbedded with conglomerates, sands and silts, exposed on the western side of the rift valley (Baker, 1958; Crossley, 1979). At its westernmost margin, the basalt onlaps against the pre-existing Kirikiti Platform, which formed between 5 and 3Ma as a result of a second phase of faulting along the Nguruman Escarpment that activated the Engorika and Kirikiti faults.

c) Singaraini Basalts (Pliocene)

These basalts, slightly younger in age (2.3Ma) but of a similar composition to the Kirikiti Basalts, occupy a position against the south-east side of the rift valley. Their areal extent is confined by the eastern wall of the rift, which formed as a result of displacement on the Ngong-Turoka fault at about 3Ma. Hence, this phase of faulting converted the South Kenya Rift from a half-graben to a true graben morphology. (Baker and Mitchell, 1976; Baker *et al.*, 1978). Collectively, the Kirikiti and Singaraini basalts form flood lavas, as much as 550m in thickness, that cover the majority of the rift floor (Baker *et al.*, 1978).

d) Miocene-Pliocene Central Volcanics

The majority of the extensive lava flows within the South Kenya Rift appear to have emanated from fissure eruptions. However, construction of a number of central volcanoes occurred during two phases in the history of rifting. Between 6.7Ma and 3.6Ma the Ngong and Ol Esayeti volcanoes were built on the eastern margin of the rift valley, prior to development of the Ngong-Turoka fault. More recently, the central rift volcanoes of Olorgesailie (2.7-2.2Ma), Lenderut (2.5-2.6Ma) and Shombole (~2Ma) erupted a mixture of nephlinites, alkali basalts, trachytes and phonolites. These volcanoes protude above subsequent flood lavas and are prominent features on the floor of the rift valley (Baker *et al.*, 1978; Baker, 1986).

e) Limuru Trachytes (Late Pliocene)

These areally extensive trachytes represent some of the earliest rift-related lavas in the Kedong Region, where they are exposed in a triangular shaped fault ledge (the Esaigeri-Esakut Platform) on the eastern rift flank (Baker and Mitchell, 1976). This region, backtilted towards the south, was formed subsequent to eruption of the Limuru Trachytes as a result of a second phase of major faulting along the eastern margin of the rift, which formed the Kedong and Kiriri fault zones. Further to the east, the flows have overtopped the northern extension of the pre-existing Ngong-Turoka fault zone and extend as a much thinner lava sheet towards Nairobi. On the rift shoulder, to the south of Kedong, the flows unconformably onlap onto a basement of Ol Esayeti Volcanics, which represent localised lavas associated with the Ol Esayeti central volcano. A total thickness of at least 400m of conformable flows has been recorded in the footwall scarps of major extensional faults. The Limuru Trachytes are characterised by a series of up to 12 massive lava flows that are typically exposed as bouldery outcrops and have abundant glomeroporphyritic alkali feldspars. (Baker and Mitchell, 1976; Baker *et al.*, 1988). $^{40}K/^{39}Ar$ data, recorded from Limuru Trachyte samples taken from the Kedong Region, put the age of this unit as 1.94Ma to 1.96Ma (Baker and Mitchell, 1976).

f) Gesumeti Trachyte Formation (Late Pliocene)

This conformable sequence of trachyte lavas and pyroclastic layers, each of which varies between 10 and 50m in thickness, crop out only very locally in the Kedong-Olorgesailie Region,

on the eastern margin of the South Kenya Rift (Baker and Mitchell, 1976; Baker *et al.*, 1988). The volcanics are limited in extent to two steep sided ridges that bound the Kedong Gorge, to the west of the Esaigeri-Esakut Platform, and which rest on a foundation of Limuru Trachyte, or against pre-existing Limuru Trachyte fault scarps. These stratigraphic relationships have allowed Baker *et al.* (1988) to describe this formation as the ' product of a localized fissure eruption which filled a narrow half-graben and which is now exposed as a thin 'facing' as a result of renewed fault movement'. Baker and Mitchell (1976) also speculate that the limited extent of the Gesumeti Trachyte can be ascribed to the extreme viscosity of the flows, which must have emanated from a north-south orientated, fault-controlled, fissure buried under the alluvial fill of the Kedong Gorge. Published $^{40}K/^{39}Ar$ ages, determined on four specimens of these lavas, lie between 1.95Ma and 2.10Ma – dates that are indistinguishable from ages determined for the Limuru Trachytes (Baker *et al.*, 1988). This data, combined with their field observations, has led Baker *et al.* (1988) to conclude that the Gesumeti Trachytes represent a localized, presumably late-stage, fissure eruption of Limuru Trachyte magma.

g) Kordjya Basalt and Ol Keju Neru Basalts (Late Pliocene)

These grey-brown olivine basalt lavas locally cover areas of the Limuru Trachytes across the rift valley. The Kordjya Basalts (2.2-1.7Ma) onlap faulted, and riftward-tilted, Kirikiti Basalt deposits over a region extending from the Kirikiti fault line, in the west, to the western margins of the Magadi Trough, where they are buried beneath later Plateau Trachyte flows (Crossley, 1979) (see figure 2.10). Immediately to the north of the Olorgesailie volcano, in the east of the rift valley, an 85m thickness of Ol Keju Neru Basalts rest unconformably on a faulted and tilted Limuru Trachyte foundation. These flows can be correlated with the Kordjya Basalts, indicating that the Esakut Platform (figure 2.10) was initially created by movement on the Esayeti and Kedong fault zones during the period from ~2.0-1.7Ma (Baker *et al.*, 1978).

h) Ol Tepesi Basalts and North Kordjya Trachyte (Late Pliocene – Early Pleistocene)

The Ol Tepesi Basalts encompass a series of basalt lavas and a distinct benmoreite flow located toward the south-east of the Kedong-Olorgesailie area, particularly around the Ol Tepesi Basin (Baker and Mitchell, 1976). In close proximity to the Kedong Graben, Baker and Mitchell (1976) report the presence of two, thin, upper Ol Tepesi Basalt flows overlapping onto an

irregular, faulted, Limuru Trachyte surface. They also note the presence of a soil horizon containing calcareous nodules that indicates exposure to weathering before inflow of the basalt lavas. The benmoreite is well exposed to the north of the Legemunge and Ol Tepesi basins and is considered to be a single lava flow, at least 150m in thickness, though geochemical evidence suggests there may be two lava flows of slightly different compositions. The rock is 'coarsely feldsparphyric....with large tabular and rhombic feldspars set in a granular matrix' (Baker and Mitchell, 1976). $^{40}K/^{39}Ar$ determinations conducted on samples of the benmoreite have yielded an accepted age of 1.65Ma, while values of 1.42Ma (Baker and Mitchell, 1976) and 1.37Ma (Fairhead *et al.*, 1972) are reported from basalt flows above the benmoreite at the top of the group.

The porphyritic North Kordjya Trachyte, which is exposed in an area on the western margin of the rift, has been correlated with the benmoreites intercalated within the Ol Tepesi Basalts, suggesting that these lavas cover extensive areas of the rift valley (Baker *et al.*, 1978; Crossley, 1979).

i) Plateau Trachytes (Early to Mid-Pleistocene)

The areally-extensive Plateau Trachytes cover a large area of the central part of the southern rift valley floor, from the Nguruman Escarpment in the west, where they are locally named the Magadi Trachytes (Crossley, 1976, 1979; Baker *et al.*, 1978), to the Kedong-Olorgesailie area in the east (Baker and Mitchell, 1976). A total of 10 or 11 flows, erupted as fissure lavas, are exposed in many of the larger fault scarps at the centre of the rift, giving a total stratigraphic thickness of at least 190m in this location (Baker, 1958; Baker *et al.*, 1978). Similarly, 12 Plateau Trachyte flows, with a combined stratigraphic thickness of 150m, can be recognised in the south-west corner of the Kedong-Olorgesailie area (Baker and Mitchell, 1976). Further east, only three flows are present, lying disconformably on a previously faulted foundation of Ol Tepesi Benmoreite and Limuru Trachyte. In some localities, the trachyte flows have been dissected by later fault reactivation, giving rise to small-scale 'faced-scarp' structures (Temperley, 1966). Fault-controlled depressions were clearly developing prior to, and coincidentally with, volcanic eruption. Further extensive grid faulting has been dissecting the Plateau Trachytes from 0.9Ma until the present day. However, the most intensive period of deformation appears to have occurred in the period 0.9-0.4Ma, since the later Barajai Trachytes

(0.4Ma) and the Legemunge lake beds are much less displaced by faulting than the earlier units (Baker *et al.*, 1978). Taken collectively, $^{40}K/^{39}Ar$ ages for the Plateau Trachytes range from 1.4Ma to 0.8Ma (Baker and Mitchell, 1976).

j) Barajai Trachytes (Late Pleistocene)

These thin, aphyric flows, located in the north of the Kedong-Olorgesailie area, were originally grouped with the Plateau Trachytes on account of their similar compositions (Baker and Mitchell, 1976). They have since been separately classified on the basis of their lower Zr/Nb ratio and higher total Fe contents (Baker *et al.*, 1988). Three distinct lavas outcrop on the southern edge of the Suswa shield, two of which continued to flow down the Kedong Gorge where they have been cross-cut by later fault movements. Baker *et al.* (1988) have tentatively regarded these flows to be the earliest eruptive phase of the Suswa Volcano. $^{40}K/^{39}Ar$ radiometric determinations on four samples taken from the upper two lava flows have yielded ages of 0.37-0.41Ma.

k) Suswa Volcanic Series (Late Pleistocene-Recent)

The Suswa Trachyte and Trachyphonolite lavas are the products of seven identifiable phases of volcanism emanating from the Suswa shield volcano. Lavas sourced from Mount Suswa extend a considerable distance to the south of the main vent, filling the Kedong Basin and reaching the northern entrance of the Kedong Graben. $^{40}K/^{39}Ar$ radiometric determinations on three samples taken from the stratigraphically lowest units in the succession constrain the age of the Suswa Volcanic Series to between 0.24Ma and 0.1Ma (Baker *et al.*, 1988). However, the youngest lavas are well exposed and have little soil cover, indicating that Suswa has been active until recent times.

2.4.4 Pleistocene lacustrine deposits

A number of lake beds and lacustrine deposits, preserved within fault-controlled troughs, are distributed across the width of the South Kenya Rift, testifying to the fact that large lakes were in existence in this region during the Pleistocene.

a) The Lake Magadi Basin

Lake Magadi consists of an evaporitic lake capped by a crust of interbedded trona $(Na_2CO_3.NaHCO_3.2H_2O)$ and black mud layers. It occupies a narrow graben in the axial part of the rift floor. As the topographic low point of the rift, this region has been a site of lacustrine deposition for much of the past 0.78Myr (Baker, 1986). The Oloronga Beds, comprising olive-green indurated silts, clays and cherts together with yellow tuff beds, are exposed at the north and southern extremities of the Magadi Basin. These 15m thick lake-beds, some of the oldest in the region, were laid down at the end of widespread volcanic deposition in the South Kenya Rift (Baker, 1958, 1986) (though localised volcanism associated with Mount Suswa still continues to the northeast). Subsequent to deposition of the Oloronga Beds, minor faulting of the rift floor, between 0.8 and 0.4Ma, resulted in a deepening of the Magadi Basin into which the succeeding High Magadi Beds were deposited (Baker, 1958, 1986). The latter were formed as a beach terrace during a lake highstand, when Lake Magadi reached a level of 13m higher than at present. The waters eventually began to subside as desiccation lowered the lake level to 92m below the maximum and, as a result, the Trona Evaporite Series began to accumulate. (Baker, 1986).

b) The Olorgesailie Formation

As defined by Isaac (1978), the Olorgesailie Formation is 'a series of well-stratified sediments consisting principally o f p ale, v olcanic s iltstones, v olcanic sandstones, d iatomites a nd brown non-volcanic siltstones'. The type section for the formation has been assembled from observations made in a small region located to the north of Mount Olorgesailie, where fluvial incision of the sediments has created a number of good exposures (Isaac, 1978). This area is of considerable interest to archaeologists as a result of major discoveries made by Louis and Mary Leakey in the early-mid twentieth century (Leakey, 1974). Excavations at what is now the Olorgesailie Prehistoric Site have uncovered numerous hominid artefacts, living areas and vertebrate fossils. Further to the north the formation is believed to underlie recent soils in the Ol Tepesi-Legemunge Graben System. A total of 14 units, with a cumulative thickness of approximately 60-80m, rest unconformably on a suite of volcanic rocks, including the Ol Keju Neru Basalts, the Plateau Trachytes and the Olorgesailie Central Volcanics (Baker, 1958; Isaac, 1978; Shackleton, 1978). A number of authors have attempted to constrain the ages of the

volcaniclastic sediments within the formation through the use of bulk $^{40}K/^{39}Ar$ radiometric determinations (Evernden and Curtis, 1965; Miller, 1967; Bye *et al.*, 1987). Deino and Potts (1990) have used $^{40}Ar/^{39}Ar$ single-crystal laser fusion, in combination with conventional $^{40}K/^{39}Ar$ bulk fusion, in order to reduce the influence of contaminant or altered grains within the sediments. They suggest that the Olorgesailie Formation began deposition at 992ka (member 1) and ceased at 493ka (member 14), though overlying sediments collected from the Ol Tepesi Beds, further to the east, indicate lacustrine conditions prevailed until 215ka.

2.4.5 Structure of the South Kenya Rift

The upper crustal structure of the rift near Lake Magadi is fairly well constrained through a combination o f s eismic r efraction d ata, s hot b y t he Kenya R ift I nternational S eismic P roject (KRISP) in 1994, and gravity measurements (Simiyu and Keller, 1998), as well as from microseismicity and seismic tomography studies (Ibs-von Seht *et al.*, 2001). Based on seismic refraction data and gravity profiles, Simiyu and Keller (1998) have subdivided the upper crust of the rift valley into four distinct units (summarised in figure 2.15):

i)   A surface layer of sediments and volcanics that ranges in thickness from a maximum of 3.5km, next to the Nguruman Escarpment, to 2.0km further east, in the vicinity of Lake Magadi.

ii)   A 4km thick layer of highly fractured quartzitic rocks (inferred from anomalously low seismic velocities ($\sim5.7kms^{-1}$)) that may date from the Neoproterozoic collision between the Mozambique Mobile Belt and the Archean Tanzania Craton.

iii)   A hard, crystalline layer, thought to represent the lowest portion of the Mozambique Belt, that varies from 12km in thickness, where it crops out east of the rift valley, to 5km beneath the Lake Magadi area.

iv)   A lowest layer of Mid-Crustal rock that may form part of the Tanzania Craton.
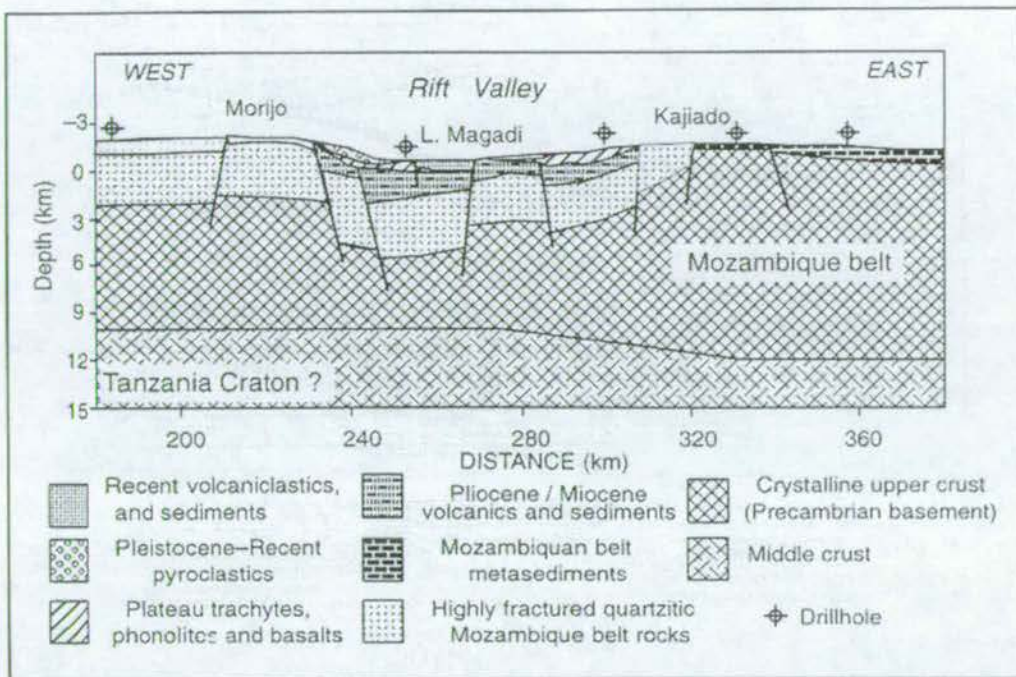
Figure 2.15 Interpreted cross-section through the upper crust of the Kenya Rift in the vicinity of Lake Magadi. This model summarises the integrated analysis of seismic, gravity and geological data in this region (from Simiyu and Keller, 1998).

The central axis of the South Kenya Rift is characterised by narrow gravity high that has variously been attributed to shallow crustal, mafic intrusions (either as a single, broad structure or as a number of dyke swarms (e.g. Baker and Wohlenberg, 1971; Fairhead, 1976; Swain, 1992; Ibs-von Seht *et al.*, 2001)) or an intra-rift horst block (Simiyu and Keller, 1998). Though seismic refraction studies have failed to yield any evidence to support the existence of major upper crustal intrusions (Simiyu and Keller, 1998), a recent analysis of regional microseismicity data (Ibs-von Seht *et al.*, 2001) suggests that the gravity high coincides with a stripe of shallow earthquake focal depths. This feature has been interpreted as an upwarped brittle-ductile transition that may have resulted from the intrusion of igneous material at depth. Over an eight-month p eriod, e arthquake activity, r anging i n m agnitude f rom 1 .5 t o 3 .7, w as recorded by a network of seismic stations located on the floor of the South Kenya Rift. The measured microseismic events fall into two main categories (figures 2.16 and 2.17):

i)   Sparse, background seismicity distributed across the entire width of the rift valley. Hypocentre depths range from 10-27km, with the deepest events located along the rift flanks (figure 2.17).

ii)   A shallow cluster of intense seismicity (accounting for 75% of the reported events) that occurred to the north of Lake Magadi over a four week period in May 1998. The epicentres were located along a NNE-SSW orientated trend and over a horizontal distance of some 10km. During the period of activity, the earthquake swarm migrated slowly northwards at a rate of 0.3km/day (figure 2.18) and a surface tension gash, several kilometres in length, opened up between two horst blocks located directly above the earthquake cluster. Focal depths for the majority of events range between 1km and 6km, with the maximum frequency occurring at 3km (figure 2.19). The cluster exhibits a sharp cut-off at 9km depth (figure 2.17), which has been interpreted as further evidence in support of a lower crustal magmatic intrusion.
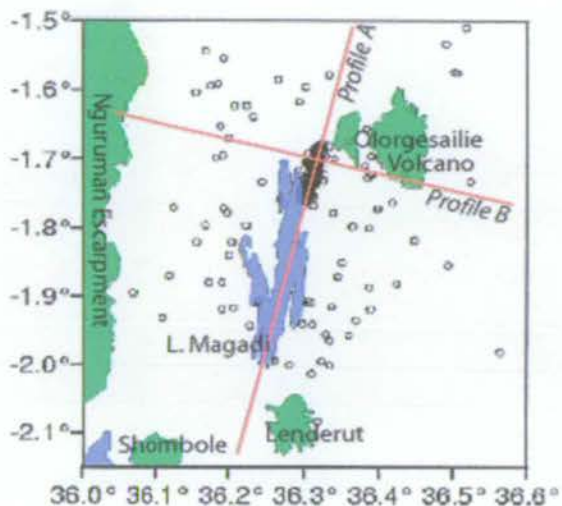
Figure 2.16 Location of epicentres for earthquake events occurring between 6/11/1997 and 17/6/1998. Note the cluster of activity situated north of Lake Magadi (modified after Ibs-von Seht *et al.*, 2001).
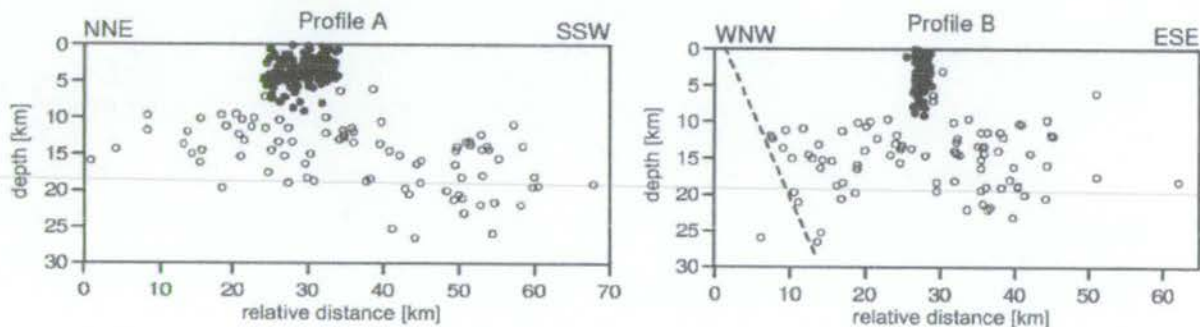
Figure 2.17 Earthquake hypocentre depth sections. Events are projected onto a plane orientated along (Profile A, 014°) and across strike (Profile B, 104°) of the main earthquake cluster. Filled circles represent events with epicentres located in the cluster region marked in figure 2.16. Dashed line: projected extent of Nguruman Escarpment (from Ibs-von Seht *et al.*, 2001).
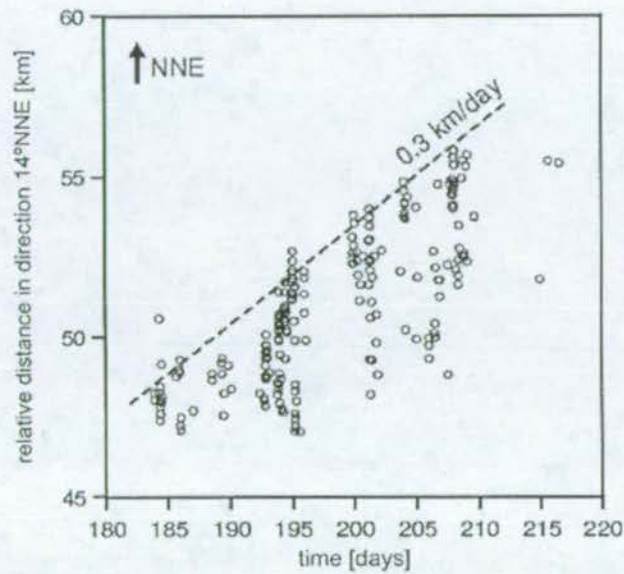
Figure 2.18 Graph showing migration of earthquake events with time in a direction of 014 NNE (from Ibs-von Seht *et al.*, 2001).
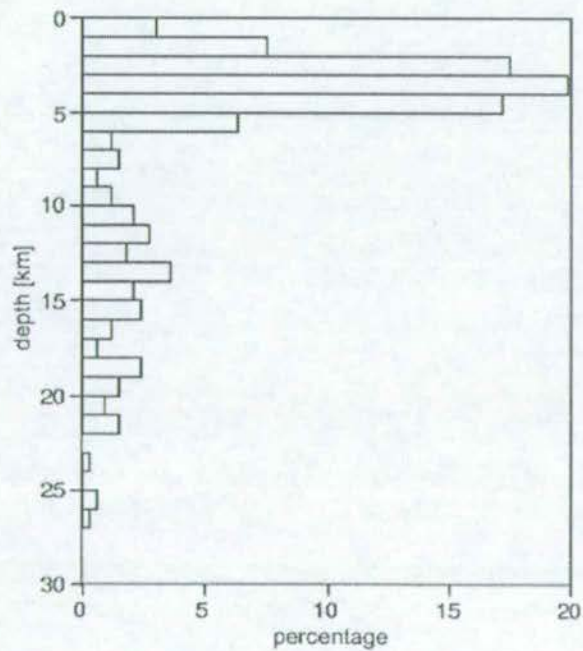
Figure 2.19 Frequency-depth distribution of well-located events in the Magadi area (from Ibs-von Seht *et al.*, 2001).

At a larger scale, there is still much debate as to the lithospheric structure of the Kenya Rift (Birt *et al.*, 1997; Byrne *et al.*, 1997; Simiyu and Keller, 1998; le Roex *et al.*, 2001). Bouguer gravity anomalies measured along line G of the KRISP 94 seismic refraction survey, which passes through the South Kenya Rift (Prodehl *et al.*, 1997), have been analysed to assist interpretation of the lithospheric structure in this region (Birt *et al.*, 1997; Simiyu and Keller, 1998). Gravity modelling has produced a good fit to the overall features of the observed gravity data, but fails to account for a 55mGal rise in gravity from west to east along the line. Birt *et al.* (1997) have approached the problem by assigning deep density contrasts to the rift structure. They suggest that at the centre of the rift, lithospheric mantle has been almost entirely replaced by hot, low-density asthenospheric mantle material as a consequence of mantle-plume circulation beneath the East African Plateau, west of the Kenya Rift. In contrast, studies of wide-angle seismic refraction profiles by Byrne *et al.* (1997) indicate the presence of two upper mantle seismic reflectors beneath the rift, which suggest that the lithospheric mantle, though thinned to some extent, has not been substantially disrupted by asthenospheric upwelling. Support for the notion of an intact subcrustal lithosphere also comes from geochemical analyses on samples of basaltic rocks (e.g. the Singaraini, Kirikiti and Ol Tepesi Basalts) recovered from the South Kenya Rift (le Roex *et al.*, 2001). The composition of these rocks suggests that the mafic rift valley magmas were generated within a relatively cool lithospheric mantle environment as opposed to within a hot upwelling plume or asthenospheric mantle.

2.4.6 Previous studies of rift-floor fault populations using remote sensing data

Gloaguen (2000) has recently undertaken a detailed tectono-structural study of the Southern Kenya Rift. The aim of his study was to investigate the tectonic evolution of the valley floor 'grid faulting' and place it into the context of regional scale extension. Observations were made using a combination of remote sensing techniques, comprising optical satellite SPOT imagery and Radarsat (SAR) imagery, that together allow spatial resolution of 20 metres, though in some cases a resolution of 5 metres was achieved. Such detailed imaging has enabled characterisation of the regional-scale structure of the Magadi fault system.

The geometries of faulting in three areas: the Naivasha, Magadi and Manyara troughs were analysed with combined SPOT/SAR imagery. Study of the fault arrays was confined to those

parameters that could be resolved on the images; namely fault zone length, fault length, segment length, segment width (which is used as a proxy for fault displacement) and fault spacing. These parameters were measured for 799 faults within the Magadi area and 174 faults around the region of Lake Naivasha.

Figure 2.20 shows a plot of fault displacement/length (D/L) against length (figure 2.20), redrawn from Gloaguen (2000), which appears to suggest that the ratio of displacement:length is not a constant but actually decreases with increasing fault length. Such an observation implies that fault growth is essentially by lateral linkage rather than increased displacement. These long, linked structures do not have the elliptical profile characteristic of isolated faults (e.g. Cowie and Scholz, 1992a; Walsh and Watterson, 1988) but instead display a more trapezoidal shape, similar to those observed for the faults of the Volcanic Tablelands (Dawers *et al.*, 1993). Dawers *et al.* (1993) s uggested that s uch p rofiles w ere characteristic o f large faults t hat h ad broken through the brittle volcanic layer and were constrained by the underlying ductile units. Gloaguen (2000) s uggests that t he long f aults of t he M agadi a rea m ay h ave d eveloped their profiles by a similar mechanism of lateral fault linkage and containment within an upper brittle layer. However, he also suggests that, in detail, the fault morphology is not truly trapezoidal but that the original segments retain their i dentity post linkage, separated by large displacement minima along the length of the fault scarp (figure 2.21). According to this model, fault segments initially grow with the elliptical scarp morphologies typical of isolated faults. Later, during linkage, the segments do not re-equilibrate but retain their original morphologies and continue to behave independently during further faulting.
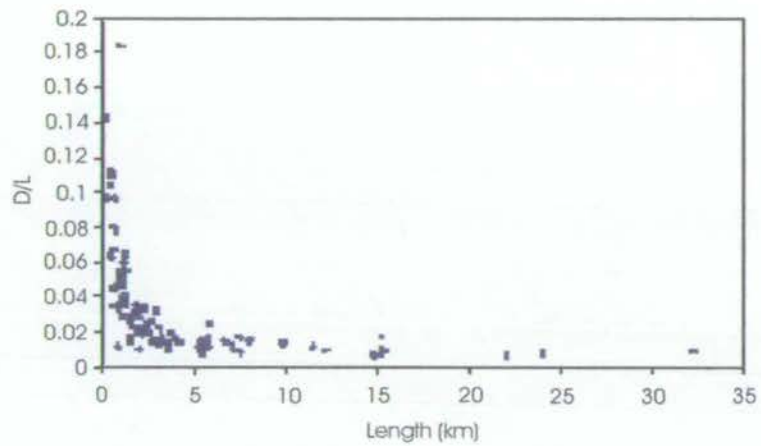
Figure 2.20 Displacement-length ratio versus fault length (modified after Gloaguen, 2000).
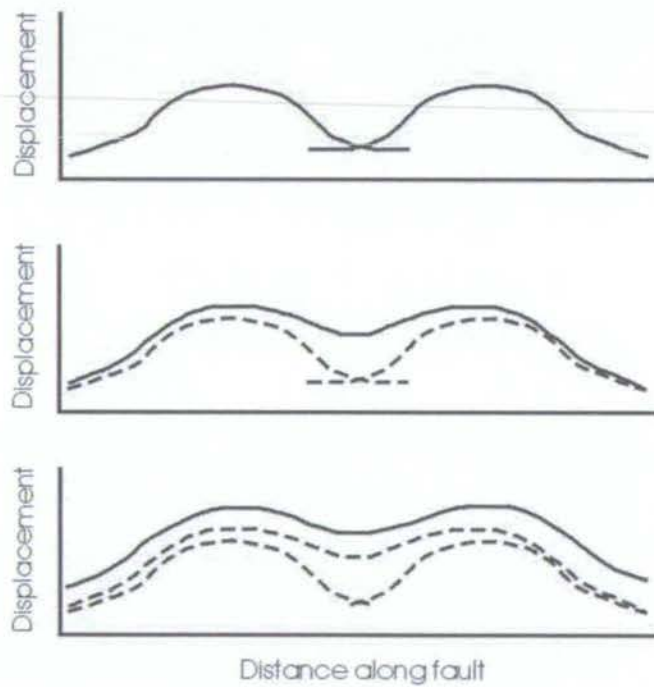
Figure 2.21 Model depicting evolution of the Magadi grid faults as a result of segment interaction and linkage (modified after Gloaguen, 2000).

2.5 Summary

The geology and structure of the Kenya Rift has been revealed through a combination of traditional geological mapping techniques (e.g. Baker, 1958, 1963; Baker and Mitchell, 1976; Crossley, 1976, 1979), remote sensing (Grimaud *et al.*, 1994; Le Turdu *et al.*, 1995, 1999; Gloaguen, 2000), interpreted seismic reflection data (Rosendahl *et al.*, 1986; Morley, 1999b), seismic refraction studies (e.g. Byrne *et al.*, 1997; Prodehl *et al.*, 1997), gravity modelling (Birt *et al.*, 1997; Simiyu and Keller, 1998), microseismicity analysis (Young *et al.*, 1991; Ibs-von Seht *et al.*, 2001) and geochemistry (e.g. le Roex *et al.*, 2001).

Evolution of the South Kenya Rift has been characterised by phases of tectonic activity interspersed with periods of areally extensive volcanism. The penecontemporaneous nature of volcanic and tectonic activity within the rift ensures that this is an ideal region in which to study and quantify the development of kilometre-scale extensional faulting since the volcanic beds act as dateable marker horizons. The geology and geochronology of specific fieldwork localities, which show optimal conditions for the quantification of fault growth, will be the subject of the next chapter.

Chapter 3: Geology and geochronology of the fieldwork localities

3.1 Introduction

It has already been established that the Magadi region of the South Kenya Rift is a suitable region in which to quantify the growth and development of kilometre-scale extensional fault arrays. However, in order to undertake the present study it was necessary to locate specific faults that showed direct evidence of activity during regional volcanism. Particular stratigraphic relationships that would indicate these 'syn-volcanogenic' fault movements are i) onlap of lava flows onto pre-existing tectonic fault blocks and ii) 'Faced fault scarps'(Temperley, 1966) i.e. lava ledges attached to the face of footwall fault blocks that formed as a result of lava onlapping against pre-existing fault scarps and being subsequently dissected by movement along the fault. In his study of the northwestern Magadi region, Crossley (1976) gives the coordinates of a number of localities where anomalous thinning and onlap of lava flows onto pre-existing fault blocks indicate the presence of contemporaneous volcanic activity and tectonism. Baker and Mitchell (1976), in their work on the geology of the Olorgesailie-Kedong region, describe a number of phases of fault movement in the Kedong Graben as shown by faults that cut lava flows with an age range of 2.1Myr.

A initial two-week period of fieldwork reconnaissance in September 2001 indicated that the Kedong Graben and Esiteti regions, as described by Baker and Mitchell (1976), would be very important areas to study (see figures 3.1 and 3.2). Both areas are characterised by fault blocks onlapped by lava flows which, in many places, have been cut by fault reactivation to form faced-scarp structures. Similarly, Crossley (1976) gives the geographic coordinates of the Ilainymok and Olooltepes regions, located close to the centre of the rift, which shown lava onlap onto pre-existing fault blocks and subsequent uplift (figures 3.1 and 3.2). The Olooltepes region, located at the centre of the rift valley, was also the site of a surface tension gash that opened during a four week period of microseismic activity in May 1998 (Ibs-von Seht *et al.*, 2001). Such a region is therefore an important study locality because it offers the opportunity to investigate the growth of a currently active fault showing a faced-scarp structure.

Figure 3.1 Artificially illuminated Landsat 7 satellite image showing main structural features of the South Kenya Rift and Northern Tanzania. Fieldwork localities are indicated with green circles. Black rectangles demarcate the regions covered in figure 3.3 (upper box) and figure 3.16 (lower box) (see figure 3.2 for more detail).

EXPLANATION
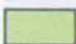
■ Lacustrine sediments, alluvium and volcanic ash	■ Upper Pliocene Limuru Trachytes
■ Mau ashes of the Naivasha region (not mentioned)	■ Upper Pliocene Singaraini Basalts
■ Suswa volcanics	■ Miocene-Pliocene central volcanoes
■ Pleistocene Plateau Trachytes	■ Miocene -Pliocene Lengitoto Trachytes and Kirikiti Basalts
■ Ol Tepesi Basalts and North Kordjya Trachyte	■ Miocene pre-rift volcanics
■ Upper Pliocene Kordjya Basalt	□ Precambrian metamorphic rocks

Figure 3.2 Geological map of the South Kenya Rift as modified from figure 2.9 to show the four fieldwork localities. Black rectangles demarcate the locations of figures 3.3 and 3.16, as indicated. (after Baker and Mitchell, 1976)

As described in section 2.4, previous authors have used $^{40}K/^{40}Ar$ geochronology to produce a regional geological history of the South Kenya Rift. While these data provide a general age framework, they do not allow a quantitative understanding of normal fault growth at a high resolution. In part, this is due to a lack of existing data, i.e. not all the important lavas have yet been dated, but also because the $^{40}K/^{40}Ar$ technique has largely been superseded by more accurate $^{40}Ar/^{39}Ar$ geochronology. Part of the remit of this project is to provide a high density of age data that can be used to accurately quantify the growth of individual normal fault blocks. This chapter introduces the locations of normal faults that were studied in the field, the petrology of the associated lava flows and the age determination techniques undertaken at the Scottish Universities Research and Reactor Centre (SURRC) in East Kilbride. Initially, there is a recap of the $^{40}K/^{40}Ar$ and $^{40}Ar/^{39}Ar$ radiometric techniques, before the latter is applied to the rocks of the study area.

3.2 Geochronological Techniques

The following description of geochronological techniques is based on work by Chambers (2000) and Harford *et al.*, (2002). The reader is referred to the original texts for a more detailed description of the methods involved.

3.2.1 $^{40}K/^{40}Ar$ Geochronology

$^{40}K/^{40}Ar$ geochronology has been the traditional method of dating rocks in the Earth Sciences due to the natural abundance of potassium-bearing minerals in a wide variety of rock types. The technique has been used extensively since the 1950's and relies on establishing the ratios of parent (^{40}K) to daughter (^{40}Ar) isotopes that result from the natural decay of ^{40}K to ^{40}Ar as a result of radioactive decay. The following decay equation describes the fraction of ^{40}K atoms that decay to ^{40}Ar in a K-bearing rock:

$$^{40}Ar = (\lambda_e/\lambda) \, ^{40}K \, (e^{\lambda t}-1) \tag{3.1}$$

Where λ is the total decay constant of ^{40}K (to both Ar and Ca), λ_e is the decay constant of ^{40}K to ^{40}Ar and t is time.

Ideally, assuming no ^{40}Ar is present at the time of rock crystallisation, it is possible to solve equation (3.1) for t:

$$t = (1/\lambda)\ln\left[(^{40}Ar/^{40}K)\,(\lambda/\lambda_e)+1\right] \qquad\qquad (3.2)$$

Absolute quantities of ^{40}Ar are measured by rare gas mass spectrometry, while ^{40}K is typically measured by standard chemical techniques such as flame photometry. The technique requires that some proportion of the rock sample is analysed for ^{40}K, while another is measured for ^{40}Ar. This can, in itself, lead to problems if there are chemical inhomogenities within the sample. Absolute concentrations of the various species can also be notoriously difficult to determine.

A major assumption of the ^{40}K/^{40}Ar technique is that no ^{40}Ar (or ^{40}K) is lost or gained after rock formation, i.e. the sample is treated as a closed system. However, it may be difficult to justify such an assumption if the rock in question has undergone a complex geological history which has resulted in ^{40}Ar loss due to burial, chemical weathering and alteration by aqueous fluids. During sample selection, rocks containing large quantities of volcanic glass should be avoided whenever possible since devitrified glass will have apparent ages lower than the real crystallisation age. Similarly, xenoliths may have excess radiogenic argon resulting in old apparent ^{40}K/^{40}Ar ages. Problems of ^{40}Ar loss and excess ^{40}Ar are hence dependant on the rock sample and its geological history; they are encountered in both ^{40}K/^{40}Ar and ^{40}Ar/^{39}Ar techniques but are more easy to reconcile in the ^{40}Ar/^{39}Ar dating method.

3.2.2 $^{40}Ar/^{39}Ar$ Geochronology

This technique is a development of the traditional ^{40}K/^{40}Ar method and measures the isotopic ratio of ^{40}Ar, generated by natural decay of ^{40}K, against ^{39}Ar, produced artificially from ^{39}K by irradiating the sample with fast neutrons in a nuclear reactor, to calculate the age of the rock. The age equation for the ^{40}Ar/^{39}Ar technique (equivalent to equation 3.2, and using similar notation) is:

$$t = (1/\lambda)\ln\left[(^{40}Ar/^{39}Ar)J+1\right] \qquad\qquad (3.3)$$

In this case, J is an irradiation parameter defined as:

$$J = (\lambda/\lambda_c) \, (^{39}K/^{40}K) \, \Delta T \int \phi(\varepsilon)\sigma(\varepsilon)d\varepsilon \qquad (3.4)$$

Where ΔT is the irradiation time, $\phi(\varepsilon)$ is the neutron flux energy at an energy of ε, $\sigma(\varepsilon)$ is the capture cross-section of ^{39}K for neutrons with an energy of ε, and the integration is effected over the whole energy spectrum of the neutrons.

The neutron flux experienced by the sample varies according to its position within the reactor. However, by placing a monitor mineral, or standard, of known age at measured positions between the samples, J can be determined using the following equation:

$$J = (e^{\lambda tm}-1)/(^{40}Ar/^{39}Ar) \qquad (3.5)$$

Where tm is the age of the flux monitor, λ is the radioactive decay constant and $^{40}Ar/^{39}Ar$ ratio is the measured ratio.

In practice, flux monitors are generally sanidine minerals of uniform $^{40}Ar/^{40}K$ ratios collected from standard localities. The monitor used during the course of this study was the USGS Taylor Creek Rhyolite Sanidine, dated at 28.34Ma. The minerals are loaded into foil packets and positioned into quartz vials at regularly spaced intervals between the sample material. The flux factor, J, can then be calculated using the above equation by measuring the $^{40}Ar/^{39}Ar$ ratio of each standard. A graph of J measured at each monitor location versus distance along the vial can then be plotted and, subsequently, the J values of the unknown samples can be found by interpolation. Errors in the J value readings are also incorporated into the age calculations.

3.3 Fieldwork localities on the eastern flank of the South Kenya Rift

At the eastern margin of the Kenya Rift, to the immediate west of the Kedong hills, lies the Kedong-Olorgesailie area (figure 3.3 and 3.4). Published work describing the regional geology of the area, including a number K-Ar age determinations, have been incorporated into section 2.4 (Baker and Mitchell, 1976; Baker *et al.*, 1988). This section will concentrate on detailed

observations of the Kedong Graben and Esiteti fault arrays within the Kedong-Olorgesailie area (figure 3.4), observed as a result of six weeks of fieldwork undertaken during October-November 2001 and September-October 2002.
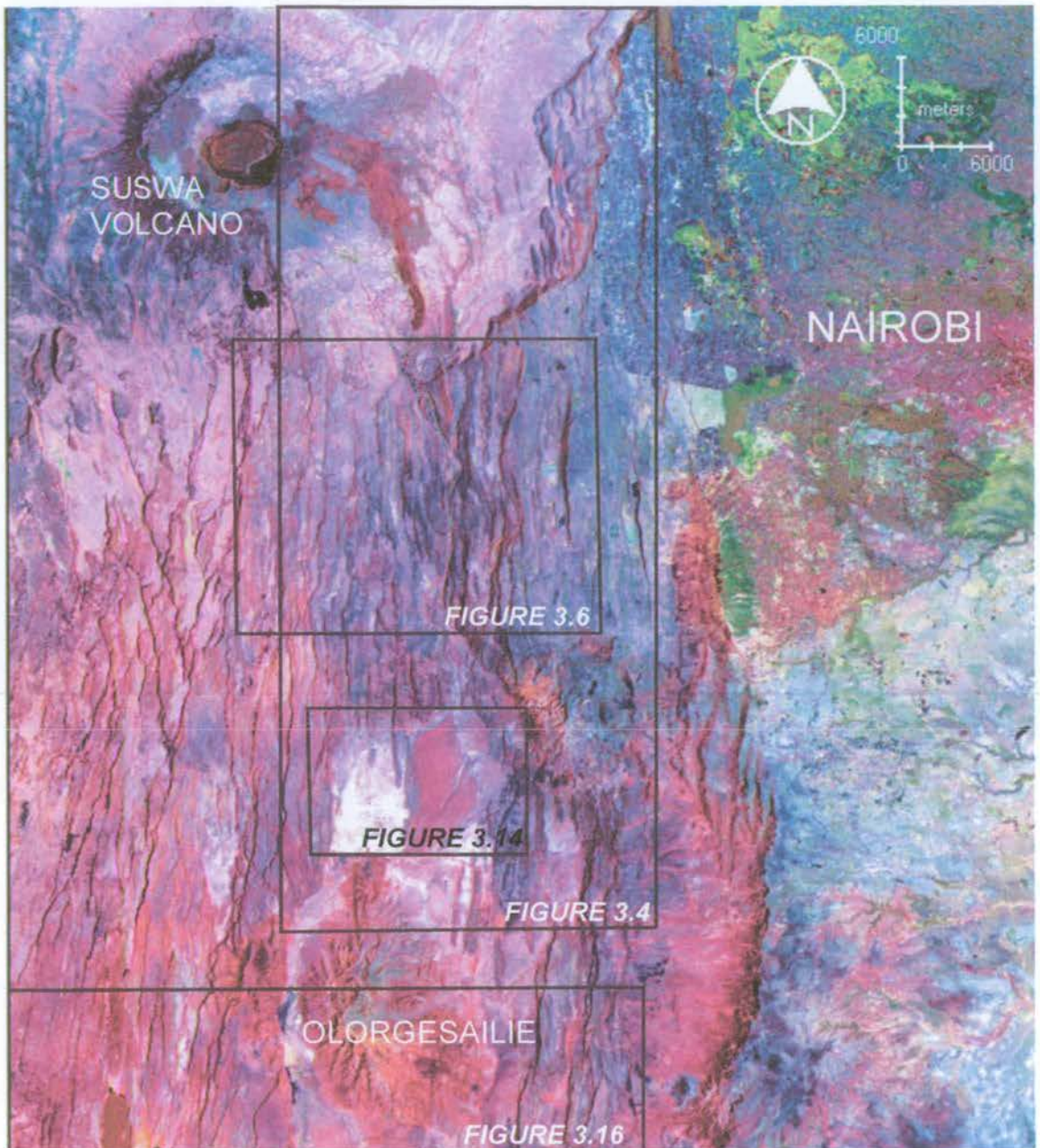
Figure 3.3 Landsat 7 satellite image of the eastern flank of the South Kenya Rift. Black rectangles indicate figure locations.
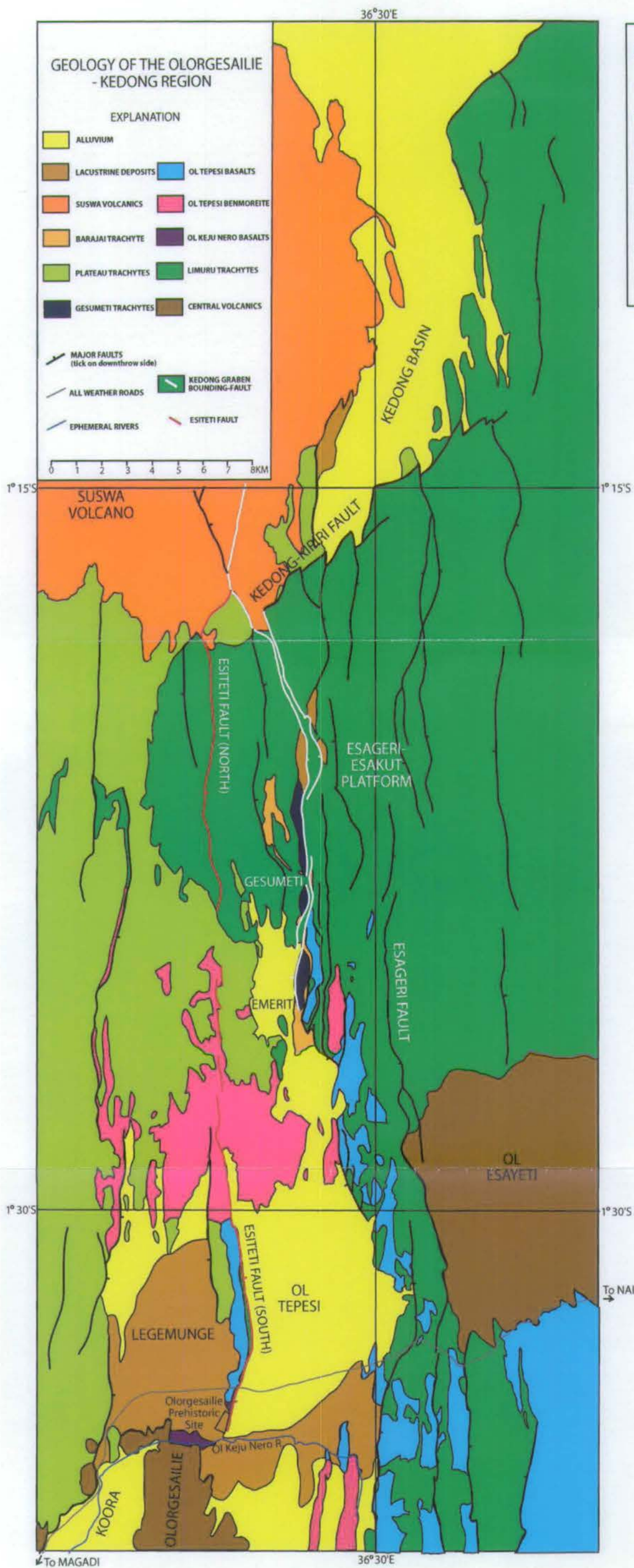
Figure 3.4 Geological map of the Olorgesailie-Kedong region. The Kedong Graben and Esiteti faults are indicated in white and red respectively. (modified after Baker and Mitchell, 1976).

3.3.1 Introduction to the Kedong Region

The geology of the Kedong Graben area, as observed from field observations and from the published geological map of Baker and Mitchell (1976), is illustrated in figure 3.5. The structural trends of this area are dominated by NNE-SSW and less importantly, NW-SE orientated fault scarps (figure 3.6). Scarps, as in most of the South Kenya Rift, are steep, subvertical features with up to 200m of vertical relief. The Kedong Graben is the narrow (maximum width of 1km) ~N-S orientated feature located toward the east of the map that extends to the south of the Kedong Basin and to the immediate west of the Esageri-Esakut Platform (figure 3.4). The western margin of the graben is bound by the Enasira fault (figure 3.7), which runs almost continuously for 18km and is named from the Masai for the large rock located at the southernmost tip of the fault. The Porosita scarp, named after the 200m high hill formed from Gesumeti Trachyte lavas at the southern tip of the scarp, bounds the eastern side of the Kedong Graben (figure 3.8). This fault is antithetic to the Enasira scarp and is less continuous, such that to the north of the Gesumeti watering hole the Porosita scarp tips out entirely, giving the Kedong Graben an 'half-graben' morphology. The northward limit of most regional faulting occurs along the line of the NE-SW trending Kedong-Kiriri fault that forms the margin of the Esageri-Esakut Platform (figure 3.3 and 3.4). From this zone northward, the remaining faults, including the Taritik fault, 'tip-out' in members of the Suswa Volcanic Series and lacustrine sediments of the Kedong Basin.
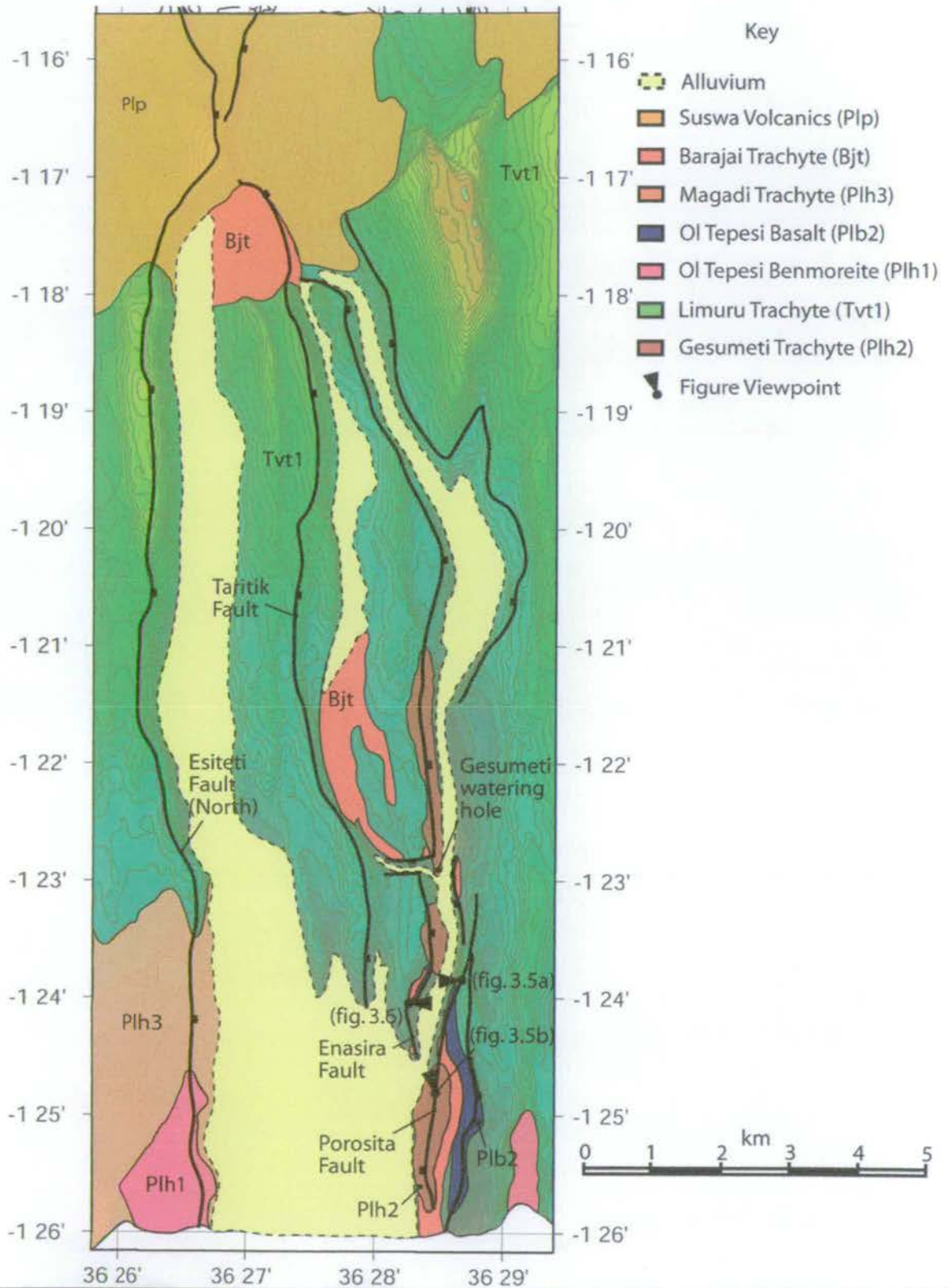
Figure 3.5 Diagram showing the geology of the Kedong Graben region. Geological ornament (based primarily on Baker and Mitchell (1976) and modified according to Baker *et al.* (1988) together with field observations during this study) is overlain on top of a digital elevation model constructed from a 1:50,000 scale topographic map of the region.
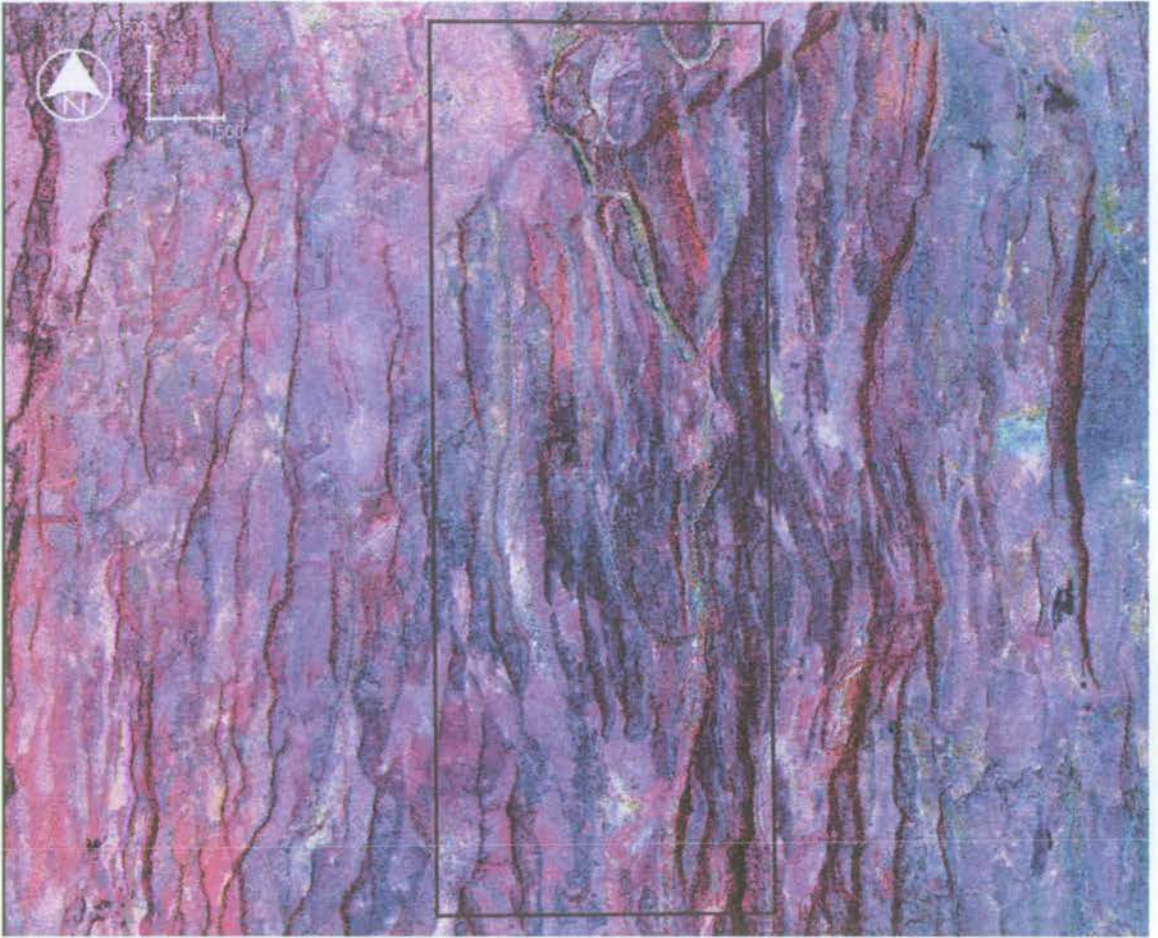
Figure 3.6 Landsat 7 satellite image showing the Esageri-Esakut Platform and the Kedong Graben region. The black rectangle indicates the area covered by figure 3.5
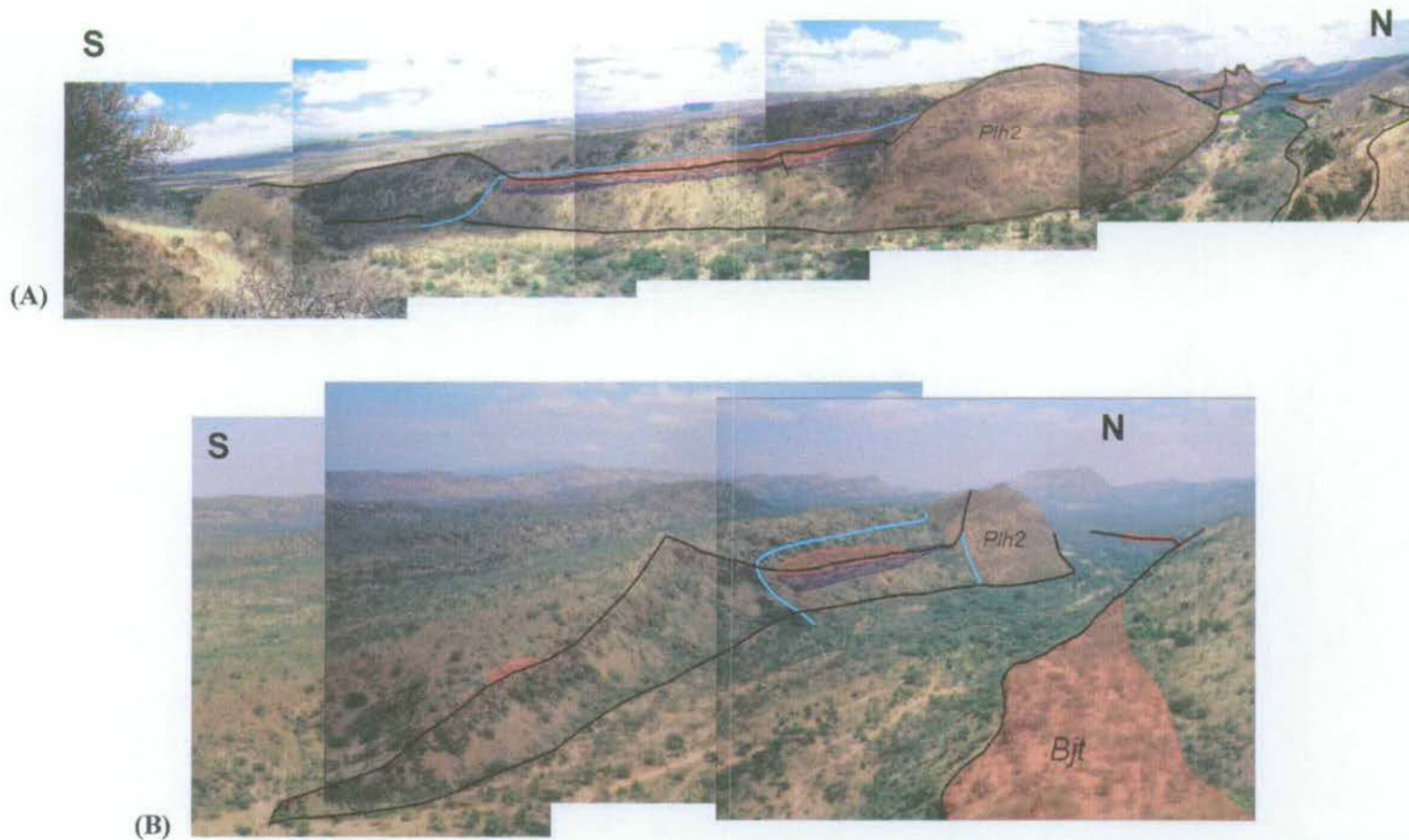
Figure 3.7 Two perspectives of the Enasira fault scarp from the eastern margin of the Kedong Graben. Coloured ornament indicates geology and fault structure: black lines - major graben-bounding scarps, pale blue lines – older faults, since cross-cut by movement along the graben faults, brown ornament – Gesumeti Trachyte formation (Plh2), dark blue ornament – Ol Tepesi Basalt flow (Plb2), red ornament – Barajai Trachyte flow (Bjt).
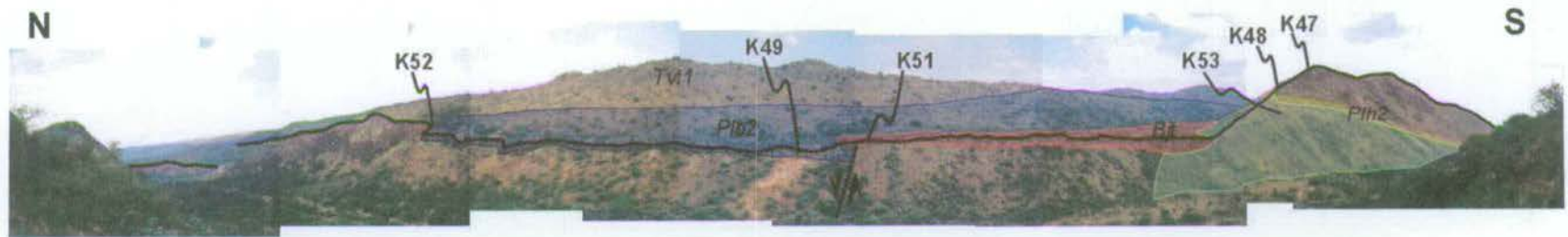
Figure 3.8 Photomontage of the Porosita scarp. Key to coloured ornament is as follows: pale green – grey-green massive trachyte (Gesumeti Trachyte Formation, Plh2), pale orange – agglomerate and tuff beds (Plh2), brown – fissile aphyric trachyte (Plh2), red-brown – feldsparphyric trachyte (Plh2), blue – Ol Tepesi Basalt (Plb2) and red – Barajai Trachyte (Bjt). Non-ornamented regions represent the Limuru Trachytes (Tvt1). Arrows indicate inferred sense of movement on a small normal fault oblique to, and since cross-cut by, the Porosita scarp.

3.3.2 The Gesumeti Trachyte Formation

Published studies (e.g. Baker *et al.*, 1988) suggest that some of the oldest rocks in the region are those of the Gesumeti Trachytes (1.95Ma to 2.64Ma), which are exposed along both walls of the South Kedong Graben. Baker and Mitchell (1976), in their table 2 (modified in this report as table 3.1), have produced a stratigraphic succession for the Gesumeti Trachyte Formation as based on observations from three localities. One of the most accessible exposures is a ~2.5km-long block with a distinctive lobe-shaped morphology and over 200m of vertical relief, located at the southern tip of the Porosita scarp. The observed succession was in rough agreement with that of table 3.1 though some flows were absent and others were not clearly exposed due to vegetation cover. The base of the section is characterised by a massive ~100m thick trachyte unit, which was sampled at the position indicated by 'K53' in figure 3.8. This rock is light grey-green in colour, very fine grained in texture and shows strong, millimetre-scale flow banding. Sparse sanidine phenocrysts (1%) indicate that this flow corresponds to the massive, microporphyritic trachyte of Baker and Mitchell (1976). Feldspar is far more abundant in the rock groundmass, associated with aegirine-augite (15%), patches of partially devitrified glass (35%) and opaque minerals (15%).

	Thickness (m)
Feldsparphyric trachyte	45
Fissile aphyric trachyte	10
Microporphyric trachyte	25
Welded tuff with obsidian fiamme	7
Stratified tuffs	12
Fissile aphyric trachyte	15
Massive microporphyritic trachyte	48
Xenolithic aphyric trachyte	30
(base of section not exposed)	

Table 3.1 Stratigraphic succession of the Gesumeti Trachyte Formation (after Baker and Mitchell, 1976)

Directly overlying the massive trachyte are three distinctive, orange, agglomeratic beds, each approximately 6-7m in thickness (figure 3.9). The basal 3-4m of each bed is very poorly sorted and contains clasts that range from individual quartz crystals and heavily-weathered rock fragments no more than a few millimetres in size, up to centimetre-sized, partially welded

fiamme of a black, fine-grained vesicular obsidian. The upper surface of each bed grades up into a bright orange, fine-grained rock (containing carbonaceous fragments) that is suggestive of a paleosol or laterite exposure surface. These beds correspond to the stratified tuffs and welded tuffs with obsidian fiamme of Baker and Mitchell (1976) (table 3.1).

Conformably overlying the tuff layers is a 3m thick bed of pale grey, fine-grained, fissile aphyric trachyte, sampled at site 'K48'. Obvious trachytic flow banding, comprising strongly aligned sanidine and plagioclase laths, can be seen in thin section. Filling interstices between the euhedral feldspar crystals are patches of glass and green-yellow pleochroic aegerine-augite.

The upper member of the Gesumeti Trachyte Formation, sampled at K47, is perhaps the most distinctive. It is characterised by a feldsparphyric lava flow, weathered orange-brown in colour. Large, euhedral sanidine phenocrysts (0.5-1cm in size; ~15% by area) are embedded in a groundmass of abundant sanidine and plagioclase laths (~70%). Also present are magnetite and patches of partially devitrified glass (~20%) (figure 3.10).

In order to undertake a geochronological analysis of the Gesumeti Trachyte Formation it was important to identify the component potassium-bearing mineral phases and the extent to which those phases may have been affected by alteration. The presence of mineral alteration or glass in the rock groundmass is detrimental to any such radiometric study (see section 3.2.1) and hence the initial work was to classify the samples according to the amount of alteration visible in thin section. Both K53 and K47 contained limited to moderate signs of alteration, confined, in the main part, to non-potassium phases in the groundmass such as the ferromagnesian minerals. However, they also contained well-preserved, K-rich sanidine phenocrysts that could be isolated from the groundmass by mineral separation techniques. These mineral separates were prepared by crushing and sieving into size fractions of >1mm, 500μm-1mm, 250-500μm, 125-250μm and <125μm. The 500μm-1mm size fraction was passed through a Franz Magnetic Separator to concentrate the sanidine and remove any ferromagnesian minerals. Each sample was then leached for 5 minutes with 1M HF in an ultrasonic bath followed by 20 minutes with warm (~50deg C) 6M HCl on a magnetic stirrer. Finally, the separates were rinsed in deionised water, placed in an ultrasonic bath for 15 minutes, and dried. 100-150mg of fresh sanidine crystals were then hand-picked from each sample and loaded into copper packets ready for irradiation. Sample packets, interspersed with packets of flux monitor standards, were loaded into quartz

vials and irradiated at 1MWh for 7 hours in the Cd-lined CLICIT facility at the Oregon State University TRIGA reactor, USA. Following a period of cooling, single crystals or a few crystals of sanidine were placed into copper pans in preparation for laser total-fusion analysis, which uses a CO_2 laser to fuse the crystals and hence release all the trapped argon gas in a single step. Initially, the contents of each pan were subjected to a steady 15 second-long burst of laser light that heated the sample to a temperature of ~700°C in order to release argon associated with any low temperature alteration phases. The main phase of fusion was composed of three stages that, for each sample, took a total of 25 minutes to complete. Firstly, the sample was fused by means of focused laser light applied for up to 5 minutes. The released gas was then expanded, under ultra high vacuum, into a small-volume gas-cleanup system with Zr-Al C50 getters at 400°C. The latter removed active gases such as hydrogen, oxygen and nitrogen prior to analysis so as to reduce the pressure scattering effects in the mass spectrometer and to prevent oxidation of the spectrometer filament. This phase took a total of 10 minutes to complete. Finally the gas composition was analysed for a period of 10 minutes in an ultrasensitive rare-gas mass spectrometer, during which time the gas extraction line was pumped. The spectrometer was calibrated using expected ^{39}Ar concentrations for samples of known K content. The argon spectra for a number of crystals of each sample (10 for K53 and 15 for K47) were analysed in this way. After every fourth analysis, the background levels of ^{40}Ar were measured by closing off the mass spectrometer from the vacuum line for a period of 10 minutes (i.e. the same amount of time as needed to measure the sample gases). These 'blank' measurements were later used to remove background levels of gas from the measured $^{40}Ar/^{39}Ar$ ratios. Fusion of monitor crystals was also undertaken in order to determine values for J as described in section 3.2.2.

Sample ages were calculated by means of an age spectrum analysis. The age was calculated as a weighted mean, where each fused crystal age was weighted by the inverse of its variance. Such an approach allows calculation of an apparent age, with the poorer data having a disproportionate effect on the result. The technique also involves a single-variable mean standard weighted deviation (MSWD) calculation to test for excess scatter. Accordingly, the weighted mean ages are:

K53: 2.254 ± 0.007Ma

K47: 2.100 ± 0.007Ma

The above errors incorporate a number of factors. Errors on individual analyses include estimates of the standard deviation of the analytical precision of the peak signals, the blank, the spectrometer mass discrimination, the reactor corrections and the half-life of ^{37}Ar. The error associated with the weighted mean age also includes the MSWD calculation of scatter and an estimate in the error of J.

Figure 3.9 Photograph showing the distinctive bedded agglomerate unit within the Gesumeti Trachyte Formation. Each bed grades upward from a poorly sorted basal section characterised by cm-scale obsidian clasts (black clasts in the photo) into a fine grained, orange laterite horizon (~50cm in thickness).
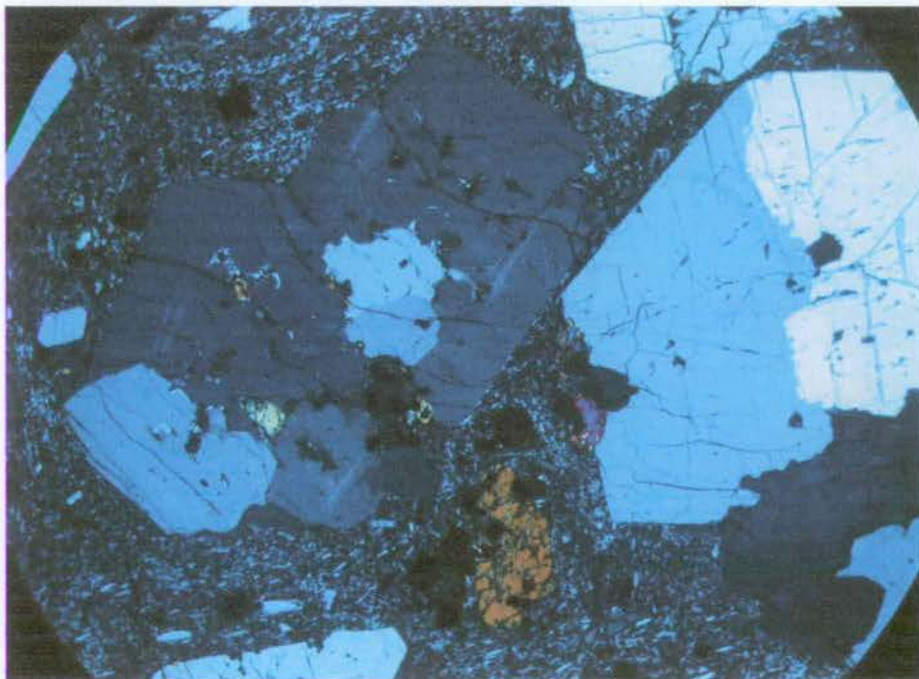
Figure 3.10 Photomicrograph of porphrytic blocky trachyte sampled at K47, showing euhedral sanidine and aegerine-augite phenocrysts (XPL, x2). Brick-shaped sanidine to left of centre is 5mm in length. The large, unaltered nature of the sanidine phenocrysts makes them ideal for single crystal laser total-fusion $^{40}Ar/^{39}Ar$ analyses.

3.3.3 The Limuru Trachytes (Kedong)

As has been mentioned in section 2.4, a 400m thickness of Limuru Trachyte lavas is exposed in the Kedong and Kiriri escarpments, south of the Suswa volcano. At least one massive flow of orange-brown feldsparphyric trachyte is exposed in the South Kedong Graben area. Red-Oxidised paleosol horizons, which represent unequivocal stratigraphic contacts between lava flows (as for the intra-formational Gesumeti Trachyte flows in section 3.3.2), were not observed in the Limuru Trachytes and hence, in the South Kedong Graben, the rock was taken to be a single lava flow. Extensional faults, ranging from 800 metres to 18km in length and 15m to 200m in displacement, cross-cut the lava cover and, in places, show backtilted, half-graben morphologies typical of those in Suez or Greece.

An upper Limuru Trachyte flow was sampled at K52 (figure 3.8). In thin section, the phenocrysts are observed to consist of euhedral K-feldspar (5mm in size; ~20% by area) and aegerine-augite (1-2mm; 5%), with the latter often found as inclusions within the former. The groundmass is composed predominantly of K-feldspar, together with minor aegerine-augite and magnetite.

The porphrytic nature of the Limuru Trachytes allowed for ^{40}Ar/^{39}Ar analyses by the laser fusion of sanidine phenocrysts that were isolated using mineral separation (see section 3.3.2 for the technique). A weighted mean age of 2.009 ± 0.004Ma was calculated from the fusion of 13 samples.

3.3.4 The Ol Tepesi Basalts

In the eastern section of the South Kedong Graben area, the Limuru Trachyte is mantled by a 8-10m thick flow of vesicular basalt, considered by previous workers to be an upper flow of the Ol Tepesi Basalts (Baker and Mitchell, 1976). The lower contact of the flow is marked by an obvious, bright-red, oxidised paleosol (see fig 3.11) that can be easily traced in the field. The basalt appears to have flowed into a fault-generated topographic depression immediately to the east of the Porosita fault block and has since been backrotated and cross-cut by more recent fault movements. Exposures of the basalt are located to the south and east of the Porosita fault

and as a narrow ledge, which has since been covered by a layer of Barajai Trachyte, halfway up the Enasira scarp.

The Ol Tepesi Basalt flow was sampled at K49 on the crest of the Porosita scarp (see figure 3.8 for location). Thin sections show the rock to contain abundant anhedral microphenocrysts of augite, showing typically high relief and moderately high birefringence (50%). Also present are randomly orientated plagioclase laths (40%), interstitial glass (15%) and magnetite (15%) (figure 3.12).

The lack of potassium-bearing phenocrysts in the Ol Tepesi Basalts meant that in order to calculate an age for the sample, it was necessary to analyse the rock groundmass. However, the relatively large amounts of volcanic glass had to be avoided as it could produce low apparent ages. To overcome this problem, the sample was crushed and sieved by the same method used in mineral separation (see section 3.3.2). However, in this case, the 250-500µm size fraction was leached in warm 6M HCl on a magnetic stirrer until the glass and alteration products were removed. After drying, 100-150 mg of the resulting leached groundmass was measured into copper packets and loaded into quartz vials. The samples were irradiated at 1MWh for 1 hour in a batch sent to the CLICIT facility at the Oregon State University TRIGA reactor in June 2003.

Following a cooling period, the copper packets were individually loaded into a double vacuum resistance furnace attached to a small volume gas-cleanup system with ZR-Al C50 getters. Each sample was then incrementally heated, at progressively higher temperatures, over a total of 17 steps. The gas released from each 15-minute heating step was then expanded into the attached gas line and allowed to cleanup for a period of 10 minutes, before being transferred into the mass spectrometer for analysis. The measured $^{40}Ar/^{39}Ar$ ratio was used to calculate an apparent age for the step. At the end of the sample analysis, the incremental heating experiments were combined to produce a weighted mean plateau age, where each increment was weighted by the inverse of its variance. This method is equivalent to that used for calculating ages in laser total fusion analyses, but in this case with each heating increment being substituted for a single total fusion experiment (see section 3.3.2). The weighted mean age for the Ol Tepesi Basalts at K49 is therefore 1.480±0.003Ma. Further details of all the incremental heating experiments described in this chapter can be found in file ihdata.xls (Appendix B).

A number of blanks were recorded during the course of each sample analysis to give an indication of background levels of gas within the vacuum system. The blank measurements were taken with the furnace switched off (i.e. cold blanks) and at increasing temperature intervals at the end of each sample run. Between experiments the furnace was baked out at high temperatures to prevent sample cross-contamination.
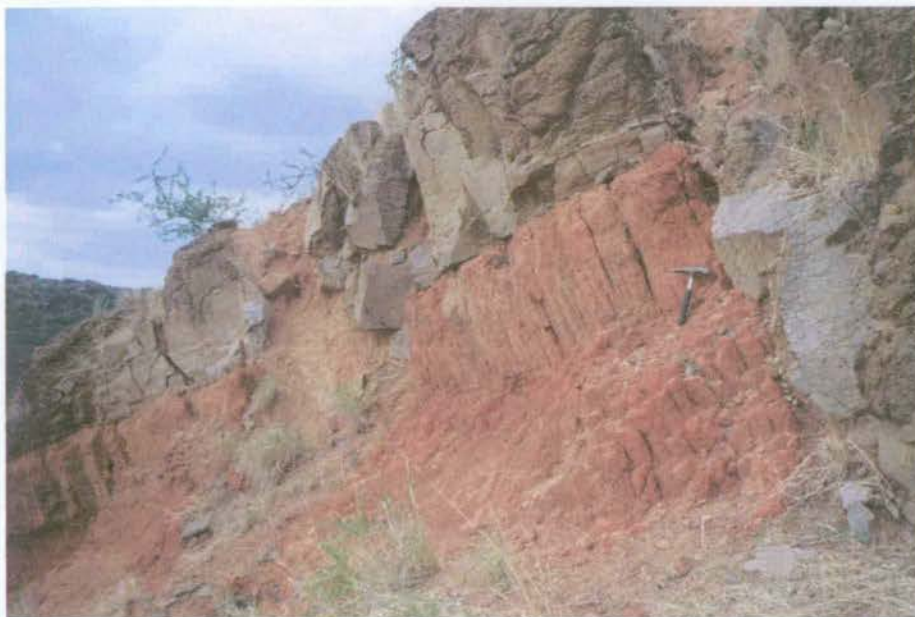
Figure 3.11 Photo showing the obvious red laterite horizon directly underlying the Ol Tepesi Basalt flow on the Porosita fault scarp.
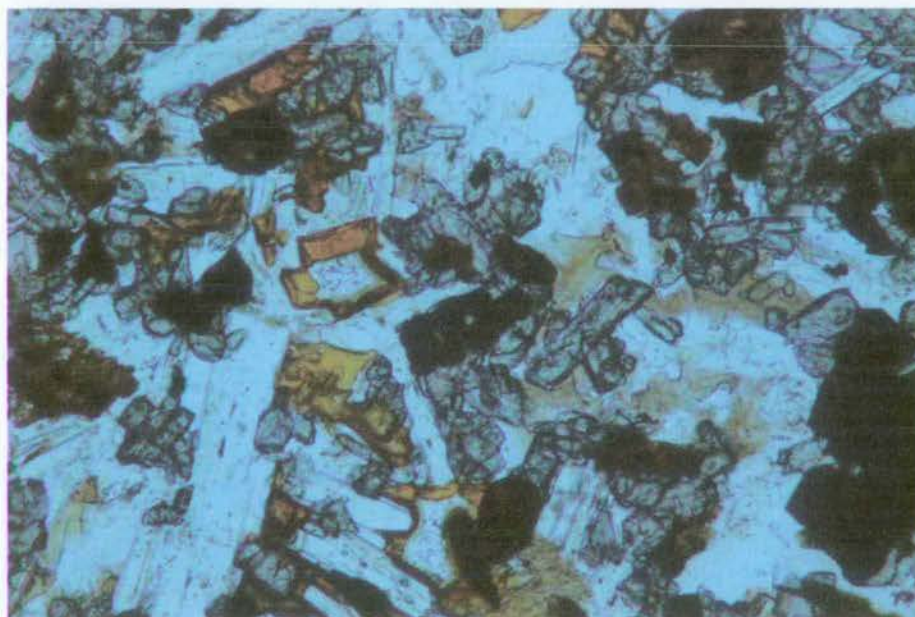
Figure 3.12 Photomicrograph of the Ol Tepesi Basalt as sampled at K49 (PPL, x10). Field of view is 1.5mm. The relatively large amounts of volcanic glass in this rock (showing as the dark orange and opaque patches) requires that any $^{40}Ar/^{39}Ar$ geochronological analysis must be undertaken on an acid-leached sample of the rock groundmass. Other minerals present are augite (high relief, pale green colour) and plagioclase feldspar (low relief, colourless)

3.3.5 The Barajai Trachyte

The Barajai Trachyte is the youngest lava of the South Kedong graben area and is exposed as a series of ledges, 10m thick, attached to a number of the fault scarps. As with the Ol Tepesi Basalt, the lava utilised topographic lows in normal fault hangingwalls as a flow pathway. Exposures suggest that the lava flowed from the north, in the hangingwall to the Taritik fault, until it was diverted eastward into the South Kedong graben, through a topographic low point in the E nasira s carp t o t he w est o f G esumeti. R enewed movement o n t he P orosita a nd E nasira faults then dissected the lava and generated 'faced scarp structures'. There is an obvious palaeosol underlying the Barajai Trachyte flow that consists of a 10cm thick horizon of subrounded clasts, stained red as a result of iron oxidation.

The nature of the flow in thin section, as sampled from site K51 (figure 3.8), is that of a trachyte with an obvious platy, trachytic texture. Sanidine laths, orientated parallel to the surface of the flow, are the most abundant feature (75-80%), though anhedral Na-rich pyroxenes (dark-green to green-yellow pleochroic) are also present (10%). The remainder is partly devitrified volcanic glass (10%) (figure 3.13). Elongate vesicles, clearly aligned parallel to the surface of the lava flow, are also prominent in both hand specimen and thin section. The collected hand-specimen showed only limited signs of alteration, with glass generally confined to distinct patches. It was therefore possible to determine the absolute age by undertaking a whole-rock incremental heating analysis by selecting small samples from the freshest parts of the rock. Whole-rock samples were prepared by drilling a series of 2-5mm thick, 5mm diameter mini-cores that were cleaned u ltrasonically in acetone, labelled a nd l oaded d irectly into q uartz v ials. The s amples were included in a batch of samples irradiated at 1MWh for 7 hours in the CLICIT facility at the Oregon State University TRIGA reactor, USA in 2002. A core was analysed using the incremental step heating method described in section 3.3.4 and yielded an age of 0.360 ± 0.001Ma.
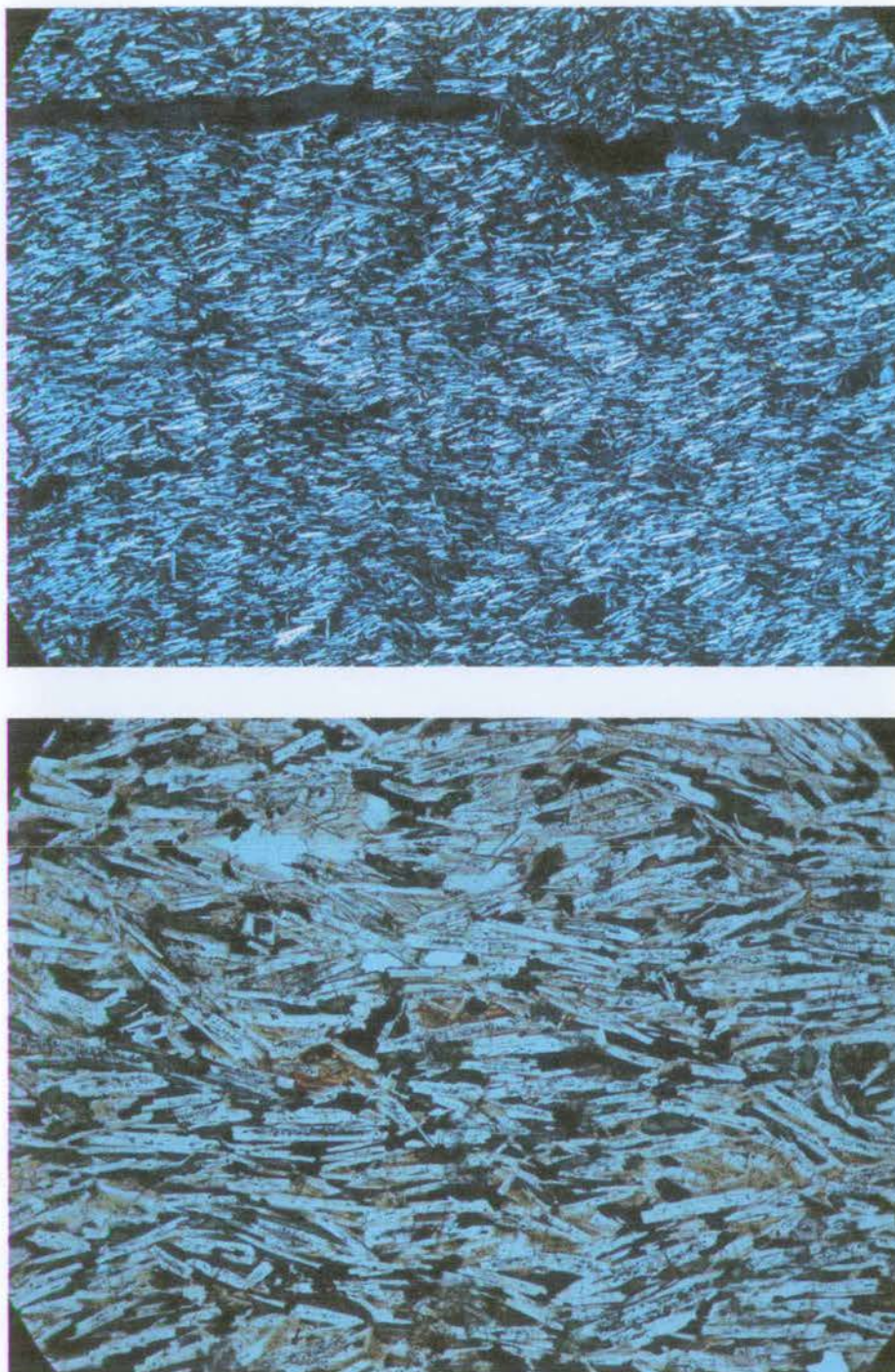
Figure 3.13 Photomicrograph images of the Barajai Trachyte collected at K51. Above: photo taken in cross-polarised light showing the trachytic texture and flow-banding characteristic of this rock (XPL, x2). Field of view: 7mm. Below: Image taken under plain-polarised light showing alignment of feldspar laths. Also present is dark-green to green-yellow pleochroic aegerine-augite. (PPL, x10; field of view 1.5mm)

3.3.7 Introduction to the Esiteti Fault

The Esiteti fault is a steep, N-S orientated, east-dipping structure that extends over a distance of ~35km from immediately east of the Olorgesailie Prehistoric Site in the south, to the Kedong-Kiriri fault in the north. Strictly speaking, the fault is composed of two underlapping segments; the Esiteti fault (south) which separates the Ol Tepesi Basin from the Legemunge Plain and the Esiteti fault (north) which dissects a foundation of Limuru Trachyte and tips out in rocks of the Suswa volcanics. The intervening zone, between these segments, is a topographic low that is gently tilted towards the east and appears to represent a fault-propagation fold that formed as a result of lateral growth of the fault segments. During eruption of the Plateau Trachytes in the west, the Esiteti fault appears to have acted as dam to some of the oldest lava sheets, with the relay zone acting as an outlet allowing the flows to move further toward the rift flank (figure 3.4). Hence, a thin blanket of Plateau Trachyte is seen to partially bury the central ~5km long portion of the Esiteti fault. The southern segment of the fault is of primary importance to the current study because it has formed from small, linked, fault segments that cut a number of lava flows.

3.3.8 The Esiteti Fault (south)

This scarp extends for a total of 15km along the margin of the Ol Tepesi Basin and is responsible for uplifting the lacustrine sediments of the Legemunge Plain to the west. Total displacement along the length of the fault is variable. Rapid changes in displacement gradient often coincide with a change in fault lithology, such that the regions of the fault showing largest displacements reside in exposures of Limuru Trachyte and Ol Tepesi Benmoreite while the lowest parts of the scarp cut Plateau Trachyte and Ol Keju Nero Basalt flows. This will be discussed in more detail in section 4.4.

Key   ■ Plateau Trachyte (Plh3)   ■ Ol Tepesi Benmoreite (Plb2)   ■ Ol Keju Nero Basalt (Plb1)   ■ Orthophyre Trachyte
      ■ Limuru Trachyte (Tvt1)
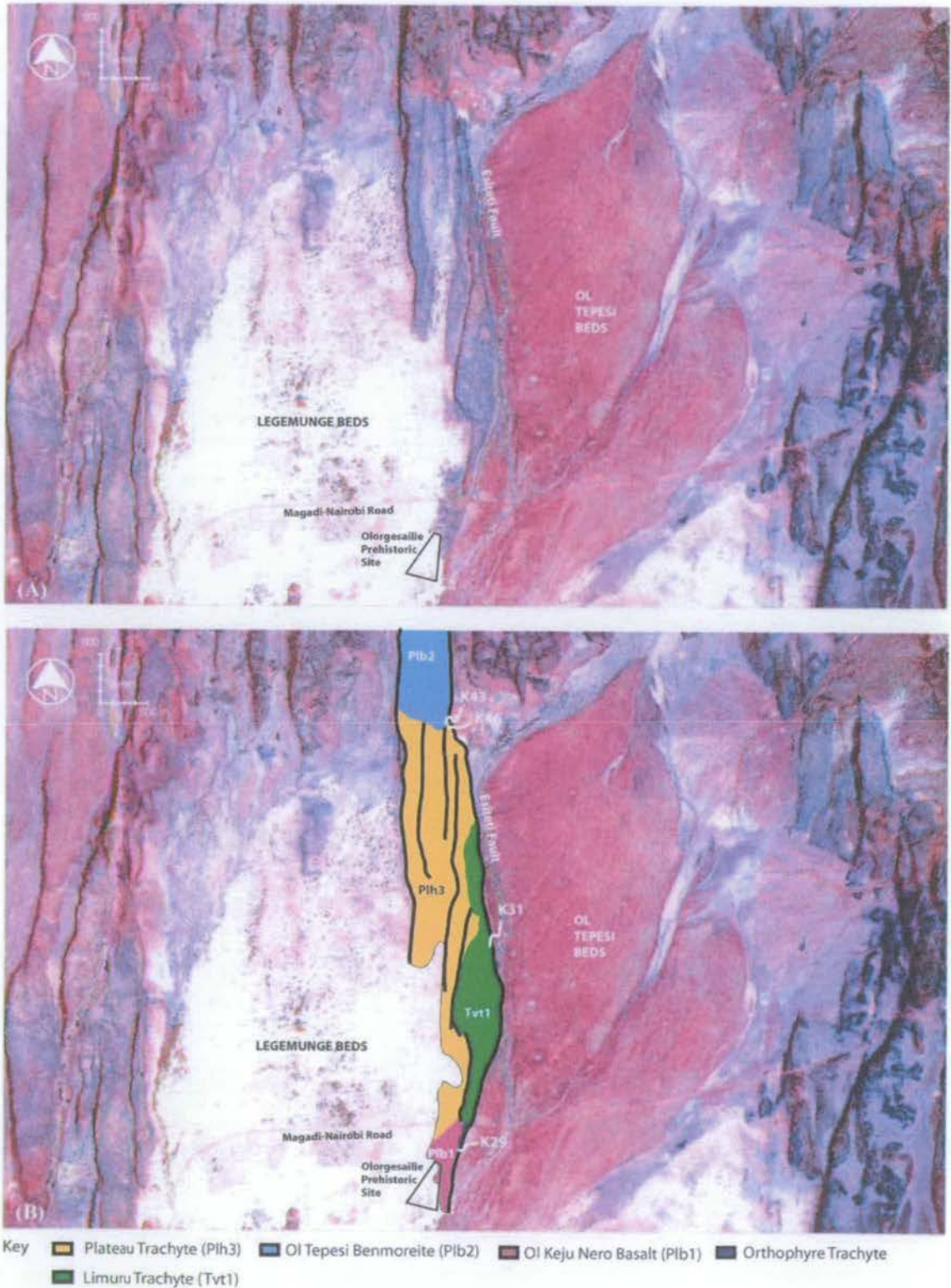
Figure 3.14 (A) Landsat 7 image of the Legemunge-Ol Tepesi area. The Esiteti Fault is the obvious structure dividing the two basins. (B) As (A), but with the principal lava flows indicated by coloured ornament. Black lines indicate the positions of normal faults. Positions of sample localities are also shown.

3.3.9 The Limuru Trachytes (Esiteti)

The Limuru Trachytes are exposed over a 4km length of the Esiteti fault scarp, from the Magadi-Nairobi road in the south, to the northern end of the Ol Tepesi Plain, where the segment is onlapped by a later trachyte flow. A handspecimen was collected at K31, towards the central part of this block (see figure 3.14).

On all scales the rock is very similar to the Limuru Trachytes of the Kedong region. However, since the rock groundmass was only slightly altered it was decided to date the sample using incremental heating analysis of whole-rock cores. Furthermore, this would provide age data complementary to the single-crystal fusion analyses undertaken on sample K52 collected from the Limuru Trachytes of the Kedong area. (see section 3.3.3 for a description).

A whole-rock core was subjected to incremental heating analysis and the corresponding weighted mean plateau age was determined as 1.995±0.004Ma.

3.3.10 The Ol Tepesi Benmoreite

The northernmost segment of the Esiteti fault consists of a horst block, with over 100m of displacement, dissecting an exposure of Ol Tepesi Benmoreite. The principal region of benmoreite exposure, which is cut by numerous, heavily forested, normal fault scarps and horst blocks, lies directly to the north of the Ol Tepesi and Legemunge sedimentary basins. In thin section, the rock has a characteristic glomeroporphrytic texture, comprising clusters of large brick-shaped sanidine (10-15mm in size; ~50% by area) and augite phenocrysts set in a groundmass of sanidine with augite and olivine microphenocrysts (figure 3.15). The sanidine rims show an obvious sieve texture that may be indicative of disequilibrium in the original melt and implies a substantial time difference between nucleation of the phenocrysts and crystallisation of the remaining melt.

A weighted mean age of 1.856Ma ± 0.010Ma was calculated for this rock from the laser total fusion of 8 sanidine phenocrysts isolated by mineral separation.

3.3.11 The Ol Keju Nero Basalts - Orthophyre trachyte

Situated immediately to the south and east of the Olorgesailie Prehistoric Site are two, kilometre-scale exposures of a dark grey vesicular rock classified by Baker and Mitchell (1976) as Ol Keju Nero Basalt. The Esiteti fault gradually tips out into the more easterly of these exposures until it becomes buried beneath the lacustrine and alluvial sediments of the Olorgesailie Formation. Following the fault along strike from the tip, there is a noticeable change in the character of the rock exposure. The fault tip consists of a narrow, bouldery, fault ridge that is obscured by thickets of acacia trees. Some 500m further along strike, a definite fault scarp becomes apparent and, at locality K29, a 6-8m high cliff exposes a dark-grey, richly porphyritic rock that is clearly different to the basalt near the fault tip. In thin section, the rock is clearly trachytic in composition, being composed of large sanidine phenocrysts (10mm in size, 15% by area) and microphenocrysts of augite in a groundmass of plagioclase and potassium feldspar. The rounded and poikolitic texture of the sanidine rims suggest that, as with the benmoreite described in section 3.3.10, these crystals may have been out of equilibrium with the remainder of the melt in the magma chamber. Pervasive iron-bearing veins suggest a late-stage alteration of the rock.

The detailed 1:10,000 scale geological map of the Olorgesailie Prehistoric Site (Shackleton, 1978) suggests that the tip of the Esiteti fault cuts a number of lavas, including an 'Orthophyre trachyte', at the location of K29. This is consistant with the observations made during the course of this study and suggests the Ol Keju Nero Formation, as mapped by Baker and Mitchell (1976), may in fact contain a number of basaltic and trachytic flows.

Total laser fusion of 10 sandine phenocryst samples isolated from sample K29 yielded a weighted mean age of 1.654 ± 0.012Ma.
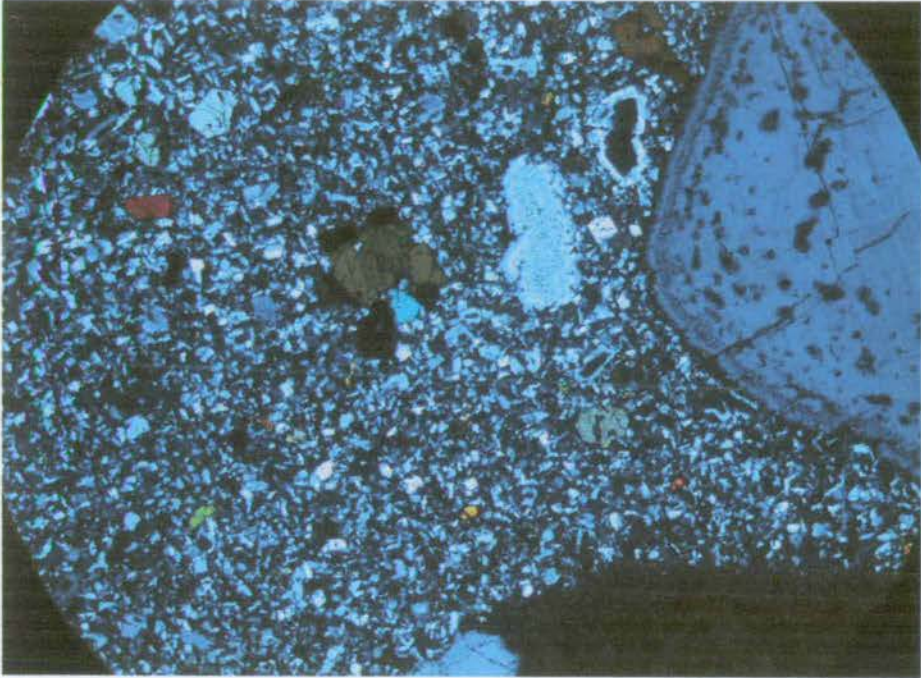
Figure 3.15 Photograph of Ol Tepesi Benmoreite taken under cross-polars (x2; field of view ~8mm). The large sanidine phenocryst to the right of the image shows a distinctive sieve texture around the rim that is indicative of disequilibrium in the melt.

3.3.12 The Plateau Trachytes

Between the topographic high points of the Ol Tepesi Benmoreite and Limuru Trachyte fault segments is a 2km section of scarp with a substantially lower displacement that cuts through two flaggy lava flows. The flows have a maximum thickness of 5m and are separated by an obvious red paleosol some 5-10cm in thickness. At the crest of the scarp the upper flow, sampled at K46, has a flaggy, vesicular surface, weathered to an orange-brown colour. In thin section, the rock is typified by occasional sanidine phenocrysts with augite inclusions, embedded in a groundmass of randomly orientated sanidine, plagioclase, augite and glass.

Baker and Mitchell (1976) originally mapped these flows as part of the Ol Tepesi Basalt group. However, analysis of the upper flow in thin section suggests that these rocks are trachytic in nature. The thin, flaggy nature of the flows suggests they may be a part of the Plateau Trachyte Formation.

A total of 11 sanidine phenocrysts, isolated by mineral separation, were analysed by laser total fusion. The resulting weighted mean age for this sample is 1.128 ± 0.007Ma. This age is very similar to values determined, during the course of this study, from accepted Plateau (Magadi) Trachyte flows located in the Ilainymok region, at the centre of the rift (see section 3.4.1). This supports the notion that the sample collected at K46 is from a Plateau Trachyte flow.

3.4. Fieldwork localities at the axis of the South Kenya Rift

As mentioned in section 3.1, Crossley (1976) identified a number of localities close to the centre of the rift where there is evidence for contemporaneous extensional faulting and volcanism. All the faults in these localities cut through flows of subhorizontally bedded Magadi Trachyte lava flows, which cover an extensive area of the axial rift floor. Faults in two such areas, the Ilainymok and Olooltepes regions, were visited during the course of this fieldwork (figure 3.16).

3.4.1 Introduction to the Ilainymok region

The Ilainymok fault is located close to the centre of the South Kenya Rift, approximately 20km west of the Magadi Township, and is accessible by 4WD from the gravel road that connects Magadi with the Nguruman escarpment, on the western rift flank (figure 3.17). The geological significance of this fault is twofold; firstly there is evidence for lavas that onlap against pre-existing fault blocks and secondly, at its northern end, the fault interacts with the NW-SE trending Magadi Transverse Zone. This latter structure is believed to have been inherited from movement on a Proterozoic lineament located in the underlying metamorphic basement, that is obliquely orientated relative to the direction of rifting. The Ilainymok fault therefore provides an opportunity to quantify normal fault growth in an oblique fault zone, which compliments analogue modelling of fault evolution in oblique rift systems (e.g. McClay and White, 1985; see also section 6.5.2).
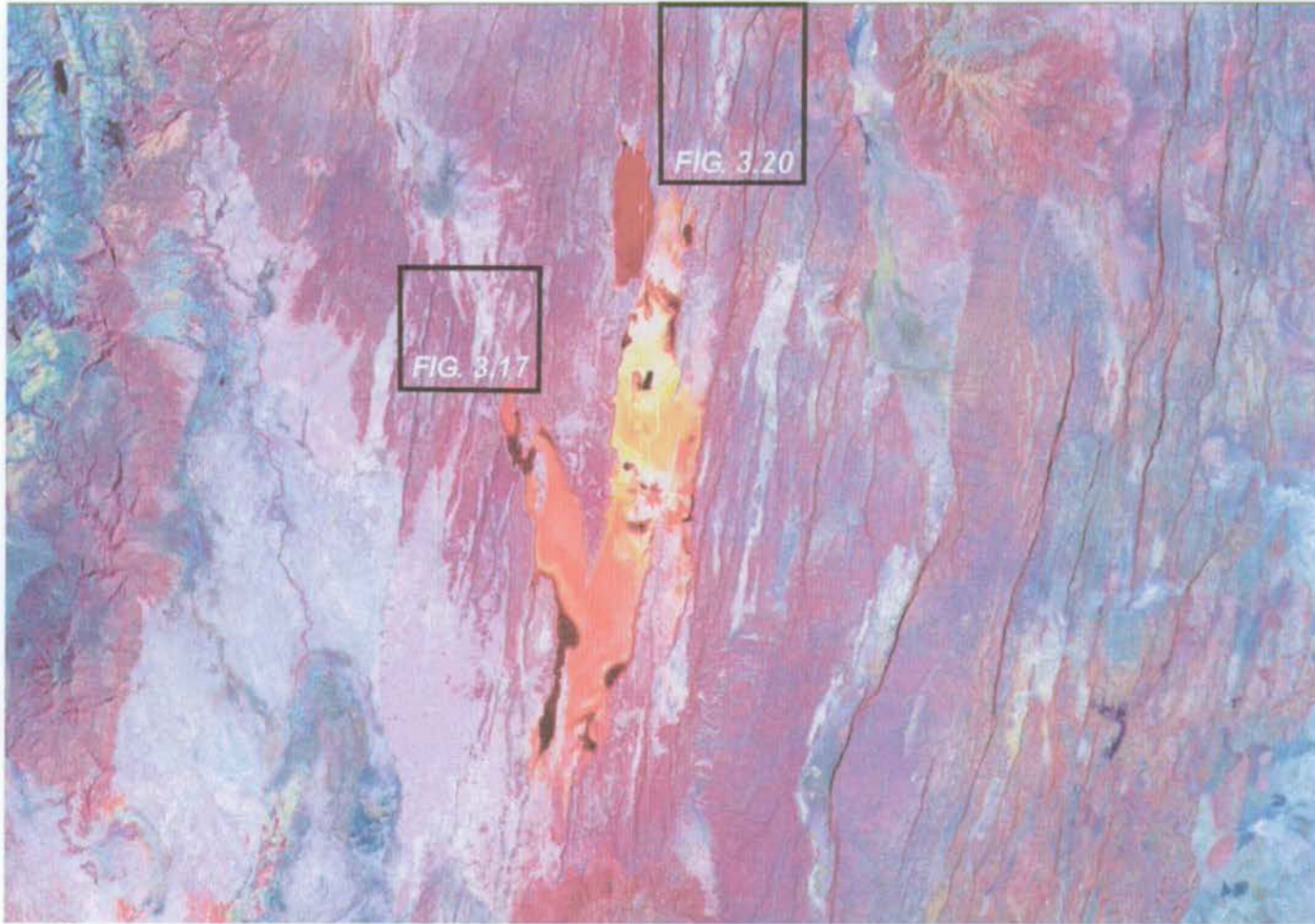
Figure 3.16 Landsat 7 satellite image of the Lake Magadi region. Black rectangles demarcate the areas covered in the figures indicated.
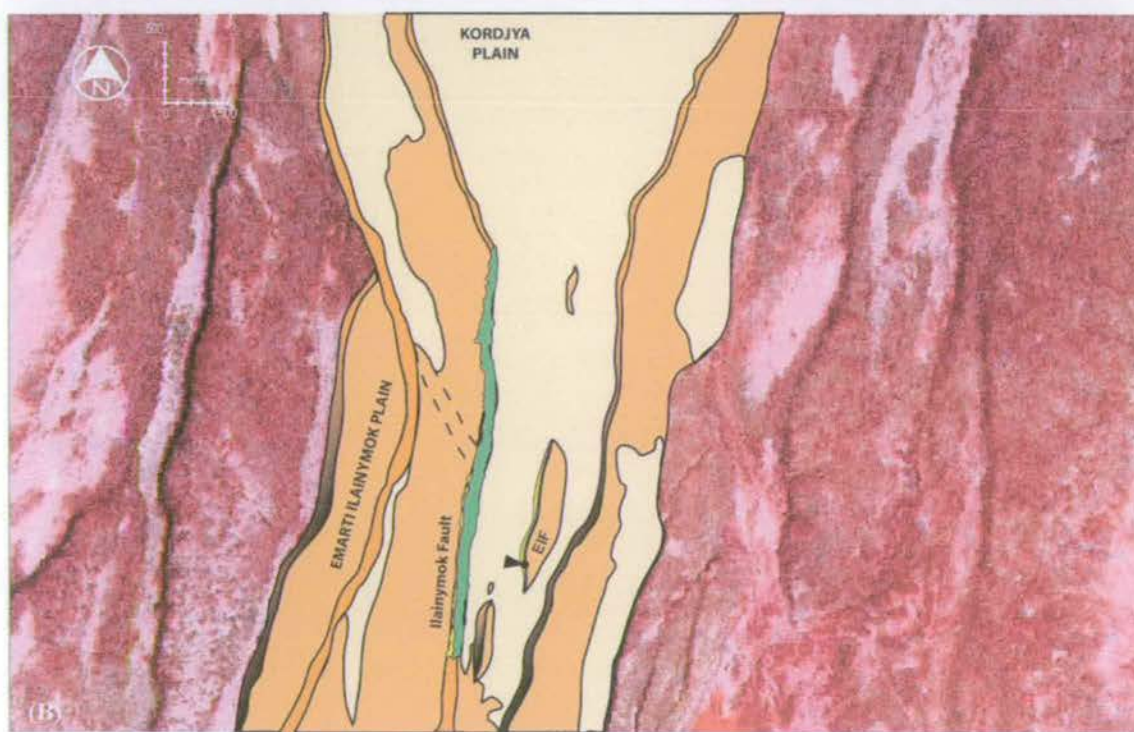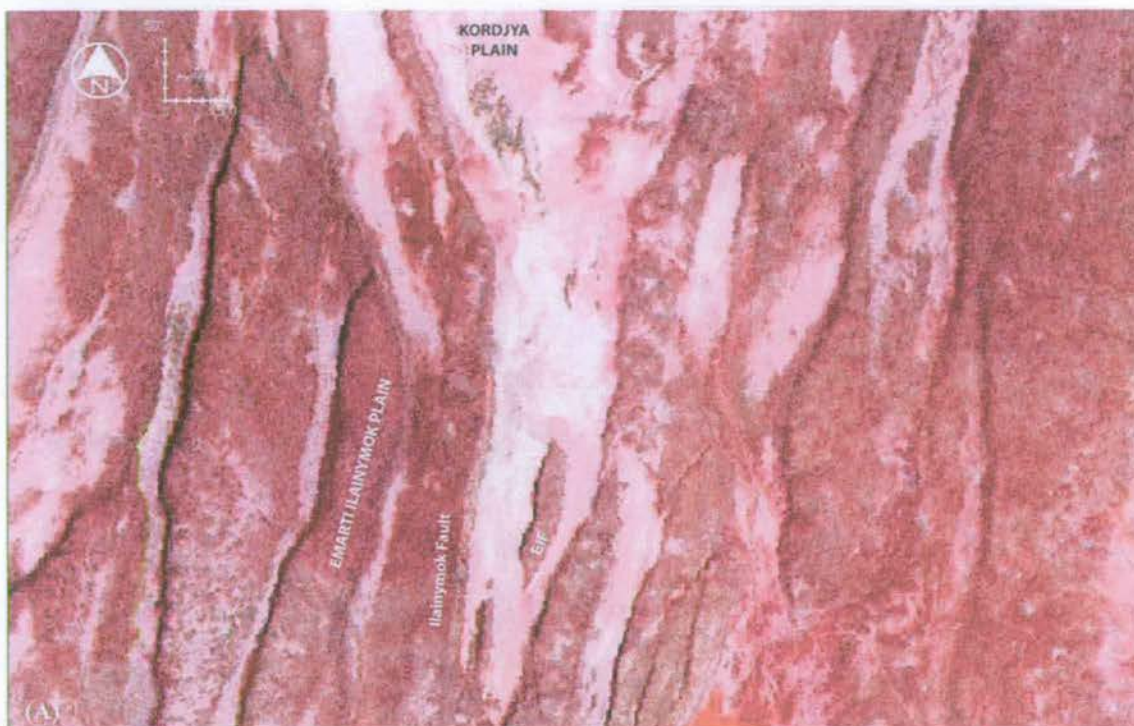
Key — Lower Magadi Trachyte flow — Upper Magadi Trachyte flow — Figure 3.18 viewpoint

Figure 3.17 (A) Landsat 7 image of the Ilainymok fault and the surrounding region. (B) As (A), but overlain by an interpreted map of the Ilainymok region. Dark orange/black – fault scarps, mid orange – exposed bedrock, pale orange – alluvium. EIF = East Ilainymok Fault.

Figure 3.18 Photomontage of the South Ilainymok Fault scarp. Coloured ornament indicates the Upper Magadi Trachyte flow. 'K10' and 'K11' are sample collection sites. Height of scarp is approximately 90 metres.

In its entirety, the Ilainymok fault, named after the neighbouring Emarti Ilainymok Plain to the west, is some 15km long. The southern section of the fault, with approximately ~100m of displacement, trends almost directly N-S and cuts through an obvious flaggy trachyte flow overlying a more poorly exposed, rubbly lava, partially obscured by grass and acacia bushes (figure 3.18). The lower of the two flows is characteristically massive, blocky lava that becomes progressively more flaggy towards its upper surface. A thin-section of the rock, taken from a sample collected at K10, shows a definite trachytic texture comprising occasional euhedral sanidine phenocrysts in a groundmass of aligned feldspar (the majority sanidine), interstitial aegerine-augite and patchy volcanic glass.

An obvious orange-red laterite horizon, up to a few metres in thickness, marks the contact between the lower and upper lava flows. The horizon contains rounded, poorly sorted boulders that further indicate the presence of an exposure surface between the flows. The upper flow (sampled at K11) forms a well-exposed orange-brown cliff, approximately 10-15m in height, which mantles the lower flow over the southern portion of the Ilainymok scarp. Again, this unit becomes increasingly flaggy and vesicular in character toward the lava surface. On a large scale, the flow is cut by a series of subvertical anastomosing joints and fractures that appear to carry small amounts of displacement (figure 3.19).

In hand specimen and thin section, the rock is characterised by mm-scale dark and light grey flow banding. The petrology is very similar to that of the underlying flow, though the upper flow is largely aphyric. Again, there is a clear trachytic texture consisting largely of feldspar (85%), aegerine-augite and partially devitrified glass.

Both rock samples were dated using incremental-heating of whole-rock cores. A sample of K10 yielded an age of 1.120 ± 0.003Ma. K11 was constrained at 0.928 ± 0.003Ma.

On a large scale, the upper surface of the lower flow has an undulating morphology with a wavelength of several hundred metres. Thinning, and in places pinching-out, of the upper flow over the crests of these undulations indicates that these were pre-existing topographic features. A further discussion of the undulations is given in section 4.5.2.
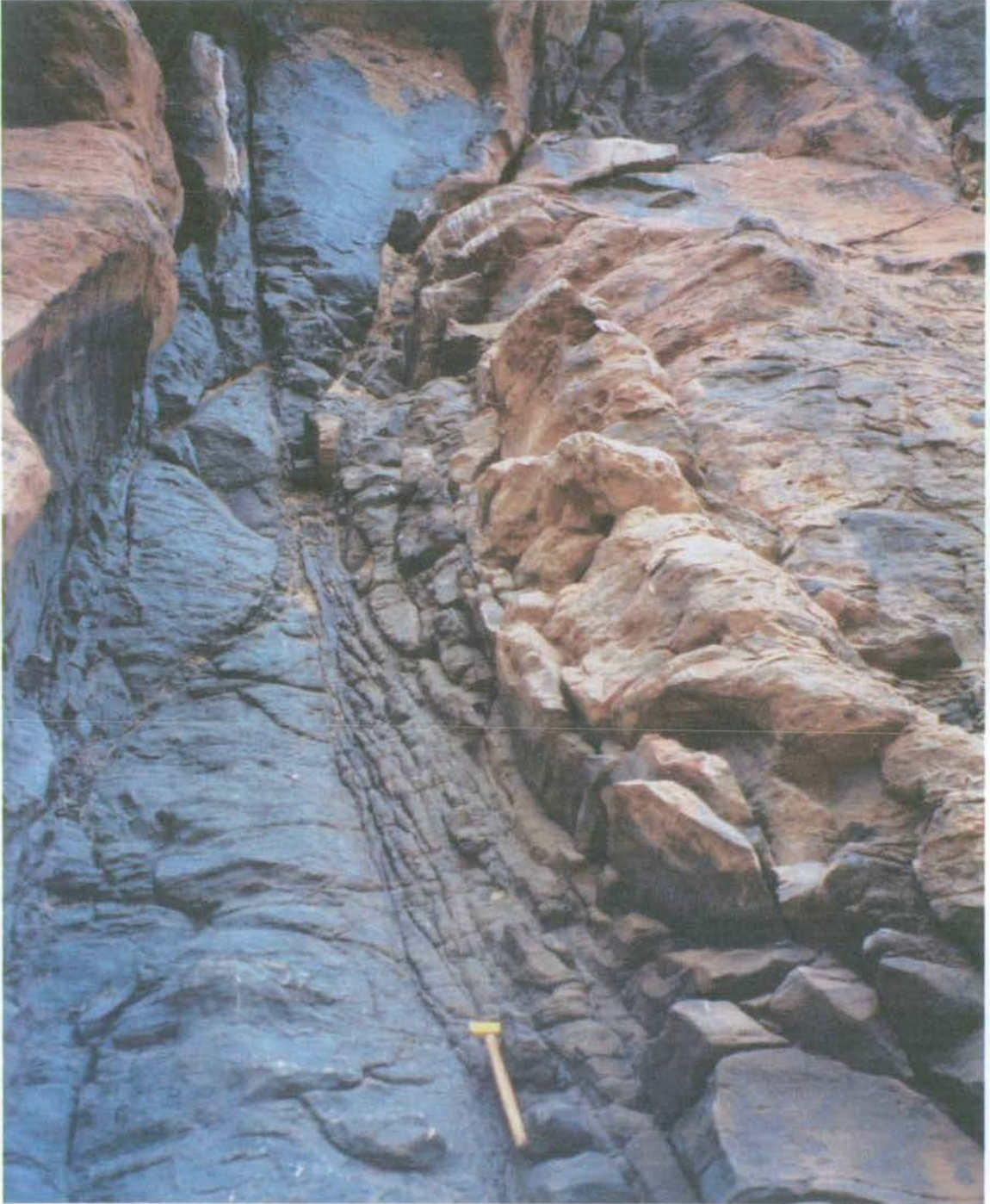
Figure 3.19 Photograph showing subvertical anastomosing fractures in the Upper Magadi Trachyte flow. Groups of such fractures are observed at regularly spaced intervals (approximately every 20m) along the footwall scarp. Offset of trachytic flow banding indicates that fractures carry a small amount of vertical displacement.

3.4.2 Introduction to the Olooltepes region

Olooltepes is located in the centre of the rift, approximately 10km north of Lake Magadi (figure 3.16, 3.20 and 3.21). This is another locality that was initially visited on the basis of previous work by Crossley (1976), who described 'north trending horsts consisting of Magadi trachytes partly flooded by younger flows of Magadi trachyte'.

A spectacular train of almond-shaped horst blocks, that resemble a line of upturned rowing boats, dominates the structure of the Olooltepes region (figure 3.22). Each block is approximately 2-5km in length, a few hundred metres in width and is separated from the next block along strike by a topographic low. Lying directly to the southwest of Mount Olorgesailie, the most northerly of the horst blocks (named Ileek Pusi) is onlapped by a 10m thick lava flow that has subsequently been dissected and uplifted by renewed faulting between the tip of the horst and the western slopes of Mount Shanamu. Recently, however, the Olooltepes area was the site of a swarm of earthquake activity that lasted for a period of four weeks in May 1998 (see also section 2.4.5) and opened a tension gash between two of the horst blocks (figure 3.22 and 3.23). Hence, through radiometric dating of the lava flows, this region offers the unique opportunity to study the growth of a currently active fault scarp over a geological timescale.

The tension gash is a ~2km long structure that cross-cuts an alluvial plain between Ileek Pusi and the neighbouring horst block immediately to the south. The expression of this feature across the surface of the alluvium is as a series of en eschelon gashes, each approximately 10-20m in length and 10-15cm in width. In places, where it breaks the surface of the alluvium, the rupture shows up to 5cm of vertical displacement. Elsewhere deformation is characterised by a centimetre-scale monocline, presumably overlying the blind fault-tip. In the four years since its appearance, erosion has caused some deterioration of the gash where it passes through the soft alluvial sediments. However, it is still possible to trace the line of the break, striking 187 degrees, across the alluvium and around the western side of the two neighbouring horsts. At the tip of the northern horst the gash follows the base of a prominent scarp, some 5m in height, which appears to have been the location of the most recent neotectonic activity (figure 3.24).
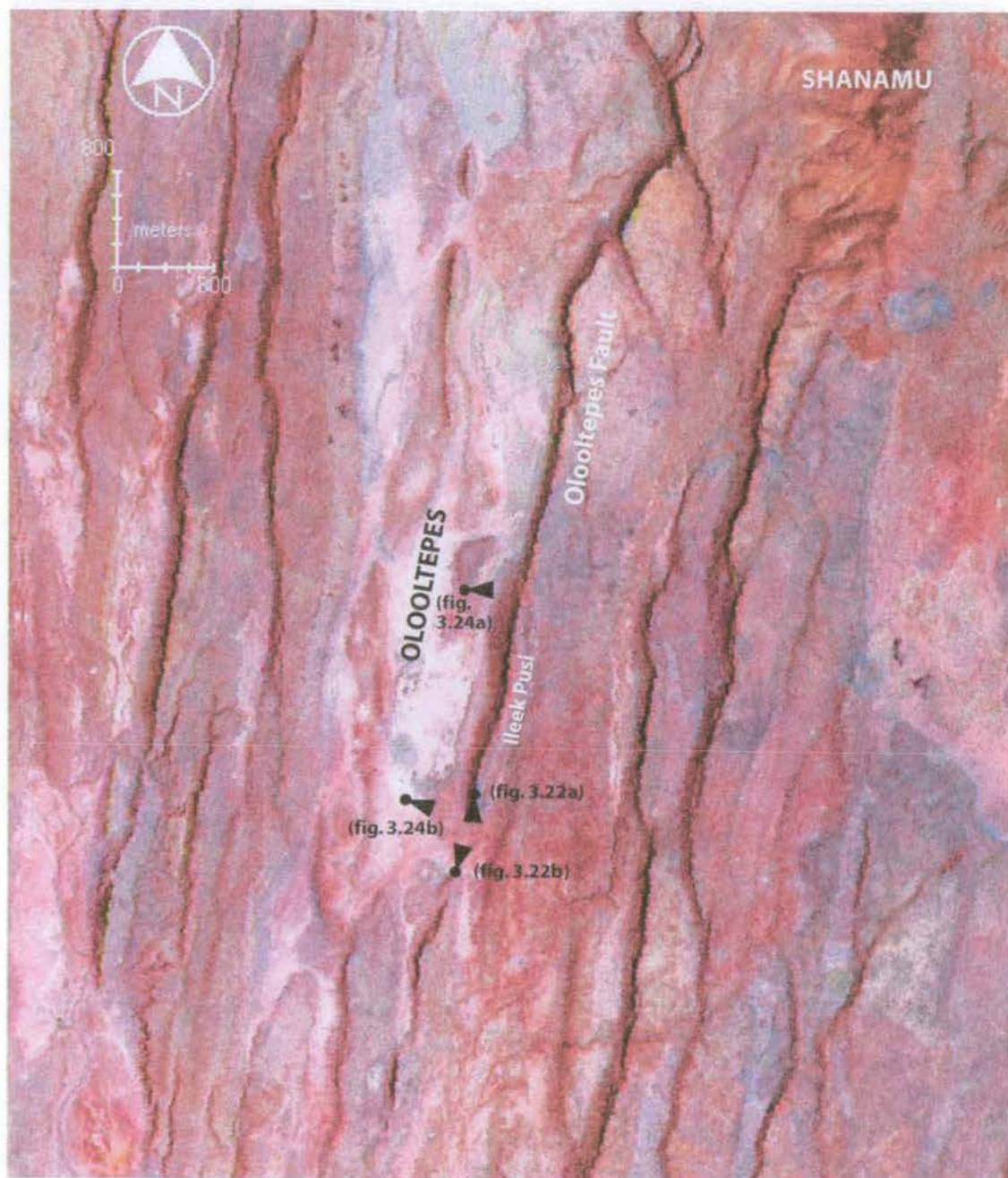
Figure 3.20 Landsat 7 satellite image of the Olooltepes region depicting the major Olooltepes fault scarp, the Ileek Pusi horst located at its southern tip and the train of horst blocks located directly to the SSW (see figure 3.21 for further detail).
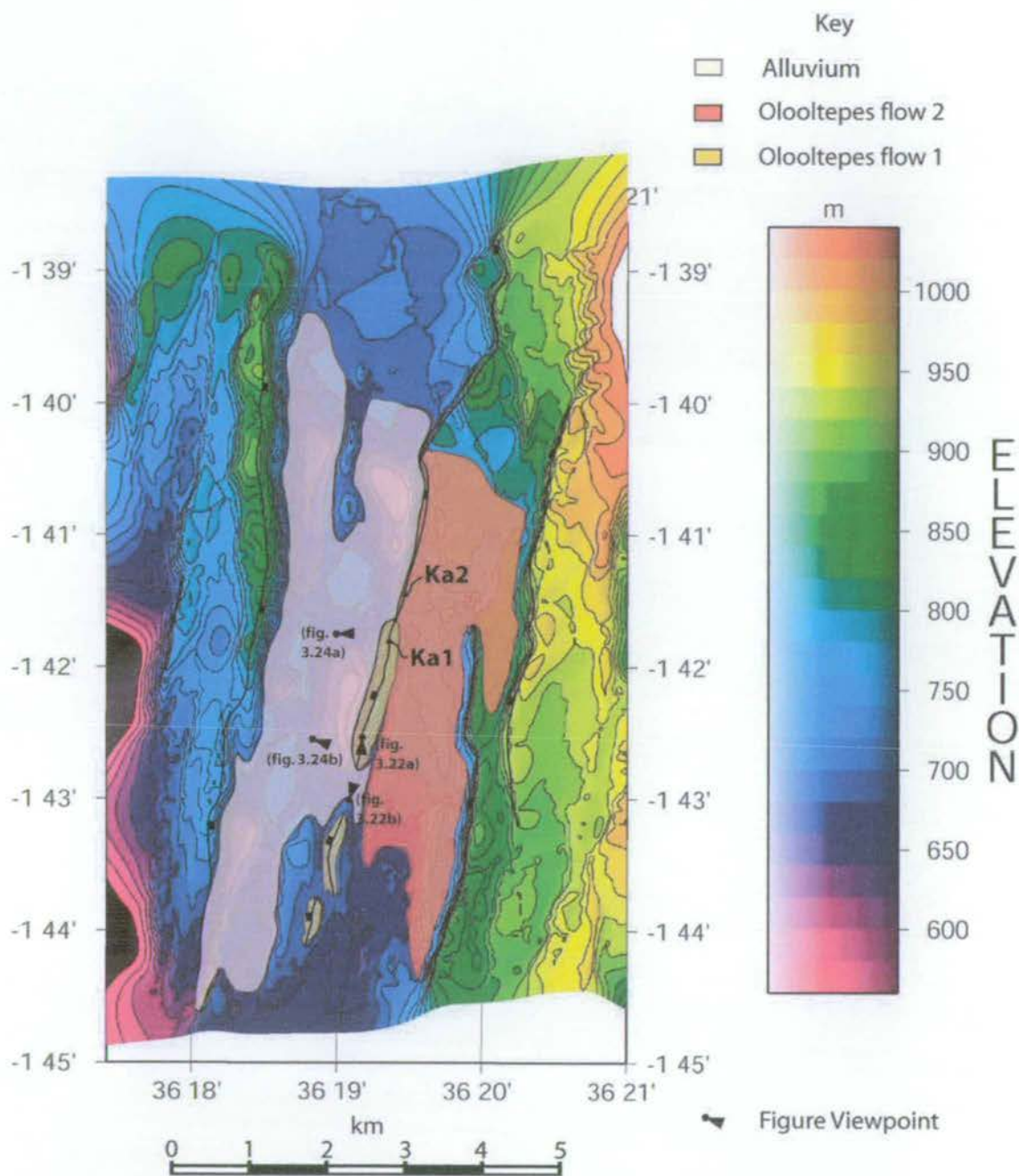
Figure 3.21 Geology and structure of the Olootepes region overlain on an elevation model constructed from 1:50,000 scale map contour data. The train of Olooltepes horst blocks that uplift Olooltepes flow 1 are shown in yellow; the approximate areal extent of flow 2 is indicated in red.
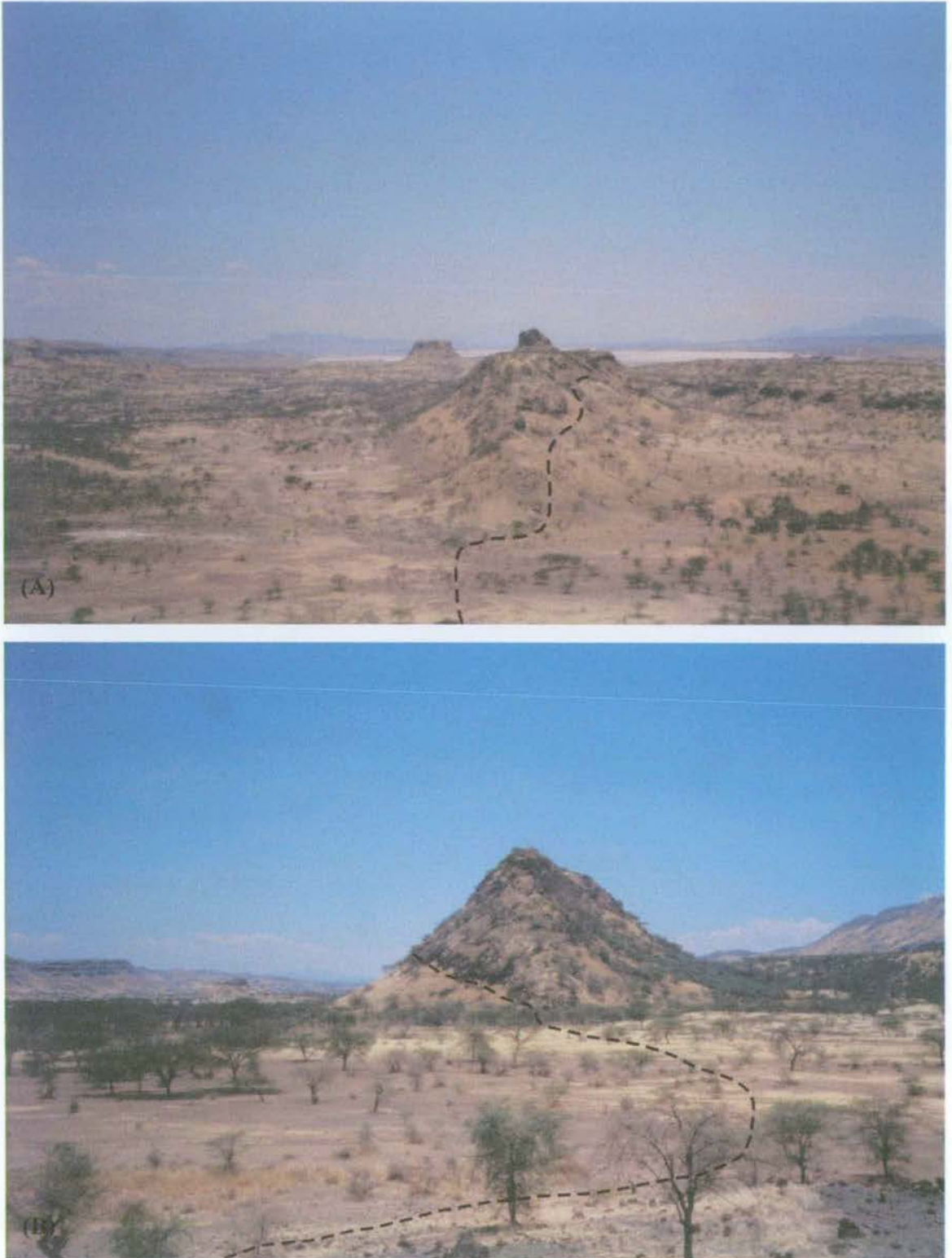
Figure 3.22 Two perspectives of the Olooltepes horst blocks. (A) view looking southwards towards Lake Magadi across the train of three horsts. (B) view looking northwards towards the tip of the Ileek Pusi horst block. The location of the tension gash between these blocks is indicated by the dashed black line.
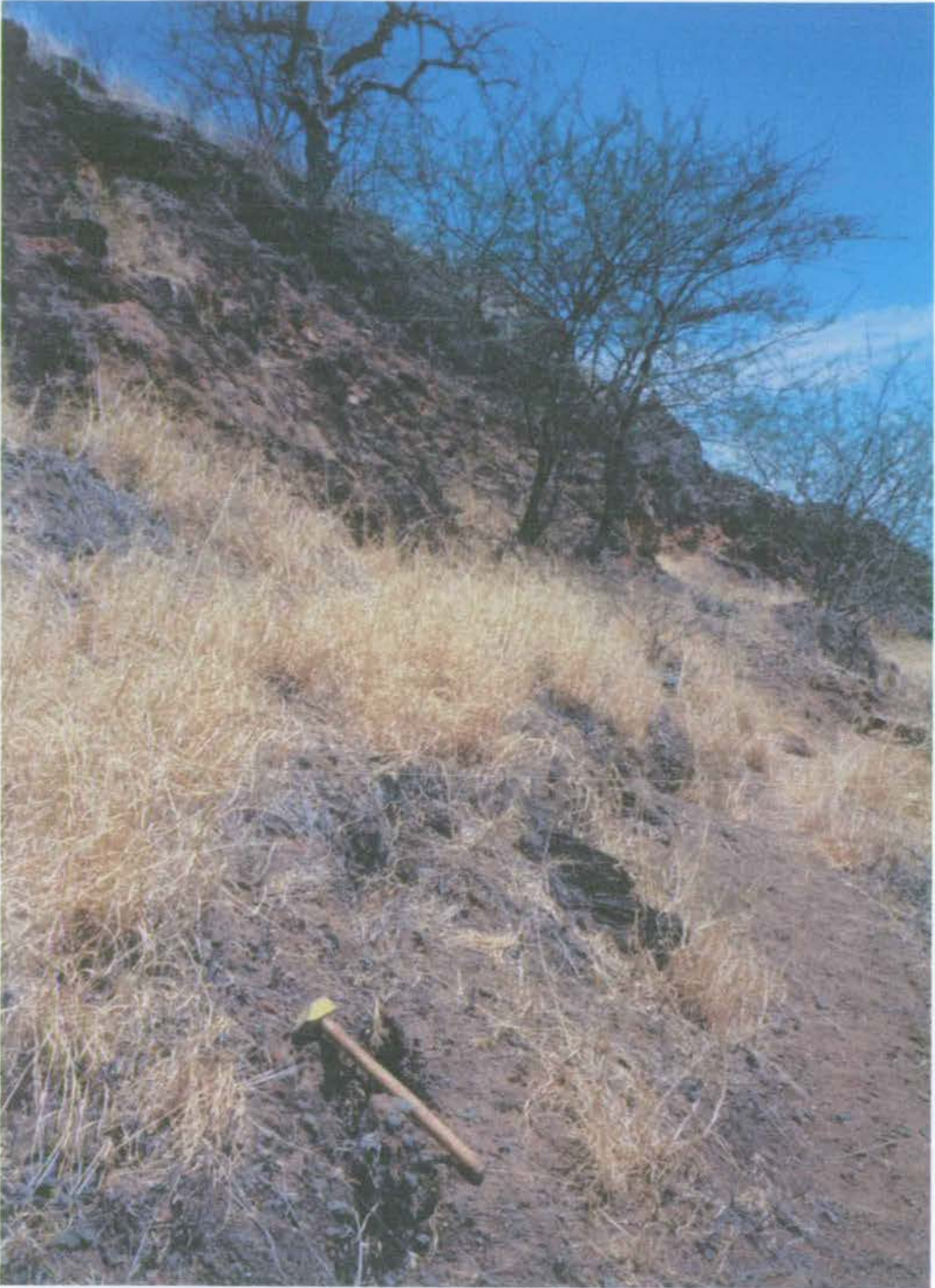
Figure 3.23 Photograph of the tension gash where it cuts through alluvium at the southern tip of the Ileek Pusi horst. The width of the break in this location is 10-15cm.

Two rock samples were collected from the northern end of Ileek Pusi horst; one from the crest of the block at Ka1 and the second from the upper surface of the onlapping flow at Ka2 (figure 3.24). The crest of the horst block, which is only 2m wide in places, is characterised by large boulders of flaggy trachyte up to 8m in diameter. Much of the trachyte along this narrow ridge appears to have been slightly moved or dislocated. The large blocks are often perched directly above a fractured fault breccia containing decimetre-scale clasts that have been subsequently cemented together. However, at Ka1 the rock appears to be relatively in situ as it shows subhorizontal bedding. In hand specimen this rock is typical of the Magadi Trachyte flows seen across the rift axis, showing mm-scale flow banding that in thin section appears as a definite trachytic texture of aligned K-feldspar and plagioclase phenocrysts. Also present are sparse phenocrysts of sanidine (1%), while augite (15%) and devitrified glassy patches (30%) are common in the groundmass.

The onlapping flow, sampled at Ka2, is typically more vesicular than that on the crest of the horst and generally more flaggy in nature. Flow banding can be recognised in thin section, though the trachytic texture is weaker than in Ka1. Petrologically, the rock is otherwise very similar to Ka1 (70% feldspar, 20% volcanic glass and 10% aegerine-augite).

Both flows were dated used incremental heating analysis of whole-rock cores. A core extracted from sample Ka1 provided an age of 1.134±0.002Ma. The age of sample Ka2 was determined at 1.116±0.002Ma.
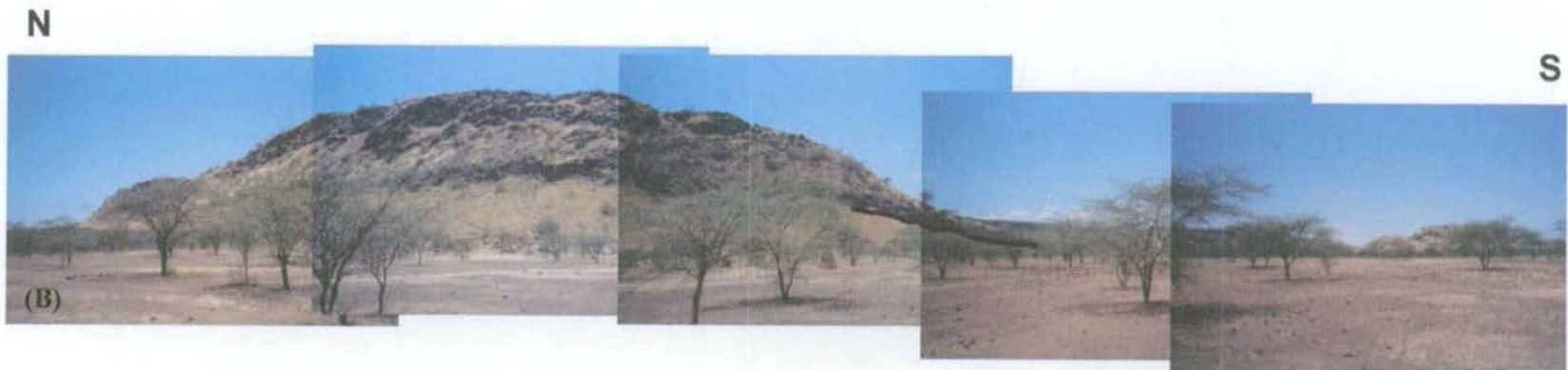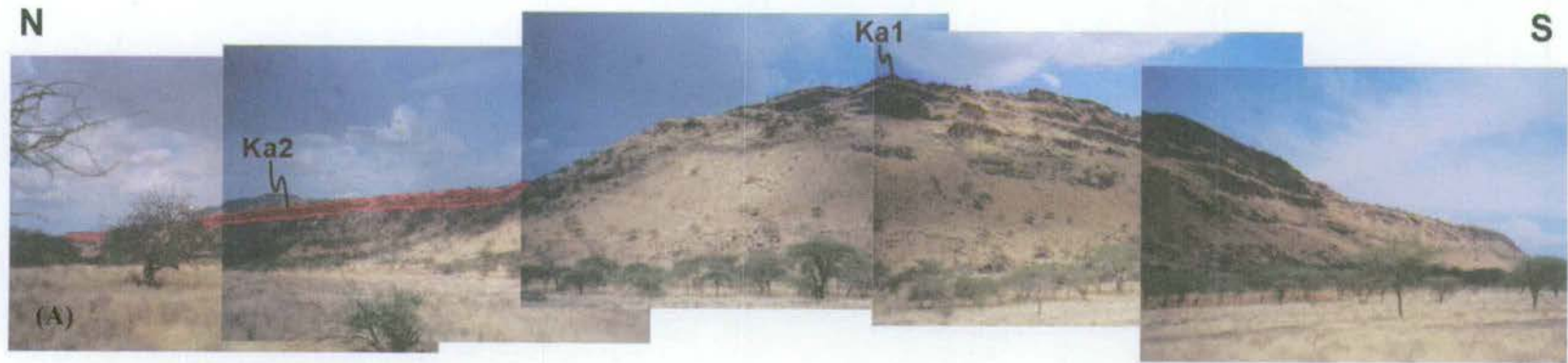
Figure 3.24 Photomontages of the Ileek Pusi horst block. (A) Northern tip of the block where it is onlapped by a thin lava flow. 'Ka1' and 'Ka2' indicate the positions of sample localities. (B) The southern tip of the horst. A black line marks the trace of the tension gash where it follows the base of a ~5m high scarp.

3.5 Summary

This chapter has introduced the principal elements of ^{40}Ar/^{39}Ar dating techniques; further details can be found in Chambers (2000) and Harford *et al.* (2002). ^{40}Ar/^{39}Ar geochronology has been undertaken on a total of 13 rock samples from the South Kenya Rift, the details of which are summarised in table 3.2. The highly potassic nature of the rift trachytes, basalts and benmoreites has made these lavas ideally suited to such analyses and analytical errors have been restricted to 0.18-0.62%. The ages discussed in this chapter show significant improvements over previously published K/Ar dates (e.g. Fairhead *et al.*, 1972; Baker and Mitchell, 1976; Baker *et al.*, 1988), which show errors of 1-10%.

The four field localities a t t he c entre (Olooltepes a nd Ilainymok) a nd e astern margin (South Kedong and Esiteti) of the South Kenya Rift were specifically identified and selected due to their excellent footwall exposures and detailed syn-rift volcanic stratigraphy and structural relationships. Having now established a detailed chronostratigraphic framework for each field area, the specific field relationships will be introduced in the following chapter, prior to a discussion of the detailed fault reconstructions in chapter 5.

Sample	Geological unit	Latitude (S)	Longitude (E)	Material	Steps[1]	Total fusion age (Ma)[2]	Error (1σ)	Total K/Ca[3]	[39]Ar(%)[4]	Age spectrum analysis		
										Age (Ma)	Error (1σ)	MSWD
K53	Gesumeti Trachytes	1.41356	36.47498	Sanidine	10 of 10	2.258	0.005	43.163	100.0	**2.254**	0.007	4.17
K47	Gesumeti Trachytes	1.41385	36.47499	Sanidine	15 of 15	2.108	0.005	6.420	100.0	**2.100**	0.007	2.92
K52	Limuru Trachytes	1.40356	36.47650	Sanidine	13 of 13	2.116	0.002	15.207	100.0	**2.009**	0.004	-
K49	Ol Tepesi Basalts	1.43200	36.47394	Groundmass	9.5-14.0	1.495	0.006	0.251	55.8	**1.478**	0.003	0.90
K51	Barajai Trachytes	1.43200	36.47394	Whole-rock	6.8-27.0	0.360	0.001	17.364	81.2	**0.360**	0.001	1.65
K31	Limuru Trachytes	1.53663	36.45473	Whole-rock	9.6-17.0	2.004	0.005	63.829	65.8	**1.995**	0.004	1.24
K43	Ol Tepesi Benmoreite	1.50593	36.44846	Sanidine	8 of 15	2.019	0.006	1.657	48.5	**1.856**	0.010	1.65
K29	Orthophyre Trachyte	1.57005	36.44995	Sanidine	10 of 10	1.646	0.007	1.380	100.0	**1.654**	0.006	3.83
K46	Plateau Trachytes	1.50593	36.44846	Sanidine	11 of 11	1.128	0.007	7.093	100.0	**1.128**	0.007	1.32
K10	Lower Magadi Trachyte	1.82417	36.20264	Whole-rock	9.8-18.5	1.126	0.002	12.670	64.2	**1.121**	0.003	3.13
K11	Upper Magadi Trachyte	1.82417	36.20264	Whole-rock	8.0-34.0	0.937	0.004	14.008	92.6	**0.937**	0.004	-
Ka1	Olooltepes flow1	1.70087	36.32312	Whole-rock	8.5-15.3	1.143	0.037	15.896	74.3	**1.134**	0.002	2.00
Ka2	Olooltepes flow2	1.69527	36.32441	Whole-rock	8.4-16.5	1.138	0.008	16.902	57.7	**1.116**	0.002	2.00

Table 3.2 Summary of [40]Ar/[39]Ar incremental heating and laser total fusion experiments on South Kenya Rift samples. Best eruption ages of the samples are highlighted in bold. All ages are calculated relative to 28.34Ma for the neutron flux monitor Taylor Creek Rhyolite Sanidine. [1]Indicates the proportion of argon gas used in the age spectrum analysis; this represents either the number of total fusion experiments used from a maximum (e.g. 8 of 15 for the Ol Tepesi Benmoreite) or the number of heating increments, expressed as the percentage of maximum furnace power (where total fusion is usually achieved between 45.0-60.0%). [2]This is the age calculated if all argon gas released from the sample is taken into account. [3]K/Ca molar ratio present in the sample. [4]This value is the percentage of [39]Ar by mass used in the age spectrum analysis.

Chapter 4: Use of Differential GPS to determine fault-scarp dimensions in the South Kenya Rift

4.1 The Global Positioning System (GPS)

4.1.1 Introduction

The Global Positioning System (GPS) is a satellite-based system that uses a constellation of 24 satellites to provide accurate positional data for a user located somewhere on the surface of the Earth. The system was originally conceived at the beginning of the 1970s as a navigation tool for the U.S. military, but has since developed major civilian applications. Depending on the required accuracy, there are a number of methods using GPS. The most popular technique, used by hikers and the military, is autonomous navigation. This uses a single, lightweight, stand-alone receiver that provides an accuracy of approximately 10-20m (since the removal of Selective Availability scrambling (SA) by the U.S. Government on May 1, 2000). Differentially corrected positioning is instead used where much greater accuracy is required (down to values of 1-5cm) such as for detailed surveying or machine operation.

4.1.2 Determination of position

All GPS methods follow the concept of satellite ranging to provide positional data. This is essentially an extension on the idea of resection, used by many surveying techniques, which locates the position of an unknown point by measuring the distance between that point and three surrounding points of known position. At any location on the Earth's surface, if the distance to one satellite is known, then the position of the GPS receiver must be at some point on the surface of an imaginary sphere which has its origin at the satellite. In theory, by intersecting three imaginary spheres the receiver position can be determined (figure 4.1). However, in practice there are four unknowns to determine; position (X,Y and Z) and time of travel of the satellite signal. Observing to four satellites allows these four unknowns to be calculated.
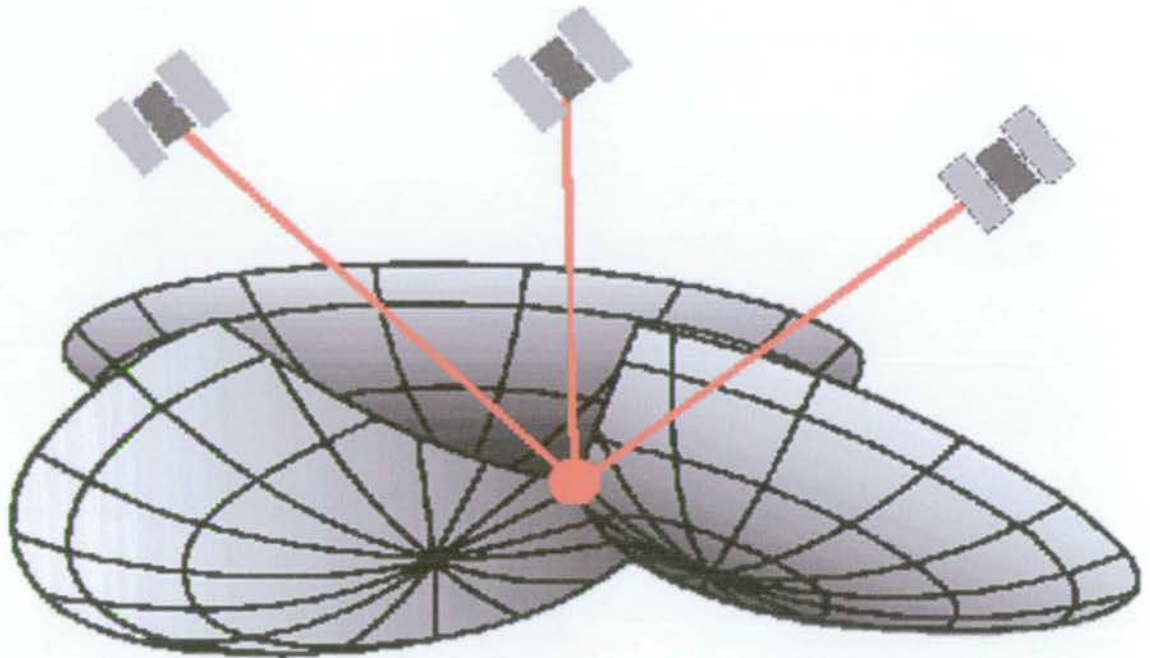
Figure 4.1 Determination of position from the intersection of three imaginary spheres. (from Leica Geosystems AG, 1999)
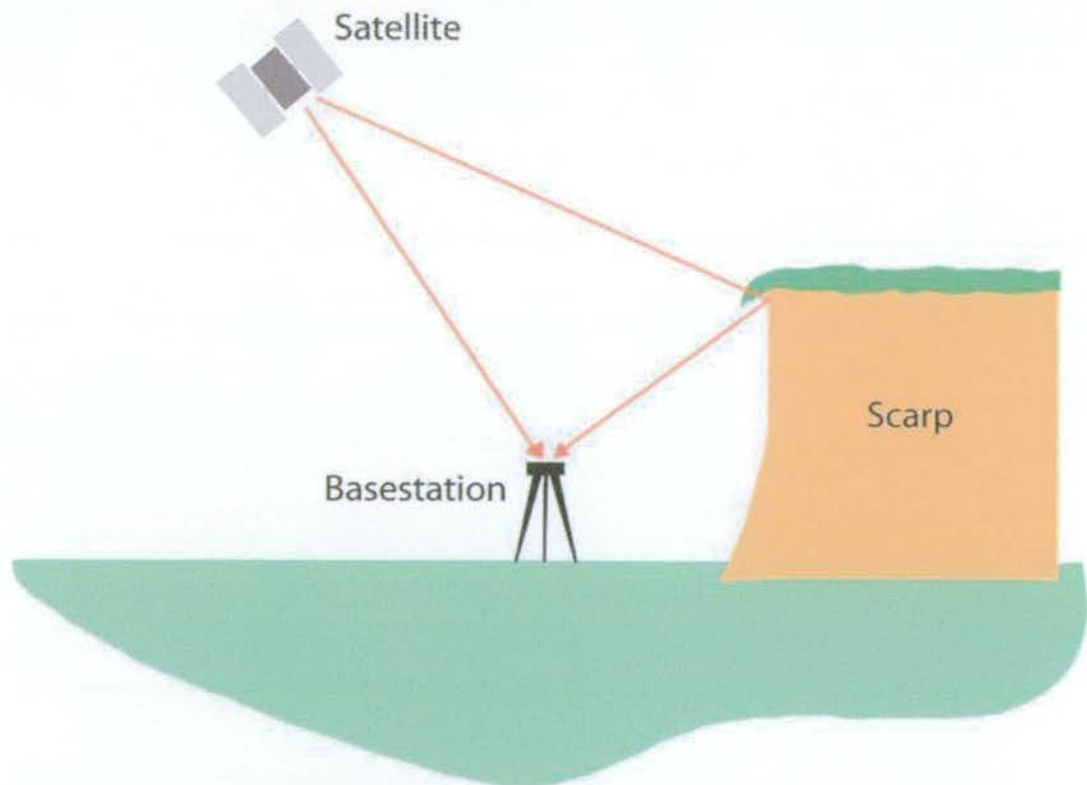
Figure 4.2 Generation of GPS Multipath errors. False positional measurements can occur when incident satellite signals are reflected from nearby surfaces (modified after Leica Geosystems AG, 1999).

4.1.3 Potential sources of error in GPS measurements

A number of sources of error are responsible for degrading the accuracy of GPS positional data, including ionospheric and atmospheric interference, satellite and receiver clock errors, multipath errors and dilution of precision (Leica Geosystems AG, 1999). Delays induced by refraction in the ionosphere are a common problem experienced by satellite signals passing through the upper atmosphere. Unfortunately, the size of such delays are not constant and vary according to satellite elevation (which influences the angle of incidence of the signal with the ionosphere), the density of the ionosphere (which depends on the amount of incoming solar radiation) and the amount of water vapour in the atmosphere. While the atomic clocks mounted in the satellite are generally very accurate (to about 3 nanoseconds), occasional clock errors can affect the positional precision and need to be corrected for. Multipath errors result from incoming signals bouncing off reflective surfaces such as lakes, buildings or fault scarps prior to reception by the ground antenna. This increases the apparent distance between satellite and receiver, leading to a false measurement (figure 4.2). Prevention of multipath errors can be achieved through the use of a choke-ring antenna attached to a receiver basestation. A choke-ring antenna incorporates 4 or 5 concentric rings around the central antenna unit that trap any indirect signals (figure 4.3).

Dilution of precision (DOP) is a consequence of the relative spacing and positions of satellites in the sky. In general, precision improves when there is a large angle of separation between satellites.

4.1.4 Differential GPS (DGPS)

Many of the major sources of signal error can be substantially reduced, or in some cases completely eliminated, by the use of differential GPS. The technique uses a combination of a reference receiver antenna and a rover antenna to increase the positional accuracy to 2-3m or less. The reference receiver, or basestation, is a fixed antenna located on a point with known co-ordinates. Co-ordinates can be entered into the basestation computer either manually, e.g. from values given on a topographic map, or automatically by allowing the receiver a fixed amount of time to track satellites and calculate an autonomous position. Once an accurate receiver position has been calculated the basestation can work out the difference between the computed position

and any further positional measurements that are received. These differences, known as range corrections, are broadcast in real-time by means of a radio data link to the rover unit. The rover consists of a mobile GPS receiver, weighing approximately 3kg (figure 4.4), which also calculates the satellite ranges but then applies the range corrections supplied by the fixed basestation unit. Such corrections allow the rover to calculate much more accurate positional data than would be possible if the uncorrected range measurements were used. In practice, real-time GPS surveying using a rover with a radio link to a reference antenna, known as Real Time Kinematic (RTK), can achieve maximum baseline accuracies in the range 1-5cm.

GPS positional data is recorded in a geodetic co-ordinate system based on the WGS84 (World Geodetic System 1984) ellipsoid. The ellipsoid is selected to be an accurate approximation of the shape of the Earth. Points are recorded in terms of latitude, longitude and ellipsoidal height (i.e. height above the surface of the ellipsoid)

As mentioned in section 4.1.2, GPS requires an unobstructed view to at least 4 satellites. Hence, problems may be encountered when surveying close to large objects such as buildings, trees and cliffs. When undertaking RTK surveying it is also necessary to ensure that there is a clear line-of-sight between the rover and basestation unit in order to maintain the continuous radio link between the two.

Figure 4.3 A choke-ring antenna (from Leica Geosystems AG, 1999)

Figure 4.4 Photograph of the GPS System series 500 receiver, terminal (keypad) and radio modem (right, with aerial) (from Geophysical Equipment Facility: Natural Environment Research Council (NERC), 2004)

4.2 GPS techniques in the field

The Differential GPS equipment used during both fieldseasons was a Leica GPS system 530, loaned from the NERC Geophysical Equipment Facility. The basestation unit consisted of a choke-ring antenna (figure 4.3) mounted on a tripod. Positional data received by the antenna were sent by cable to an on-board computer terminal (figure 4.4), powered by a 12V external battery, and stored on a PCMCIA flashcard. Reference antenna height was set by means of adjusting the length of the tripod legs and measured using an adjustable height-hook tape measure. A tribranch mounting, with a built-in spirit level, allowed the choke-ring to be maintained at a horizontal level.

The basestation was generally established at the base of a footwall scarp and usually at least 250m away from the cliff exposure so as to provide an unobstructed view of the sky. In order to determine an initial autonomous position, the basestation was set to track satellites for a period of 30 minutes, using the single-point position function, after which time it would begin to broadcast satellite corrections to the rover unit, via the radio-link. The maximum transmission range of the radio signal, given a clear view of the basestation, was approximately 4km. However, loss of reference data, caused by kinks in the fault footwall and, in places, thick vegetation, often made it difficult to collect data more than ~1-2km away. If the reference transmission was lost, the accuracy of the rover data dramatically decreased and it was then necessary to re-establish the basestation in a new location. Each basestation position was marked-out on the ground so that, if necessary, it could be located and reoccupied at a later date.

The rover comprised a lightweight antenna mounted atop a 2m-long aluminium pole connected, via a cable, to the terminal. The main GPS receiver unit weighed approximately 3kg and was contained in a specially adapted rucksack that also contained a radio antenna for receiving reference data corrections (figure 4.4 and 4.5). The power source for the rover consisted of two plug-in 6V camcorder batteries. Positional data received by the rover unit was stored on a PCMCIA flashcard inserted into the main computer terminal. Data collected during the day was downloaded and backed-up onto a laptop computer every evening with the aid of Leica SKI-Pro GPS management software.

In all the field localities, differential GPS was used to record positional data along the length of the fault scarps. Following initial reconnaissance, a number of traverses were selected in order to produce an accurate measure of the relief along the fault blocks and map the position and the extent of the lava flows relative to the fault scarps. Positional data could be selected and stored in two principal formats (figure 4.6). In most circumstances, where a traverse was easy to negotiate, i.e. a geological contact was easy to follow and there was little vegetation, the GPS receiver was set to automatically record positional data every metre along the ground. In situations of thick vegetation cover, or where it was difficult to continuously follow contacts along steep scarp fronts, points were recorded manually whenever it was possible to achieve accurate positional data. The maximum positional accuracy achievable on open ground was approximately 4cm in latitude and longitude and 8cm in ellipsoidal elevation. However, in reality, accuracy was influenced by the view of the sky and, in general, positional errors recorded at the base of fault scarps, close to the rockface or in thick vegetation, were larger than those measured along the crest of the scarps. Points of less than 5m accuracy in terms of latitude and longitude were automatically rejected from the final database.

The general procedure adopted to measure relief along the fault footwall scarp was to walk out a traverse, firstly along the scarp base, which was generally the cut-off between the footwall scarp and the upper surface of the hangingwall sedimentary fill, and later along the crest of the scarp. Walking-out the base of the scarp, as a first priority, made it possible to gain an initial impression of the scarp morphology and the location of any potentially interesting features, such as onlapping lava flows, that could be mapped on a later traverse. The largest errors in positional data were often recorded close in to the base of fault scarps where there was a restricted view of the sky and often thick vegetation cover. In some instances the problem had to be resolved by moving slightly further out from the base of the scarp, but, in general, traverses were no more than ~50m away from the rockface. Though the accuracy of measurements taken in such areas was not ideal, it was unusual for errors in latitude and longitude to be greater than 2m. The exposed crest of each fault scarp offered fewer problems in terms of data accuracy since the view of the sky was relatively unobstructed. Most datapoints recorded along scarp-crest traverses had an error of no more than ± 4cm in latitude and longitude and ±8cm in elevation. The limits of lava exposure could also be constrained by walking out geological contacts with differential GPS. Where the base of a lava flow was exposed at the front of a fault scarp it was usually possible to survey obvious laterite palaosol horizons (e.g. figure 3.11).

Figure 4.5 Photograph showing the main GPS rover assembly: an antenna mounted on a 2m pole and a receiver/radio modem stowed in a rucksack. The black aerial protruding from the top of the rucksack is for receiving the radio data-link from the reference antenna. In the background of the photo are the faults of the Ilainymok region, described further in section 4.5.
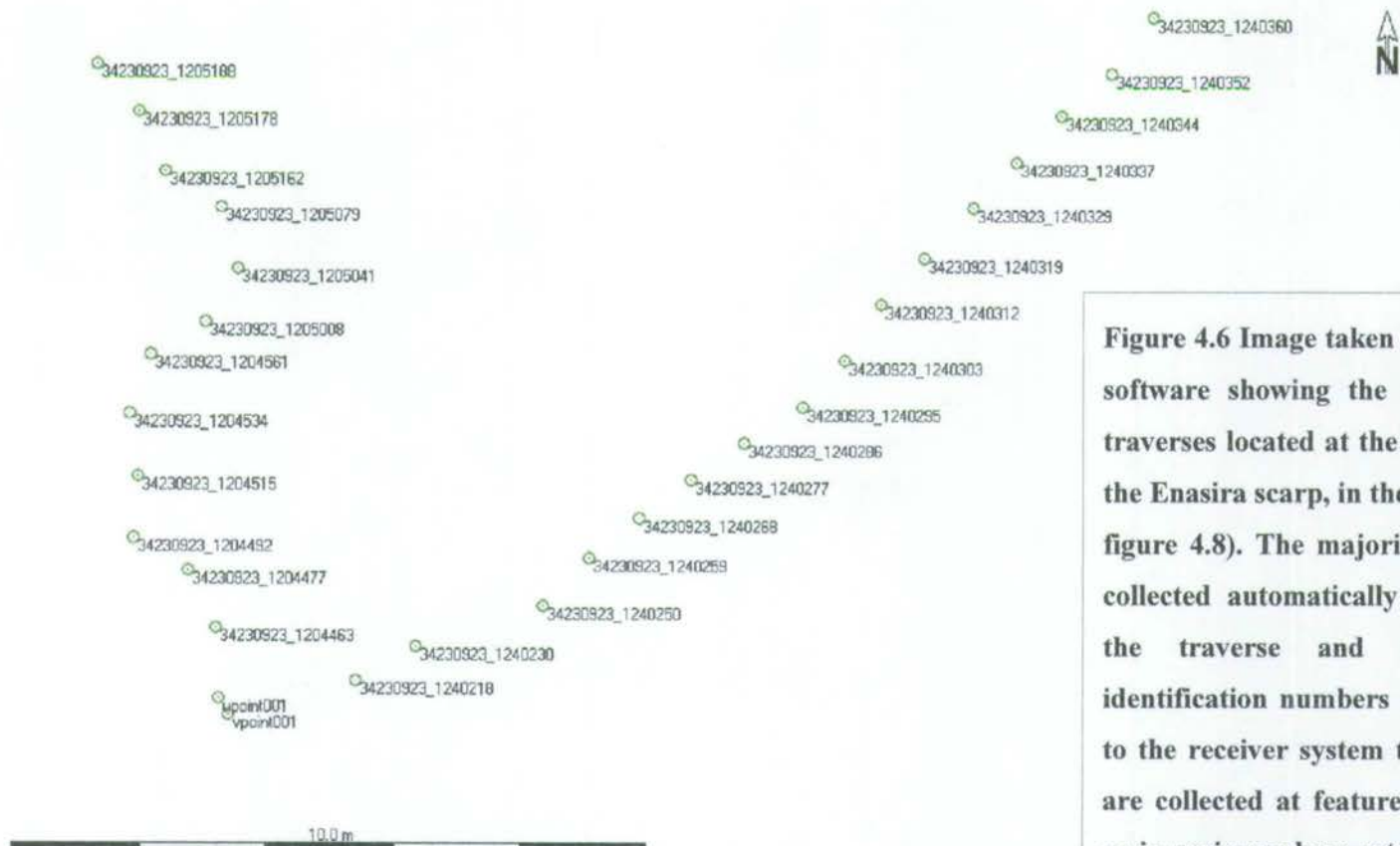
Figure 4.6 Image taken from Leica SKI-Pro software showing the detail of two GPS traverses located at the southernmost tip of the Enasira scarp, in the Kedong region (see figure 4.8). The majority of the points are collected automatically every metre along the traverse and are tagged with identification numbers that vary according to the receiver system time. Manual points are collected at features of special interest or in regions where satellite coverage is not consistently good. In this diagram, manual points labelled upoint001 and vpoint001 represent the starting points for the two traverses.

4.3 The South Kedong Graben

4.3.1 Introduction

A total of 56 traverses were made across the South Kedong region, following the base and crest of fault scarps and the contacts between lava flows. The steep fault scarps and relatively large relief in this area made it difficult to maintain a consistently clear line-of-sight between rover and reference antennas and the survey was regularly troubled by a loss of reference data. In order to alleviate this, GPS basestations were established at a total of seven locations, four, for ease of access, at the base of the Kedong Graben and the remaining three, to help elevate the basestation above low level obstructions, at positions on fault footwalls (figure 4.8).

The traverses define a roughly rectangular area some 6km in length by 3km in width (figure 4.7 and 4.8). Figure 4.8 is a topographic plot of the area constructed using the GPS traverses as a framework and interpolated with Generic Mapping Tools (GMT) software. The tools are a package of associated programs aimed primarily at construction of map and graphical images from coordinate input data. GMT version 3.4.3 (e.g. Wessel and Smith, 1998, 2003) is available as free software from http://gmt.soest.hawaii.edu/. Columns of geodetic data were exported from SKI-Pro and manipulated within a Microsoft Excel spreadsheet to convert them into the correct format for the GMT programs (namely three columns of data; first column of longitude values, second column of latitude and third column ellipsoidal elevation). The GMT Blockmean and Surface functions were applied to the input data in order to create a uniform gridded dataset from the spatially heterogeneous GPS data. A narrow grid-spacing, equivalent to 10^{-4} of a degree, was deliberately chosen to maximise the accuracy of the plots. Hence, each grid box represents an area of ~11.1m by ~11.1m on the ground, within which the GPS elevation values were averaged. The GMT Gridview function was then applied to the resulting gridded dataset in order to produce a UTM (Zone 36) projected, perspective view of the area of interest, colour-coded for surface relief (figure 4.8). The black lines in the diagram illustrate the position of each traverse. Files containing GPS data collected along each traverse are given in Appendix A (see section 5.2 for further details). Local geological information from field mapping has been overlain onto the above image using Adobe Illustrator drawing software (figure 4.9).

As described in section 4.1.4, GPS positional data is recorded in geodetic format (latitude, longitude and elevation) within the reference ellipsoid of WGS84. In order to calculate fault length data, it is necessary to convert these geodetic data into Universal Transverse Mercator (UTM) grid co-ordinates. This was achieved using geographic conversion software, GEOTRANS v2.2.2, available from the U.S. National Imagery and Mapping Agency (NIMA) website (http://164.214.2.59/GandG/geotrans/geotrans.html). GEOTRANS (Geographic translator) is an application capable of converting geographic coordinates among a wide variety of coordinate systems, map projections, grids, and datums and can also bulk transform a large number of coordinates contained in text files. It was therefore possible to convert GPS positional data into UTM zone 36 grid coordinates by exporting latitude, longitude and elevation values from Microsoft Excel in text format. Note that, since no information has been provided regarding the local geoid anomalies, ellipsoidal elevation values cannot be converted to elevations above mean sea level (MSL). Hence elevations shown on GMT plots, both in this, and the following chapters are ellipsoidal elevations rather than heights above mean sea level. However, this is not a problem as, for the purposes of this study, we are only interested in relative fault displacements rather than the absolute elevations.
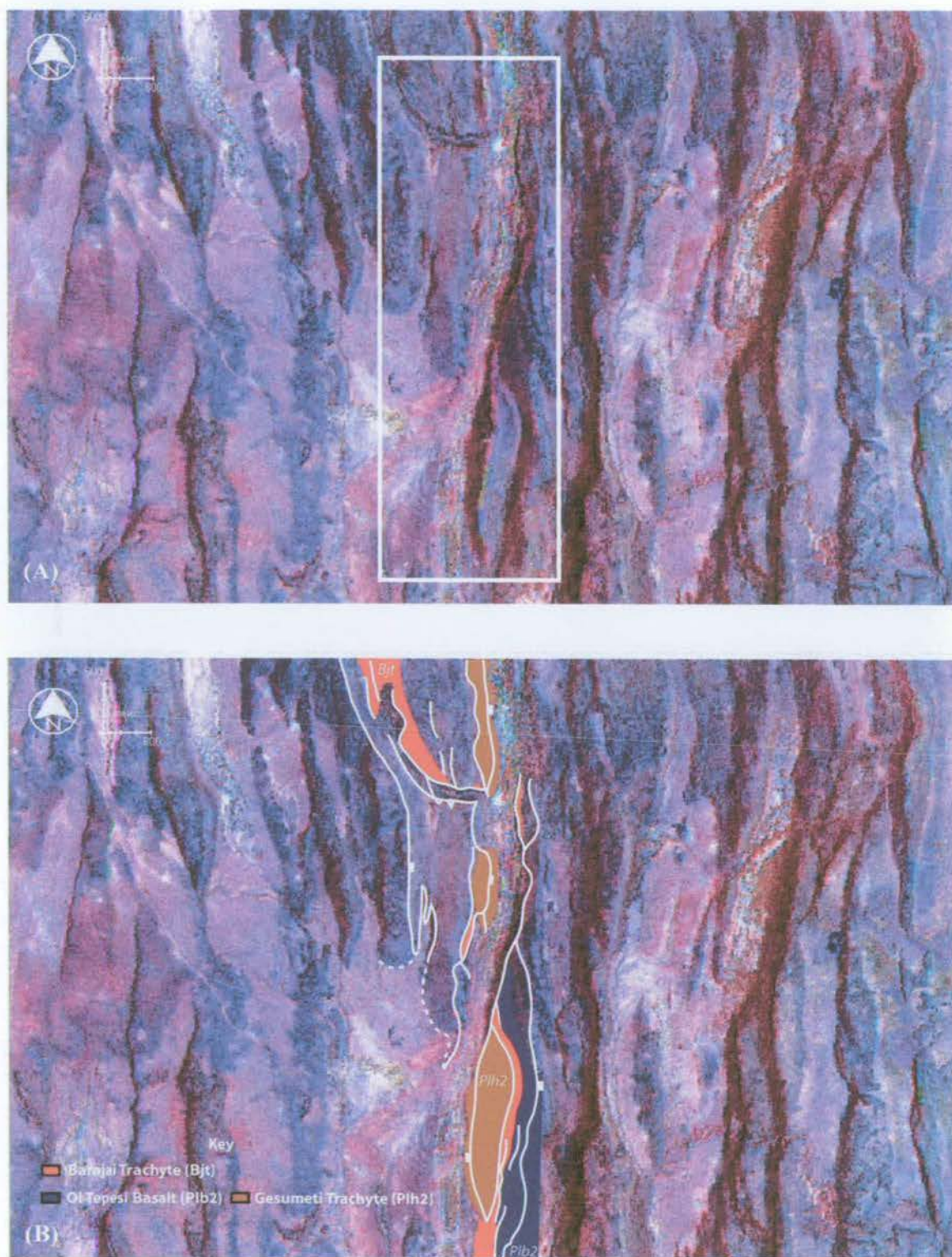
Figure 4.7 (A) Landsat 7 satellite image of the South Kedong Graben region. Shadows highlight the west-facing scarps. The location of figure 4.8 and 4.9 is indicated by the white rectangle. (B) As (A), but overlain with a coloured ornament to show geological structure and stratigraphy.
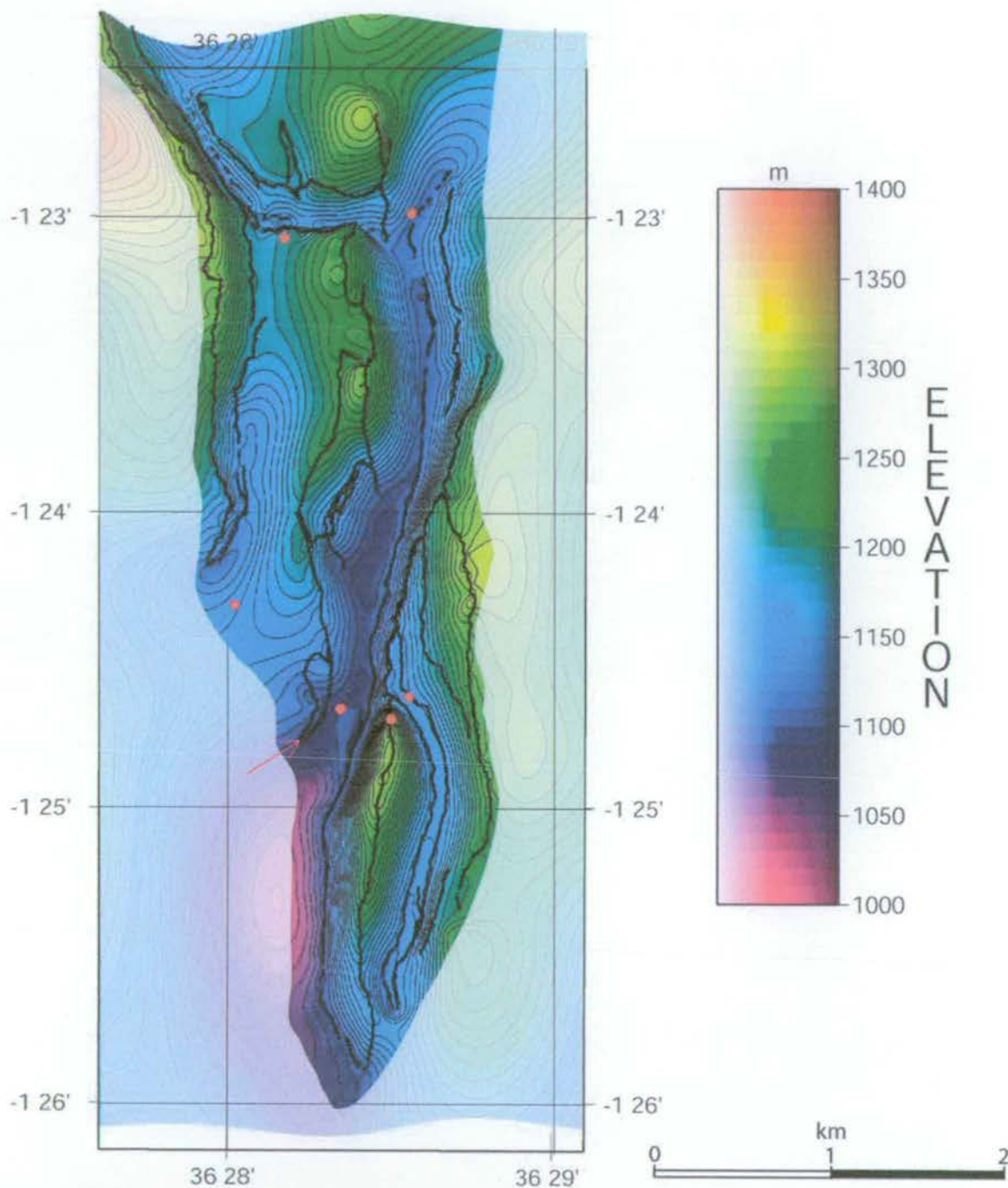
Figure 4.8 GMT plot of the South Kedong Graben area constructed from a series of differential GPS traverses (shown by black lines). Red dots indicate the positions of GPS basestations. Arrow indicates the location of GPS data recorded at the tip of the Enasira fault, shown in detail in figure 4.6. Semi-transparent mask hides regions of limited data coverage.
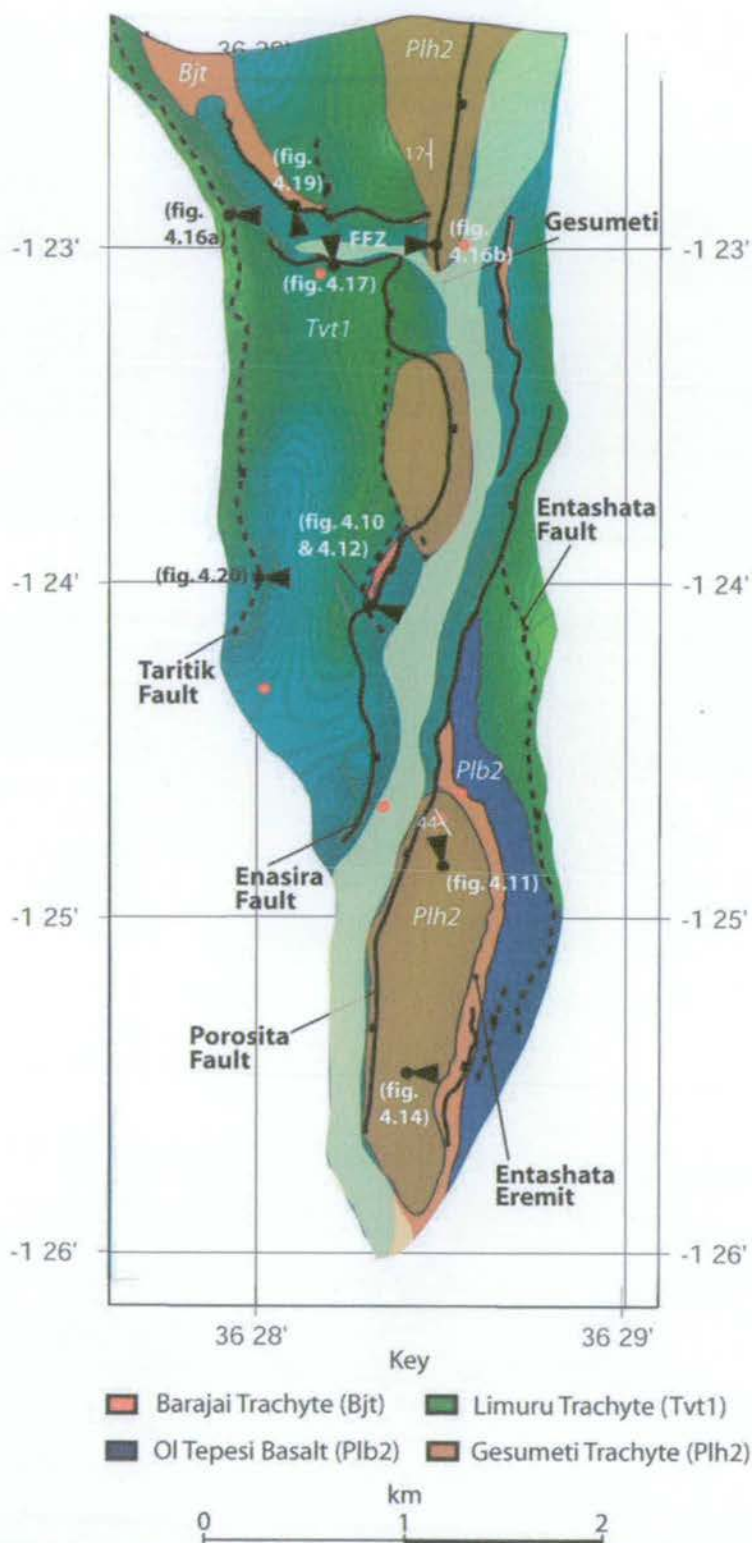
Figure 4.9 GMT plot overlain by a geological motif. Black lines indicate the locations of faults, dashed where inactive, as indicated by cross-cutting relationships. Red dots are the locations of GPS basestations. Viewpoint symbols indicate the positions from whence photographs were taken, as shown in the figures indicated. Alluvial fill is indicated in pale yellow. White mask hides regions of limited data coverage.

Displacement-length profiles have been plotted for each fault using the Unix-based Gnuplot program. Gnuplot offers an advantage over other graphical programs, such as Microsoft Excel, in that it can be easily instructed to plot data using a constant length ratio between the x and y-axes. This feature is useful for plotting true-scale map cross-sections or, in this case, fault displacement-length profiles.

Since most faults in the South Kenya Rift strike within approximately ten degrees of true N-S orientation, it is acceptable to produce the displacement-length profiles by plotting UTM northing values against GPS elevations. Areas in the field where it was necessary to move away from the general N-S trend, e.g. at the end of fault segments, show up as irregularities in the Gnuplot profiles due to the projection of 3D data onto a 2D plane (an example of this is the 'overhang' in the Porosita profile at 4.1km along the scarp as seen in figure 4.10). However, the accuracy of the positional data means that such irregularities may be easily identified on the plots.

Displacement values are calculated by subtracting graben-floor elevations from scarp crest elevations. As the graben floor is buried under a blanket of sedimentary alluvium, it is impossible to accurately determine the position of flow strata in the hangingwall to either of the graben bounding faults and therefore displacement values must represent minimum fault displacements. Displacement-length plots for the bounding faults of the Kedong Graben are shown in figure 4.10 and 4.11.
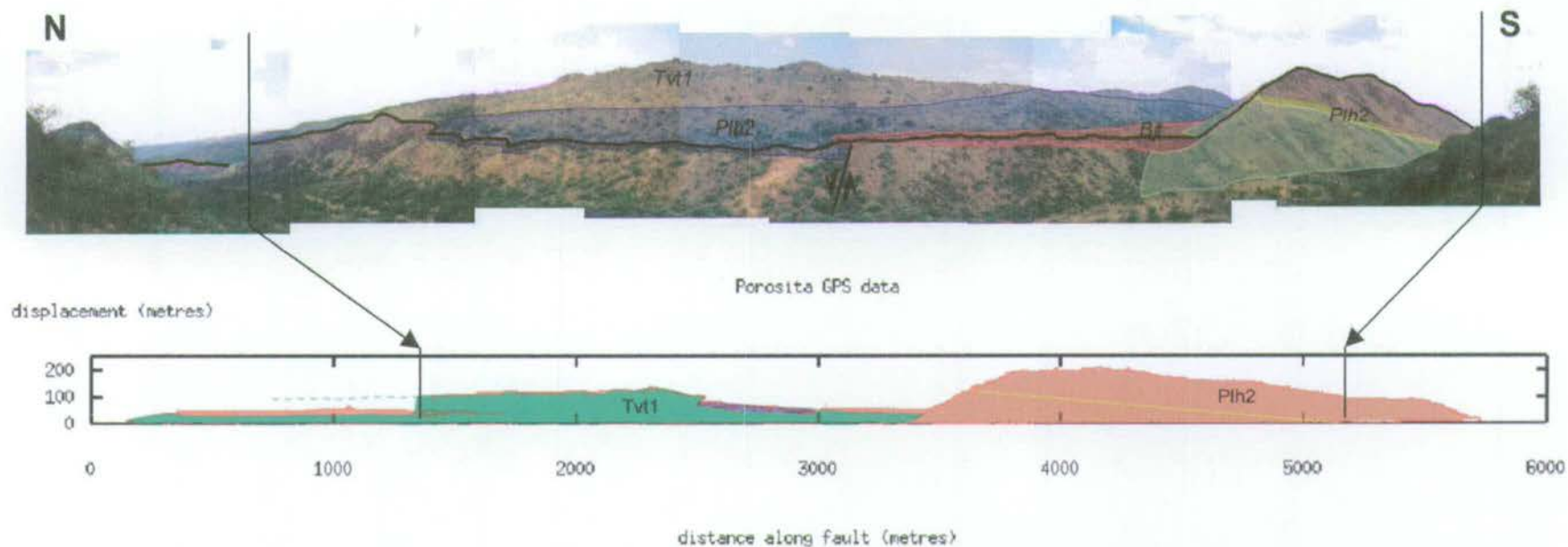
Figure 4.10 Photomontage (above; replotted from figure 3.8) and true-scale displacement-length profile (below) along the Porosita fault scarp. Red lines and curves on the displacement-length profile indicate the position of GPS datapoints; geology is indicated by a semitransparent overlay with the same ornament as used in figure 4.9. The yellow line shows southward component of dip of the Gesumeti Trachyte agglomerate horizons. Dashed green line indicates the approximate continuation of the Porosita scarp towards the north (not surveyed). An explanation of the photomontage is given in figure 3.8.

S N

Plh2

Bjt

Enasira GPS data

displacement (metres)

200
100
0

0   500   1000   1500   2000   2500   3000   3500   4000

distance along fault (metres)
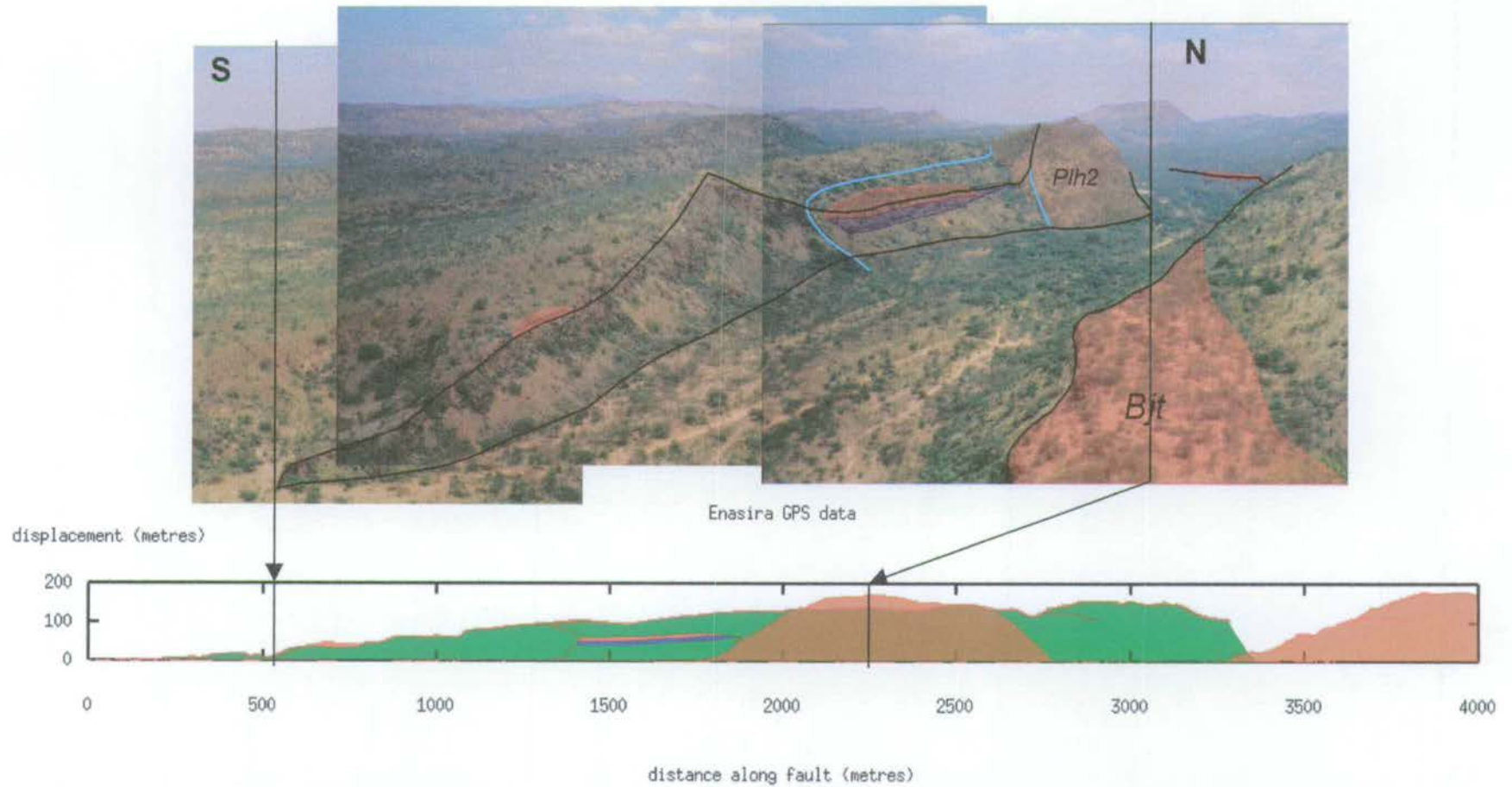
Figure 4.11 Photomontage (above; replotted from figure 3.7) and true-scale displacement-length profile along the Enasira fault scarp. Geology along the displacement-length profile is indicated by a semitransparent overlay above a plot of GPS positional data. An explanation of the photomontage is given in figure 3.7.

4.3.2 Structure of the South Kedong Region

The annotated GMT plot shown in figure 4.9 clearly shows the graben-bounding faults of Porosita (east) and Enasira (west) together with the southern tip of the Taritik fault, which lies immediately to the west of the Kedong Graben. As can be seen from the profile in figure 4.10, the southern tip of the Porosita scarp consists of a prominent, ~2.5km long, bell-shaped horst block composed of the Gesumeti Trachyte Formation. With a crestal relief of some 200m above the floor of the Kedong Graben, this block represents the section of the Porosita scarp with the largest amount of cumulative displacement. Structural measurements, collected from obvious cleaved surfaces orientated parallel to flow banding in the fissile trachyte unit at K48, show the rock to be dipping at 38 degrees towards the west, with a strike of 150 degrees. Short GPS traverses walked out along exposures of two of the agglomerate horizons elucidate the gentle southward component of this dip as viewed from the west of the Porosita scarp (figure 4.10). The strong component of dip towards the west means that the beds of the Gesumeti Trachytes are tilted towards the hangingwall of the Porosita fault rather than backtilted away from the fault, as would be expected from conventional fault block rotation models. This observation suggests significant faulting initially took place along a fault bounding the western side of the horst, prior to later activity along the length of the Porosita scarp. Furthermore, the gentle southward dip of the beds suggests that this early fault must have curved around the northern end of the trachyte horst, backtilting it towards the south.

In their discussion of the Gesumeti Trachytes of the Kedong Graben, Baker and Mitchell (1976) describe the southernmost exposure of Gesumeti Trachyte on the Porosita scarp (figure 4.9) as resting 'unconformably on a west-tilted Limuru Trachyte foundation' (see section 2.4.3f). However, as the base of the Gesumeti Trachyte Formation is not exposed at this location, it is impossible to determine the stratigraphic relationship of the two units. The eastern contact between the Gesumeti Trachyte block and the Limuru Trachyte, which is indeed west-tilted, appears to be a faulted contact and gives no information on the relative ages of these two units. Faulted contacts are also observed between the Limuru Trachytes and the longer, continuous Gesumeti Trachyte ridge exposed along the Enasira scarp, bounding the western margin of the Kedong Graben. There is little evidence for Gesumeti lavas and pyroclastics banked against a steep pre-existing fault scarp of Limuru Trachytes, as suggested by Baker and Mitchell (1976). Most importantly, the new $^{40}Ar/^{39}Ar$ ages given in chapter 3 (see tables 3.2 and 5.1) show that

the youngest member of Gesumeti Trachyte Formation is some 91±8kyr *older* than the Limuru Trachytes. The Gesumeti Trachytes cannot, therefore, represent a late-stage product of Limuru Trachyte volcanism as suggested by Baker *et al.*, 1988.

At a distance of 3.4km along the scarp profile (figure 4.10), the northern tip of the Porosita horst block is onlapped by a 10m thick flow of Barajai Trachyte, marked at its base by a 10cm thick red, rubbly palaeosol. At a position of 3km along the profile, the northern margin of the Barajai Trachyte flow slightly oversteps onto a thin (10m thick) flow of Ol Tepesi Basalt, which, from this point north, mantles the top of the Porosita scarp until x=2.5km. The base of the scarp, underlying both flows, is generally heavily vegetated and poorly exposed. However, beneath the northern margin of the Ol Tepesi Basalt the scarp cuts through a massive orange-brown flow of Limuru Trachyte. From the typical characteristics of Limuru Trachyte exposures observed elsewhere, it is likely that this rock underlies both the Ol Tepesi Basalt and Barajai Trachyte as far as the Gesumeti Trachyte horst in the south. Further north, total throw on the fault gradually increases from ~50m at x=3km to a maximum of ~130m at x=2.25km. The large amount of cumulative displacement at this location results from the convergence of the Porosita scarp with another fault that merges from the east (figure 4.9). At its southernmost end, this latter fault, which is located to the immediate east of the large Gesumeti Trachyte horst block, has a north-south orientation and dips to the east such that the footwall block is backtilted towards the Porosita horst. The intervening narrow half-graben is named Entashata Eremit by the Masai, which means 'land overlooking the settlement of Eremit'. Following this nomenclature, the east-dipping fault that converges with the Porosita scarp is named the Entashata fault. Figure 4.12 is a combined fault displacement-length profile that shows both the Porosita and Entashata scarps.
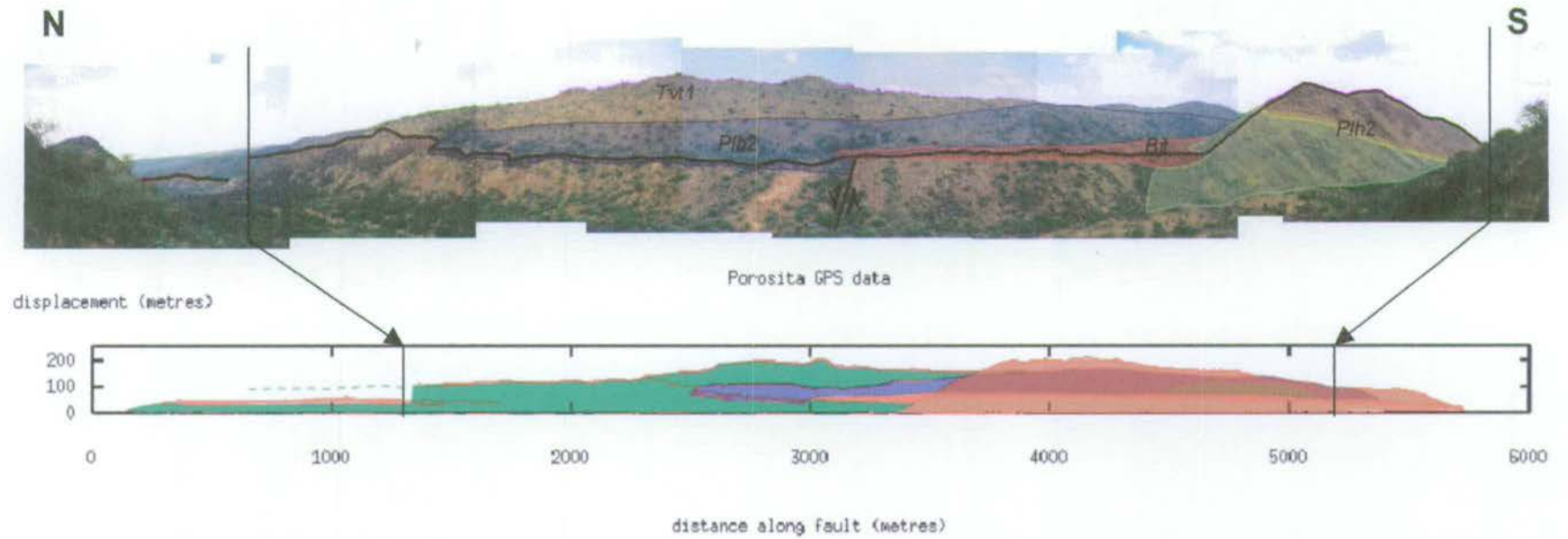
Figure 4.12 Photomontage and true-scale composite displacement-length profile along the Porosita and Entashata fault blocks. The Entashata fault lies behind the Porosita scarp, directly to the east.
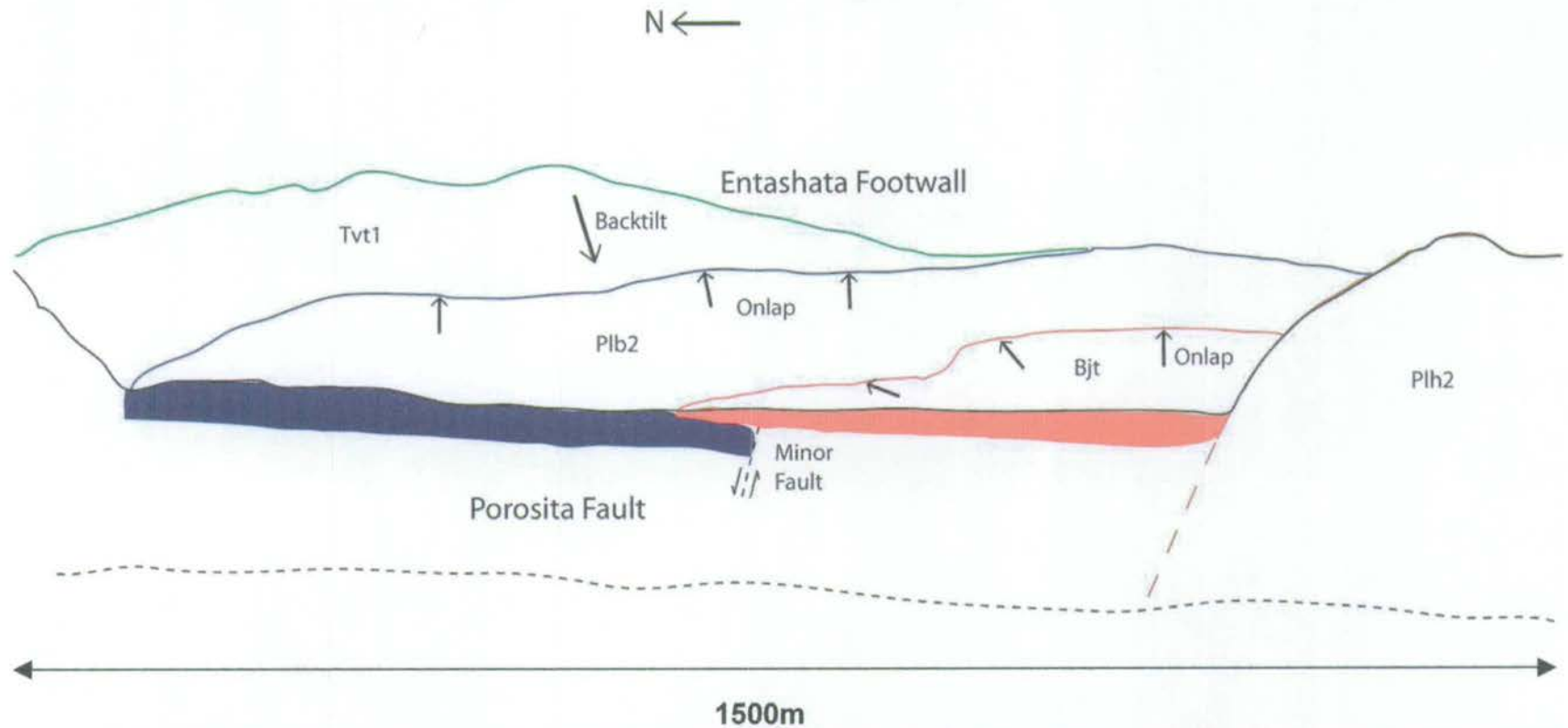
Figure 4.13 Sketch showing the field relationships of lava flows mapped along the central section of the Porosita Fault. The Ol Tepesi Basalt flow (Plb2) forms a veneer on the back of the Entashata footwall block and onlaps against an area of Limuru Trachyte (Tvt1) at the crest of the Entashata scarp (this apparently represents a pre-existing section of the fault). Further movements along the Entashata Fault backrotated the basalt flow prior to later eruption of the Barajai Trachyte (Bjt), which is exposed as a 10m thick horizontal lava bed covering the floor of the Entashata Eremit half-graben.

During eruption, both the Ol Tepesi Basalt and the Barajai Trachyte have used Entashata Eremit as a flow conduit. Whereas the Ol Tepesi Basalt forms a lava veneer on the back of the Entashata block, the Barajai Trachyte is essentially a horizontal bed that covers the floor of the half-graben. This indicates a period of tectonic activity and block rotation associated with the Entashata fault that occurred subsequent to eruption of the basalt but prior to eruption of the Barajai Trachyte (see figure 4.13).

Where the Barajai Trachyte exits the southern end of the Entashata half-graben, a remnant of the flow onlaps against the southern tip of the Gesumeti Trachyte horst block. At this location, structural measurements indicate that the flow is tilted towards the south with a dip of up to 30 degrees. Slightly further to the north, between 4.5km and 5.5km in figure 4.12, minor extensional faulting has produced a 4m high scarp in the floor of the valley that downthrows the Barajai Trachyte to the west (figure 4.14). Barajai Trachyte exposed in the footwall to this small fault is characterised by prominent curved crinkles on the upper surface of the flow. Flow crinkles such as these are a common feature of pahoehoe-type lavas, especially in areas where lavas flow slowly due to a low topographic gradient. It is likely that once the lava had exited from Entashata Eremit onto the Ol Tepesi floodplan its flow rate would have decreased causing rapid lava ponding and formation of surface flow crinkles. Gregg and Fink (2000) have produced a series of laboratory simulations of lava flow emplacement with the aim of modelling the effect of topographic slope on flow dynamics. Experiments were conducted using heated polyethylene glycol (PEG), which has a temperature-dependent rheology, extruded at a constant rate beneath cold sucrose solution onto a uniform slope that was varied between 1 and 60 degrees. With increasing extrusion rate and slope angle, the workers document a change from folded flows with surface crusts buckled transversely to flow direction to straight, leveed flows, solid only at the flow margins. Such observations help to explain the development of the flow crinkles on the surface of the Barajai Trachyte flow as it exited the Entashata Eremit half-graben and began to pond on the Ol Tepesi Plain.
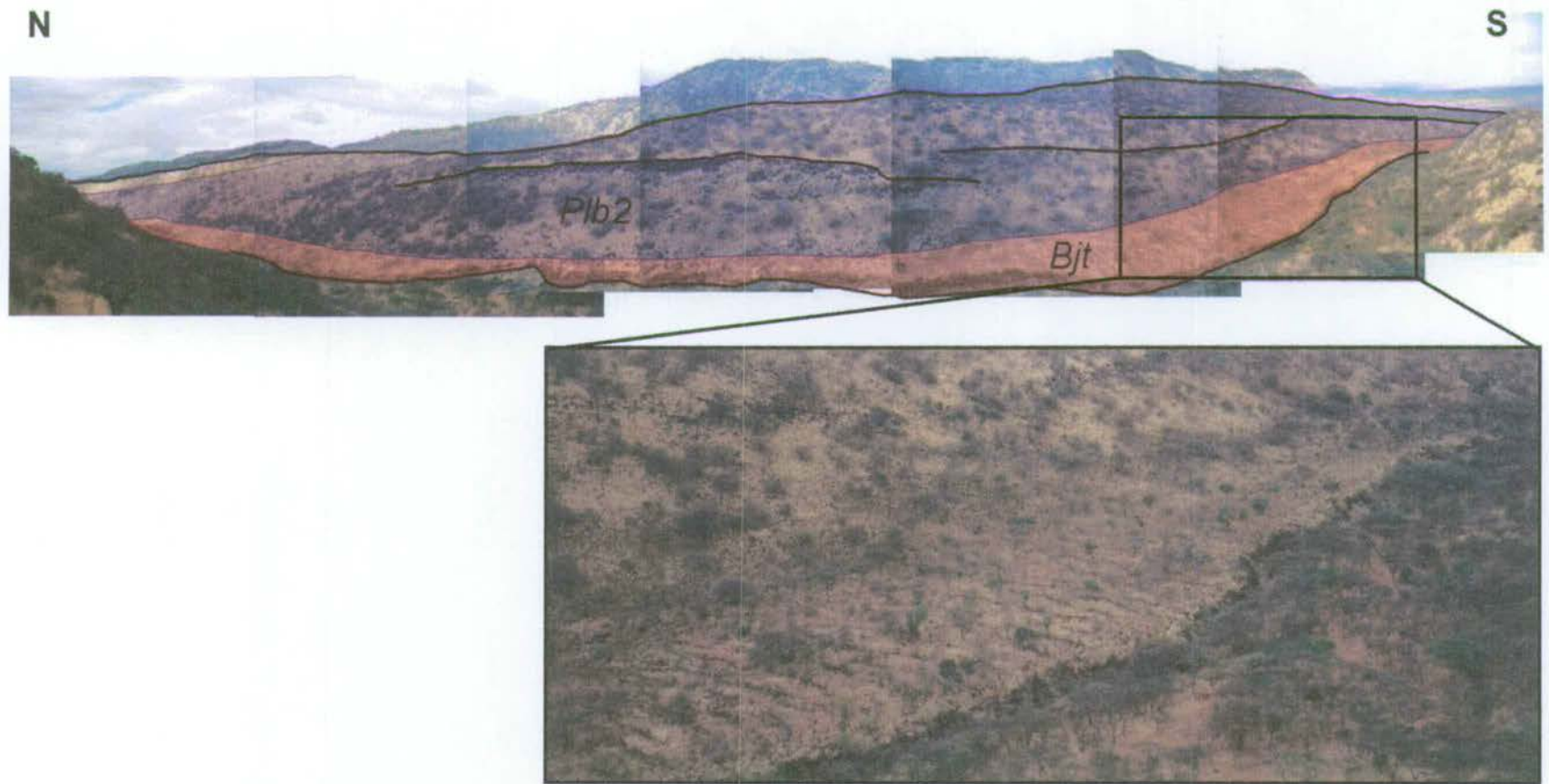
Figure 4.14 View from the Porosita horst looking towards the dip-slope of the Entashata footwall block. Black lines indicate the locations of extensional faults. In the foreground, the upper surface of the Barajai Trachyte (Bjt) lava is characterised by curved flow ridges or 'crinkles' that are concave towards the south.

Between x=2.25km and 1.4km along the profile shown in figures 4.10 and 4.12, the throw along the Porosita scarp decreases as it begins to curve towards the east. The most northerly section of the Porosita scarp is a 1.5km length splay from the main fault that continues with a NNE-SSW trend and has some 50m of displacement. The scarp is mantled for much of its length by a 10m thick ledge of Barajai Trachyte. North of the Porosita scarp, the Kedong gorge takes on a half-graben morphology as the normal fault is replaced, along-strike, by a rollover anticline into the Enasira scarp located to the west.

The Enasira scarp extends over a length of 18km along the western margin of the Kedong Graben. An interpreted fault displacement-length profile along the southernmost section of the Enasira scarp is shown in figure 4.11 (see also figure 4.15). This region of the fault appears to be composed of an hierarchy of morphologically distinct fault segments. On a large scale, the southern tip of the Enasira scarp comprises a fault block some 3.3km in length that has formed from the linkage of three segments. The most prominent of the segments is a horst block composed of Gesumeti Trachyte, located between x=1.8km and x=2.75km. Though slightly smaller in terms of both length and displacement, this block is morphologically similar to that located at the southern tip of the Porosita scarp and appears to have formed as a result of uplift along two N-S trending curved faults. In this case, however, the conformable units of the Gesumeti Trachyte Formation are tilted toward the west at an angle of 17 degrees indicating that the majority of recent uplift has occurred, to the east, along the Enasira fault. Directly to the south of this horst, reactivation of the Enasira fault has cut across a pre-existing NW-SE trending fault segment that curves into a more N-S orientation at it northernmost tip (figure 4.9 and 4.11). Movement along the Enasira scarp has dissected two thin (~10m thick) flows of Ol Tepesi Basalt and Barajai Trachyte that cover the hangingwall to this early fault, creating a narrow lava ledge against a 1km long section of the scarp (figure 4.15). Towards the southern tip of the Enasira fault, at 0.7km along the profile of figure 4.11, a second exposure of Barajai Trachyte, not more than five metres in thickness lies on the crest of the scarp.
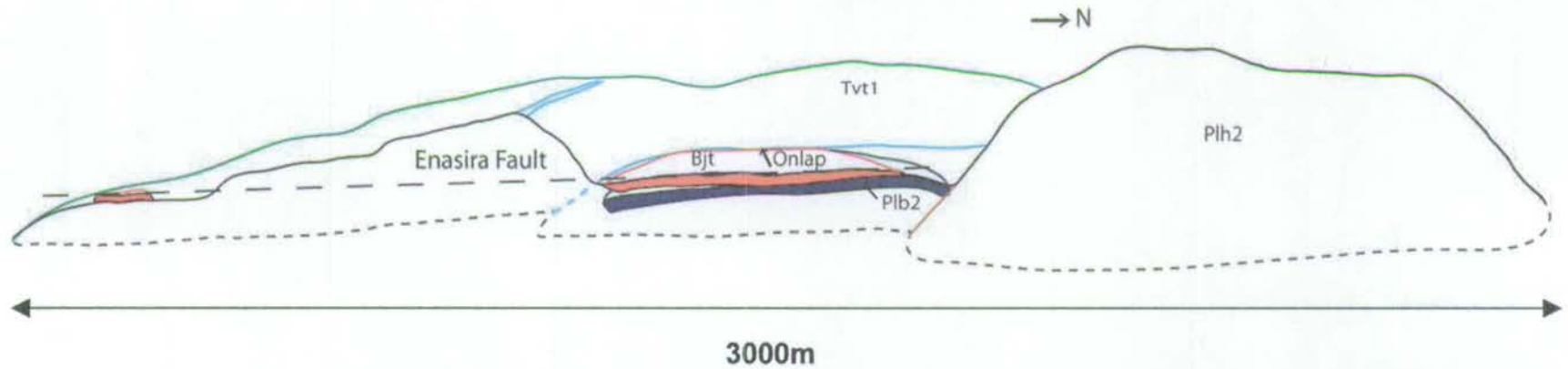
Figure 4.15 Sketch showing the onlapping relationships of the Ol Tepesi Basalt (Plb2) and Barajai Trachyte (Bjt) lavas against segments of the Enasira Fault scarp. An early phase of tectonic activity in this region resulted in uplift along three short fault strands (shown in pale blue). Ol Tepesi Basalt and Barajai Trachyte lavas accumulated in the hangingwall to one of these early scarps (at the centre of the diagram) and have since been cross-cut and uplifted by later movement along the linked Enasira Fault to form a narrow lava ledge or faced-scarp structure (cf. Temperley, 1966). A second exposure of Barajai Trachyte at the southern tip of the fault allows correlation of these lavas along strike. The dashed black line indicates the interpolated surface of the Barajai Trachyte between lava exposures.

Viewed from the east, as is the case in figure 4.11, the large fault block at the southern end of the Enasira scarp has a wedge-shaped appearance bounded to the south by the gentle tip-gradient of the fault and to the north by a steep north-dipping fault scarp. The latter fault represents the southern wall of a narrow E-W trending fault graben, no more than 150m in width, which intersects with the footwall of the Enasira scarp (figure 4.16). The northern wall of the graben dips steeply toward the south and bounds the southern margin of another segment of the Enasira scarp located immediately to the north. Displacement on these 'footwall faults' is at a maximum where they link with the Enasira fault and gradually decreases westward over a distance of ~600m (figure 4.17). Where they intersect with the N-S trending Taritik fault, situated to the west of Enasira, both faults curve sharply towards the north and form a narrow fault-bound gulley, approximately 25m deep (figure 4.16 and 4.17). The faults tip out entirely in a set of small fault splays at the base of the Taritik fault. The general along-strike displacement decrease is a reflection of the tilt associated with the Enasira footwall block and it is therefore likely that the footwall faults initiated in order to accommodate the strain that was associated with growth of the Enasira fault segments. Hence, as displacement accumulated on the northern and southern fault segments of the Enasira scarp, part of the strain was taken up contemporaneously in the Footwall Fault Zone (FFZ). These footwall faults may therefore be regarded as two east-west orientated segments of the Enasira fault scarp that connect the major N-S orientated fault segments.

Both walls of the footwall graben cross-cut a number of small N-S trending faults, including two obvious graben features and a small backtilted normal fault block that has been cut into three rock pillars by movement on the footwall faults (see figure 4.17). It is still possible to see the original tilt of the fault block preserved on the upper surface of the pillars. A 10m thick blanket of Barajai Trachyte lava (figure 4.17) mantles the northern wall of the FFZ. In places, the flow directly overlies the small N-S trending fault blocks, indicating that these structures have remained inactive since eruption of the lava and are now rotated onto the back of the Enasira footwall block. One such feature, the Ndepen fault, has a length of some 400m and a maximum displacement of 14m. This fault is only onlapped by Barajai Trachyte lava at its southernmost tip, allowing it to be accurately surveyed in the field. A displacement-length profile along this fault is shown in figure 4.18. Along the southern wall of the FFZ, the tips of two small fault graben, which can be traced across from the northern wall of the FFZ, have been uplifted and deformed by rotation of the Enasira footwall block (figure 4.19).
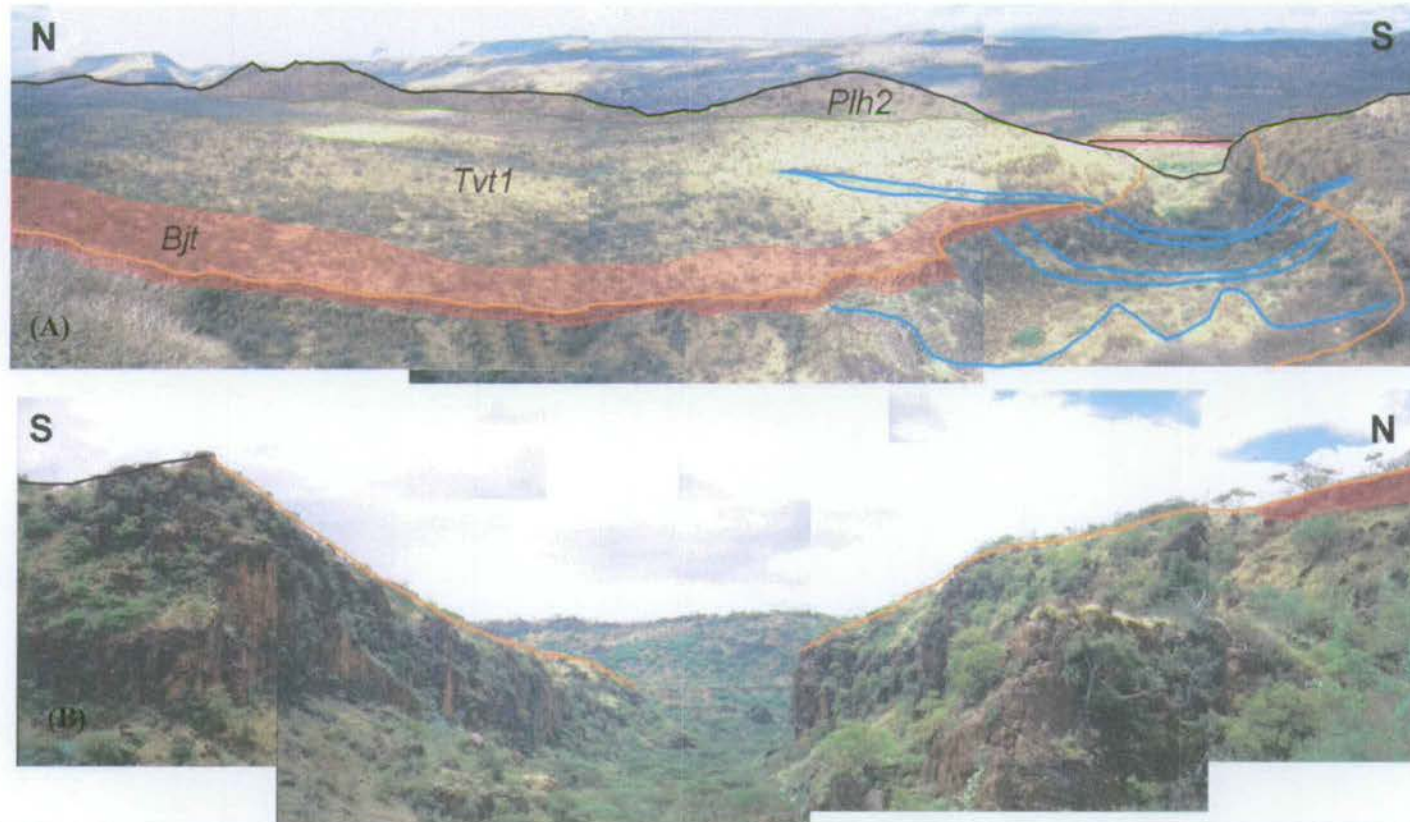
Figure 4.16 Overview of the footwall fault zone (FFZ) lying to the west of the Enasira fault scarp. (A) View from the Taritik fault across the Enasira scarp footwall block. (B) Entrance to the FFZ as viewed from the Kedong Graben to the east. The Taritik fault can be seen in the background of this photograph. Coloured lines indicate three phases of extensional faulting as witnessed from cross-cutting relationships; black: most recent movements along the Enasira scarp, orange: faults bounding the FFZ, that cross-cut Barajai Trachtye (Bjt) and blue: small faults and fault graben that are buried under a veneer of Bjt and have been cross-cut by the FFZ.
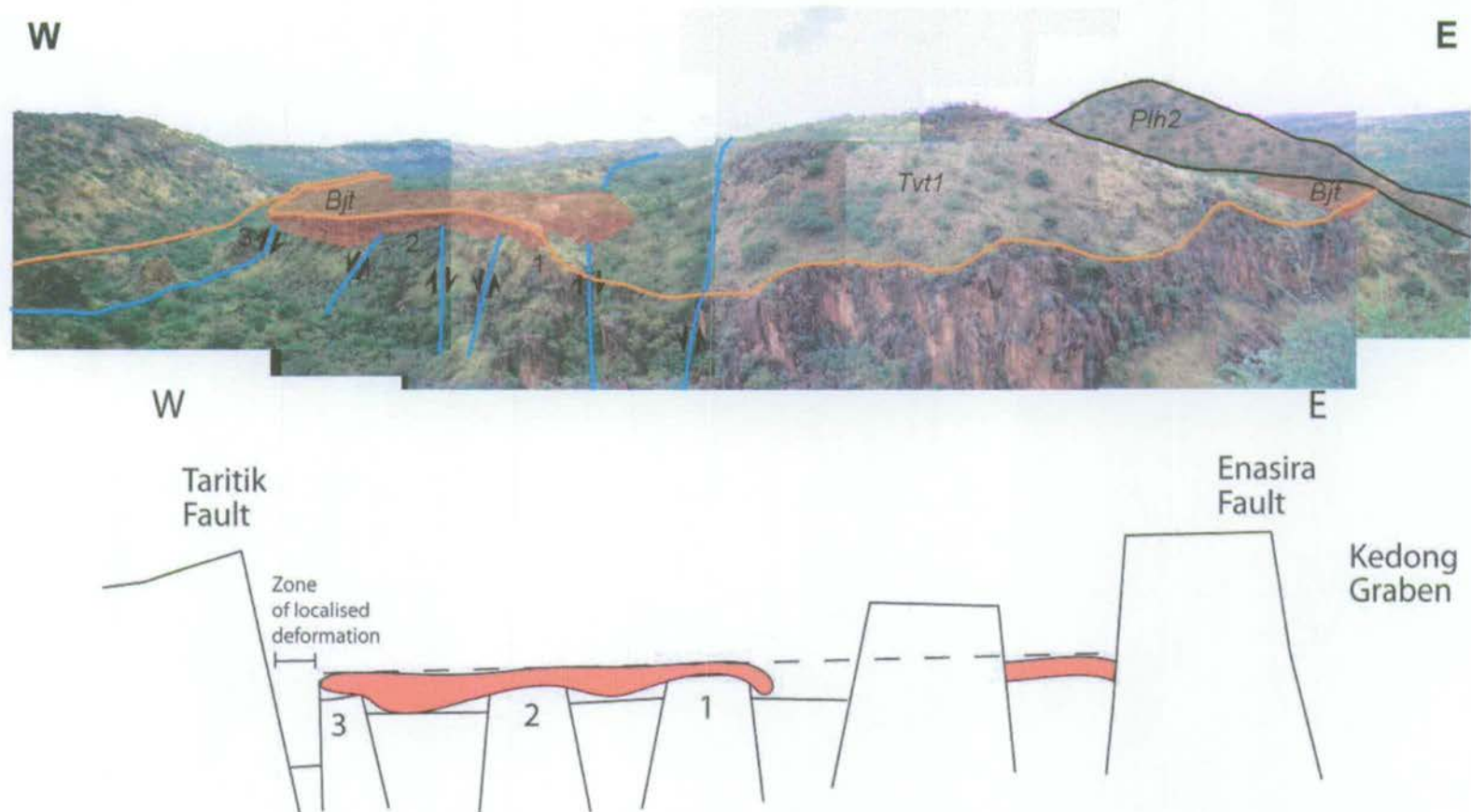
Figure 4.17 Photomontage along the northern wall of the FFZ. Coloured lines indicate the phases of faulting described in figure 4.16. Note the early faulting that has since been blanketed by a Barajai Trachyte flow and dissected by movement along the FFZ. Interpretive diagram of the fault structure along the northern wall of the FFZ. Numbers allow correlation of the normal fault horst blocks with the photograph. Dashed line indicates the interpreted surface of the trachyte as interpolated from lava exposures

S   Ndepen fault data   **N**

displacement (metres)

distance along fault (metres)
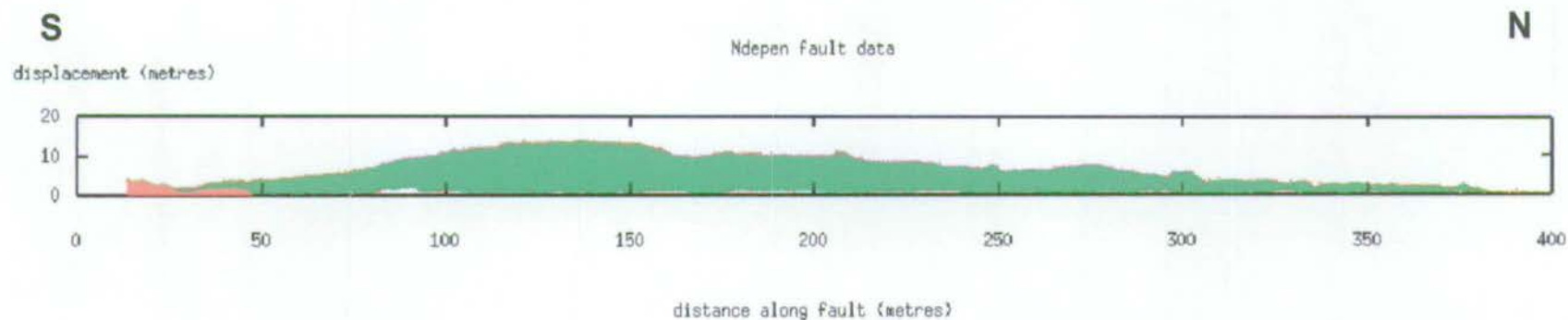
Figure 4.18 Displacement-length profile along the Ndepen fault. This small, N-S trending fault only accumulated a maximum vertical displacement of 14m and became inactive prior to eruption of the Barajai Trachyte, which buries its southernmost tip. Red lines indicate locations of GPS data; semitransparent overlay represents the local geology (following the key in figure 4.9).
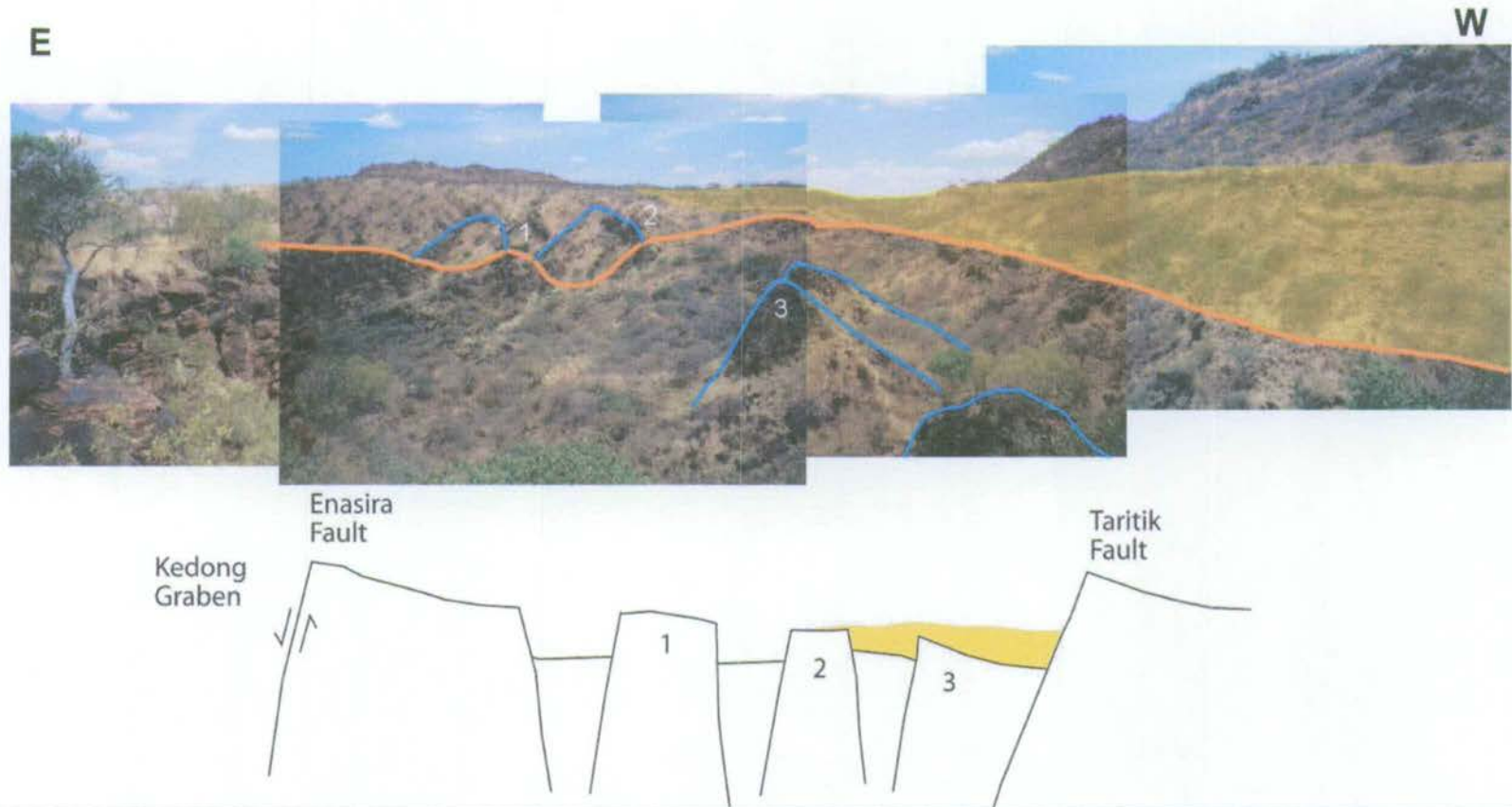
Figure 4.19 View and interpreted structure along the southern wall of the FFZ. At this position the fault curves around towards the north, uplifting a wedge of alluvial sediments in the hangingwall to the Taritik fault. Also clearly visible are three backtilted rock pillars on the floor of the FFZ that represent an early fault block (indicated by the number 3) since dissected by later fault movements. The tips of two small fault graben that have been rotated onto the back of the Enasira scarp are also indicated towards the left of the photograph (blue lines). Numbered horsts represent the southward continuations of those shown in figure 4.17.

Located to the north of the footwall fault zone and in the hangingwall of the Taritik fault scarp, the Ndepen Plain appears to have been a major conduit for Barajai Trachyte lava flowing south from Mount Suswa. In contrast to many of the other hangingwall basins within the South Kedong region, the stratigraphy of the Taritik hangingwall basin is remarkably well exposed. Traverses along the base of the Taritik scarp show that the Barajai Trachyte lavas have been relatively unaffected by faulting, suggesting that there has been relatively little movement on this fault since lava eruption. However, faulting in the immediate vicinity of the footwall fault graben, where the faults curve sharply towards the north, has produced some localised uplift of alluvial sediments in the hangingwall to the Taritik fault (see figure 4.19). At the southern tip of the Taritik fault, a small E-W trending fault scarp cuts across the hangingwall to the Taritik fault, downthrowing rock towards the south. The effect of this fault is to hard-link the Taritik fault to the Enasira fault, such that recent fault movements have passively uplifted and rotated the former on the back of the latter (see figure 4.20 and 4.21).

Immediately to the north of the footwall fault zone, the crest of the Enasira footwall scarp has exposed another block of Gesumeti Trachyte. Only ~500m of this northern fault segment was surveyed during the course of this study as increased vegetation and inaccessibility in the Central Kedong Graben prevented relocation of the GPS basestation further to the north along the Enasira hangingwall. The Gesumeti Trachyte Formation is exposed as a relatively narrow sliver of rock along the face of the Enasira scarp and is also faulted, on its western side, against the Limuru Trachytes. Continued growth of this fault segment has created a gentle southern tip consisting of a narrow fault ridge that obstructs, and has slightly uplifted, the entrance to the footwall fault graben. This 8m-high ridge cuts through a poorly-sorted, conglomeratic rock containing subrounded clasts of vesicular lava set in a fine grey sandy matrix. As this fault tip dissects the base of the pre-existing footwall fault graben, it is likely that the conglomerate may represent some kind of alluvial material that was originally deposited in the base of the graben. Further north along the fault tip, as the displacement gradient begins to increase, there is an obvious well-exposed contact between the conglomerate and the massive microporphyritic trachyte at the base of the Gesumeti Trachyte Formation. The contact is characterised by a bright orange laterite surface overlain by a highly sheared and altered horizon of Gesumeti Trachyte. Pervasively sheared and heavily brecciated trachyte is observed on both sides of the narrow fault ridge, again indicating that the Gesumeti Trachyte was uplifted as a horst block. Westward-tilted volcanic agglomerate and fissile trachyte units situated towards the top of the

scarp at this location confirm that the Enasira fault, bounding the eastern side of the block, has been the more active of the two faults in recent times. However, movement along the western margin of the horst created a triangular-shaped, downthrown platform to the west that has been infilled by a 10m thick blanket of Barajai Trachyte and which was later cross-cut by movement along the northern footwall fault (figure 4.17 and 4.22). Continued along-strike propagation of the northern Enasira fault segment and resulting uplift and abandonment of the footwall fault graben suggests that this section of the Enasira fault is in the process of hard linkage (see figure 4.22).
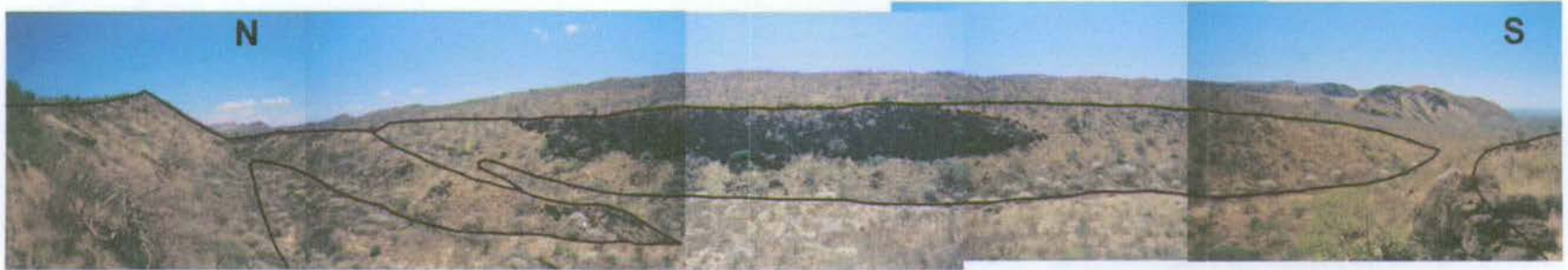
Figure 4.20 View looking to the east, up the dip-slope of the Enasira footwall block, from the southern tip of the Taritik fault. Black lines lie along breaks in slope that envelope normal fault scarps (the dashed line demarcates a vertical scarp formed during reactivation along the pre-existing fault). The small fault graben developed in this area is testament to the fact that the Taritik fault is now hardlinked to movement along the Enasira fault. From this point northward, the Taritik fault is being passively rotated on the footwall to the Enasira scarp.
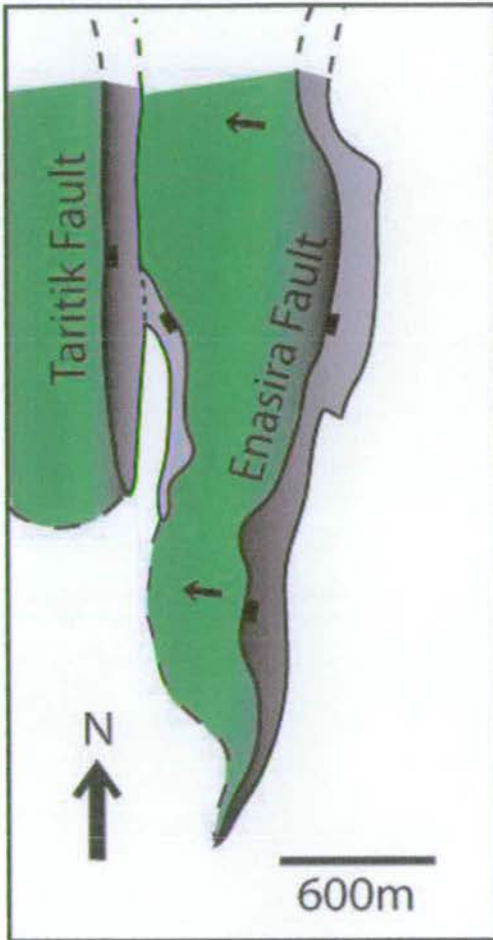
Figure 4.21 Structural model showing linkage between the Taritik fault tip and the Enasira fault as a result of movement along a small ~E-W to NW-SE orientated fault that uplifts the hangingwall to the Taritik fault in the north.
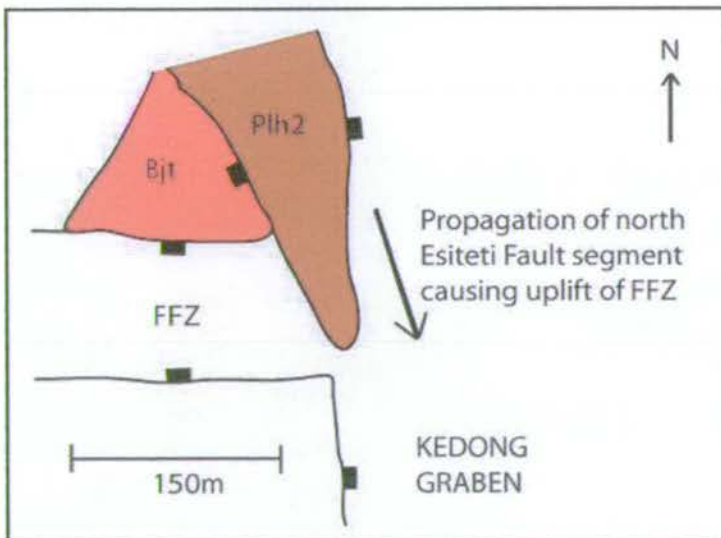
Figure 4.22 Cartoon map showing the intersection of the Kedong Graben with the Footwall Fault Zone (FFZ). Immediately to the north of the FFZ, fault activity initially occurred along both margins of the Gesumeti Trachyte horst (Plh2). However, recent movement (along the Enasira Fault) has been located along the eastern margin of the horst, resulting in uplift of the FFZ.

4.4 The Esiteti Region

4.4.1 Introduction

By employing the method described in section 4.2, the GPS rover was used to survey the base and crest of the Esiteti fault scarp as well as lava flow contacts and obvious palaeosol horizons. The major GPS traverses are illustrated in figure 4.23 (associated positional data is given in file Esiteti.xls, Appendix A). Basestations were established in four different locations in order to survey a ~10km length of the scarp. Geodetic data was downloaded, converted to UTM co-ordinates and plotted as described in section 4.3.1. A displacement-length profile for the Esiteti scarp is shown in figure 4.24

Along the entire length of the Esiteti scarp, post-tectonic, alluvial sedimentary deposits obscure the bedrock hangingwall cutoff and, as a result, the cumulative fault displacements shown in figure 4.24 are minimum values determined by subtracting elevations determined at the base of the scarp from fault crestal elevations. However, an absolute offset has been determined for the Olorgesailie lacustrine sediments where they are locally exposed in the fault hangingwall at the northern end of the measured scarp section.
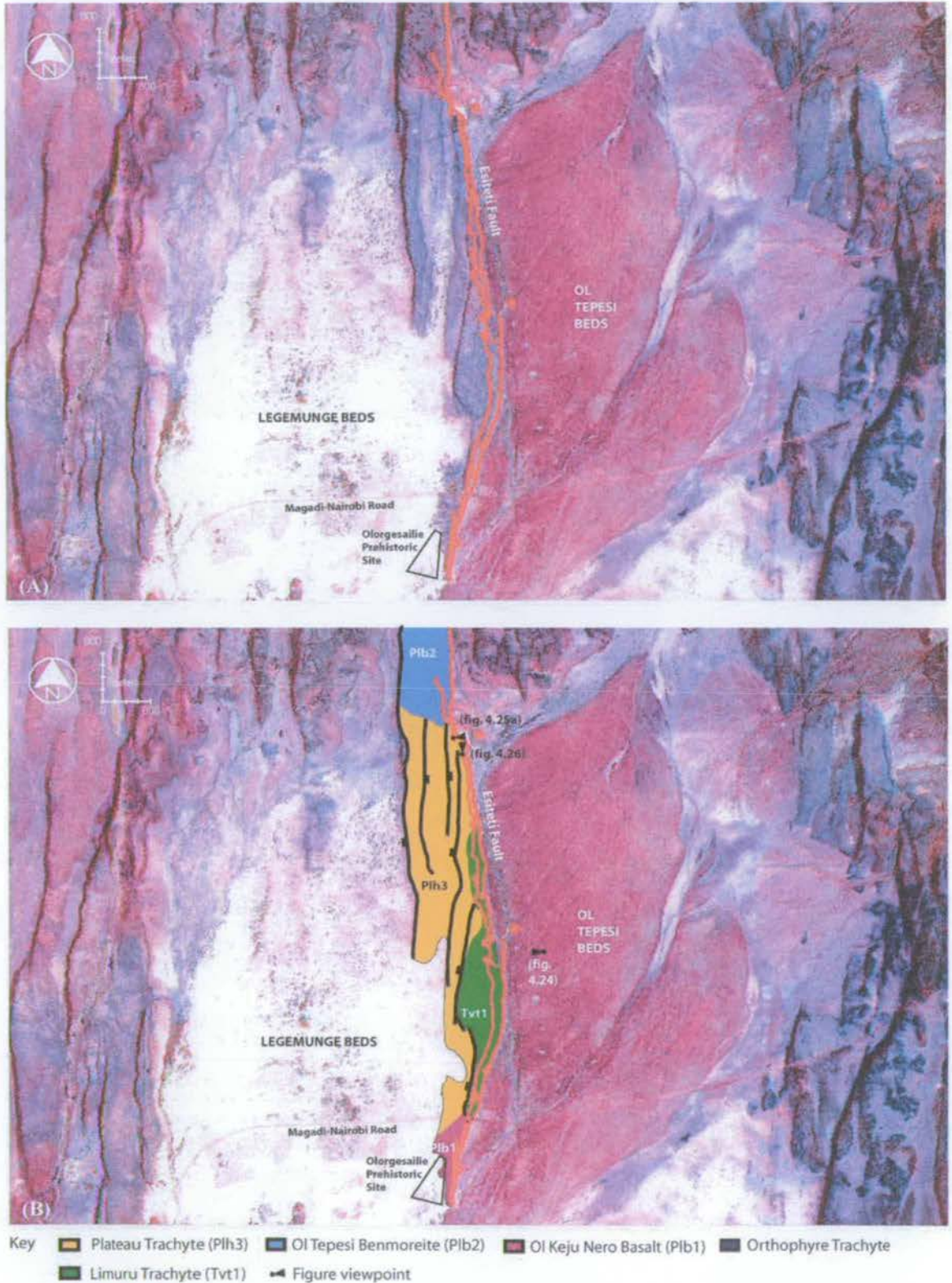
Figure 4.23 (A) Landsat 7 image of the Legemunge-Ol Tepesi area. The Esiteti fault is the obvious structure dividing the two basins. Red lines indicate the location of the main GPS traverses; dots indicate GPS basestations. (B) as in (A), but with the principal lava flows indicated in coloured ornament.
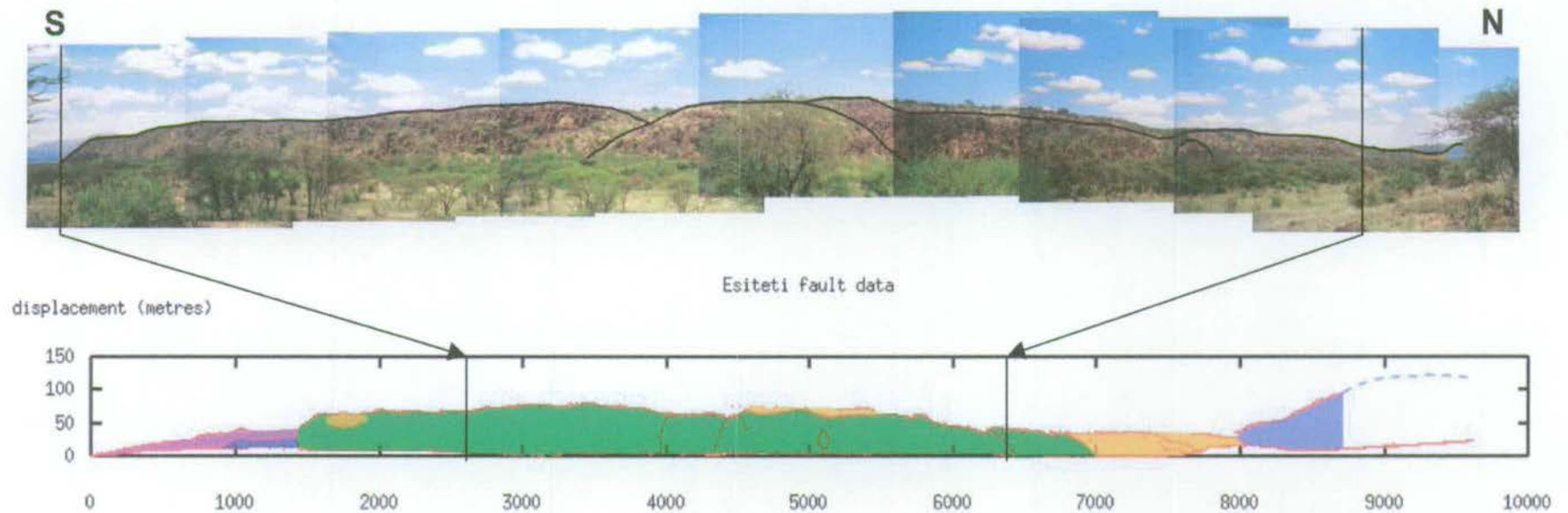
Figure 4.24 Photomontage (above) and displacement-length profile (vertical:horizontal scale 4:1) along the South Esiteti fault (below). Red lines on the displacement-length profile indicate the position of GPS datapoints; geology is indicated by a semitransparent overlay with the same ornament as used in figure 4.23. Dashed blue line approximates the continuation of the Esiteti fault crest towards the north. The photograph of the central Limuru Trachyte (Tvt1) block illustrates the closely spaced fault segments described in the text.

4.4.2 Structure of the Esiteti Region

As briefly mentioned in section 3.3.8, the South Esiteti fault extends for a total of 15km and dissects five volcanic units, ranging in age from 1.995±0.004Ma to 1.128 ± 0.007Ma, and the sediments of the Olorgesailie Formation, which were deposited between 0.992±0.039Ma and 0.493±0.001Ma. Limuru Trachyte lavas are exposed over a continuous 7km long section of the fault, and as such make up the vast majority of the footwall scarp. In plan view, this section of the scarp has a asymmetric horst-like morphology such that to west of the main Esiteti scarp a subordinate overlapping array of steeply dipping normal faults downthrow the sediments of the Legemunge Plain some 20-30m to the west (figure 4.23). However, the majority of the strain in this area is taken up on the east-dipping Esiteti fault, where total displacements are typically around 50-80m. Although the entire scarp has a rough N-S trend, the section that cuts the Limuru Trachytes has a slight eastward curvature such that in the south the fault trends in a NNE-SSW orientation while in the north it trends more towards the NNW. The change in scarp orientation is also accompanied by a difference in scarp morphology. Extending from the southern tip of the Esiteti fault to the inflexion point located 3.2km along the profile shown in figure 4.24 (see also figure 4.23), the scarp is heavily vegetated with long grass and acacia bushes. Only to the north, where the fault trends towards the NNW, does the rock crop out in large cliff exposures some 20-25m in height. The exposures have an overlapping arrangement and are separated from each other by a series of narrow ramps or gullies, such that they have the appearance of closely spaced fault segments (figure 4.24). The face of each exposure is cut by a series of unevenly spaced vertical shear zones, no more than five metres in width, which consist of a number of anatomising fault strands separated by lens-shaped 'blocks' of coherent rock. The lack of layering in the Limuru Trachytes made it difficult to gauge the amount of movement along the fault strands. However, similar structures that were identified along the face of the Ilainymok fault scarp (see figure 3.19) caused vertical offset of prominent flow-bands in the Plateau Trachytes by a distance of a few millimetres. In plan view it is clear that the position of the overlapping cliff exposures coincides with the intersection of two west-dipping, NNE-trending faults with the main Esiteti scarp (figure 4.23). Uplift along these faults may have increased displacement on the southern Esiteti scarp and probably produced the unusual arrangement of faults and shear zones that characterise this area.

Between 6km and 7km along the scarp, displacements decrease from ~70m to 40m and the northern end of the Limuru Trachyte block is onlapped by two conformable flows of Plateau Trachyte. Both f lows are a pproximately 10-15m in thickness and are separated by a narrow laterite horizon. Two further exposures of Plateau Trachyte were observed at the crest of the Limuru Trachyte block, one as a thin mantle between x=4450m and x=5090m and the second as a narrow facing between x=1690m and x=1870m.

The maximum displacement on the Esiteti fault, as it passes through the most northerly of the Plateau Trachyte exposures, is consistently around 40m until it rapidly decreases to zero where the fault segment tips out below lacustrine sediments at x=7.7km on figure 4.24 (see also figure 4.25). The sediments consist of 11 intercalated pale-grey sandstones, orange siltstone and white diatomaceous horizons that have been uplifted and tilted towards the northeast by movement on the Esiteti fault. The contact between the Plateau Trachyte and the overlying sediments appears to be fairly conformable, as stratigraphic dips are consistently 10-12 degrees in both units. The diatomite beds and fine-grained sandstones were usually no more than 5-50cm in thickness and weather proud of the surrounding powdery siltstones and clays. The sediments appeared to be of similar composition to the beds of the Olorgesailie Formation, as documented in Isaac (1978), especially those of member 13, which is described as 'pale yellowish to brownish silty claystone with i nterdigitated diatomite beds, capped by a hard bed o f t uffaceous diatomite'. However, precise correlation was made difficult by the 8km separation between this small sedimentary exposure and that documented by Isaac (1978) at the Olorgesailie Prehistoric Site.

Immediately to the west of the Esiteti segment tip, a 100m wide semi-breached relay ramp transfers displacement across to the tip o f a neighbouring fault segment that d issects t he Ol Tepesi Benmoreite (figure 4.26). The latter segment forms the eastern bounding scarp of a large, 600m wide Benmoreite horst that has been uplifted by over 100m. The relay ramp is dissected by three N-S trending faults, the most westerly of which curves sharply over a distance of ~300m and links with the major Benmoreite block (figure 4.23).

The extreme southern tip of the Esiteti fault dissects the Orthophyre Trachyte and Ol Keju Nero Basalts that onlap against the pre-existing Limuru Trachyte block where the Magadi-Nairobi road crosses the fault scarp (figure 4.23). The vegetated nature of this section of the scarp made

it difficult to accurately define the contact between the two lavas and therefore if there was any fault growth contemporaneous with lava deposition.

Figure 4.25 Lacustrine sediments at the northern tip of the Esiteti fault. (A) Red line delimits the area of exposure of the sediments. (B) View looking north across the diatomaceous beds towards the Benmoreite fault segment (see text for details). This image highlights the tilt of the bedding planes towards the northeast.

Figure 4.26 View looking north towards the relay zone between the Limuru Trachyte fault segment and the large Benmoreite segment located immediately to the west. The colour overlay refers to the geological ornament used in figure 4.23. The red line demarcates the area of Olorgesailie Formation exposure, as shown in figure 4.25

4.5 The Ilainymok Region

4.5.1 Introduction

A total length of ~3km of the Ilainymok fault scarp was surveyed using differential GPS equipment. As the total length of the fault is some 10km, the measured region only represents the important central section of the scarp, where there is an apparent interaction with NW-SE orientated faulting (see section 3.4.1). Positional data along the crest and base of the scarp were automatically collected at 1m intervals along each traverse. However, in places, the steep nature of the fault and areas of substantial rock overhang reduced the overall data quality along the contact between the two Magadi Trachyte flows exposed at the scarp front. In such areas, where satellite coverage was adequate, it was preferable to collect data manually. The locations of the GPS traverses are shown in figure 4.27 (see files Ilainymok.xls and Ilainymokeast.xls, Appendix A for the raw data). The exposed nature of the ground in this region meant that only one basestation position (see figure 4.27) was required to survey the Ilainymok scarp. Again, sediment in the hangingwall prevented determination of absolute fault displacements. Minimum fault displacements calculated between the base and crest of the Ilainymok scarp are shown in figure 4.28.

For completeness, GPS measurements were also collected along the crest and base of the East Ilainymok fault in order to describe the morphology of a small, relatively isolated fault. A profile of minimum displacements along this fault, which cuts through the Upper Magadi Trachyte flow, is shown in figure 4.29.

4.5.2 Structure of the Ilainymok Region

Displacements along the crest of the Ilainymok scarp, relative to the upper surface of the hangingwall sedimentary fill, show a steady increase from ~60m in the extreme south to ~90m at a distance of 1.2km along the profile in figure 4.24. Between x=1200m and x=2500m, displacements steadily decline and level off at a value of ~20m. Along the northern section of the fault, displacements remain relatively uniform.

Key ▨ Lower Magadi Trachyte flow   ▢ Upper Magadi Trachyte flow   ▶● Figure Viewpoint
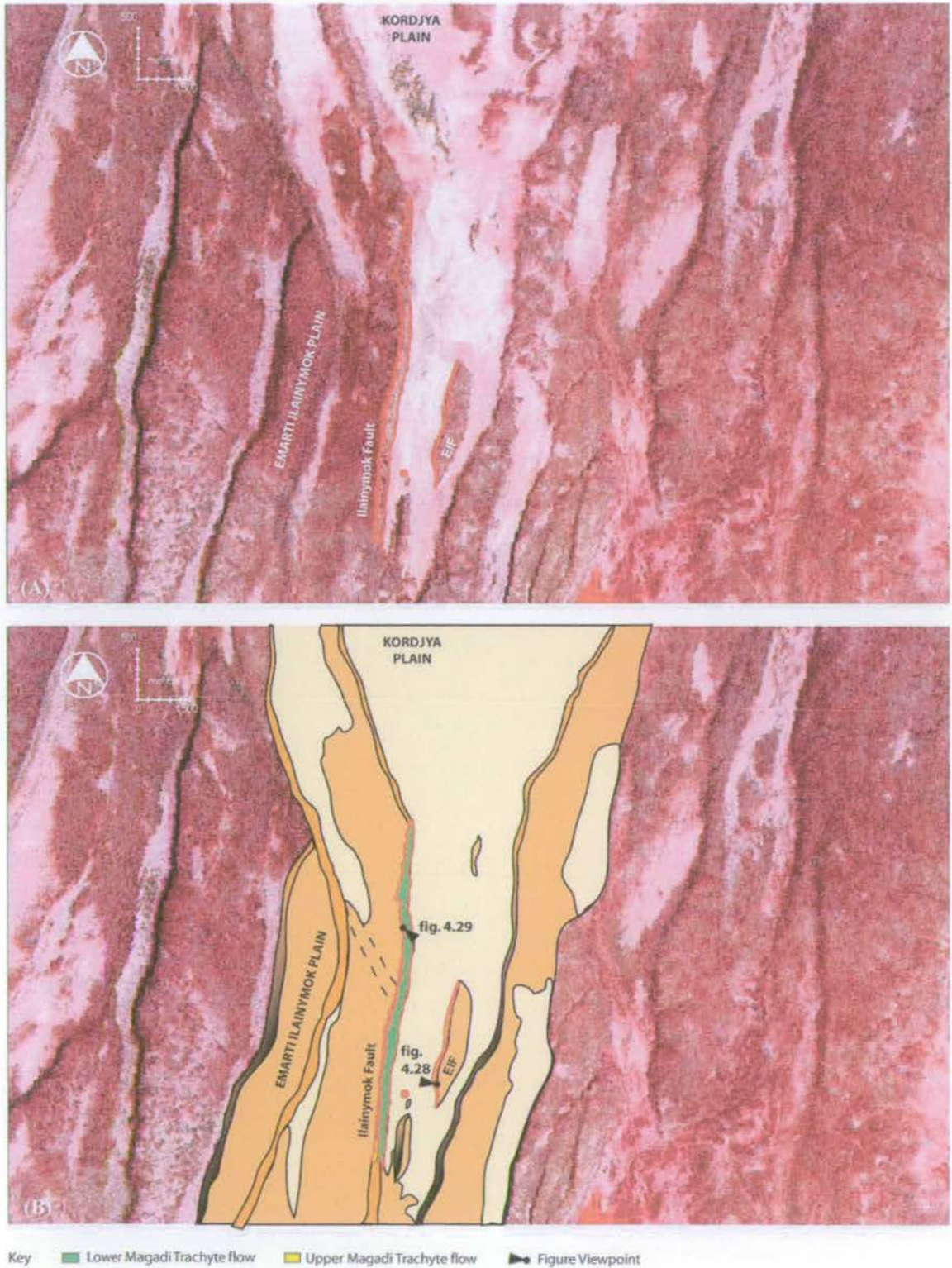
Figure 4.27 (A) Landsat 7 image of the Ilainymok region. Locations of GPS traverses are indicated by red lines. Filled red circle is the position of the GPS basestation. (B) As (A), but also showing the principal structure of the Ilainymok region highlighted by a colour overlay. EIF = East Ilainymok Fault.
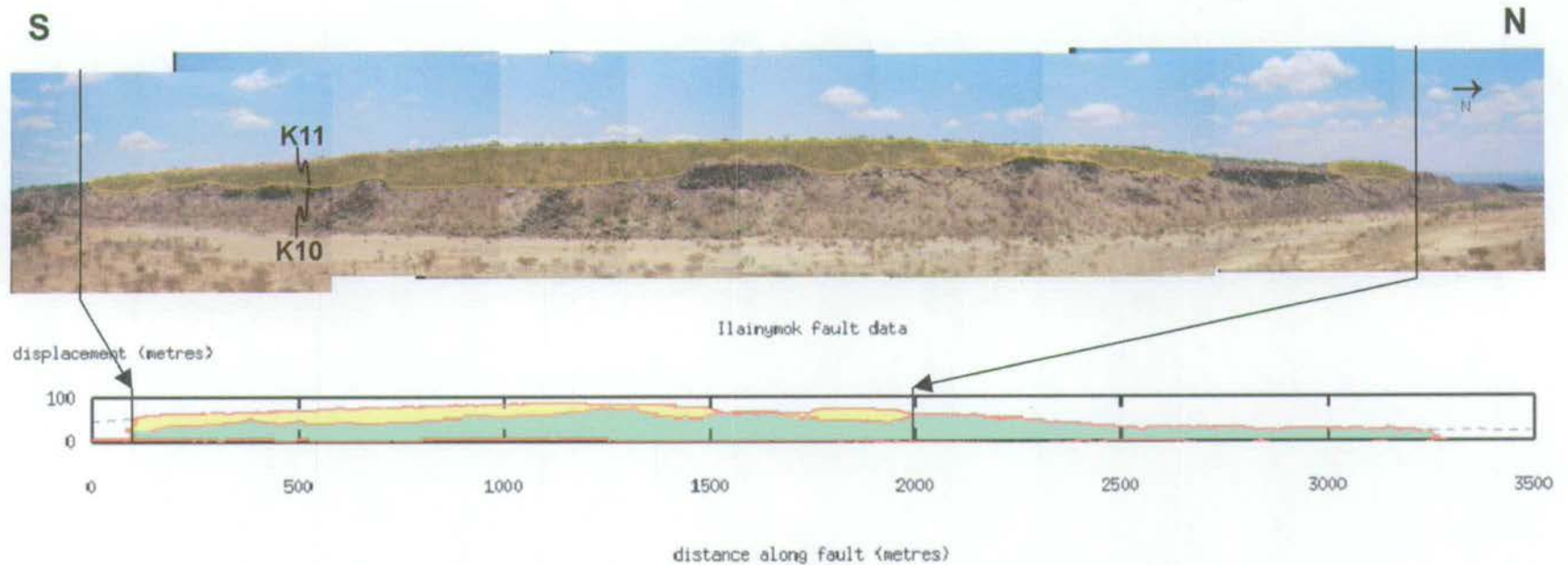
Figure 4.28 Photograph (above; replotted from figure 3.18) and displacement-length profile (below) along the Ilainymok scarp. Geological overlay corresponds to the key in figure 4.27. Solid red lines on the displacement-length profile indicate the locations of GPS data; dashed lines represent the approximate lateral continuation of the Ilainymok fault, beyond the surveyed section of scarp.
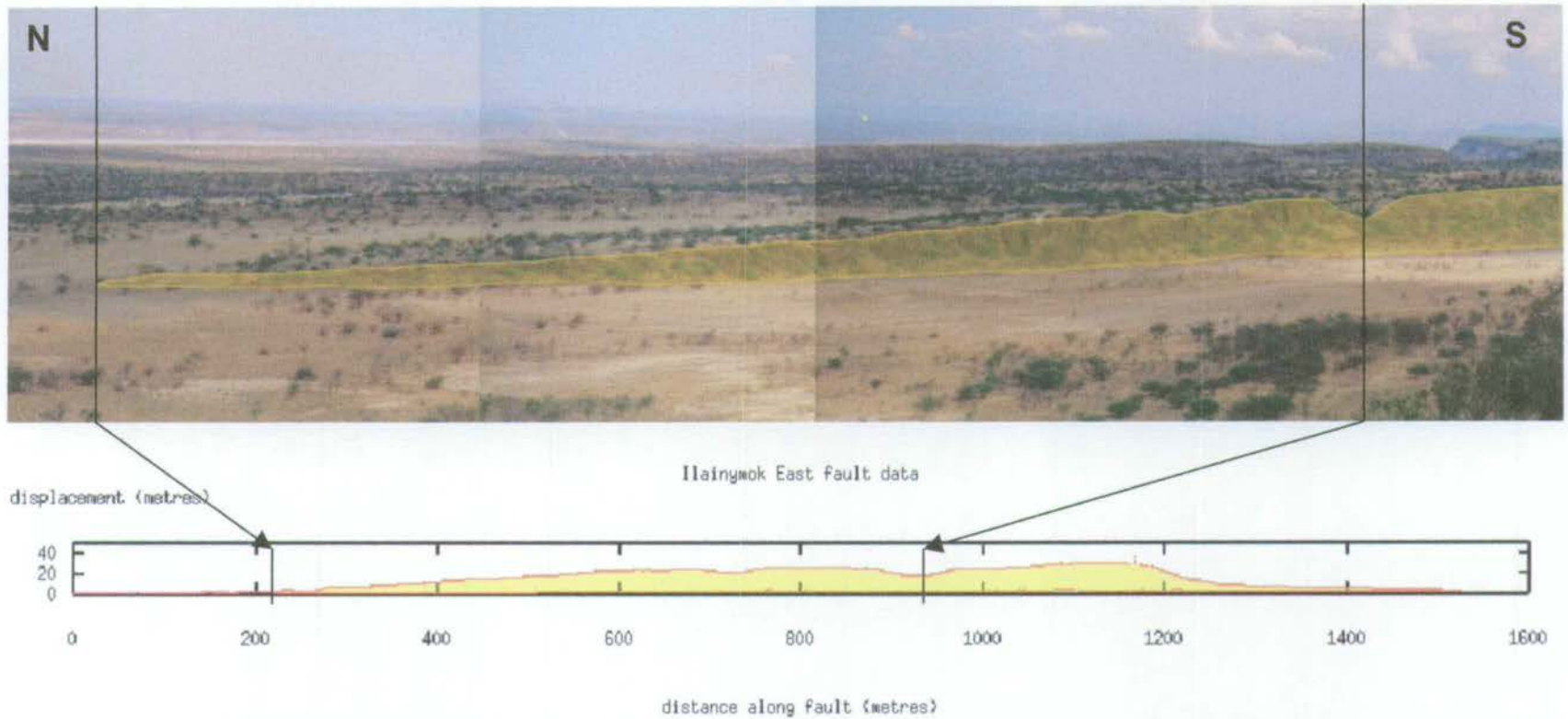
Figure 4.29 Photomontage (above) and displacement-length profile (below) along the East Ilainymok fault. Yellow transparencies on both images represent the Upper Magadi Trachyte flow of the Ilainymok region, as shown in figure 4.27. Red lines on the displacement-length profile indicate the location of GPS data.

The data plotted in figure 4.28 illustrates the undulating nature of the contact between the two flows exposed in the footwall of the Ilainymok scarp. At the southern end of the measured profile, the long wavelength increase in displacement along the flow contact reflects the similar increase along the surface of the upper flow. The maximum displacement achieved along this horizon is 85m at a distance of 1 320m along the profile and occurs close to the position of where a small oblique fault cuts the lavas and downthrows the laterite horizon by ~6m towards the north.

Short wavelength undulations along the flow contact, on the order of a few hundred metres in scale, are superimposed upon the long wavelength displacement profile. To the south of the overall displacement maximum these short wavelength irregularities are no more than 100m in length and are entirely buried under the upper lava flow. They are best exposed as rock protrusions of the lower flow into the overlying lava, the edges of which have been dissected by intense radially and concentrically orientated shear zones (see figure 4.30). Further to the north, the undulations are of a slightly larger wavelength (~200m) and were apparently large enough to act as barriers during eruption of the upper lava flow, which onlaps against one of these pre-existing features. Even where they are buried by the overlying flow, the undulations were obviously important topographic features and the intense shearing around their 'tips' indicates that they may represent a train of small, bell-shaped, N-S orientated normal fault segments in an early stage of development. It is possible that some of the smaller irregularities along the flow contact may represent the original morphology of the lower flow surface. However, two observations make this unlikely. Firstly these features are not of a uniform scale, nor are they regularly spaced, as might be expected if they were a product of lava deposition. Secondly, the flow undulations closely resemble the bell-shaped morphology of the East Ilainymok fault (figure 4.29) and the train of N-S orientated fault blocks located immediately to the east of the Ilainymok fault (figure 4.27). These latter faults may be regarded as a fault train in a phase of incipient linkage that might be analogous to, albeit on a slightly larger scale, the small fault segments cutting the Lower Magadi Trachyte flow of the Ilainymok fault.

Figure 4.30 Radial and concentric shearing (indicated with dashed lines) at the tip of a flow undulation on the upper surface of the Lower Magadi Trachyte flow, Ilainymok.

4.6 The Olooltepes Region

4.6.1 Introduction

The GPS basestation was established at two locations in the Olooltepes region (figure 4.31 and 4.32). The first was at the location of the tension gash, described in section 3.4.2, that extends between two horst blocks in this region. The gash can be regarded as an incipient fault linking the horsts and as such can be treated like the other scarps in this study. Hence, the initial traverse was started at the crest of the southernmost of the two horsts, continued on the 'footwall' side of the tension gash, across the alluvial plain between the blocks, and finished at the crest of the northernmost (Ileek Pusi) horst. As mentioned in section 3.4.2 this gash forms a series of 10-15cm wide en-echelon fractures that dissect the surface of the alluvial sediments and continue around the western flanks of the two neighbouring horsts. A second traverse was taken in the 'hangingwall' to the tension gash, at the base of the major fault blocks. For completeness, a third traverse was made along the line of the surface break itself. The locations of the traverses are shown in figure 4.31 and 4.32.

The second basestation was established at the other end of the Ileek Pusi horst block, where the fault tip was onlapped by a 10m thick lava, prior to fault reactivation (see section 3.4.2). Positional data was collected at the crest and base of the fault scarp and along the laterite horizon underlying the onlapping flow. As with the other regions discussed, data was collected automatically at the crest and base of the scarp, where satellite coverage was generally very good, but manually in places along the laterite horizon where the view of the sky was obscured by rock overhangs.

A displacement-length profile constructed from the GPS data and additional elevation values taken from a 1:50,000-scale topographic map is shown in figure 4.33. As for the fault profiles described in the previous sections of this chapter, the fault displacements can only be regarded as minimum values, determined from the vertical separation between basal and crestal GPS traverses, due to the presence of alluvial sediments in the hangingwall to the Olooltepes scarp.

Figure 4.31 Landsat 7 satellite image of the Olooltepes region showing the location of GPS traverses (red lines) and GPS basestation positions (filled red circles).
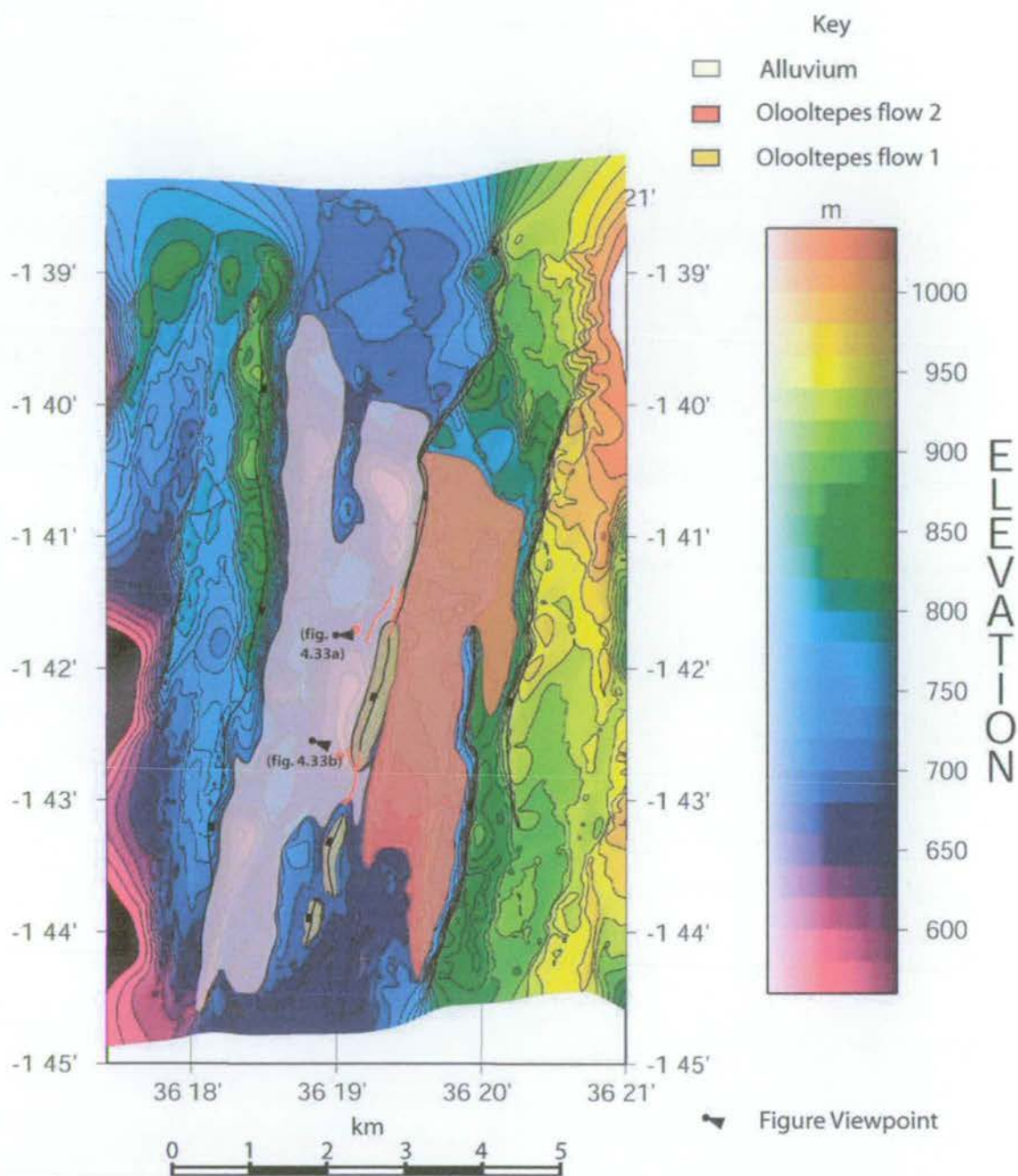
Figure 4.32 GMT plot generated from 1:50,000 scale Kenyan map data. Red lines indicate GPS traverses. Filled red circles are basestation positions. Local geology is highlighted with coloured ornament.
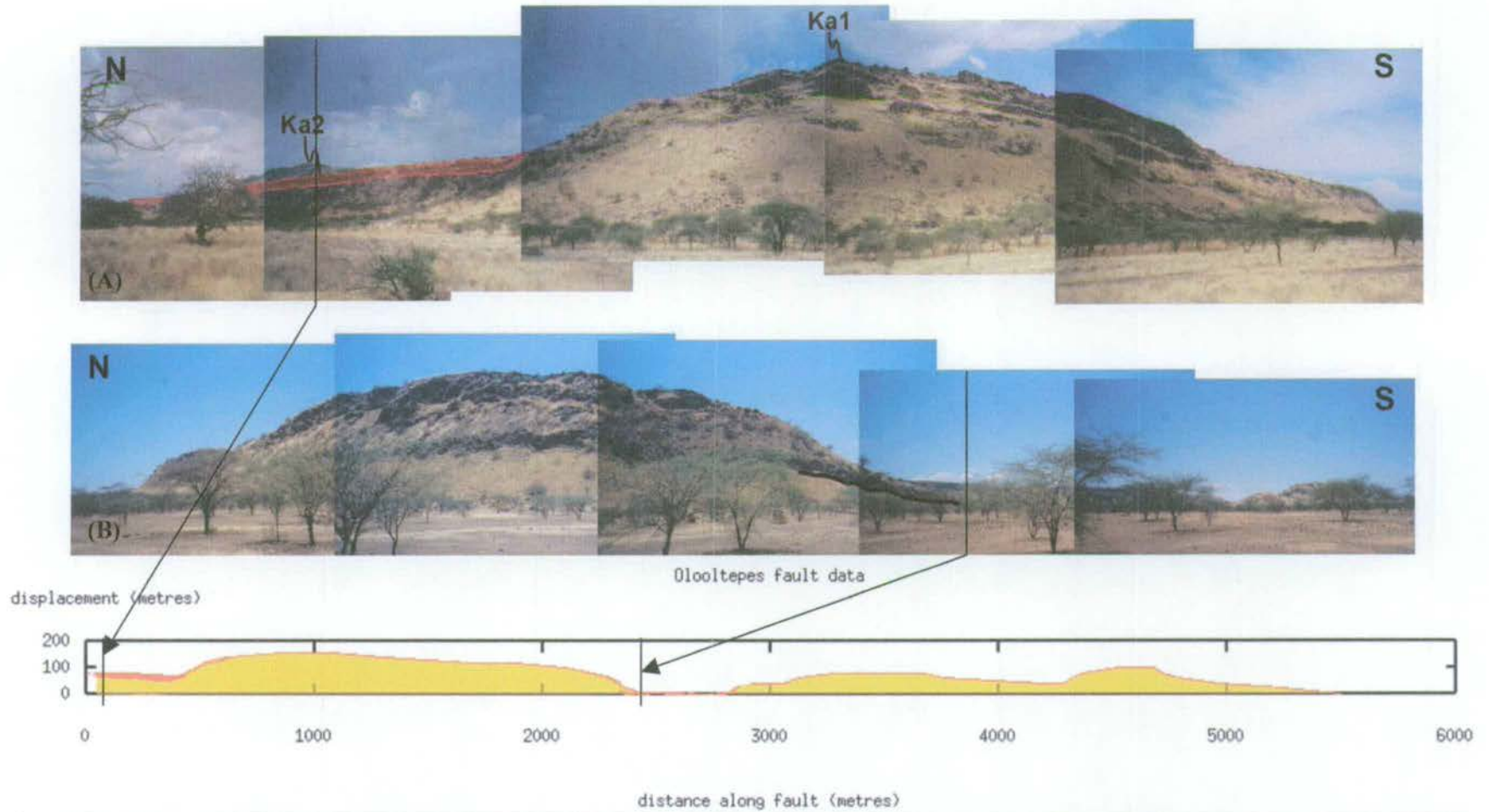
Figure 4.33 The Olooltepes fault scarp. Photomontages of the northern (above) and southern (centre) tips of the Ileek Pusi horst are shown in their correct positions relative to a displacement-length profile along the Olooltepes fault train (below). Photograph annotations are explained in figure 3.24. Geological ornament on the displacement-length profile is as shown in figure 4.32.

4.6.2 Structure of the Olooltepes Region

The composite displacement-length profile shown in figure 4.33 shows the three principal horst blocks of the Olooltepes region and the location of the onlapping Magadi Trachyte lava (flow 2). Since deposition of the onlapping flow, fault reactivation has uplifted the northern end of the Ileek Pusi horst block by 59m, while the southern tip has remained relatively fixed. This is reflected in the steady decrease in elevation, from north to south, along the crest of the block. The southern tip of the Ileek Pusi horst is the site of a tension gash that opened between the two neighbouring fault blocks during a period of renewed earthquake activity in May 1998 (see section 2.4.5). A possible interpretation is that the initially independent fault blocks, which are located along a strike of ~014 degrees, are slowly undergoing surface linkage (though the faults may already be linked at depth, see sections 1.2.3 and 6.4.2 for a further discussion).

4.7 Summary

The purpose of this chapter was to introduce the fundamental concepts of GPS and, more specifically, the capability of differential GPS to record positional data with a maximum accuracy of ±4cm in terms of latitude and longitude and ±8cm in terms of elevation. Differential GPS has been used to elucidate the detailed structure and morphology of surface faulting in four localities within the South Kenya Rift (South Kedong Graben, Esiteti, Ilainymok and Olooltepes). The structural characteristics of each region have also been documented in this chapter. When integrated with the geochronological data introduced in chapter 3, the observed fault structure and volcano-stratigraphic relationships can be used to reconstruct definitive fault growth histories and establish both vertical displacement rates and, where available, lateral propagation rates. The methodology and details of these fault restorations will be the subject of the next chapter.

Chapter 5: Fault Reconstructions and Interpretations

5.1 Introduction

5.1.1 A lava flow as an equipotential surface

The observed stratigraphic relationships, between pre-existing normal fault scarps and younger lava flows in the South Kenya Rift, allow the possibility of reconstructing detailed growth histories for the faults described in chapters 3 and 4. While fault displacement-length profiles are a useful method of depicting along–strike variations in scarp morphology they do not provide any quantitative information on fault growth history. Where the South Kenya Rift is so useful, therefore, is that the region is dissected by a number of fault scarps that were active penecontemporaneously with regional volcanism.

An individual lava flow represents the product of an instantaneous volcanic eruption that can be dated, using $^{40}Ar/^{39}Ar$ geochronology, to provide an accurate geological marker horizon. Assuming that the lava is not too viscous, it can be treated as an equipotential surface, that is, a surface of equal gravitational potential, and can be used to produce a datum for the ground surface at the time of eruption. This latter assumption is an important one and has been relied on in order to reconstruct detailed growth histories for the faults introduced in chapters 3 and 4. While it is reasonable to assume that basalts, which are poor in silica and hence relatively non-viscous, will behave in this manner, silica–rich trachytes are generally considered to be more viscous in nature and therefore the surface of such flows may not be a reflection of an equipotential. However, the high alkali content of the Kenya Rift trachytes, exceptionally combined with high concentrations of halogens (especially fluorine and chlorine) confers low viscosity and highly mobile flows can then spread over wide areas (Upton, 1996).

Lava viscosity is influenced, to a large degree, by the size and concentration of phenocrysts in the melt. Large numbers of phenocrysts will increase the lava viscosity and decrease the lava flow-rate following eruption. The majority of lavas erupted within the South Kenya Rift are trachytic in composition, though, as previously described in section 2.3, benmoreites and basalts

are also present in significant quantities. Field observations show that, in general, the aphyric trachytic and basaltic flows have a uniform thickness over a large areal extent and can therefore be regarded as an equipotential surface. Other more massive and richly porphrytic lavas, such as the Ol Tepesi Benmoreite, Limuru Trachyte and upper Gesumeti Trachyte flows were probably much more viscous in nature. The viscosity of such flows should limit their areal extent and may produce flow-surface topography. Certainly, the Ol Tepesi Benmoreite is restricted to a relatively small (~90km^2) area located immediately to the west of the Esageri-Esakut platform and the Gesumeti Trachyte is confined to a narrow strip of exposure along the margins of the Kedong Graben (though more of these flows may be buried beneath younger lavas) (see figure 3.4). In contrast, however, the Limuru Trachytes were erupted in large volumes over a wide area of the eastern rift margin. For the majority of the lavas in the South Kenya Rift there is very little noticeable, large-scale, flow-generated topography associated with the upper surface of the flow. It is therefore relatively simple to distinguish fault-generated topography from the natural eruption-related topography on the lava surface.

5.1.2 Restoration of fault displacements – footwall stratigraphy

Reconstruction of fault growth over a geological timescale depends on the availability of stratigraphic information in both the footwall and hangingwall to the fault. To accurately restore the total vertical displacement accrued across a simple, isolated normal fault it is necessary to have information on the elevation of a marker horizon, cut during the period of fault activity, in both the footwall and hangingwall regions of the fault scarp and along strike of the fault (figure 5.1a and 5.2). If the age of the marker horizon is known, such information will allow calculation of precise displacement rates along the length of the fault. The faults documented in this study are observed to dissect and uplift lavas that were erupted contemporaneously with fault development. As discussed in Chapter 4, these lavas are often observed as thin flows that onlap against pre-existing fault blocks. Although exposures of lava are commonly observed as discontinuous ledges, it is relatively straightforward to correlate between exposures in the field as a result of their lithological and petrological similarities. Most of the flow ledges are also underlain by obvious laterite horizons that can be easily mapped out on the ground.

Faults in the South Kenya Rift are observed to be long, flat, structures characterised by gentle tip gradients. An idealised displacement-length profile along the strike of a typical rift-floor

fault is shown in figure 5.2. The method used to estimate the position of the lava surface between footwall lava exposures depends, to a large extent, on the section of scarp that was surveyed. Since many rift floor faults are 'trapezoidal' in shape, displacements along the central sections of the faults are relatively uniform along strike. Closer to the fault tips, displacements are often observed to decrease to zero in a linear fashion. Hence, throughout this study, a linear correlation is used to interpolate between footwall lava exposures, with the gradient of the interpolated 'construction' line depending on the proximity of the fault tip. Therefore, dissected lava horizons lying distant from the fault tip can be modelled by a horizontal lava surface, whereas those at, or close to, the end of the fault approximate a uniformly dipping surface (see figure 5.2).
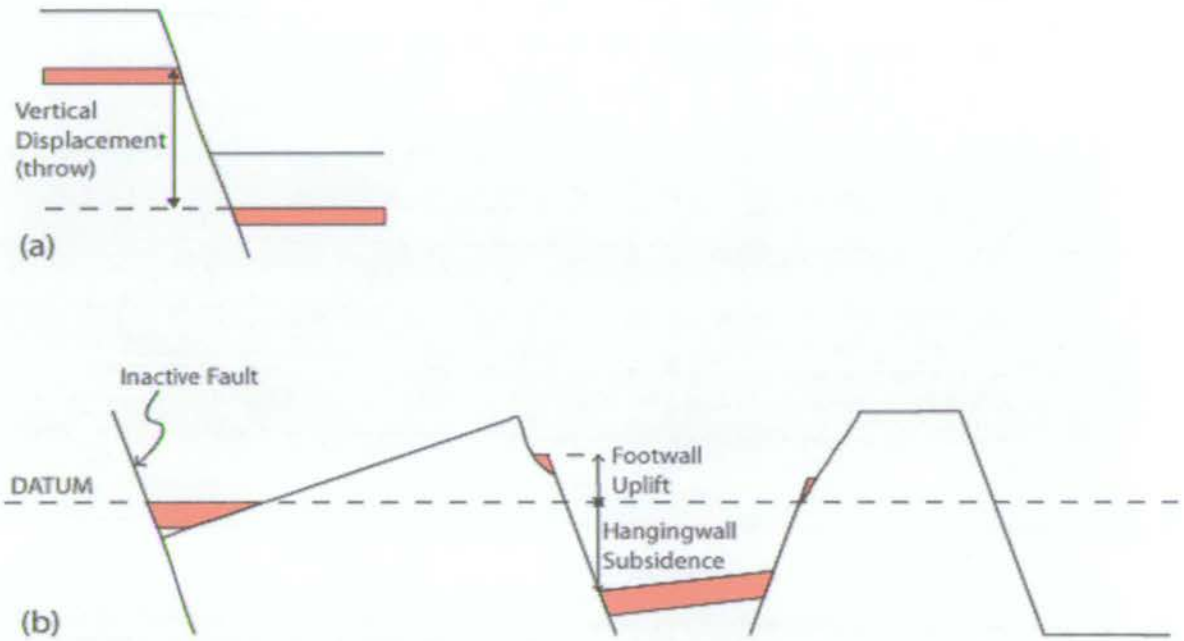
Figure 5.1 Accurate reconstruction of fault growth over a geological timescale depends on the structural complexity of the region concerned. A) For a single, isolated fault the vertical displacement (throw) can be easily calculated by using the relative offset of a marker horizon across the fault. This requires knowledge of horizon elevations, in both the footwall and hangingwall to the fault. B) For a closely-spaced network of faults, where a marker horizon may have been displaced by differing amounts on different fault scarps, then it is necessary to establish the position of a pre-faulting datum surface to which faulted sections of the marker horizon can be restored. The datum may represent the surface of an undeformed section of the marker horizon that is relatively distant from the region of active faulting. Note that footwall uplift:hangingwall subsidence has been identified as ~1:6 from neotectonic studies (e.g. Stein and Barrientos, 1985; see figure 5.2), though this may not be the case over longer timescales.
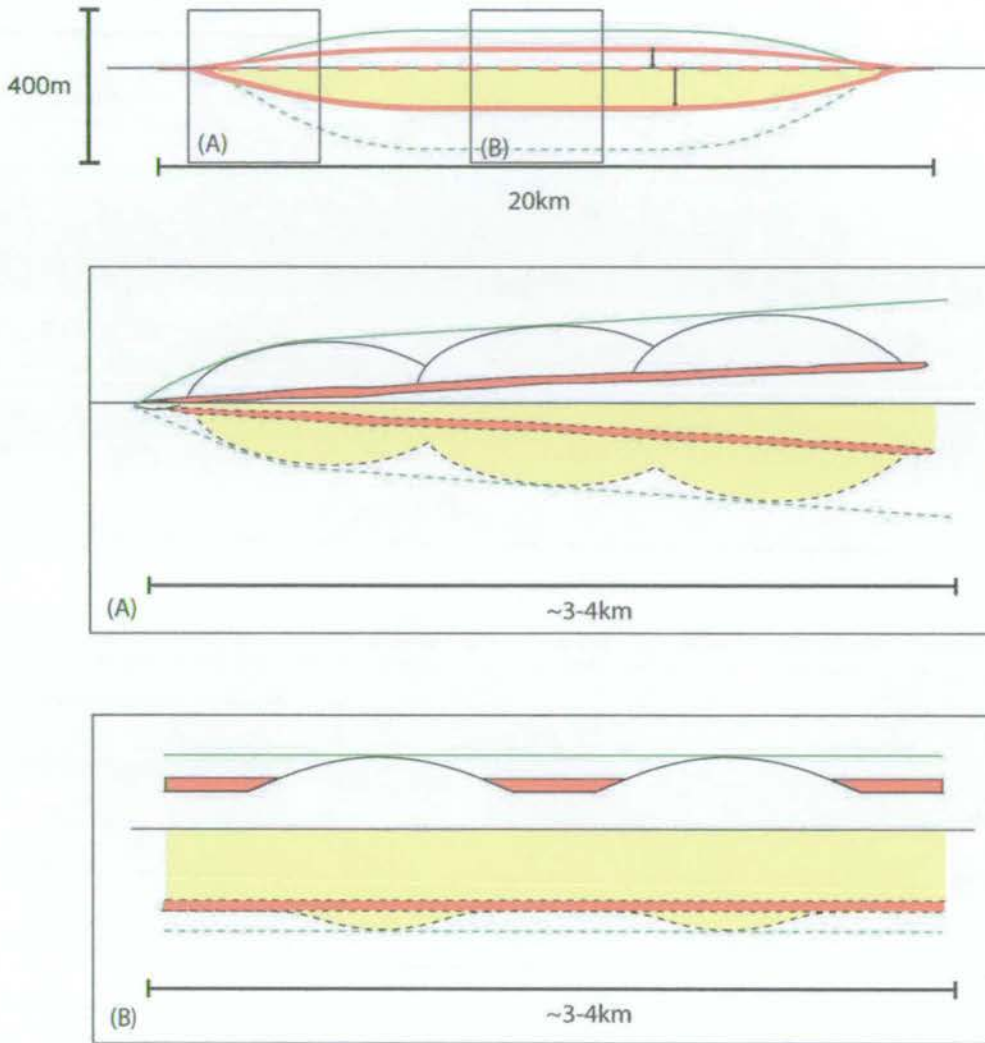
Figure 5.2 Cartoons to show idealised along-strike, rift-floor fault morphology and relationship to syntectonic volcano-stratigraphy (note that these figures have been vertically exaggerated). Upper figure shows the 'flat', trapezoidal nature of the rift floor faults. Green lines envelope total fault displacement (dashed in hangingwall). Red lines indicate the location of a thin syntectonic lava flow that onlaps against pre-existing fault blocks (as a lava ledge attached to the footwall scarp and as a layer on the floor of the fault hangingwall). Footwall uplift and hangingwall subsidence of this lava is illustrated (with arrows) relative to a reference datum (shown as the dashed red line; see section 5.1.4). Regions shown in yellow represent undefined hangingwall stratigraphy (e.g. hangingwall alluvium). The horizontal black line indicates the surface of hangingwall stratigraphy. (A) Figure showing idealised fault-tip morphology. Curved black lines envelope displacements on pre-existing faults. Note that the onlapping footwall lava dips linearly towards the fault tip. (B) Central section of the fault. In this case, the onlapping lava lies horizontally along the crest of the footwall scarp, between the pre-existing fault blocks, rather than as preserved ledges.

5.1.3 Restoration of fault displacements – hangingwall stratigraphy

In order to accurately determine fault displacements it is also necessary to identify the location of hangingwall stratigraphy. In many field-based studies of normal faulting it has often been difficult to accurately determine the position of hangingwall cutoffs because they are frequently buried under a layer of sediment that accumulates in the immediate hangingwall to the fault. For example, in their study of fault development in the Canyonlands graben system, Utah, Trudgill and Cartwright (1994) document Quaternary alluvial deposits, between 5m to >50m in thickness, that partially fill the deepest grabens. In such cases, if there is sufficient exposure, it may be possible to make some direct estimate of the alluvial thickness where the sediment has been dissected by fluvial action.

Many of the faults surveyed during the course of this study have sediments covering hangingwall marker horizons. In two areas, the South Kedong region and the Esiteti region, hangingwall sediment thicknesses can be reasonably well constrained. In the Esiteti region, the thickness of the Olorgesailie Formation sediments, which lie in the hangingwall to the Esiteti fault, are documented as 50-60m (e.g. Shackleton, 1955; Bye *et al.*, 1987). Alluvial fill in the South Kedong region appears to be no more than ~20m in thickness, since bedrock is exposed in places along the floor of the Kedong graben system. However, along many of the fault scarps there is little uplift and erosion of hangingwall sediments and, as a result, it is difficult to make any direct measurement of sediment thicknesses. It was therefore necessary to estimate hangingwall stratigraphic thicknesses by applying a footwall uplift to hangingwall subsidence ratio of 1:2 (which is shown to be reasonable for the faults where hangingwall thicknesses can be directly estimated; e.g. in the Kedong region - see sections 5.2.1a and 5.2.4) and assuming that fault scarp displacements above the surface of the hangingwall sediment surface represent footwall uplift. Hence, along these faults the largest errors in the calculated displacement rates are associated with uncertainties in the hangingwall sediment thickness (see section 5.1.7b).

The along-strike hangingwall location of volcanic stratigraphy is poorly known in parts of the South Kedong, Ilainymok and Olooltepes regions, where the hangingwall depocentres are completely filled with lacustrine and alluvial sediments. For these scarps, the minimum vertical displacements (between GPS traverses measured along the crest and base of the fault in the

field) are assumed to represent values of footwall uplift, allowing calculation of absolute displacements by applying a 1:2 ratio of footwall uplift to hangingwall subsidence, using:

Total vertical displacement = ('minimum' displacement + ½ sediment thickness) ± ½ sediment thickness. (Figure 5.3)

Where the final term in the above line represents the uncertainty in sediment thickness (see also section 5.1.7b).

As a result of the uncertainties associated with hangingwall sediment thickness, it has been impossible to accurately measure total fault displacements along strike. Therefore, the displacement-length profiles shown in this chapter and Chapter 6 have 'minimum' displacements plotted on the y-axis. However, it is possible to calculate true displacement rate values at positions of D_{max} by adjusting minimum displacement values to take account of hangingwall sediment thickness according to the above procedure.
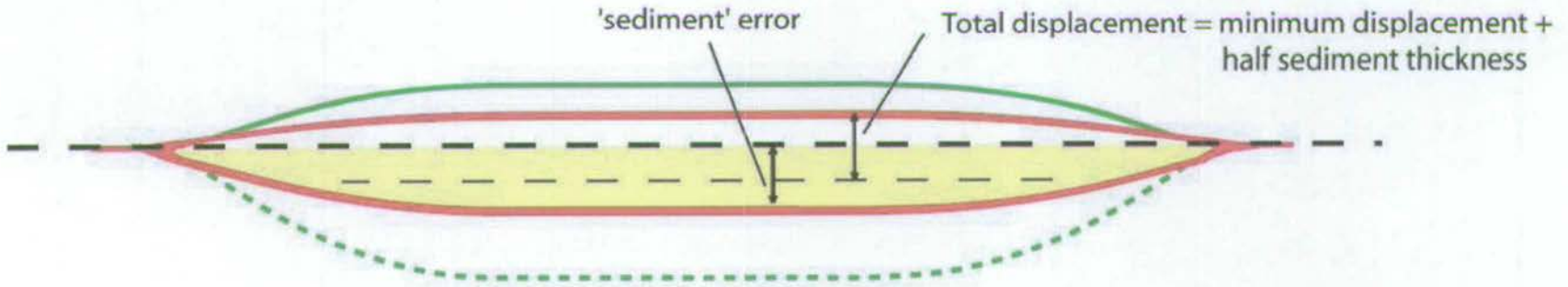
Along-strike fault profile (not to scale)

Figure 5.3 Idealised along-strike fault profile, showing the relationship between measured 'minimum' displacements and inferred total displacements. Surface of hangingwall sediment is indicated by the thick, black dashed line; half sediment thickness is shown by the thin dashed line. In this case, the hangingwall depocentre is assumed to be entirely filled with sediment such that the 'minimum' displacement is a measure of footwall uplift. Total displacement is then calculated by assuming a footwall uplift to hangingwall subsidence ratio of 1:2 (see section 5.1.7b) and adding half the estimated hangingwall sediment thickness to the minimum displacement value. The geological error in the total displacement is then ± ½ sediment thickness.

5.1.4 Ratios of footwall uplift to hangingwall subsidence – use of a reference datum

In order to calculate the relative amounts of footwall uplift and hangingwall subsidence associated with a fault it is necessary to identify a pre-faulting reference datum to which a marker horizon can be restored (figures 5.1b and 5.4). In terms of the South Kenya Rift lavas, such a datum would be a 'palaeo-landsurface' that represents the pre-existing topography onto which the lava was erupted. Without knowledge of the initial elevation of this surface prior to faulting it is impossible to constrain the subsequent amounts of footwall uplift and hangingwall subsidence associated with each fault in the network. The principal ingredient in identifying the palaeo-landsurface is to find an area, relatively close to the faulted area of interest; that is mantled by the same lava flow but which has not been affected by subsequent deformation. In such an area it is possible to measure the regional topographic gradient and apply that gradient to the neighbouring faulted area as a reference datum. Implicit in this method is the assumption that, on a regional-scale, the surface over which the lava was erupted had an identical slope in both the faulted and non-faulted areas. This is reasonable since, over a scale of several kilometres, pre-existing fault-generated topography and flow surface topography are both short wavelength features. Figure 5.4 shows a cartoon illustrating two-stage fault development in a region inundated by lava following an initial phase of fault movement. In this case, lava in the footwall to the through-going fault has suffered little tectonic deformation subsequent to eruption and the topographic slope of the un-deformed lava surface can be applied to the remainder of the region as a reference datum. Having established an acceptable surface datum it is then possible to restore the upper surface of each onlapping lava flow back to that datum by adjusting displacements associated with each fault segment. In the current study, the elevations of un-deformed lava flows close to a main zone of faulting have been used to reconstruct the fault growth history of the South Kedong region. The method used to undertake this reconstruction will be detailed in section 5.2.

With knowledge of all three elements; namely i) location of footwall stratigraphy, ii) location of hangingwall stratigraphy and iii) location of a reference datum, it is possible to both backstrip a normal fault block and gain knowledge of the footwall uplift to hangingwall subsidence ratio.
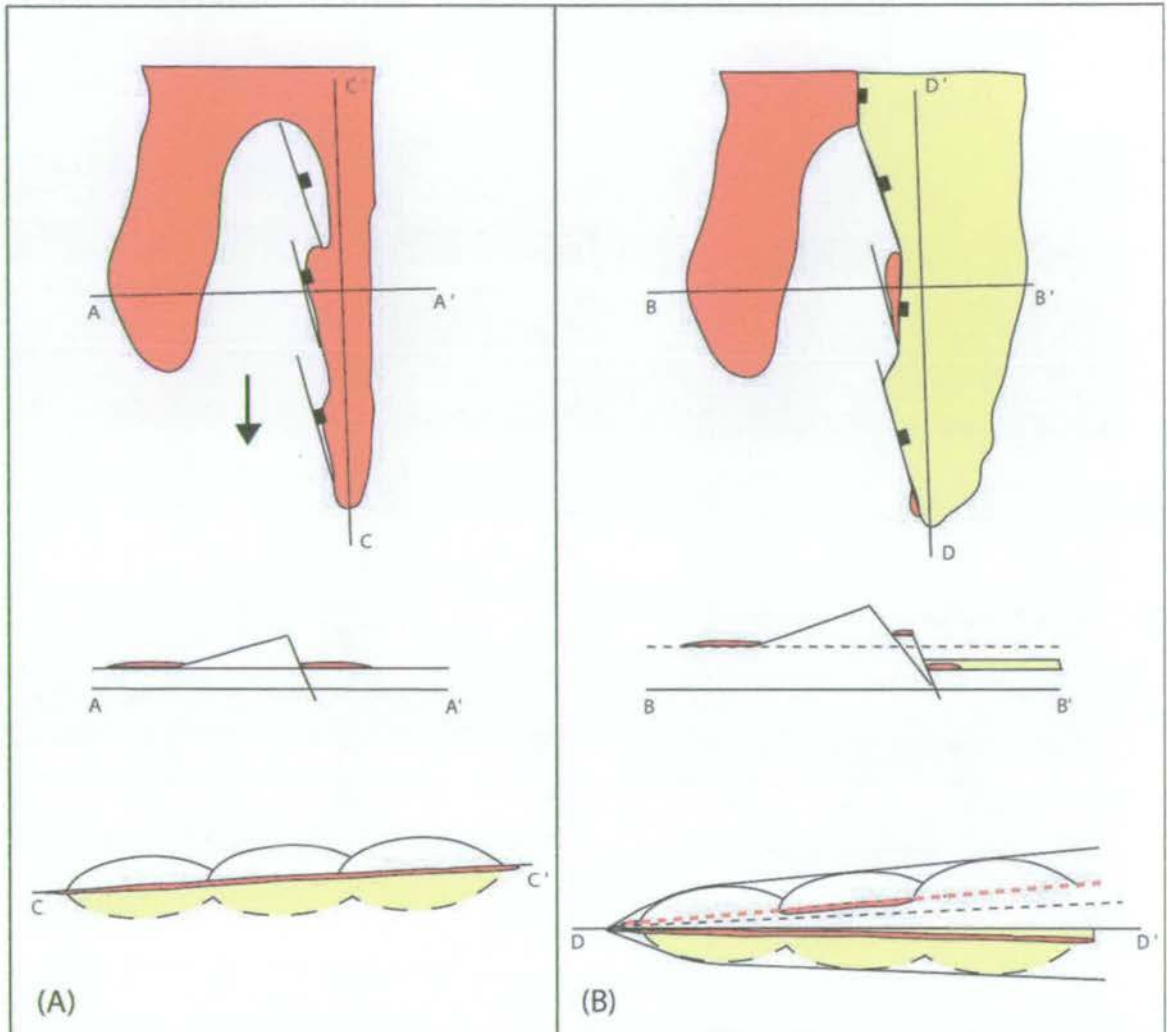
Figure 5.4 Idealised cartoons to show fault development in a volcanic setting, as based on deformation in the South Kedong region. (A) Initial situation. Local topography is characterised by three overlapping normal faults arranged en echelon. Arrow indicates regional palaeoslope. A-A' is a cross-section through the central fault across strike. Following the initial phase of faulting, a thin lava flows into the fault hangingwalls and behind the footwall fault blocks. C-C' is an along strike profile showing the arrangement of the three 'bell-shaped' fault blocks. (B) Three pre-existing fault blocks link laterally to the form the tip of a larger, through-going, fault. Cross-section shown by B-B' illustrates the amount of footwall uplift and hangingwall subsidence relative to the pre-faulting datum (shown as the dashed line) which can be established from the gradient of the lava surface where unaffected by tectonic deformation (immediately behind the fault footwall). D-D': Dashed red line indicates the location of the interpolated lava surface along the fault footwall block. Dashed black line shows the position of the pre-faulting reference datum.

In their studies of neotectonic faulting, Stein and Barrientos (1985) and Barrientos *et al.* (1987) have analysed the fault geometry generated as a result of instantaneous, coseismic slip during the large (M=6.9) 1983 Borah Peak earthquake that occurred along the Lost River fault in the Western United States. In that study, levelling data collected from benchmarks located in the epicentral area, that were surveyed in 1933 and 1948, were re-levelled in 1983 and 1984, following the earthquake. The relative changes in benchmark elevation between the surveys are illustrated in figure 5.5. This diagram shows the amount of footwall uplift and hangingwall subsidence relative to a datum horizon that was identified by extending the across-strike profile far enough northeast and southwest of the fault so that there was no significant change in the relative elevation changes of the benchmarks. The ratio of footwall uplift to hangwall subsidence along the Lost River fault can be seen to be ~1:6 (Stein and Barrientos, 1985). However, it is still unknown as to whether this value applies to fault displacements accumulated over longer timescales. In the current study, ratios have been calculated to between 1:1.4 and 1:2. These latter values are in accordance with normal faulting over geological timescales as described by McLeod *et al.*, 2000 and have been used, as discussed in section 5.1.3, to estimate vertical fault displacements where hangingwall depocentres are completely filled by alluvial and lacustrine deposits (e.g. for the Ilainymok and Olooltepes fault scarps).

5.1.5 Fault Restorations

In order to backstrip the faults described in this study, it was necessary to restore GPS data collected along the crest of each fault scarp and the upper surface of the onlapping footwall lavas to their pre-faulting positions as indicated by the reference datum surface. Since there is a clear linear relationship between footwall lavas exposures along strike (see section 5.1.2), the reconstructions described in the following sections (5.2-5.5) involve simple linear operations that either rotate or translate the positional data to their restored positions (i.e. in the reverse sense to the fault development cartoon shown in figure 5.4). For example, consider the imaginary case of a thin lava (~10m thick) that onlaps against the tip of a pre-existing fault block, which has since been reactivated so as to rotate the onlapping lava (see figure 5.6). To restore the lava surface to its pre-faulting position, as indicated by the reference datum (which in this case is assumed to be horizontal), it is necessary to undertake the following simple operation:

171

$H(x)restored = H(x)initial - [(L(x) - L(1)) \cdot \tan(\theta)]$

and $\tan(\theta) = [H(2)-H(1)]/[L(2)-L(1)]$

Where: $H(x)restored$ is the restored height of point x, $H(x)initial$ is the initial height of point x, $H(1)$ is the height of point 1 (located at the fault tip), $H(2)$ is the height of point 2 (located towards the centre of the fault; note that $H(2)$ is larger than $H(1)$), $L(x)$ is the latitude (or length along the profile) of point x, $L(1)$ is the latitude (or length along the profile) of point 1 and $L(2)$ is the latitude (or length along the profile) of point 2 (in this case the latitude of point 2 is higher than the latitude of point 1).

Note that *latitude* values rather than *lengths* have been used in this initial calculation (a similar technique has been used in the reconstructions described in the following sections). In practice, it is unimportant whether latitude or length values are used for these operations since it is only the height values that are being adjusted and, as mentioned in section 4.3.1, most of the rift faults strike within 10° of true north-south orientation, so it is possible to use latitudes as a direct proxy for fault length. However, it was decided use the raw GPS latitude values in order to preserve the accuracy of the data throughout the reconstruction. The latitude values were subsequently converted to UTMs using the Geographic Translator (GEOTRANS) software described in section 4.3.1, from which along-strike length values could later be determined.

Once the surface of the onlapping lava flow is restored to the level of the reference datum, it is then possible to restore GPS traverses collected from other positions on the fault, such as along the scarp crest (shown by the solid green line in figure 5.6), by rotating each GPS point by an amount equivalent to that required to rotate a point lying on the surface of the lava, at the same latitude, back to the reference datum.

The nature of the restoration used depends to a large degree on the section of fault scarp under analysis. A lava located in close proximity to the fault tip may have a gentle dip along strike that can be restored by a rotation around the tip using the method shown in figure 5.6. However, the majority of the scarp sections described in this study lie distant from the fault tips. In such cases the fault may be backstripped by a simple operation that vertically translates GPS points measured along the upper surfaces of onlapping lava flows and adjusts all other points

according to that reference frame. Such operations have been used extensively for reconstruction of the Esiteti and Olooltepes fault scarps and will be described in more detail in sections 5.3 and 5.5.

Essentially, the reconstruction of each fault must be approached independently, according to the structural and stratigraphic relationships observed in the field. The step-by-step fault reconstructions for those scarps surveyed in the South Kenya Rift will be described in detail throughout sections 5.2-5.5.

5.1.6 Construction of palaeo-topographic maps

The South Kedong region is unique in terms of the four regions to be surveyed in that it is characterised by areally extensive lava flows that have been offset by a number of normal fault blocks. Therefore, each fault that offsets a dated lava horizon could be backstripped independently using the methods described above. Furthermore, the closely spaced nature of the fault scarps in this region have allowed construction of a sequence of 3D palaeo-topographic maps by inputting, at each time-step, restored elevation and length data for each fault scarp into Generic Mapping Tools (GMT) software. A further explanation of the GMT software and the GPS traverses used to construct these plots is given in section 4.3.1. Note that, as a consequence of the data averaging functions that GMT performs in order to produce 3D models, it is impossible to extract accurate displacement or displacement rate data directly from these diagrams. The palaeo-topographic maps should therefore be regarded merely as illustrative tools documenting the development of the South Kedong region. These figures will be discussed further in section 5.2.
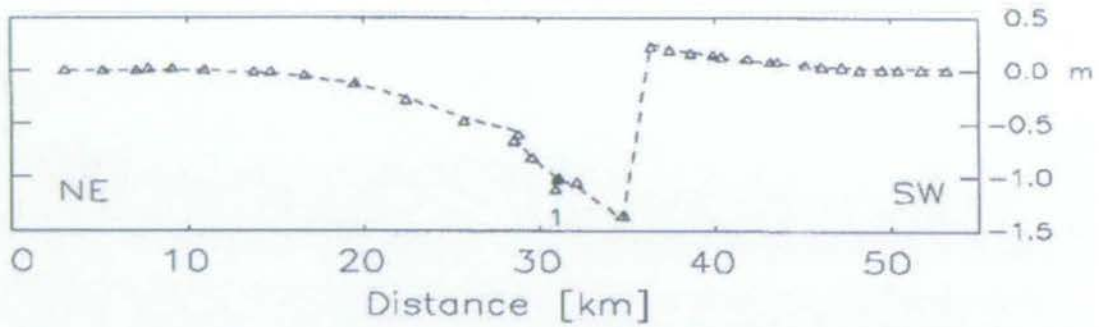
Figure 5.5 Cross-section through the Lost River fault (footwall towards the southwest) showing the observed co-seismic elevation change of benchmarks after the 1983 Borah Peak, Idaho, earthquake (from Barrientos *et al.*, 1987).
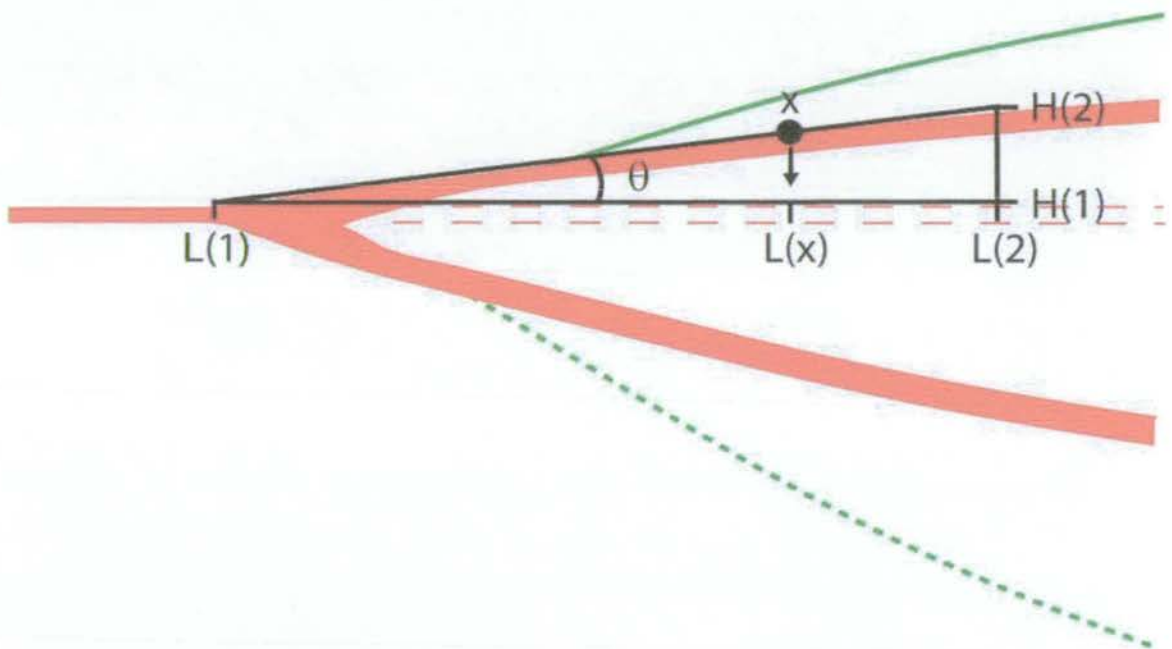
Figure 5.6 Cartoon illustrating the onlap relationship of a thin lava flow onto the tip of the pre-existing fault block shown in figure 5.2. Black lines highlight the method of restoring the uplifted footwall lavas back to the level of the horizontal reference datum (indicated by the dashed red line). See text in section 5.1.5 for details of the reconstruction.

174

5.1.7 Sources of error

Errors in calculated displacements and hence, displacement rates, comprise quantifiable analytical errors and estimated geological errors.

a) Analytical errors:

Quantifiable errors in both displacement and displacement rate values are taken to the 68% (1σ) confidence level and incorporate GPS analytical errors (taken as $\pm$ 8cm in terms of elevation; see section 4.2), $^{40}Ar/^{39}Ar$ dating errors (given in table 5.1 of section 5.6, see also section 3.3.2) and standard deviations of GPS points away from the 'best-fit' construction lines joining footwall lava exposures (see sections 5.2 to 5.5). The resulting compound errors were calculated and listed in table 5.1 (section 5.6).

b) Geological considerations:

Perhaps the largest errors in displacement rate values are those resulting from the uncertainty in locating hangingwall lava stratigraphy. For the majority of faults analysed during the course of this study, volcanic hangingwall stratigraphy is buried beneath an unknown thickness of alluvium. However, in two cases; namely the Enasira and Entashata faults of the South Kedong region, the presence of a reference datum horizon and relatively little hangingwall sedimentation has allowed the calculation of a footwall uplift to hangingwall subsidence ratio in the range 1:1.4 to 1:2 (see also sections 5.1.4). A value of 1:2 is in accordance with observations along the Esiteti fault where the vertical relief of the footwall scarp is some 30m above the surface of the Olorgesailie Formation that fills the fault hangingwall, the thickness of which has been independently determined as between 50 and 60m (e.g. Shackleton, 1955; Bye *et al.*, 1987). In all cases, to take account of the hangingwall sedimentary wedge, displacements measured above the surface of the hangingwall fill (i.e. the minimum displacements) have been added to a value equal to the half-thickness of the hangingwall sediments, with the thickness error represented by the half-thickness value (see section 5.1.3 and figure 5.3). Assuming a value of 1:2 it is then possible to estimate a total displacement at D_{max} and hence calculate a vertical displacement rate.

Fault displacement-length ratios and tip-propagation rates are influenced by fault-tip position, which is generally difficult to constrain due to the presence of hangingwall sedimentary deposits. Fault lengths have been determined directly from GPS data or, where the fault extends beyond the available GPS data coverage, from 1:50,000 scale topographic maps. Since the tip positions of the longest faults are constrained from map data, rather than from GPS, the errors in fault length are significantly larger for these structures than for small faults. However, the overall error as a proportion of length is similar for all the documented faults. Therefore, an error of ±10% has been applied to each minimum fault length and the resulting values have been rounded to give the estimated total length.

Fault length data have been provided alongside some of the along-strike displacement-length fault profiles included in this chapter. However, as with the vertical displacements, lengths shown in these figures should be regarded as minimum values that have additional errors associated with the uncertainty in fault-tip position.

Vertical displacement, displacement rate and fault length data, together with their associated error values, are summarised in table 5.1, at the end of this chapter.

Another non-quantifiable error affecting displacement values is erosion. However, the well-preserved nature of the hard volcanic rocks making up these scarps, and the relatively young age of the faults, suggests that erosion has never had a major influence on the morphology of the fault blocks.

Displacement rate values are defined, to a large extent, by the temporal distribution of dateable lava flows. Unlike the situation in shallow marine or lacustrine environments, the geological record of the Kenya Rift is not continuous. Volcanic time-marker horizons are erupted rapidly and episodically between relatively long periods of quiescence. If fault growth is also episodic then periods of rapid uplift may not be recognisable if the length of the time period in question is below the temporal resolution of the volcanic record. Hence, the displacement rates recorded in the following sections are time-averaged over the period between volcanic marker horizons.

5.2 The South Kedong Region

The following fault reconstructions have been undertaken using the GPS positional data collected a long the traverses described in section 4.3.1. The raw data for the South Kedong region is included in Appendix A as a number of Microsoft Excel files. The precise Geodetic coordinates of datapoints referred to in the following section, that were collected along the Enasira fault, Porosita fault, Entashata fault and around the Footwall Fault Zone, are provided in files named Enasira.xls, Porosita.xls, Entashata.xls and FFZ.xls respectively.

5.2.1 Reconstruction at 0.360±0.001Ma

Since the Barajai Trachyte is exposed as a number lava sheets and ledges across an extensive area of the South Kedong region (figure 5.7), it could be used as a marker horizon to produce an accurate reconstruction of recent fault movements. In order to do this, as described in section 5.1.4, it was necessary to identify a reference datum that could be used to restore each lava ledge b ack to i ts original position at the time of eruption. As the Barajai Trachyte exposure located in the immediate hangingwall to the Taritik fault is relatively unaffected by recent deformation, GPS positional data collected along the upper surface of this flow provides valuable information on the pre-existing gradient down which the trachyte originally flowed. In order to construct an average datum surface, that was representative of the entire region, it was also necessary to define a second area that had not suffered significant deformation since deposition of the Barajai Trachytes. Though the small exposure of Barajai Trachyte located at the southern tip of the Enasira fault has certainly been cut by faulting, its position towards the tip of the fault means that the amount of subsequent displacement is limited. For the purposes of the current study, the position and elevation of this latter flow region was also taken to be representative of the palaeo-topography.

Given the two areas where the elevation of the landsurface is known at the time of Barajai Trachyte deposition, it was possible to construct an average topographic gradient down which the lava flowed at ~0.360±0.001Ma. In order to make the construction, two manually recorded GPS points of known accuracy were selected from each area, one from the surface of the trachyte flow at the base of the Taritik fault (kpoint 007; see Appendix A – Enasira.xls for the

precise location of this point) and the second from the flow at the tip of the Enasira fault (qpoint 001; see Appendix A – Enasira.xls). The slope of the line connecting the projections of the two points into the plane of the Enasira displacement-length profile (see figures 5.7 and 5.8) represents the regional topographic gradient down which the Barajai Trachyte would have flowed at the time of eruption – i.e. a gentle southward slope. The elevation of any point lying along this line is given by:

$$H(x) = H(qpoint001) + [(L(qpoint001) - L(x)) \cdot \tan(\theta_1)] \tag{5.1}$$

And $\tan(\theta_1) = [H(kpoint007) - H(qpoint001)] / [L(qpoint001) - L(kpoint007)]$ \hfill (5.2)

Where: $H(x)$ is the elevation at point x, $H(qpoint001)$ is the elevation at qpoint001, $H(kpoint007)$ is the elevation at kpoint007, $L(x)$ is the latitude of point x, $L(qpoint001)$ is the latitude at qpoint001 and $L(kpoint007)$ is the latitude at kpoint007.

Inputting the positional values of the two control points into (5.1) gives:

$$H(x) = 1131.73 + (1.41 - L(x)) \cdot 2035.42 \tag{5.3}$$

Given the position and magnitude of the average palaeoslope, it was possible to restore the various exposures of Barajai Trachyte lava, which have been displaced by recent fault movements, back to their initial positions along the datum. Each fault reconstruction will now be considered in detail.
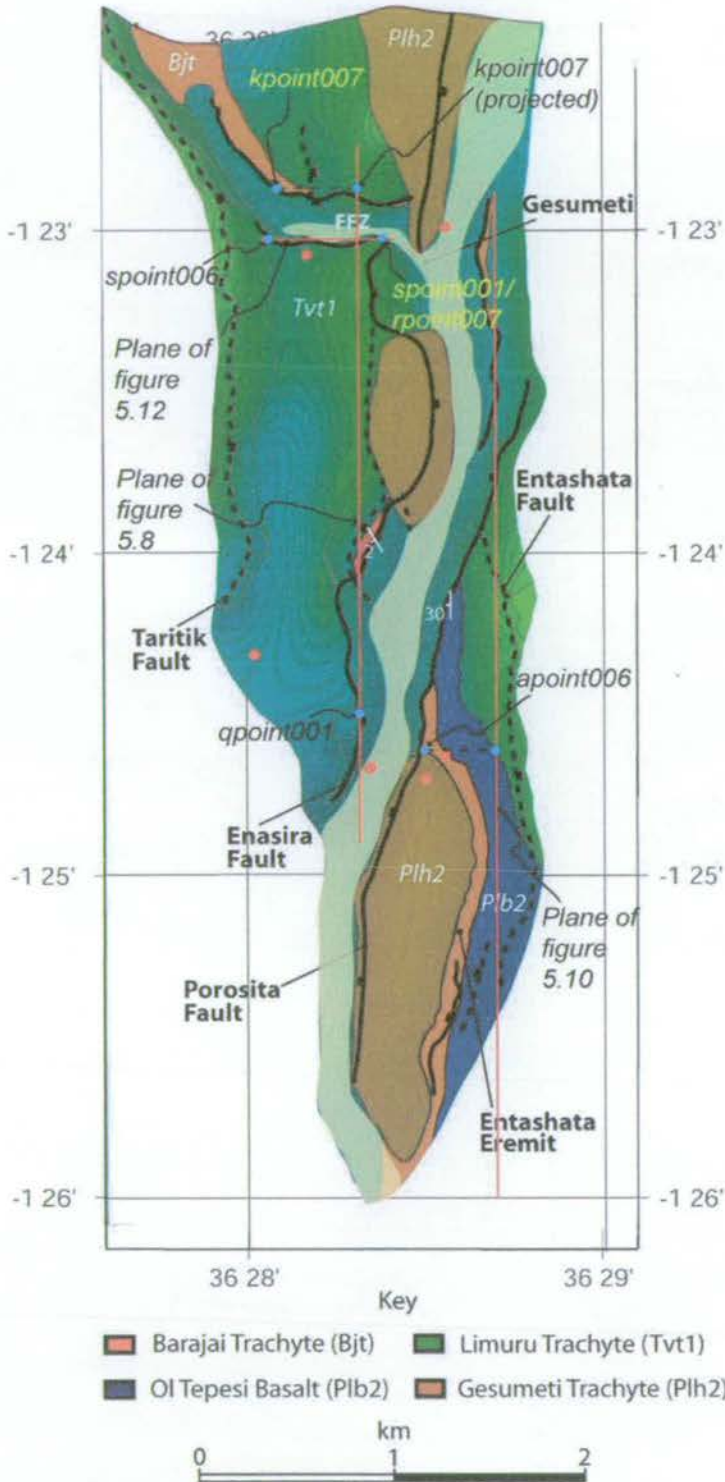
Figure 5.7 Geological map of the South Kedong region replotted from figure 4.9. Solid black lines indicate active faults while dashed black lines are faults that are inactive at present. Pale blue dots represent GPS positional points described in the text. Red lines are lines of section into which positional data have been projected to create the displacement-length profiles in the figures indicated.
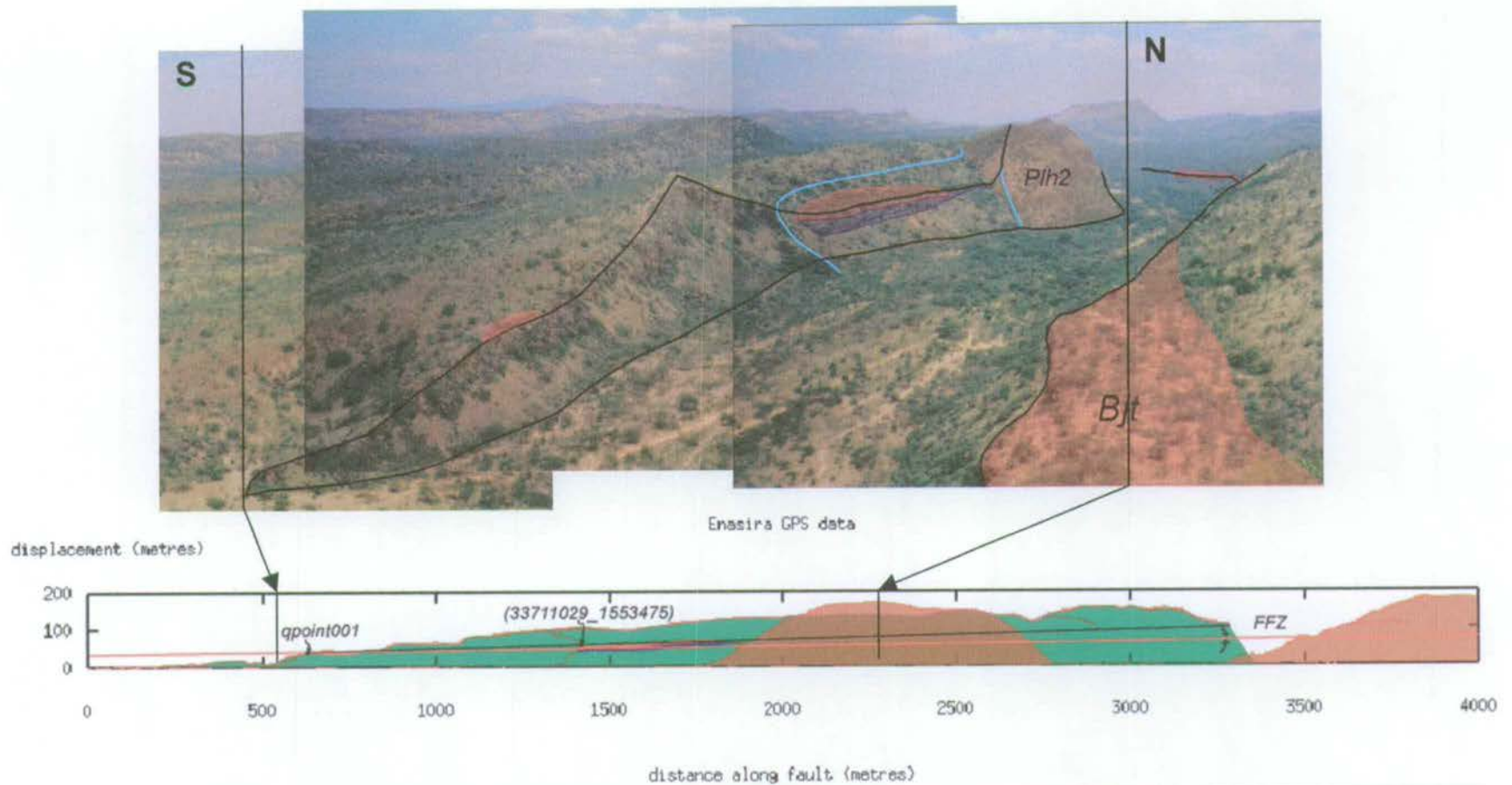
Figure 5.8 Photomontage and true-scale displacement-length profile along the Enasira fault, modified from figure 4.11. Above: Black lines on the photograph represent lines of active faulting within the last 0.360±0.001Ma. Pale blue lines are older, now inactive, fault lines, the longest of which is the tip of the Porosita Hill fault (see section 5.2.3). An explanation of the geological motif is given in figure 3.7. Below: Black line in the d/L profile – construction line, red line – Barajai Trachyte datum as described in section 5.2.1.

a) The Enasira fault

As described in section 4.3.2, two narrow ledges of Barajai Trachyte lava are attached to the face of the Enasira fault scarp. The Enasira fault's displacement-length profile, showing the locations of these lava ledges and construction lines for the following fault restoration, is replotted in figure 5.8. The small exposure located at the southern tip of the fault had already been used to construct the position of the lava datum, as discussed above, and therefore was maintained as a fixed reference point during the fault reconstruction. As can be seen from figure 5.8, the larger exposure of trachyte, located at the centre of the profile, is currently at a higher elevation than the proposed datum horizon. Field evidence shows that movement on a small-scale fault associated with the Gesumeti Trachyte horst block has deformed the northern end of this exposure. This accounts for the slight upwardly-curved appearance of the flow on the GPS profile. However, in general, the upper surface of this lava ledge lies roughly along a straight line connecting the reference point (qpoint001) with the point of intersection between the southern footwall fault and the Enasira fault scarp (rpoint007; see Excel file Enasira.xls, Appendix A). Figure 5.8 shows that the operation required to position the lava ledges along the datum line is a rotation centred about the reference point at the southern tip of the fault. However, in order to accurately perform this operation it is necessary to have a good control on the position of the construction line. A useful control point is located at the southern edge of the main lava ledge (automatically recorded GPS point with ID tag: 33711029_1553475 (see Appendix A - Enasira.xls)). The advantage of this area is that deformation and erosion has not substantially affected the lava flow and the positional control is excellent.

The final phase of the reconstruction is to rotate all the positional data along the scarp by the same amount as that required to rotate the construction line on top of the datum.

The equation for the construction line is given by:

$$H(x) = H(qpoint001)+[(L(qpoint001)-L(x))\cdot\tan(\theta_2)] \quad\quad (5.4)$$

And:

$$\tan(\theta_2)=[H(33711029\_1553475)-H(qpoint001)]/[L(qpoint001)-L(33711029\_1553475)] \quad (5.5)$$

Where: H(x) is the elevation at point x, H(qpoint001) is the elevation at qpoint001, H(33711029_1553475) is the elevation at autopoint 33711029_1553475, L(x) is the latitude of point x, L(qpoint001) is the latitude at qpoint001 and L(33711029_1553475) is the latitude at autopoint 33711029_1553475.

The difference between elevations located along the construction line (given by 5.4) and elevations on the reference datum (given by 5.3) simplifies to:

$$\Delta H(x) = [(L(qpoint001)-L(x)).\tan(\theta_1)]-[(L(qpoint001)-L(x))\cdot\tan(\theta_2)] \tag{5.6}$$

Where: $\Delta H(x)$ is the height difference between the lines at point x.

Hence, transformation of the GPS positional points was achieved by subtracting (5.6), at any point x, from the present elevation at point x. As the datum represents the palaeo landsurface, only data points located above the datum after transformation represent topography in existence at time of Barajai Trachyte deposition. Other points were fixed to lie along the datum.

As described in section 5.1.4, by establishing a reference datum it is possible to determine amounts of footwall uplift and hangingwall subsidence along strike. The above reconstruction suggests a footwall uplift to hangingwall subsidence ratio in the order of ~1:2. Even taking into account a thin veneer sediment in the hangingwall to the Kedong graben, this value is substantially smaller than that of 1:6 documented from neotectonic studies (e.g. Stein and Barrientos, 1985; Barrientos *et al.*, 1987) and more in line with a value of 1:1.4 as determined from the Entashata Fault (see section 5.2.4).

For the purposes of this reconstruction, the elevations of GPS points collected along the northern segment of the Enasira scarp, to the north of the Footwall Fault Zone, were not modified from their present positions because there are no Barajai Trachyte lavas onlapping this section of the fault. Although it appears to be somewhat arbitrary, this decision is supported by further evidence from the northern wall of the Footwall Fault Zone which suggests that it is reasonable to maintain the northern section of the Enasira scarp in its present position (see section 5.2.1c).

A displacement-length profile for the Enasira scarp at 0.360±0.001Ma is shown in figure 5.9. This plot clearly illustrates the independent nature of the two fault segments making up the southern section of the Enasira scarp, separated by an obvious topographic low.
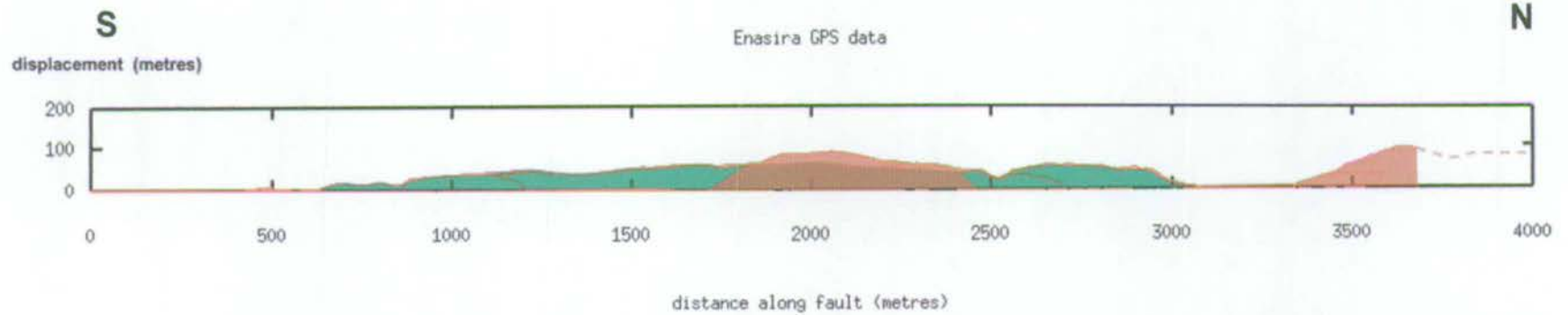
Figure 5.9 Reconstruction of the Enasira fault at 0.360±0.001Ma. At this time the scarp consisted of two independent fault segments separated by a topographic low between x=3000-3500. Dashed line indicates the approximate continuation of the Enasira fault towards the north

b) The Porosita fault

Figure 5.10 shows the Barajai Trachyte datum overlain on the displacement-length plot of the Porosita scarp redrawn from section 4.3.1. Where it is exposed at the face of the scarp, the upper surface of the Barajai Trachyte dips gently towards the south with a gradient equivalent to that of the datum horizon, though it is now elevated above datum level.

Restoration of the scarp was achieved by reducing the elevations of all the GPS data along the Porosita profile by a figure of 18m, which represents the height difference between the trachyte datum and the upper surface of the Barajai Trachyte at the position of flow onlap onto the Gesumeti Trachyte horst block (marked apoint006 on figure 5.10; see Appendix A – Porosita.xls). This control point, located on the upper surface of the trachyte flow, was chosen because of the uniform nature of the flow surface at this location as compared with that at the northern end of the exposure, which was generally more eroded and covered in vegetation. Vertical translation of the data points by this method produces a good fit along the majority of the Barajai Trachyte flow surface.

As with the Enasira scarp, any GPS points lying below the trachyte datum line, following the restoration procedure, represent parts of the fault that were below the groundsurface at 0.360±0.001Ma. These points were either ignored or their elevations were altered to lie along the datum horizon.

A reconstruction of the Porosita displacement-length profile at 0.360±0.001Ma is shown in figure 5.11. This plot shows the location of the Porosita horst in front of the Entashata Eremit flow conduit and the backtilted Entashata footwall block. Displacements are plotted relative to the Barajai Trachyte datum horizon.
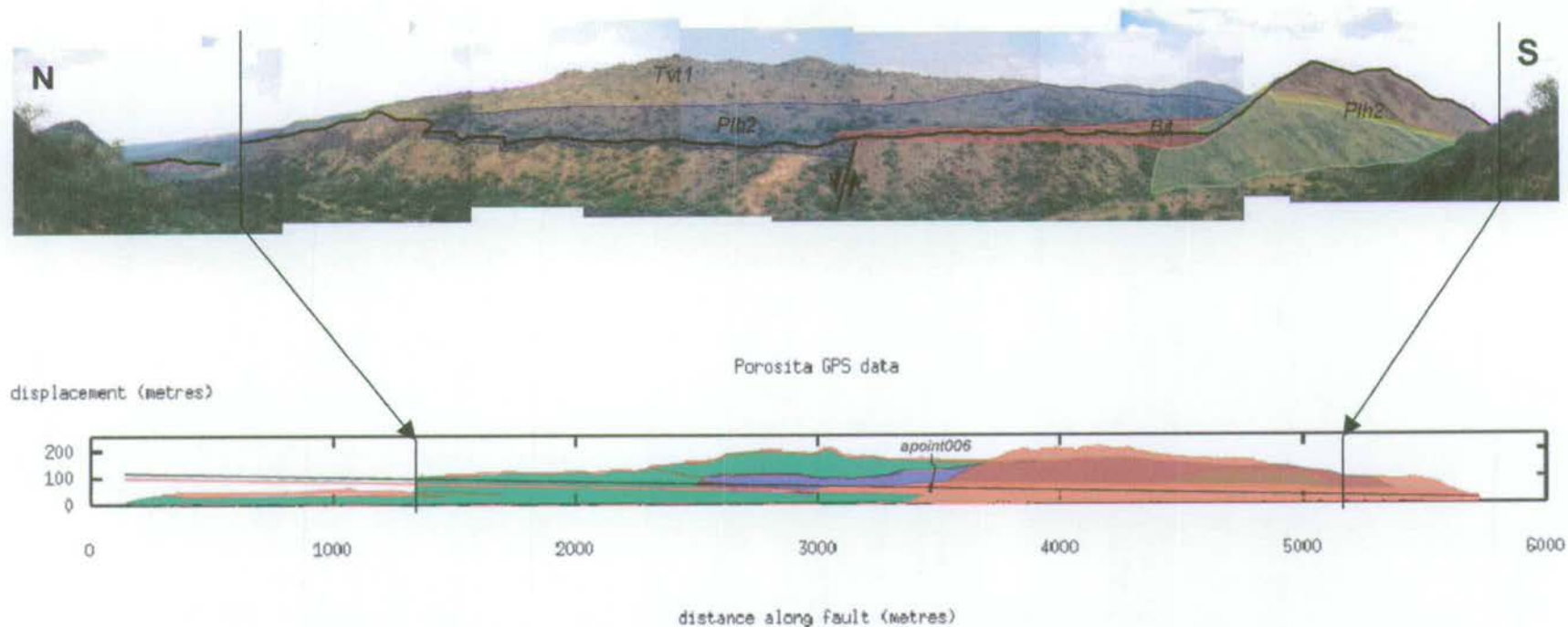
Figure 5.10 Photomontage (above) and true-scale displacement-length profile (below) along the Porosita fault as modified from figure 4.12. Below: Black line on the d/L profile – construction line, red line – Barajai Trachyte datum as described in section 5.2.1.

N
S

displacement (metres)

Porosita GPS data

200
100
0

0   1000   2000   3000   4000   5000   6000

distance along fault (metres)
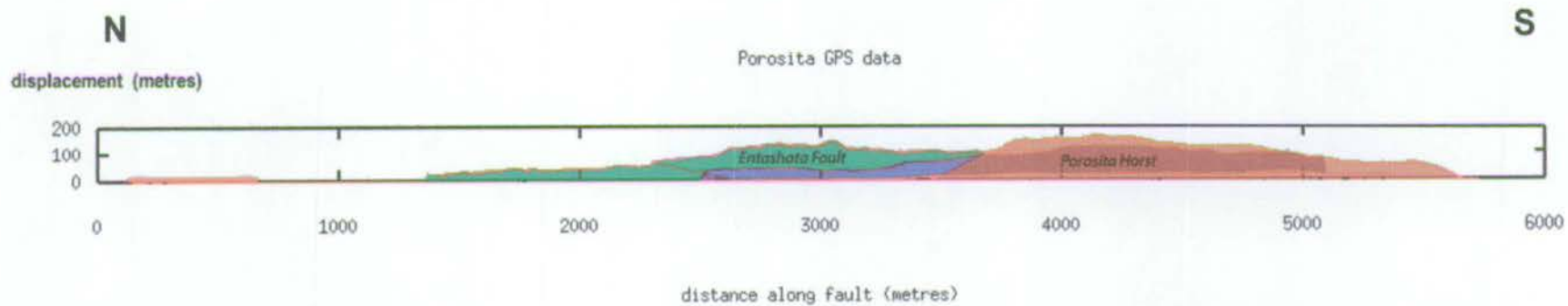
Figure 5.11 Reconstruction of the Porosita and Entashata fault scarps at 0.360±0.001Ma. Displacements plotted on the y-axis are relative to the Barajai Trachyte datum.

c) The Footwall Fault Zone

Reconstruction of movement along the Footwall Fault Zone was achieved by a similar approach to that used in section 5.2.1a. The presence of a Barajai Trachyte lava ledge on the crest of the northern footwall fault indicates that the majority of displacement on the fault zone occurred after 0.360 ± 0.001Ma. As described in section 4.3.2, displacements along the southern wall of the fault graben are at a maximum at the point of intersection with the Enasira scarp and slowly decrease to zero against the Taritik fault (figure 5.12). It is therefore possible to treat the reconstruction as a simple rotation around a fixed point at the western end of the fault, which lies on the Barajai Trachyte datum. In order to perform the operation, two GPS points were selected from the traverse taken along the crest of the fault scarp, one at the intersection point with the Enasira scarp (spoint001 (see Appendix A – FFZ.xls)) and the other at the base of the Taritik scarp (spoint006 (see Appendix A – FFZ.xls)), which was considered to be fixed. The construction line connecting these points and the position of the Barajai Trachyte datum is shown in figure 5.12. The slope of the line is given by:

$$\tan(\theta_3)=[H(spoint001)-H(spoint006)]/[L(spoint001)-L(spoint006)] \qquad (5.7)$$

Where: $\tan(\theta_3)$ is the slope of the construction line, H(spoint001) is the elevation at spoint001, H(spoint006) is the elevation at spoint006, L(spoint001) is the latitude at spoint001 and L(spoint006) is the latitude at spoint006.

The operation required to rotate the construction line to the position of the trachyte datum is given by:

$$H(x)_{0.360} = H(x) - [(L(x)-L(spoint006))\cdot\tan(\theta_3)] \qquad (5.8)$$

Where: $H(x)_{0.360}$ is the height at point x at 0.360 ± 0.001Ma (after transformation), H(x) is the elevation at point x and L(x) is the latitude of point x.
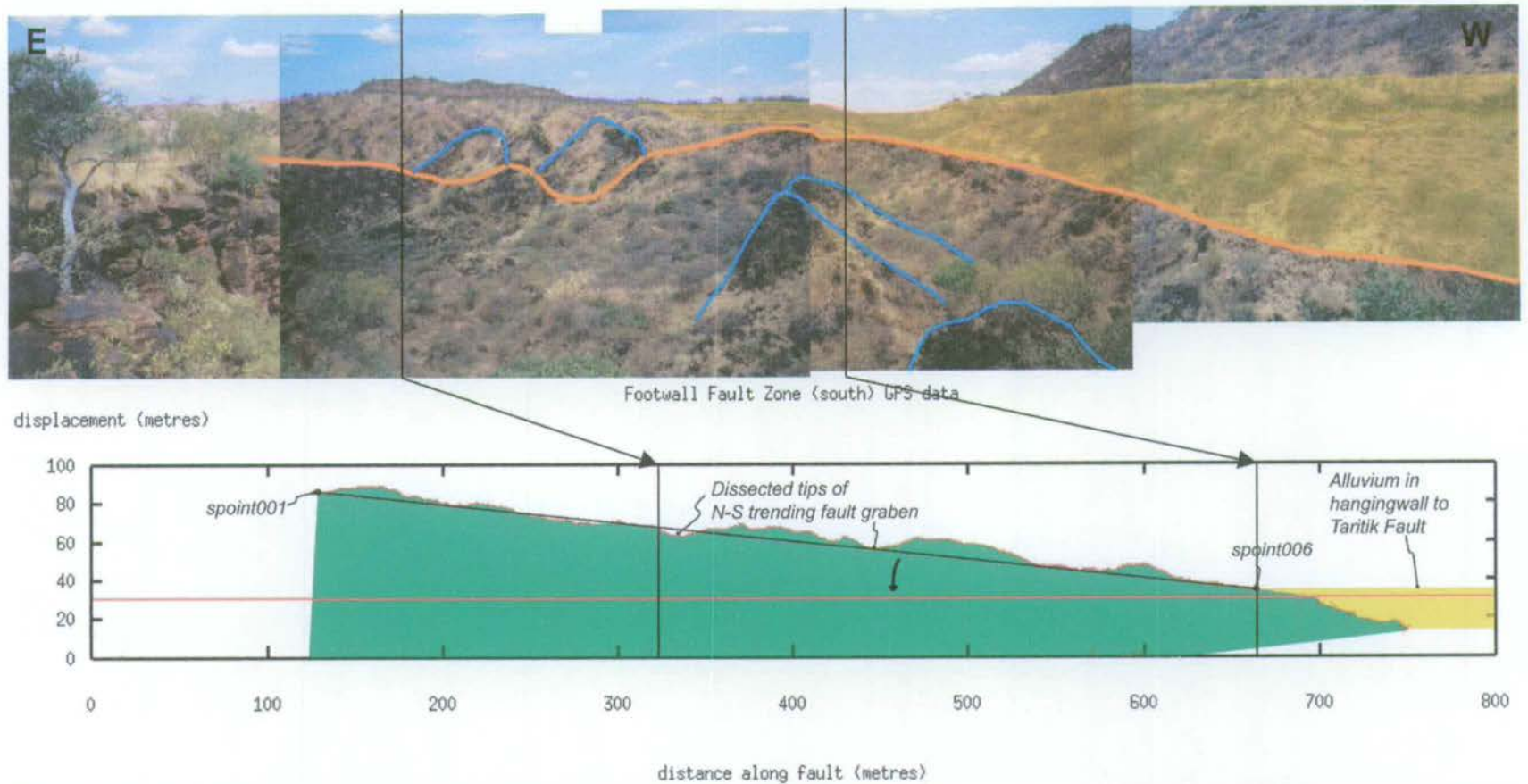
Figure 5.12 Photomontage (above) and displacement-length profile (below) along the southern Enasira footwall fault. Above: An explanation of photograph annotations is given in figure 4.19. Below: Annotated GPS points are used to define a construction line (indicated in black) along which points of the GPS crestal traverse are rotated to the level of the Barajai Trachyte datum (shown as a solid red line). Points collected on the floor of the FFZ graben are similarly raised to the level of the datum line.

It is important to note that while the southern wall of the footwall fault graben shares a common line of intersection with the southern segment of the Enasira fault, the method used for its reconstruction is entirely independent of that used for the Enasira scarp. Therefore, a useful check on the internal consistency of these restorations is to compare the relative height values for the GPS point collected at the position of intersection of the two scarps (labelled as rpoint007 on the crest of the Enasira fault (Appendix A – Enasira.xls) and spoint001 on the southern footwall fault (Appendix A – FFZ.xls)):

	Elevation before restoration	Elevation after restoration
Enasira (rpoint007)	1215.45±0.08m	1181.24±2.06m
Footwall fault (spoint001)	1215.30±0.08m	1181.09±3.19m

Both results are very similar and within prescribed error of each other and the value predicted from the datum line (=1179.60m). The magnitude of the above error values vary according to whether the elevations are prior to, or post, fault restoration. Error values reported prior to fault restoration (±8cm in terms of elevation at the 68% (1σ) confidence level) represent the analytical error of the differential GPS system. Errors after restoration represent the standard deviation of the GPS points away from the construction lines described above. In the case of the Enasira scarp, the 'best-fit' error of ±2.06m is the standard deviation of elevations collected along the upper surface of the Barajai Trachyte ledge, away from the construction line joining qpoint001 with rpoint007. Similarly, the standard deviation of elevations away from the line connecting spoint001 and spoint006 on the southern wall of the Footwall Fault Zone is ±3.19m (see also section 5.1.7a).

The observed difference in displacement of rpoint007 (106±4m) in figure 5.8 as compared with spoint001 (87±4m) in figure 5.12 is due to the height difference between the floor of the Kedong Graben and the floor of the Footwall Fault Zone, both of which are used as the datum surfaces in the respective displacement-length profiles. As described in section 4.3.2, the floor of the FFZ is currently raised above the floor of the Kedong Graben as a result of segment linkage along the Enasira fault. This observation accounts for the majority of the 19m difference in displacement between the two plots, though a portion may be due to errors (up to ±4m in terms of elevation) on datapoints collected along the floor of the FFZ, where the narrowness of the graben obscured the view of the sky.

The most significant displacement along the Footwall Fault Zone appears to have been associated with the southern fault. Movement along the northern wall of the zone has largely been confined to the extreme eastern end of the fault as a reactivation of the Gesumeti Trachyte horst block along the northern segment of the Enasira scarp. Hence, while the southern segment of the Enasira scarp moved as a broad, coherent block that was backtilted towards the west as part of a half-graben against the Taritik fault, deformation along the northern fault segment appears to have been confined to reactivation of the pre-existing Gesumeti Trachyte horst block at the front of the Enasira scarp. As such, the Barajai Trachyte lava blanketing the western section of the northern footwall fault appears not to have been significantly affected by faulting since the time of lava deposition. The narrow, triangular-shaped lava ledge located towards the eastern end of the scarp has suffered some minor deformation associated with localised movement along the Enasira scarp. However, the upper surface of this flow has only been uplifted a maximum of 6-7m above the level predicted from the trachyte datum at that point. It was therefore decided to keep the northern wall of the fault zone fixed at its current elevation during restoration of fault movements across this region.

To take account of the apparent subsidence along the floor of the footwall fault graben, GPS positional data collected from this area were set to lie along the trachyte datum horizon. As discussed in section 4.3.1, this can only be regarded as 'apparent' subsidence since the base of the graben is covered by an unknown thickness of sediment.

d) The Taritik fault

In order to make a full reconstruction of the South Kedong region at 0.360±0.001Ma, the final area to consider is the southern tip of the Taritik fault. According to fault orientation, the Taritik scarp can be subdivided into two distinct sections, a N-S orientated section, that extends for ~2.1km from the fault tip in the south to the intersection with the Footwall Fault Zone in the north, and a curved section of scarp that has a more NW-SE orientation and continues to the north of the footwall faults. As described in section 4.3.2, there is no evidence that this latter section of the Taritik fault has been active since eruption of the Barajai Trachyte at 0.360±0.001Ma.

Directly to the south of the Footwall Fault Zone, the Enasira block is backtilted into the hangingwall of the Taritik scarp, giving the landsurface a half-graben morphology. Though in most places filled by a 15m thickness of alluvial sediments, there is no evidence for any Barajai Trachyte deposition in the hangingwall to the southernmost section of the Taritik fault. Instead, the Barajai Trachyte flow was funnelled around to the east by the pre-existing faulted topography, through the topographic low point between the Enasira fault segments and into the precursor Kedong Graben. This indicates that the topography to the south of the Enasira Footwall Fault Zone must have acted as a barrier to the Barajai Trachyte, preventing it from flowing directly southwards between the Taritik and Enasira faults. Hence, uplift and rotation of the southern segment of the Enasira fault was in evidence prior to 0.360±0.001Ma.

As described in section 4.3.2, the hangingwall to the Taritik fault is cross-cut by a small east-west orientated scarp, downthrown to the south, that acts to link the southern tip of the Taritik fault with the tip of the Enasira fault. Hence the latest phase of activity along the South Enasira fault effectively caused passive rotation of the Taritik scarp, on the back of the Enasira footwall block. However, during fault reconstruction, GPS data collected along this rotated section of the Taritik scarp were maintained at their present-day elevations. Since both the Enasira and Taritik faults are connected across strike, this is obviously an oversimplification, as movements along the Enasira fault would have caused some uplift of the Taritik fault. The essential problem with reconstructing this area is that the lack of Barajai Trachyte lavas makes it difficult to place any constraints on fault movements. Such problems arise wherever there is an inadequate exposure of a marker horizon (see also section 5.2.4). During the course of this study, only faults whose growth history could be accurately constrained from lava marker horizons have been individually analysed and plotted on displacement-length profiles. Faults that are less well constrained have been included in the GMT-based plots for completeness, but their positional data cannot be relied on for estimates of displacement rates.

5.2.2 GMT plot at 0.360±0.001Ma

Positional data (latitude, longitude and ellipsoidal elevation) along each restored GPS traverse were assembled into a single text file and plotted up in GMT to show the topography of the South Kedong region at 0.360±0.001Ma (figure 5.13). In figure 5.14 the topographic plot has been overlain with transparencies showing the geology as determined from field observations.

The advantage of showing topographic elevations, on a plot such as this, is the information it provides on the regional southward gradient underlying the local fault-generated topography. This slope is a representation of the Barajai Trachyte datum, or 'palaeo-landsurface', that controlled the southward flow of the Barajai Trachyte lavas subsequent to their eruption from Mount Suswa. The obvious major disadvantage is that absolute elevation values are extremely difficult to determine accurately since they may be influenced by variables outside of the scope of the available data. Movement associated with large faults outside of, but in close proximity to, the study area, such as along the Esageri and Kedong faults to the east and north respectively (see figure 3.4), will alter elevations across the South Kedong region by an unknown amount. More importantly, the above reconstruction has been based on the assumption that the control points used for construction of the Barajai Trachyte datum are fixed in time and space. Though the lack of displacement along the Taritik fault suggests that this is probably acceptable for kpoint007 (figure 5.7), qpoint001 is another matter. This latter point was selected because its proximity to the tip of the Enasira fault would limit the amount of displacement it could have experienced. However, alluvial sediments blanketing the floor of the Kedong Graben make it difficult to accurately locate the position of the fault tip and hence qpoint001 will certainly have been uplifted to some extent during this most recent phase of faulting.

An alternative method of presenting the data, that is less sensitive to absolute changes in elevation, is in the form of a relief plot. These plots have been constructed relative to a fixed datum and are therefore immune to external elevation changes. A relief plot of the South Kedong region at 0.360±0.001Ma is shown in figure 5.15. The datum surface for this plot is the projection, into three dimensions, of the datum horizon given in equation (5.3). Figure 5.16 shows the same plot overlain by a geological motif.

Both GMT-based plots show the steep-sided fault-generated topography that characterised the South Kedong Graben at 0.360±0.001Ma. The Barajai Trachyte flowed into the region from the north, utilising the pre-existing topographic lows in the hangingwall to the Taritik and Enasira faults. In the floor of the Footwall Fault Zone (FFZ), the lava was diverted to the east and into the hangingwall to the Enasira fault. Further to the south, the flow bifurcated around the Porosita horst block such that part of the lava flowed down the pre-cursor Kedong Graben while another part flowed along the Entashata Eremit half-graben to the southeast. As the Trachyte

exited onto the Oltepesi Plain then, with the reduced gradient, it began to pond, causing the formation of flow surface crinkles.

Between 0.360±0.001Ma and recent, movement along the Porosita and Enasira faults lowered the floor of the Kedong Graben and resulted in formation of the Footwall Fault Zone (FFZ). Nucleation of an E-W orientated fault, located approximately 1km to the south of the FFZ, hard-linked the southern tip of the Taritik fault to the tip of the Enasira fault. This created a single, west-tilted fault block bound to the east by the Enasira fault and to the west by the northern section of the Esiteti fault (see figure 3.5).
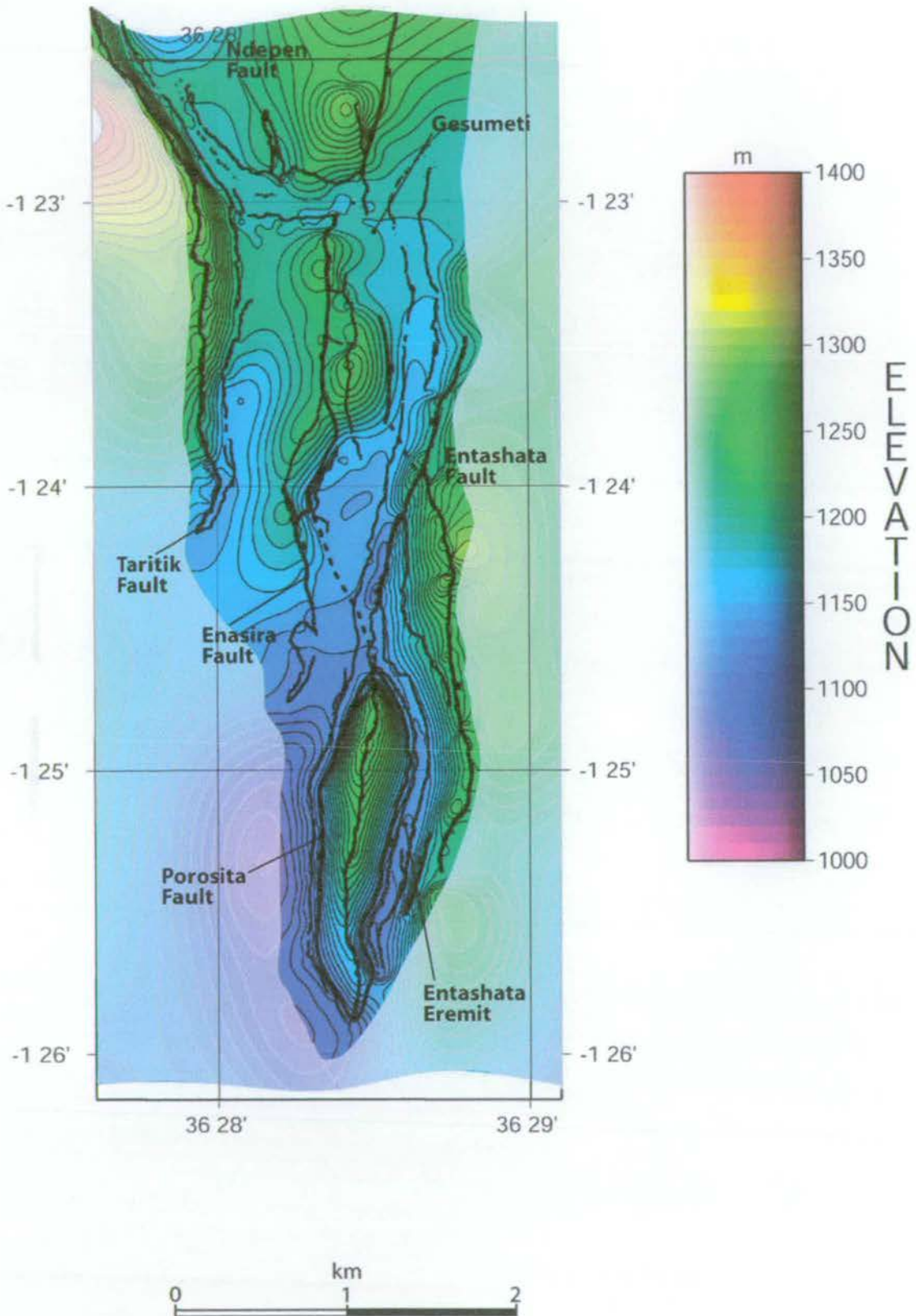
Figure 5.13 Topographic map of the South Kedong region at 0.360±0.001Ma. The map is plotted in GMT from restored GPS traverses, as described in section 4.3.1. Black lines indicate the location of normal faults, where solid lines are faults active at 0.360±0.001Ma and dashed lines are faults that became inactive by 0.360±0.001Ma.
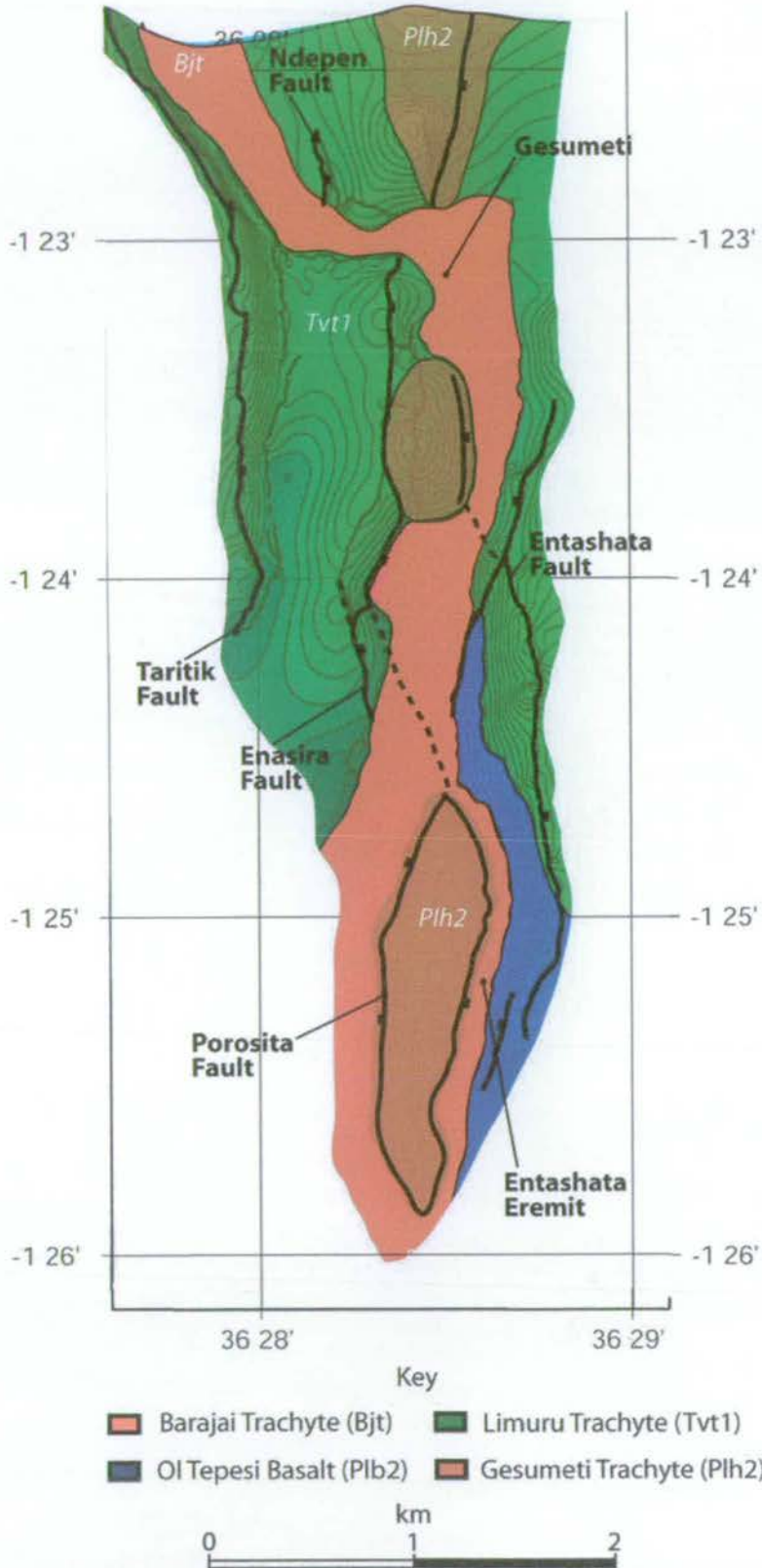
Figure 5.14 Geological map of the South Kedong region at 0.360±0.001Ma as an overlay on figure 5.13.
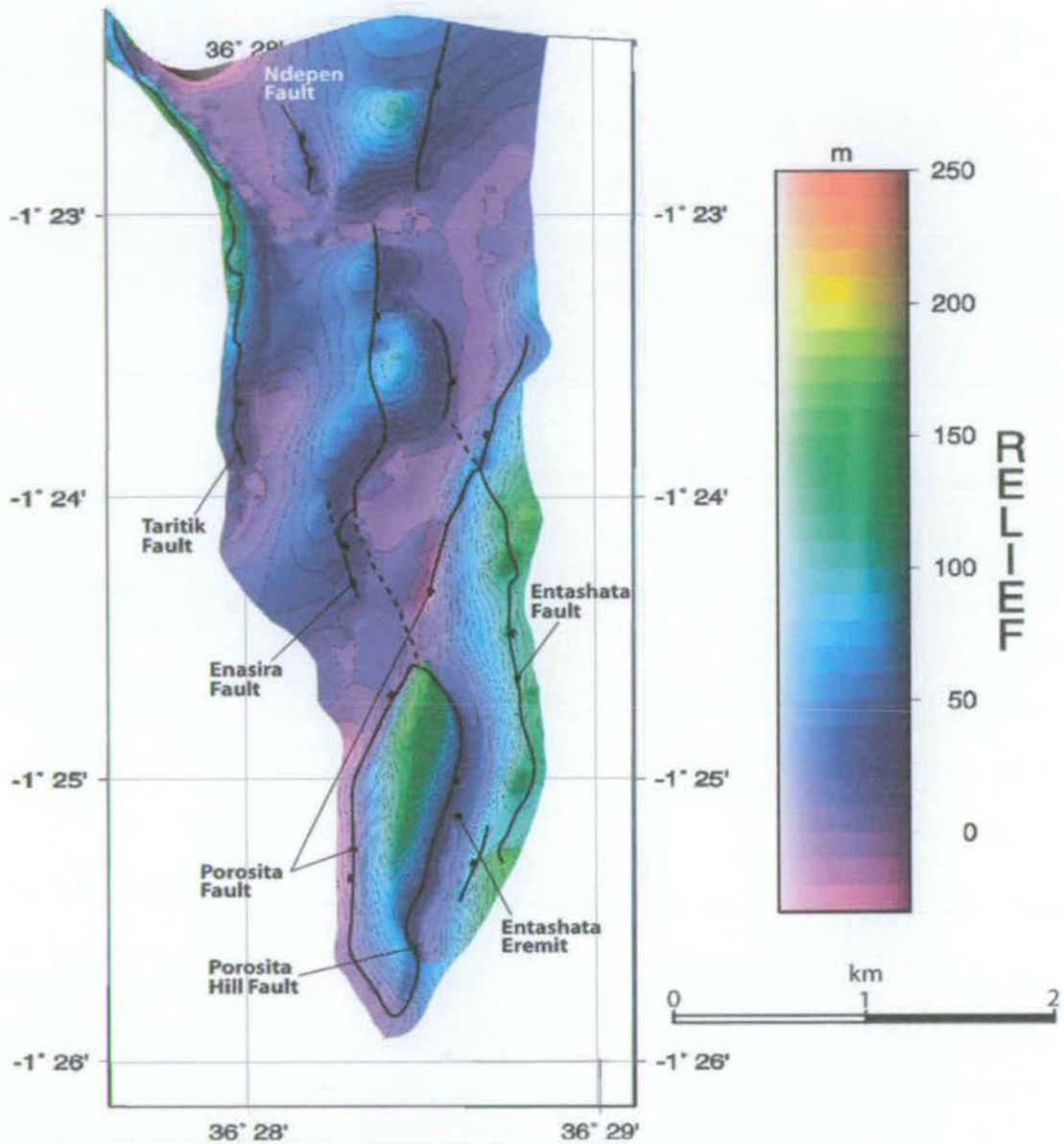
Figure 5.15 Plot of relief above the Barajai Trachyte datum surface at 0.360±0.001Ma. As with figure 5.13, this plot was constructed using restored GPS traverses. White mask hides regions of limited data coverage.
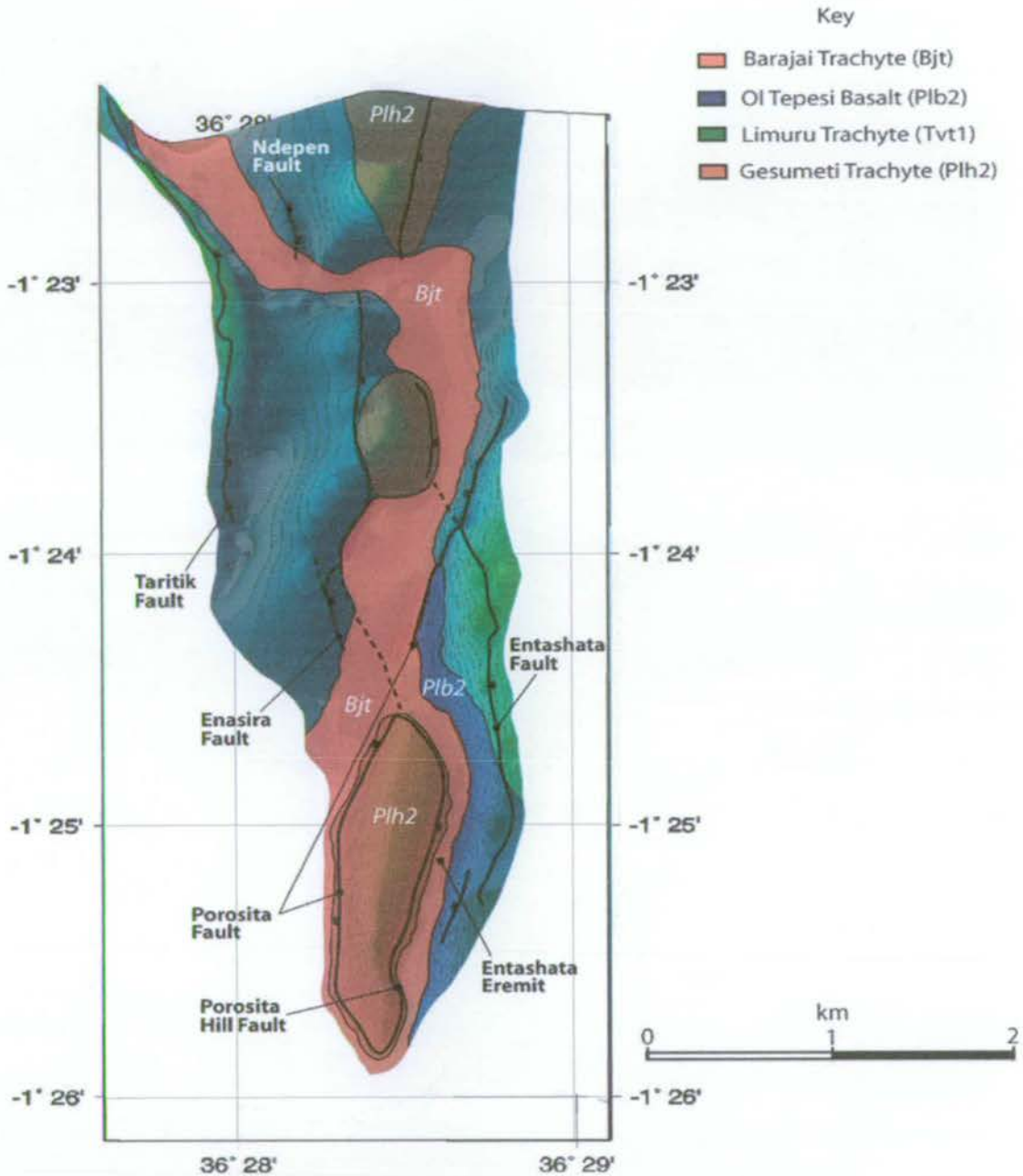
Figure 5.16 As figure 5.15 but with an overlay showing the geology of the South Kedong region at 0.360±0.001Ma. At this time the Barajai Trachyte lava flowed from Mount Suswa into the Kedong Graben by utilising low topography in the hangingwalls to pre-existing fault scarps.

5.2.3 Reconstruction at 1.478±0.003Ma

Any fault reconstruction is only as good as the marker horizon used to restore the tectonic deformation. The Ol Tepesi Basalt (dated at 1.478±0.003Ma-see chapter 3) is another thin lava flow that onlaps and mantles pre-existing fault blocks and yet has been displaced by later fault movements. It is, however, less areally extensive than the Barajai Trachyte, being largely confined to the southeast of the South Kedong region. The Ol Tepesi Basalt therefore offers valuable information, in particular, on the growth of the Entashata fault, but is less useful for reconstruction of some of the more distant faults. However, it is certainly possible to draw inferences about the general structure of the South Kedong Graben at 1.478±0.003Ma.

The method employed to create the reconstruction at 1.478±0.003Ma is based loosely on that used in the previous section, though in this case the input values are the transformed positional data used for the 0.360±0.001Ma restoration.

a) Construction of datum

Again, to construct a datum for the Ol Tepesi Basalt, it is necessary to locate an area of the flow that has not undergone significant deformation since deposition. The basalt is exposed in two major localities, the first as a narrow ledge, directly underlying a flow of Barajai Trachyte, attached to the southern segment of the Enasira scarp, and the second on the back of the tilted Entashata footwall block (see figure 5.17). Where the flow has been cut by movement along the Porosita fault, it is observed to have an almost constant thickness of approximately 10m, which indicates that the lava was erupted onto a roughly horizontal surface prior to being backtilted by movement along the Entashata fault. The location and relatively small areal extent of this lava suggests that it was confined to a narrow NW-SE trending depocentre, roughly in the same position as Entashata Eremit, but which extended further towards the northwest where it merged with the precursor Enasira fault. This qualitative interpretation is based largely on field exposures of the basalt and the location of early NW-SE trending fault scarps, described in section 4.3.2, that have been cross-cut, more recently, by reactivation along the N-S trending Enasira fault. Interpolating between the basalt exposures, across the position of the Kedong Graben at 0.360±0.001Ma, shows the possible original extent of the Ol Tepesi Basalt and the locations of the pre-existing NW-SE trending faults (figure 5.17). The more southerly of these

structures forms the natural continuation of the curved fault that bounds the eastern margin of the Porosita horst block (from here on named the Porosita Horst fault), while to the north, an extension of the Entashata fault intersects with the large Gesumeti Trachyte block on the Enasira scarp. A likely scenario is that movement along both faults was responsible for forming the half-graben geometry of Entashata Eremit and caused tilting of the Ol Tepesi lavas through fault-block rotation. Field studies show that the dip of the basalt horizon changes substantially between the two principal exposures. Along the rotated footwall block of the Entashata fault, the lavas dip fairly consistently at 30 degrees towards the west or southwest, depending on the along-strike fault location, whereas to the west, along the Enasira fault, the basalt dip is insignificant (~2 degrees, based on the vertical offset of GPS points), especially after reconstruction of the fault at 0.360±0.001Ma. The reason behind these variations is a rapid decrease in displacement along the controlling faults as they merge with, or die out against, the Enasira fault. The original northward extension of the Entashata fault, which has since been downthrown by formation of the Kedong Graben, is likely to have tipped-out completely against the rigid Gesumeti Trachyte block that would later form part of the Enasira fault. Similarly, displacement along the Porosita Horst fault decreases westward as it curves sharply towards the north and merges with the Enasira fault. The small amount of southward dip associated with the basalt ledge on the Enasira scarp is probably a consequence of movement along the western section of the Porosita Horst fault.
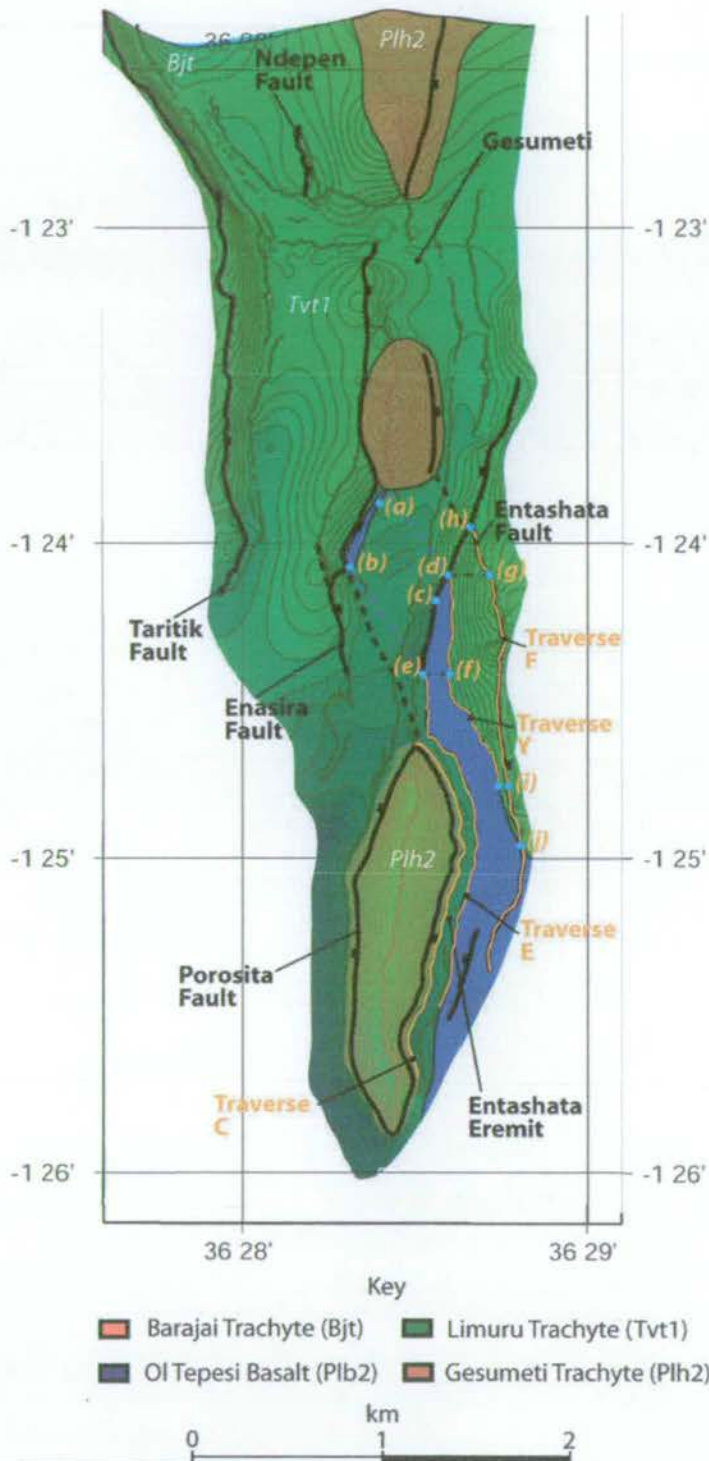
Figure 5.17 Geological map of the South Kedong region at 0.360±0.001Ma with the Barajai Trachyte lavas removed. Pale blue points indicate the locations of specific GPS points mentioned in the text: (a) lpoint009, (b) lpoint002, (c) autopoint [33711027_1142013], (d) apoint014/ypoint001, (e) apoint009, (f) autopoint [34230927_0916373], (g) autopoint [34230919_0937204], (h) fpoint001, (i) autopoint [34230919_1030543] and (j) fpoint004. Orange lines represent GPS traverses that were used during reconstruction of the Entashata fault.

Given the above information, it is possible to construct a datum horizon representing the upper surface of the Ol Tepesi Basalt immediately after eruption. Since there is evidence that the lava was deposited on a horizontal surface, only one fixed control point is needed for a restoration of the fault blocks in the South Kedong region. A suitable point is lpoint009 (Appendix A – Enasira.xls), located at the northern end of the basalt ledge on the Enasira scarp and in a position not to have experienced any uplift along the Entashata scarp (see figure 5.18). The average surface of the basalt flow can be characterised by the line joining lpoint009 with lpoint002 (located at the southern end of the ledge) (Appendix A – Enasira.xls). The geometric operation required to remove the displacement on the northern tip of the Porosita Horst fault and hence restore the Ol Tepesi Basalt ledge back to the horizontal is given by:

$$H(x)_{1.478} = H(x)_{0.360} + [(L(x)-L(lpoint009)) \cdot tan(\theta_4)] \tag{5.9}$$

$$\text{and } tan(\theta_4) = [H(lpoint009)-H(lpoint002)]/[L(lpoint002)-L(1point009)] \tag{5.10}$$

Where: $H(x)_{1.478}$ is the elevation at point x at 1.478 ± 0.003Ma, $H(x)_{0.360}$ is the elevation at point x at 0.360 ± 0.001Ma, H(lpoint002) is the elevation at lpoint002, H(lpoint009) is the elevation at lpoint009, L(x) is the latitude of point x, L(lpoint002) is the latitude at lpoint002 and L(lpoint009) is the latitude at lpoint009.

Unfortunately, while the above reconstruction provides a useful insight into movement on the Porosita Horst fault, it cannot supply any information as to the relative displacements along other fault segments that make up the South Enasira scarp. Due to a lack of positional information in such areas the elevations have not been adjusted from values used in the 0.360 ± 0.001Ma reconstruction.
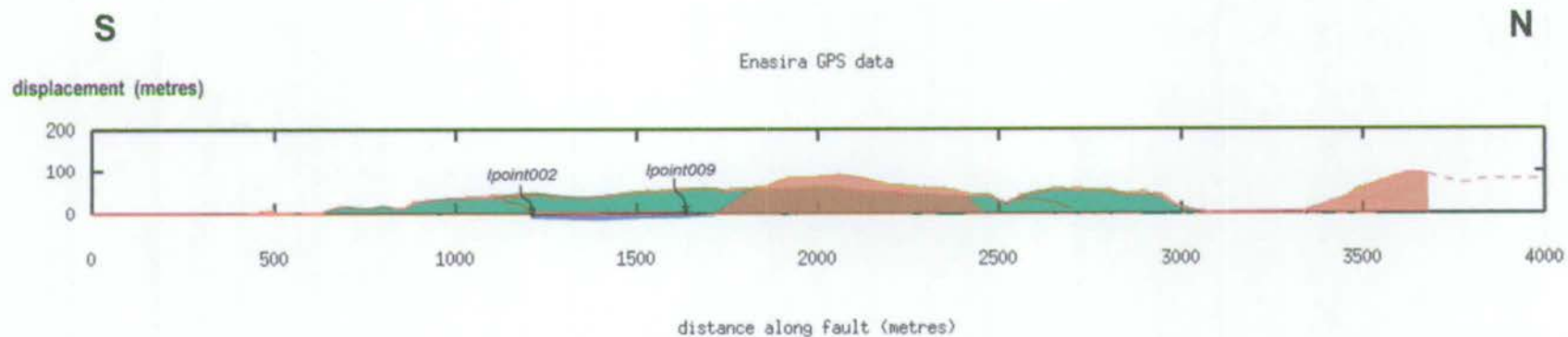
Figure 5.18 Displacement-length profile along the Enasira fault at 0.360±0.001Ma, replotted from figure 5.9. Annotated GPS points are those used in reconstruction of the scarp at 1.478±0.003Ma.

Where the Ol Tepesi Basalt is a particularly informative marker horizon is in the reconstruction of movements along the Entashata fault (see figures 5.19 and 5.20). The general procedure involves the restoration of positional points lying along the upper surface of the basalt flow, back to the horizontal datum surface. Along the crest of the Porosita scarp this consists of an operation to rotate points around a fixed pivot point that is at the same elevation as fixed-point lpoint009 on the Enasira scarp (taken as autopoint 33711027_1142013; see Appendix A – Porosita.xls)) (figures 5.17 and 5.19). Immediately to the north of the pivot, between apoint014 (Appendix A – Porosita.xls) and the projection of lpoint009, the crestal traverse is rotated in an anticlockwise direction in order to model the elevations that existed prior to substantial uplift of the Entashata footwall, after deposition of the Ol Tepesi lavas. This operation is illustrated diagrammatically in figure 5.19 and can be described in the following way:

$$H(x)_{1.42}=H(x)_{0.36} - [(L(x)-L(33711027\_1142013))\cdot\tan(\theta_5)] \tag{5.11}$$

And:

$$\tan(\theta_5) = [H(33711027\_1142013)-H(apoint014)]/[L(apoint014)-L(33711027\_1142013)] \tag{5.12}$$

Where: $H(x)_{1.478}$ is the elevation at point x at 1.478±0.003Ma, $H(x)_{0.360}$ is the elevation at point x at 0.360±0.001Ma, $H(33711027\_1142013)$ is the elevation at autopoint 33711027_1142013, $H(apoint014)$ is the elevation at apoint014, $L(x)$ is the latitude of point x, $L(33711027\_1142013)$ is the latitude at autopoint 33711027_1142013 and $L(apoint014)$ is the latitude at apoint014.
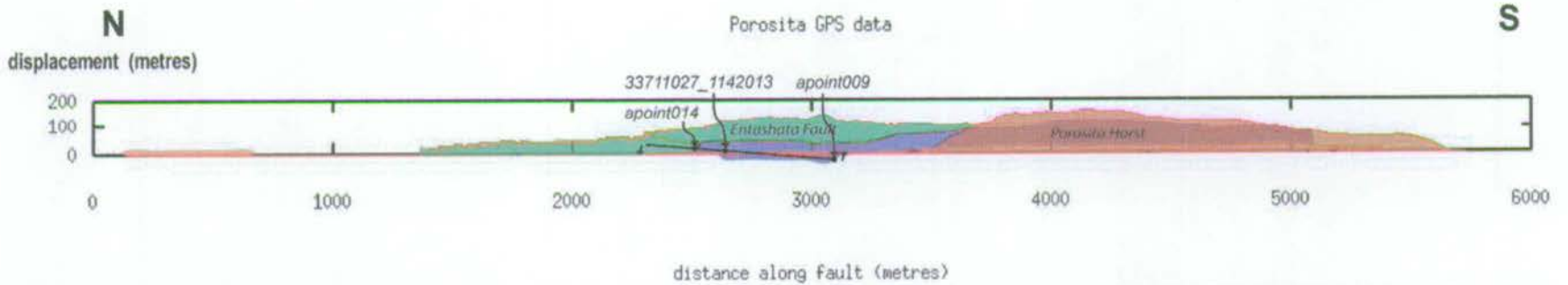
Figure 5.19 Profile of the Porosita and Entashata faults at 0.360±0.001Ma, replotted from figure 5.11 to show the rotation of GPS points used in reconstruction of the Entashata and Porosita Hill faults at 1.478±0.003Ma. Annotated GPS points are those described in section 5.2.3. The black line represents the construction line used to rotate GPS points collected along the upper surface of the Ol Tepesi Basalt back to the horizontal datum surface (shown as a solid red line).
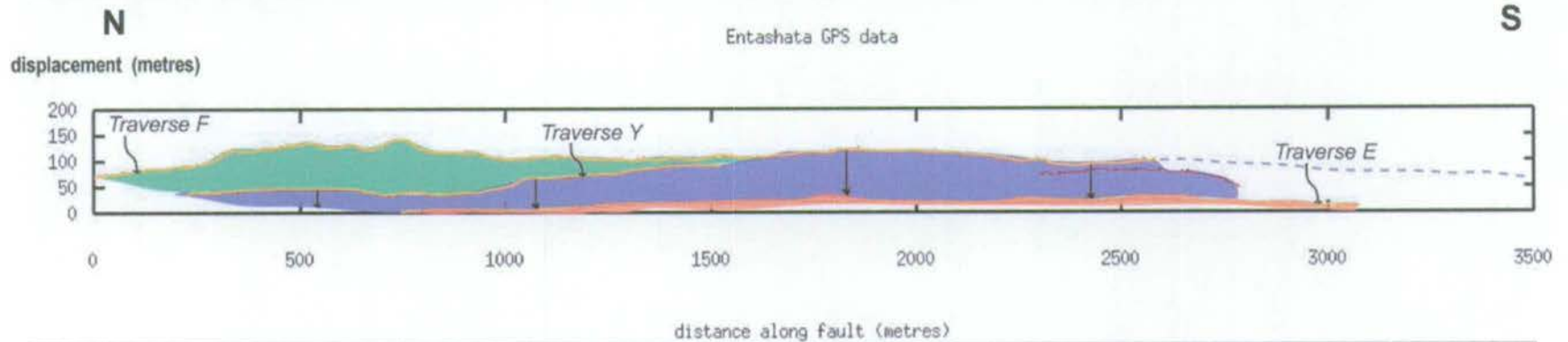
Figure 5.20 Profile along the Entashata fault at 0.360±0.001Ma, as independent from the Porosita scarp. GPS traverses indicated in orange are those also shown in figure 5.17. Vertical arrows illustrate the transformation of points lying along traverse Y during reconstruction of the Entashata fault at 1.478±0.003Ma.

To the south of the pivot point, the same traverse is rotated in a clockwise direction between the southern edge of the basalt exposure (apoint009; see Appendix A – Porosita.xls) and the projection of lpoint009 to remove the effect of hangingwall subsidence associated with the Porosita Horst fault (figure 5.19). Elevations along this section of the traverse were modified according to the following equation:

$$H(x)_{1.478} = H(x)_{0.360} - [(L(x)-L(33711027\_1142013)) \cdot \tan(\theta_6)] \tag{5.13}$$

And:

$$\tan(\theta_6) = [H(33711027\_1142013)-H(apoint009)]/[L(33711027\_1142013)-L(apoint009)] \tag{5.14}$$

Where: $H(x)_{1.478}$ is the elevation at point x at 1.478 ± 0.003Ma, $H(x)_{0.360}$ is the elevation at point x at 0.360 ± 0.001Ma, $H(33711027\_1142013)$ is the elevation at autopoint $33711027\_1142013$, $H(apoint009)$ is the elevation at apoint009, $L(x)$ is the latitude of point x, $L(33711027\_1142013)$ is the latitude at autopoint $33711027\_1142013$ and $L(apoint009)$ is the latitude at apoint009.

The Ol Tepesi Basalt exposure terminates abruptly at apoint009. Though poorly exposed, the rubbly nature of the contact and the presence of a narrow, eroded gulley suggest that the basalt is downthrown against a small fault with a similar NW-SE orientation as the Porosita Horst fault (see photomontage in figure 5.10). The footwall to this fault is heavily vegetated but is likely to consist of heavily brecciated Limuru Trachyte lavas. It is impossible to be certain as to whether movement along this fault occurred entirely after basalt deposition, since there is a lack of basalt lavas on the footwall. However, it appears to be a relatively small structure, with a minimum of 10m of displacement, which has since been buried along strike under a blanket of Barajai Trachyte. The lack of basalt on the footwall may indicate that it acted as a small dam preventing lava from flowing further towards the south. Certainly the Porosita Horst fault would have acted as a substantial barrier to the basalt flows. The result of these observations is that it is difficult to be precise as to the reconstruction of the Porosita scarp between apoint009 and the northern tip of the Porosita horst at 1.478 ± 0.003Ma. The most parsimonious model is to consider this section of the scarp as part of the backtilted footwall block of the Entashata fault by rotating elevations recorded at the base of the Barajai Trachyte flow anticlockwise according to equation (5.13), as rewritten below:

$$H(x)_{1.42}=H(x)_{0.360} - [(L(x)-L(33711027\_1142013)) \cdot \tan(\theta_6)] \qquad (5.15)$$

$$\tan(\theta_6) = [H(33711027\_1142013)-H(apoint009)]/[L(33711027\_1142013)-L(apoint009)] \quad (5.16)$$

Where: $H(x)_{1.478}$ is the elevation at point x at 1.478 ± 0.003Ma, $H(x)_{0.360}$ is the elevation at point x at 0.360 ± 0.001Ma, $H(33711027\_1142013)$ is the elevation at autopoint $33711027\_1142013$, $H(apoint009)$ is the elevation at apoint009, $L(x)$ is the latitude of point x, $L(33711027\_1142013)$ is the latitude at autopoint $33711027\_1142013$ and $L(apoint009)$ is the latitude at apoint009.

GPS positional data recorded in the Entashata Eremit half-graben make it possible to understand the lateral growth of the Entashata fault (figures 5.17 and 5.20). Since both the Barajai Trachyte lavas and alluvial sediments blanket the floor of the graben, it is impossible to discern the faulted margin of the Ol Tepesi Basalt at the base of the backtilted Entashata footwall block. However, where the contact is exposed at the face of the Porosita scarp, it directly underlies the edge of the Barajai Trachyte lava at the eastern side of the graben. The sediment cover at this locality (apoint009) does not appear to be more than ~2m in thickness and is regarded as insignificant for the purposes of this reconstruction. Hence an estimate of the subsidence along the basalt surface at the eastern margin of Entashata Eremit can be taken from the difference in elevation at apoint009 before and after the restoration produced using equation (5.13). This value has been applied as a bulk transformation of all datapoints along traverse E (shown in figure 5.17) using:

$$H(x)_{1.478}=H(x)_{0.360} + [H(apoint009)_{0.360} - H(apoint009)_{1.478}] \qquad (5.17)$$

Where: $H(x)_{1.478}$ is the elevation at point x at 1.478 ± 0.003Ma, $H(x)_{0.360}$ is the elevation at point x at 0.360 ± 0.001Ma, $H(apoint009)_{0.360}$ is the elevation at apoint009 at 0.360 ± 0.001Ma and $H(apoint009)_{1.478}$ is the elevation at apoint009 at 1.478 ± 0.003Ma. $[H(apoint009)_{0.360} - H(apoint009)_{1.478}] \sim 24$m.

It is then possible to restore the onlap contact of the Ol Tepesi Basalt against the pre-existing Entashata footwall block, according to latitude, by fixing elevation values collected along the

contact to elevation values calculated in equation (5.17) (see figure 5.20). Hence, points lying along traverse E and traverse Y at the same latitude will have identical elevations following restoration. This method takes into account the gentle southward slope of Entashata Eremit as well as the necessity for the basalt surface to have been deposited horizontally. The northern end of traverse Y, where Entashata Eremit is cross-cut by the Porosita scarp and hence there is a lack of constraint from traverse E, has been adjusted by interpolation between the last constrained value (at autopoint 34230927_0916373; see Appendix A – Entashata.xls) along the traverse (see figure 5.17) and the restored elevation of ypoint001 (Appendix A – Entashata.xls) by:

$$H(x)_{1.478} = H(ypoint001)_{1.478} + [(L(x) - L(ypoint001)) \cdot \tan(\theta_7)] \quad\quad (5.18)$$

And $\tan(\theta_7) = [H(34230927\_0916373)_{1.478} - H(ypoint001)_{1.478}]/[L(34230927\_0916373) - L(ypoint001)] \quad\quad (5.19)$

Where: $H(x)_{1.478}$ is the elevation at point x at 1.478 ± 0.003Ma, $H(ypoint001)_{1.478}$ is the elevation at ypoint001 at 1.478 ± 0.003Ma, $L(x)$ is the latitude of point x, $L(34230927\_0916373)$ is the latitude at autopoint 34230927_0916373 and $L(ypoint001)$ is the latitude at ypoint001.

Similarly, each GPS point recorded at the crest of the Entashata fault (traverse F) is adjusted to its pre-1.478 ± 0.003Ma position by subtracting the difference between the elevations, before and after restoration, of the point at the same latitude on traverse Y. The extreme northern and southern ends of traverse F are unconstrained by traverse Y and are adjusted by interpolation. The northern section can be represented by the line joining the last point on the constrained traverse (at autopoint 34230919_0937204) with the intersection point of the Enashata and Porosita fault scarps (at fpoint001), and is given by:

$$H(x)_{1.478} = H(fpoint001)_{1.478} + [(L(x) - L(fpoint001)) \cdot \tan(\theta_8)] \quad\quad (5.20)$$

And $\tan(\theta_8) = [H(34230919\_0937204)_{1.478} - H(fpoint001)_{1.478}]/[L(34230919\_0937204) - L(fpoint001)] \quad\quad (5.21)$

Where: $H(x)_{1.478}$ is the elevation at point x at 1.478±0.003Ma, $H(fpoint001)_{1.478}$ is the elevation at point fpoint001 at 1.478±0.003Ma, H(34230919_0937204) is the elevation at autopoint 34230919_0937204, L(x) is the latitude of point x, L(34230919_0937204) is the latitude at autopoint 34230919_0937204 and L(fpoint001) is the latitude at fpoint001.

Restoration of the southernmost section of the traverse can be similarly achieved by interpolation of elevations between the southern end of the constrained traverse (at autopoint 34230919_1030543) and fpoint004 (Appendix A – Entashata.xls), which is the first exposure of Ol Tepesi Basalt at the crest of the Entashata scarp and is fixed at a height of 1150m. This operation is given by:

$$H(x)_{1.478} = H(34230919\_1030543)_{1.478} - [(L(x) - L(34230919\_1030543)) \cdot \tan(\theta_9)] \qquad (5.22)$$

And $\tan(\theta_9) = [H(34230919\_1030543)_{1.478} - H(fpoint004)_{1.478}]/[L(34230919\_1030543) - L(fpoint004)]$ \qquad (5.23)

Where: $H(x)_{1.478}$ is the elevation at point x at 1.478±0.003Ma, $H(fpoint004)_{1.478}$ is the elevation at point fpoint001 at 1.478±0.003Ma, H(34230919_1030543) is the elevation at autopoint 34230919_1030543, L(x) is the latitude of point x, L(34230919_1030543) is the latitude at autopoint 34230919_1030543and L(fpoint004) is the latitude at fpoint004.

Positional data collected immediately to the south of fpoint004, where the footwall crest is mantled by basalt, are also set to a restored elevation of 1150m.

The morphology of the Entashata footwall is sufficiently well constrained by the GPS traverses shown in figure 5.17 to produce a fairly accurate representation of Entashata fault growth between 1.478±0.003Ma and present. A displacement-length plot for the Entashata fault at 1.478±0.003Ma is shown in figure 5.21. Displacements in this figure are plotted relative to the Ol Tepesi Basalt datum.
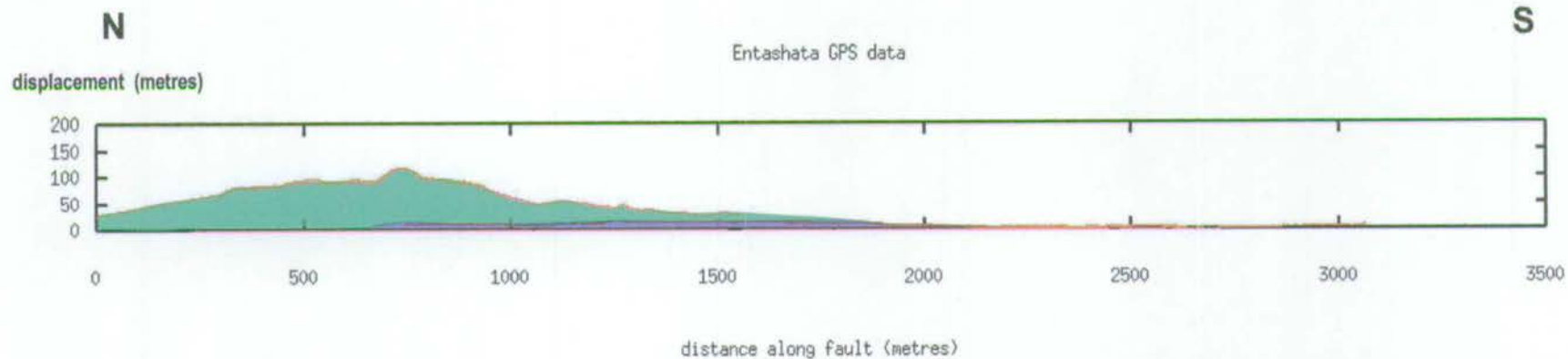
Figure 5.21 Displacement-length profile along the Entashata fault at 1.478±0.003Ma. Displacements are plotted relative to the Ol Tepesi Basalt datum fixed at y=0 on the profile.

In all other areas of the South Kedong region, the absence of Ol Tepesi Basalt makes fault restoration more problematic. However, some general assumptions regarding the topography allow construction of a GMT plot for the region at 1.478±0.003Ma, even though an accurate knowledge of fault displacements is limited.

5.2.4 GMT plot at 1.478±0.003Ma

The topography of the South Kedong region at 1.478±0.003Ma is shown as a relief plot in figure 5.22. As for the restoration at 0.360±0.001Ma, positional data (latitudes, longitudes and displacements relative to the datum surface) were exported and plotted using GMT. In order to produce the plot it was necessary to make restorations of all the GPS traverses across the region, even those not directly constrained by the Ol Tepesi Basalt datum. These restorations will now be described further.

Heights along the western margin of Entashata Eremit (traverse C) (figure 5.17) were restored to their positions at 1.478±0.003Ma by fixing them to elevations at points of the same latitude along traverse E. Adjustments to elevations along the crest of the Porosita horst block were undertaken, somewhat arbitrarily, by reducing the height of each datapoint by some 39 metres. This value represents the height difference, before and after restoration, of apoint014, located at the intersection of the Porosita and Entashata scarps, and hence approximates uplift of the Entashata footwall. Although it is unlikely that uplift along the Porosita Hill fault was identical to that along the Entashata block, both faults were certainly active at the same time and are likely to have experienced similar magnitudes of displacement. Using this assumption, it is possible to make an approximate determination of the footwall uplift to hangingwall subsidence ratio across the Porosita Hill fault, since the magnitude of downfaulting in the immediate hangingwall to the fault, as determined from equation (5.15), is some 54m. This suggests a footwall uplift to hangingwall subsidence ratio of close to 1:1.4, which is substantially lower than that of 1:6 indicated from published studies of neotectonic fault geometry (e.g. Stein and Barrientos, 1985). Even given the approximate nature of the above calculation, a ratio of 1:6 is far too high for the Entashata fault, since it implies hangingwall subsidence of some 240m; a value that is too large to accord with the observed topography (see figure 3.5).

The relatively small areal extent of the Ol Tepesi Basalt lava indicates that it must have been confined to the north and south by the footwalls of the Entashata fault and the Porosita Horst fault respectively. Where they are now downthrown by the Kedong Graben, an estimate of the original elevations of these faults can be interpolated from their heights at the position of intersection with neighbouring faults. In this way, the elevation of the Entashata scarp crest at the intersection with the Porosita fault is 1179±8m after restoration, while the natural continuation of the Porosita Horst fault as it merges with the Enasira fault has an elevation of 1185±2m.

The simplest way to reconstruct the areas that are not well constrained by the Ol Tepesi Basalt flow is to fix the minimum elevation value to 1180m. Hence, any GPS point with an elevation of less than 1180m, after restoration, is fixed to that value. This appears to be somewhat arbitrary, but is, in fact, the simplest solution to fit with the available data. This is especially the case at the tip of the Taritik fault, where all the GPS points located to the south of the present position of the E-W cross-fault linking the Enasira and Taritik faults were set to a value of 1180m.

The plot shown in figure 5.23 clearly illustrates how the Ol Tepesi Basalt lava utilised the fault-generated conduit of Entashata Eremit to flow into the South Kedong region from the southeast. The basalt lava was confined to a relatively small area by the northeast-southwest trending Entashata and Porosita Hill faults. Outside of this immediate area, especially around the Taritik fault to the northwest, the topography at 1.478±0.003Ma is less clearly understood and is based primarily on the later fault topography at 0.360±0.001Ma.
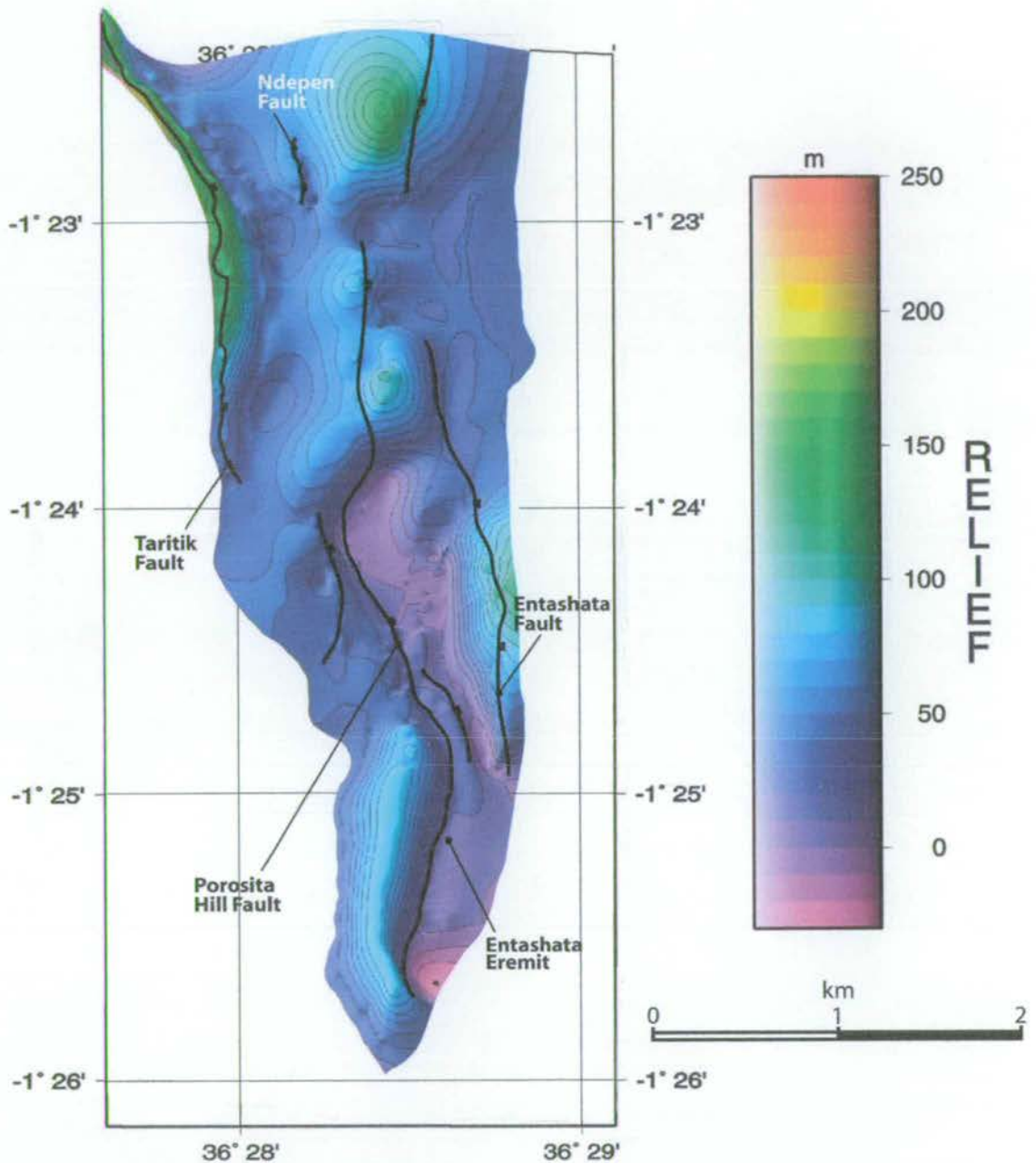
Figure 5.22 GMT-based plot of topographic relief across the South Kedong region at 1.478±0.003Ma. Relief values are shown relative to the Ol Tepesi Basalt datum. At this time, the regional structure was dominated by the NW-SE-trending Entashata and Porosita Hill fault lineaments.

Key
- Ol Tepesi Basalt (Plb2)
- Limuru Trachyte (Tvt1)
- Gesumeti Trachyte (Plh2)
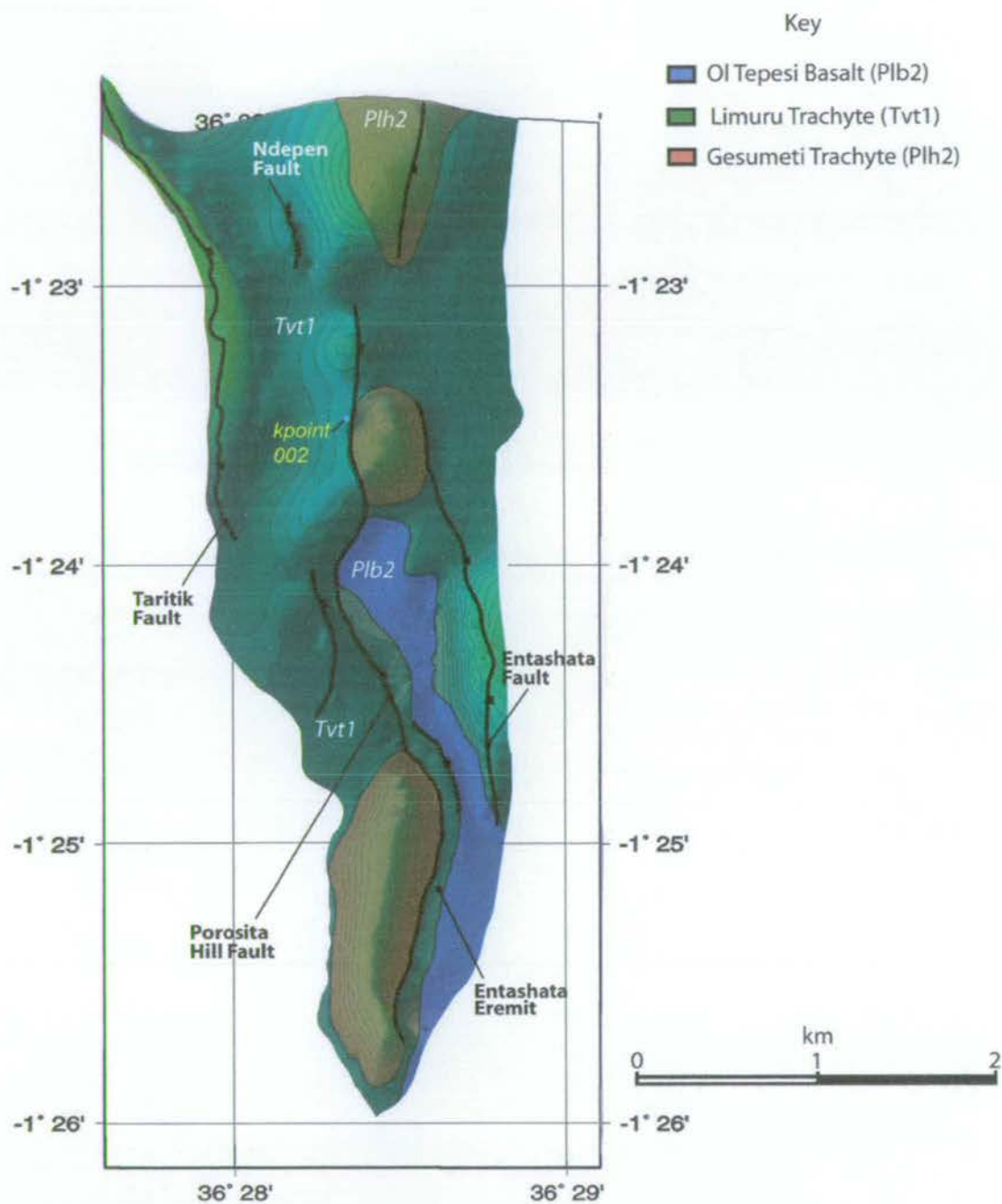
Figure 5.23 As figure 5.22 but with an overlay showing the geology of the South Kedong region at 1.478±0.003Ma. At this time Ol Tepesi Basalt lava was funnelled from the southeast along the Entashata Eremit half-graben. Also shown, located in the footwall to the Enasira fault, is kpoint002, which is used in the regional reconstruction at 2.100±0.007Ma (see section 5.2.6 for further details).

5.2.5 Reconstruction at 2.100±0.007Ma

The other time period which offers an important insight into the development of the South Kedong region is that immediately following uplift of the Gesumeti Trachyte horsts and prior to deposition of the Limuru Trachyte lavas.

It is impossible to accurately reconstruct fault displacements along the Gesumeti Trachyte horst blocks as the base of the Limuru Trachytes are not visible in this area and hence the absolute thicknesses of these latter flows are unknown. It is, however, possible to determine minimum displacements by fixing elevation data, recorded everywhere other than the Gesumeti Trachyte horst blocks, to a value of 1014m. This value represents an estimate of elevation at kpoint002, in the footwall to the Enasira Scarp, after a height of 230m, equivalent to the maximum thickness of the Limuru Trachytes at the northern end of the Kedong Graben, has been 'removed'. kpoint002 was specifically chosen because it is located in one of only a few areas where the contact between Limuru Trachyte Formation and the Gesumeti Trachytes has been relatively unaffected by major, post-depositional fault movements (see figure 5.23). Elevation data recorded along the top of the Gesumeti Trachyte blocks are maintained at values calculated for the 1.478±0.003Ma restoration. By assuming a constant thickness of Limuru Trachyte, this reconstruction is obviously a bit over-simplistic, but it does provide an estimate of minimum displacements along the Gesumeti Trachyte horsts.

5.2.6 GMT plot at 2.100±0.007Ma

The GMT-based plot of relief across the South Kedong region at 2.100±0.007Ma, fixed to a horizontal datum surface with an elevation of 1014m, clearly shows the location of the N-S orientated train of Gesumeti Trachyte fault blocks (figure 5.24 and 5.25). These steep-sided horsts had developed a substantial amount of relief prior to eruption of the Limuru Trachytes at 2.009±0.004Ma. A composite fault displacement-length profile, constructed through the major horsts by selecting relevant GPS data, is shown in figure 5.26.
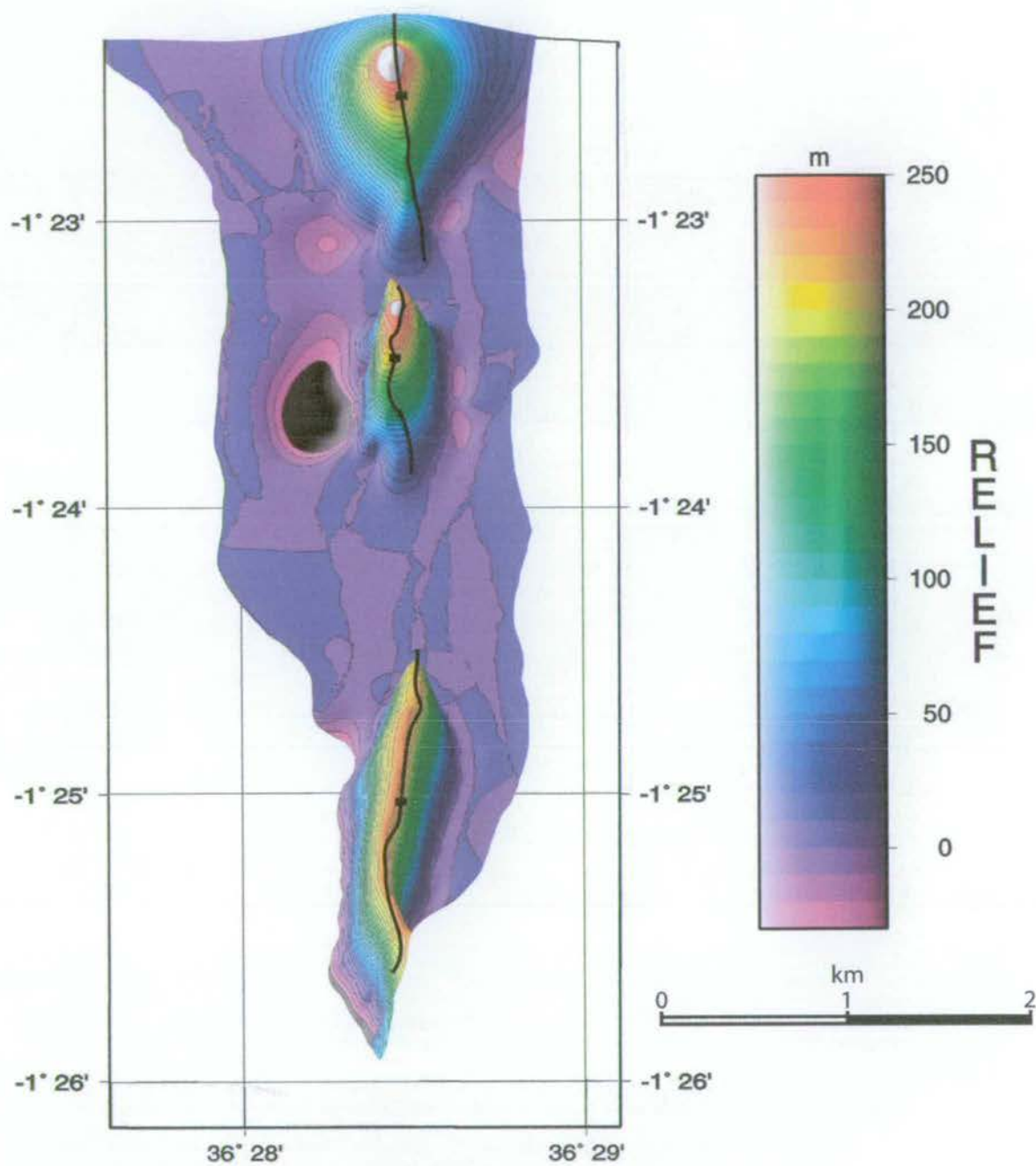
**Figure 5.24 GMT plot of topographic relief across the South Kedong region at 2.009±0.004Ma.**
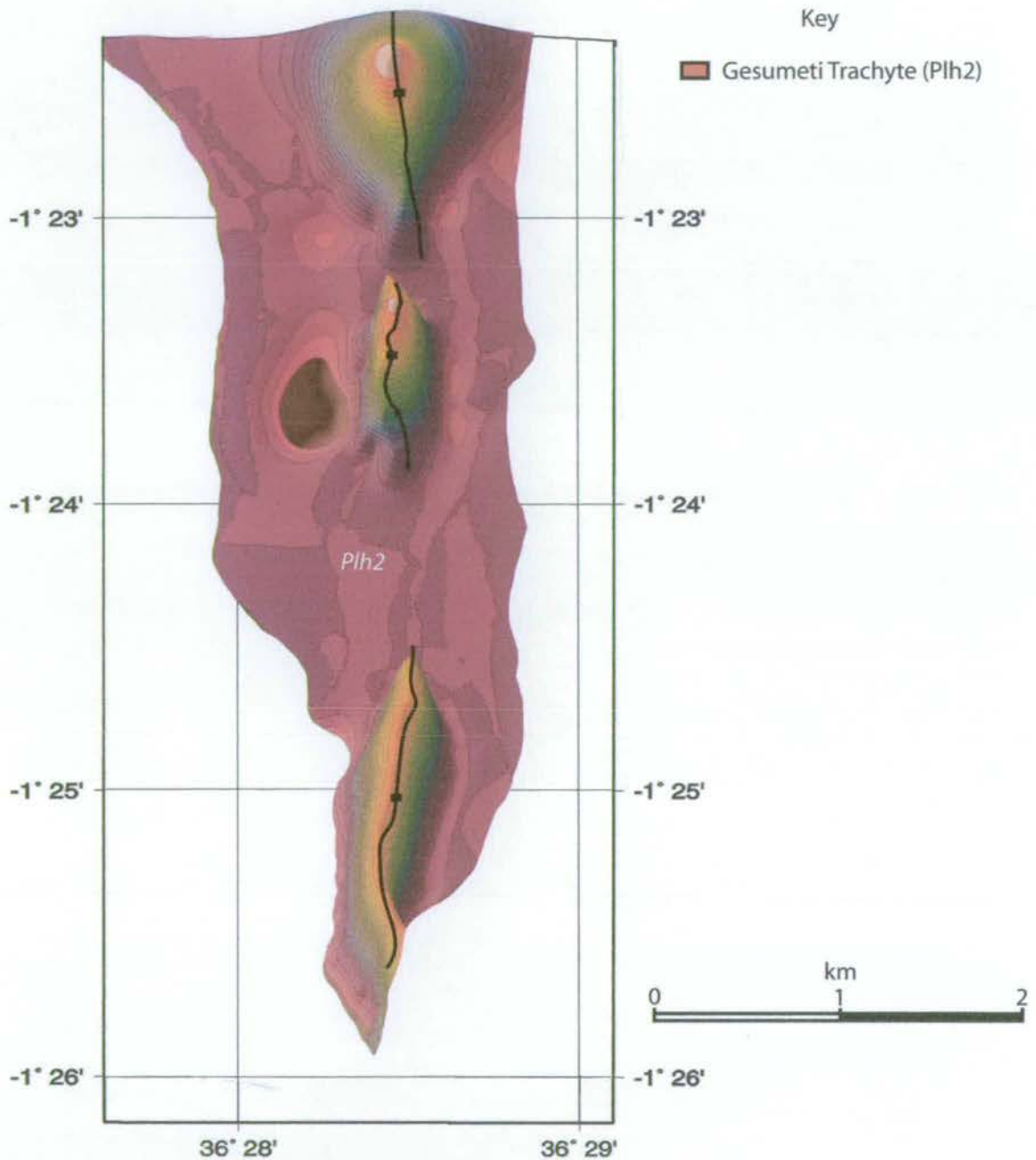
Figure 5.25 As figure 5.24, but with an overlay showing the geology of the South Kedong region at 2.009±0.004Ma. The regional structure is dominated by a train of north-south trending Gesumeti Trachyte horst blocks.
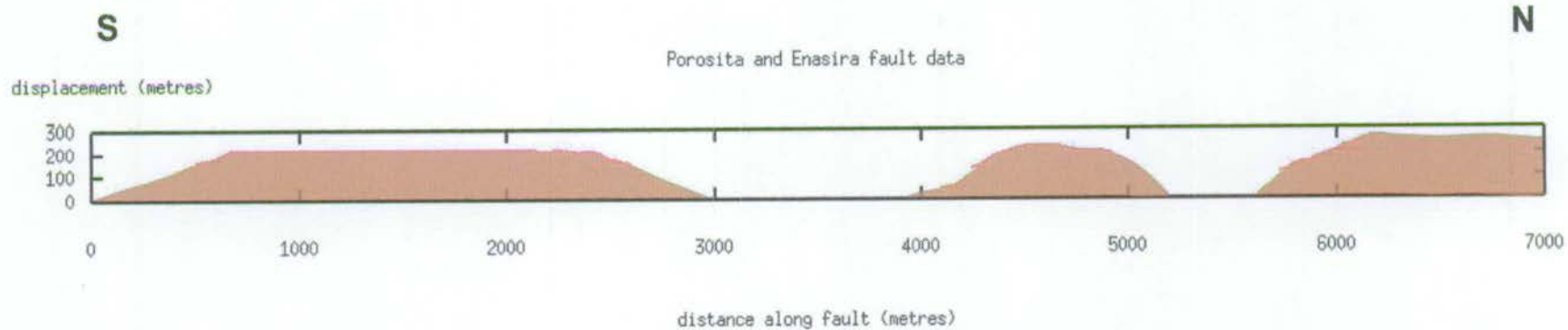
Figure 5.26 Displacement-length profile orientated along the strike of the Gesumeti Trachyte horst blocks shown in figure 5.25. Displacement values are measured relative to the inferred upper surface of the Gesumeti Trachyte Formation, where unaffected by faulting.

5.2.7 Geological history of the South Kedong Region

The fault reconstructions described in the previous sections provide information that can be used to build up a detailed understanding of the geological history of the Kedong Graben region. Highly accurate differential GPS surveying techniques (see chapter 4) combined with $^{40}Ar/^{39}Ar$ radiometric determinations on samples collected from flows in the Kedong region allow a quantitative insight, in terms of fault displacement and tip propagation rates, into the development of the scarps in this region.

a) 2.254±0.007Ma - 2.100±0.007Ma

By 2.100±0.007Ma, the last of the Gesumeti Trachyte Formation had been erupted into the Kedong region. For at least the previous 150 thousand years, beginning at 2.254±0.007Ma (determined from sample K53, see section 3.3.2), a conformable sequence of trachyte, tuff and agglomerate was deposited across the local area. The absolute areal extent of this formation is unknown since it is presently only exposed in the uplifted 'bell-shaped' horst blocks along the margins of the Kedong Graben. Though the source of the lavas is unknown, the limited nature of the exposure has led previous workers to suggest that the Gesumeti Trachytes are the result of a localised fissure eruption (Baker and Mitchell, 1976; Baker *et al*, 1988).

b) 2.100±0.007Ma – 2.009±0.004Ma

Initial uplift of the three distinctive Gesumeti Trachyte horst blocks began in the 91kyr period between deposition of the feldsparphyric upper lava of the Gesumeti Trachyte Formation (sampled at K47) and eruption of the Limuru Trachytes. A GMT-based relief image of the South Kedong region immediately prior to the influx of Limuru Trachyte lavas at 2.009±0.004Ma is replotted in figure 5.27, accompanied by a composite fault displacement-length profile in figure 5.28 (the positional data used to construct figure 5.28 are supplied in Microsoft Excel file Porosita+Enasiradldata(2.009Ma).xls, Appendix A). As can be seen from figure 5.27, the horsts lie in an almost direct N-S orientation. Displacement-length ratios (d/L) are 0.12±0.05 at 1500m, 0.32±0.13 at 4600m and 0.12±0.05 at 6200m. Vertical displacement rates and d/L ratios for these blocks have been calculated by assuming a hangingwall sediment thickness of 300m, which seems reasonable, given the uncertainty in the calculation of the

'minimum' fault displacements during this period. The maximum displacement rate of any of these blocks is 4.70 ± 1.70mmyr^{-1} at x=6200m.
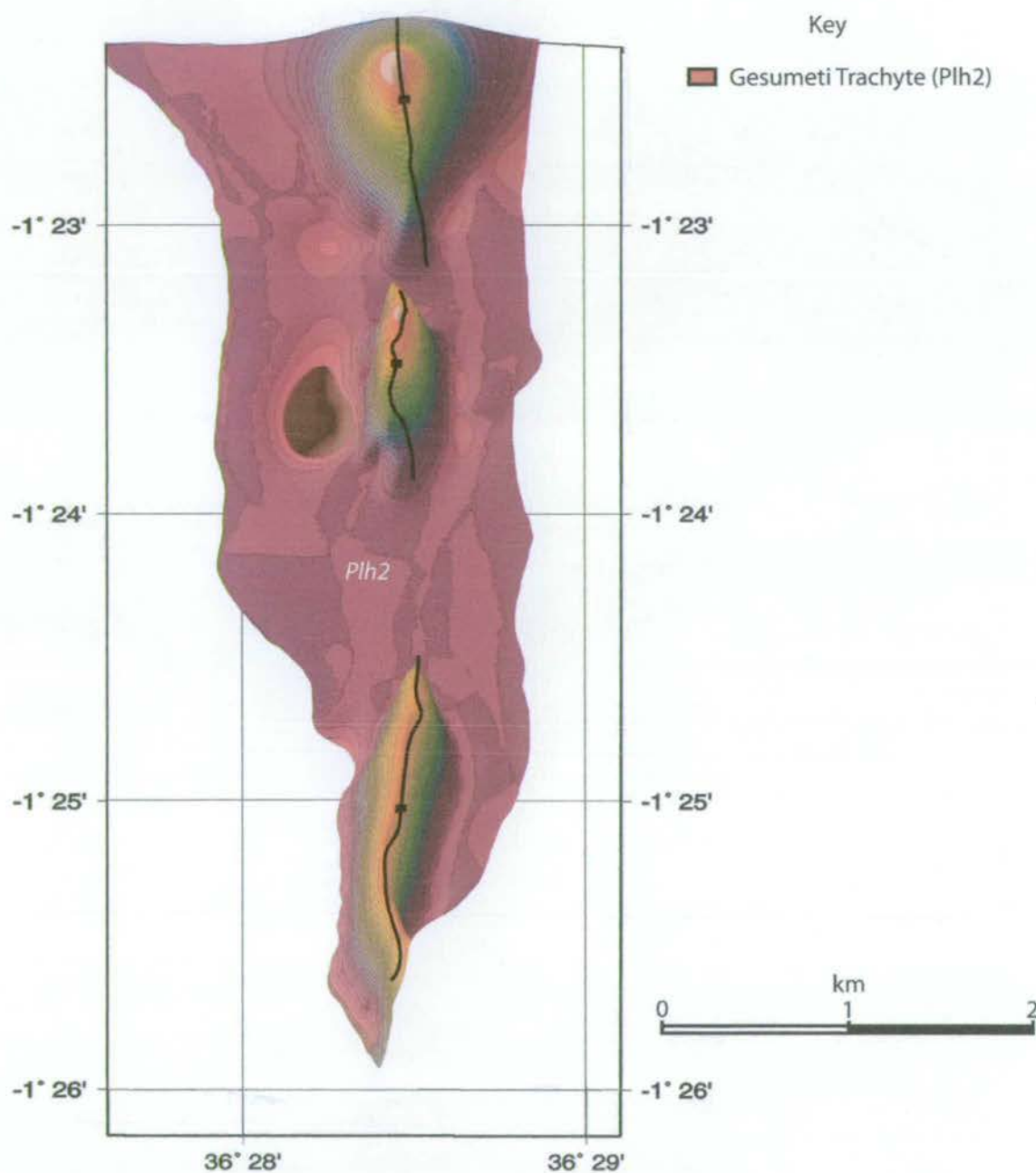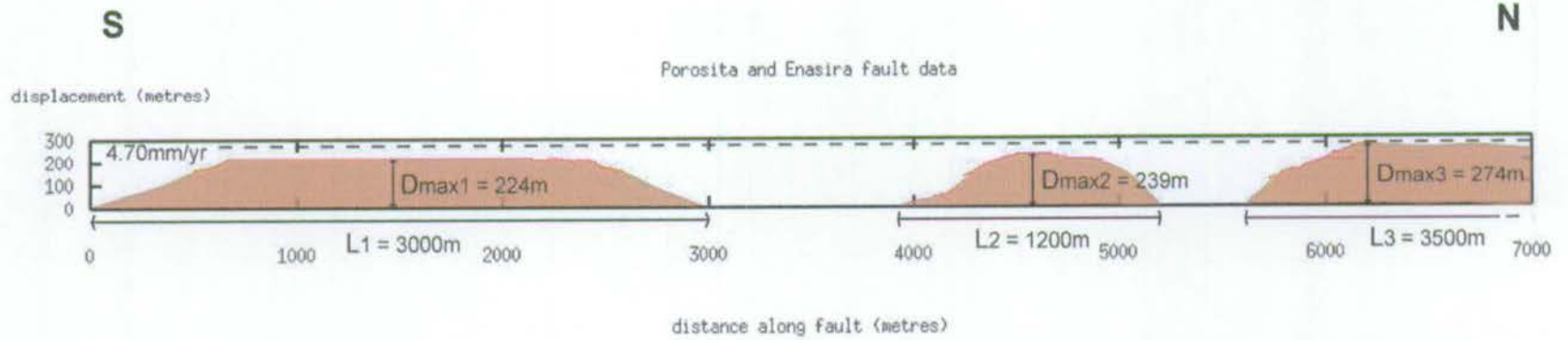
Figure 5.28 Displacement-length profile along strike of the Gesumeti Trachyte horst train at 2.009±0.004Ma, modified from figure 5.26 to show values of fault segment length and displacement. Maximum uplift rate of the blocks was ~4.7mmyr^{-1} in the 91kyr period between deposition of the Gesumeti Trachyte Formation and the Limuru Trachyte lavas.

c) 2.009±0.004Ma – 1.478±0.003Ma

Immediately following the final eruption of the Limuru Trachytes, the pre-existing Gesumeti Trachyte horsts would have appeared to be a series of 'islands' surrounded by a 'sea' of Limuru Trachyte lava. The maximum relief of the horst crests above the upper surface of the neighbouring trachyte 'sea' was approximately 30m, as measured from the relatively unfaulted region to the west of the main Enasira horst (near kpoint002; see figure 5.22 and 5.23).

Between 2.009±0.004Ma and 1.478±0.003Ma, faults began to nucleate within the Limuru Trachytes. The GMT relief plot shown in figure 5.29 illustrates the inferred topography of the South Kedong region at 1.478±0.003Ma. Substantial deformation of the Limuru Trachytes occurred as a result of movement along the curved Entashata and Porosita Hill faults. Both faults were active in a N-S to NW-SE orientation, but only the Entashata fault is well constrained by the aerial coverage of Ol Tepesi Basalt lava. The earliest phase of activity along the Entashata fault was confined to the ~2km long northernmost section. A displacement-length profile for the Entashata fault at 1.478±0.003Ma is replotted in figure 5.30. The maximum displacement rates during this period were located around x=736m at 0.27±0.05mmyr^{-1} and the d/L ratio for the active section of the Entashata fault was 0.07±0.01. Since the Entashata fault is well exposed, vertical displacement rates were calculated by assuming a hangingwall sediment thickness of 50m. The positional data used to create the plot shown in figure 5.30 are given in Excel file Entashatadldata(1.480Ma).xls, Appendix A.

Apart from the southeast of the region, where there is a large areal extent of Ol Tepesi Basalt, it is generally hard to constrain fault growth in the remainder of South Kedong region between 2.009±0.004Ma and 1.478±0.003Ma. The absolute morphology of the faults west of the Enasira scarp at 1.478±0.003Ma is not clearly known, though it is likely that some faulting had been initiated by this time. The nature of the fault network shown in the GMT plot of figure 5.29 is therefore somewhat speculative in this area and may not have been as well developed as shown. However, as described in the following section, by 0.360±0.001Ma the Taritik fault and the small faults located on the back of the Enasira footwall block were fully developed.
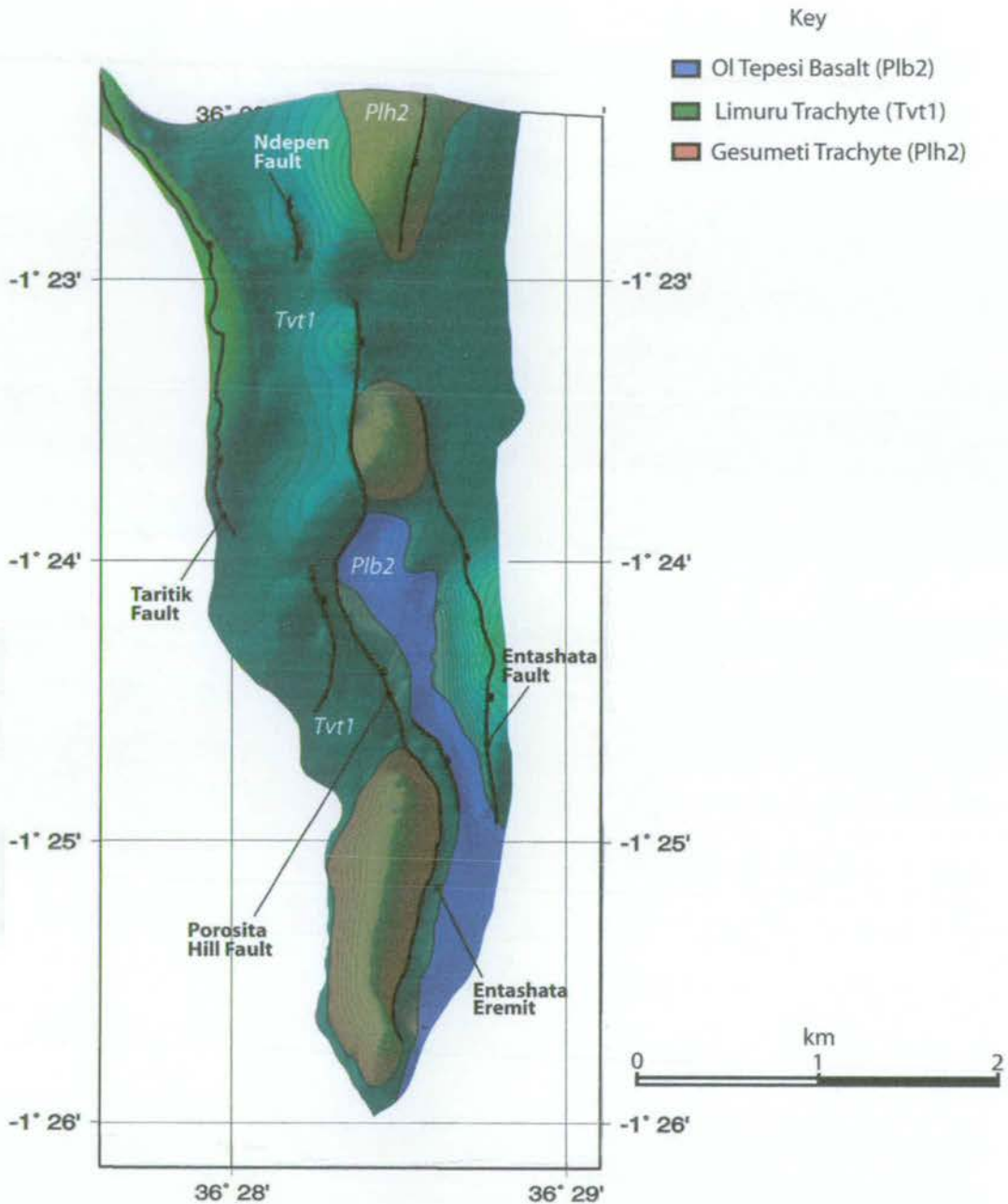
Figure 5.29 Geological map of the South Kedong region at 1.478±0.003Ma, replotted from figure 5.23. Following eruption of the Limuru Trachyte lavas at 2.009±0.004Ma, major faulting was established with a dominantly NW-SE orientation, partially reactivating faults bounding the margins of pre-existing Gesumeti Trachyte horsts. At 1.478±0.003Ma the southeast of the region had been inundated by Ol Tepesi Basalt lava.
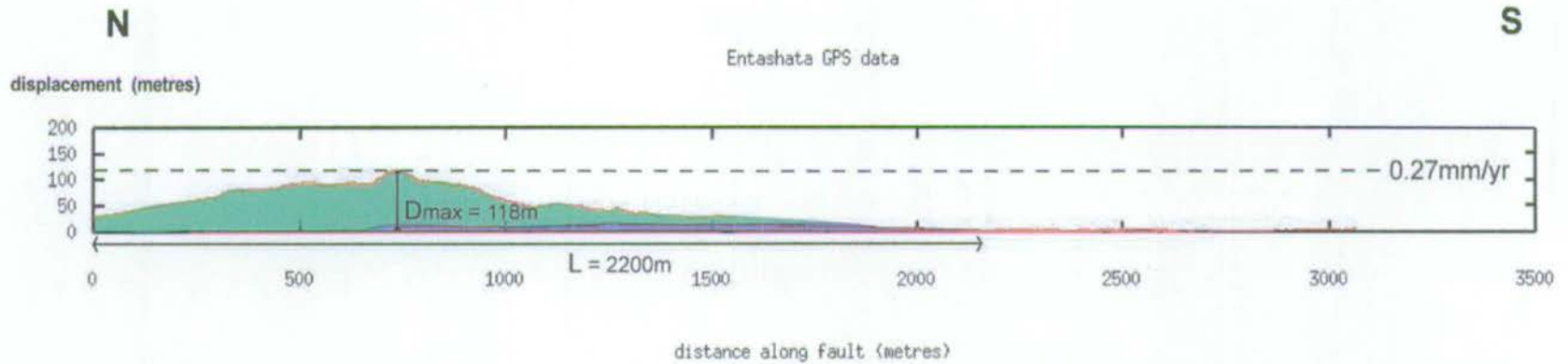
Figure 5.30 Displacement-length profile along the Entashata fault scarp at 1.478±0.003Ma, modified from figure 5.21. The vertical displacement rate between 2.009±0.004Ma-1.478±0.003Ma, as measured at the position of Dmax, was 0.27mmyr[-1].

At 1.478±0.003Ma, a ~10m thick flow of Ol Tepesi Basalt flooded the extreme southeast of the South Kedong region and the back of the Entashata footwall block by utilising the pre-existing topographic low along Entashata Eremit that was generated as a result of movement along the Porosita Hill and Entashata faults.

d) 1.478±0.003Ma - 0.360±0.001Ma

This period was characterised by continued growth of pre-existing faults in a N-S to NW-SE orientation combined with nucleation of a second set of cross-cutting faults with a more N-S to NNE-SSW orientation that represent the precursor Kedong Graben. Figure 5.31 shows the GMT relief plot of the South Kedong region at 0.360±0.001Ma.

The Entashata fault continued to develop during this phase of faulting, though the majority of displacement was by now being accrued to the south of the initial position of maximum displacement as the fault propagated in a southward direction. Figure 5.32a is a displacement-length profile along the Entashata fault at 0.360±0.001Ma (see file Entashatadldata(0.360Ma).xls, Appendix A for the displacement-length dataset) showing the position of D_{max} at that time. The d/L ratio for the scarp at 0.360±0.001Ma is 0.04±0.01. A separate graph of displacement accrued along the length of the Entashata fault between 1.478±0.003Ma and 0.360±0.001Ma is shown in figure 5.32b. The maximum displacement rate, calculated at x=1860m along the profile in figure 5.32b by assuming a hangingwall sediment thickness of 50m for this well exposed fault, was 0.14±0.02mmyr^{-1}. The displacement-length data used to create this plot is provided in Excel file Entashatadisp(1.478-0.360Ma).xls (given in Appendix A).

Key
- Barajai Trachyte (Bjt)
- Ol Tepesi Basalt (Plb2)
- Limuru Trachyte (Tvt1)
- Gesumeti Trachyte (Plh2)
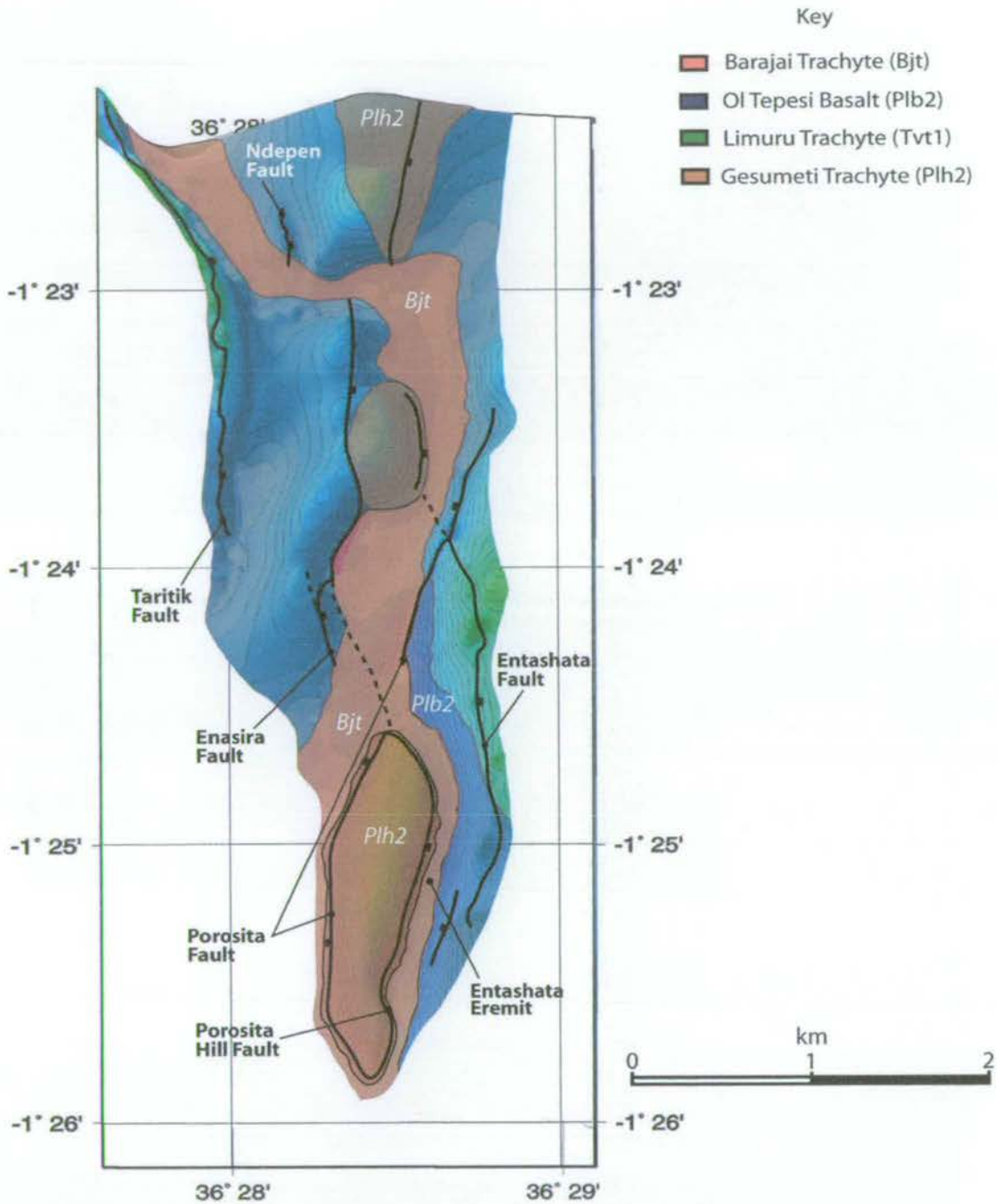
Figure 5.31 Geological map of the South Kedong region at 0.360±0.001Ma, replotted from figure 5.16. Further reactivation of faulting along the Gesumeti Trachyte horsts between 1.478±0.003Ma and 0.360±0.001Ma resulted in the formation of small fault segments at the margins of the pre-cursor Kedong Graben. This phase of faulting cross-cut the pre-existing NW-SE trending Entashata and Porosita Hill faults, which were both inactive by 0.360±0.001Ma. At this stage the incipient Kedong Graben operated as a conduit for Barajai Trachyte lava that flowed from Mount Suswa at 0.360±0.001Ma.
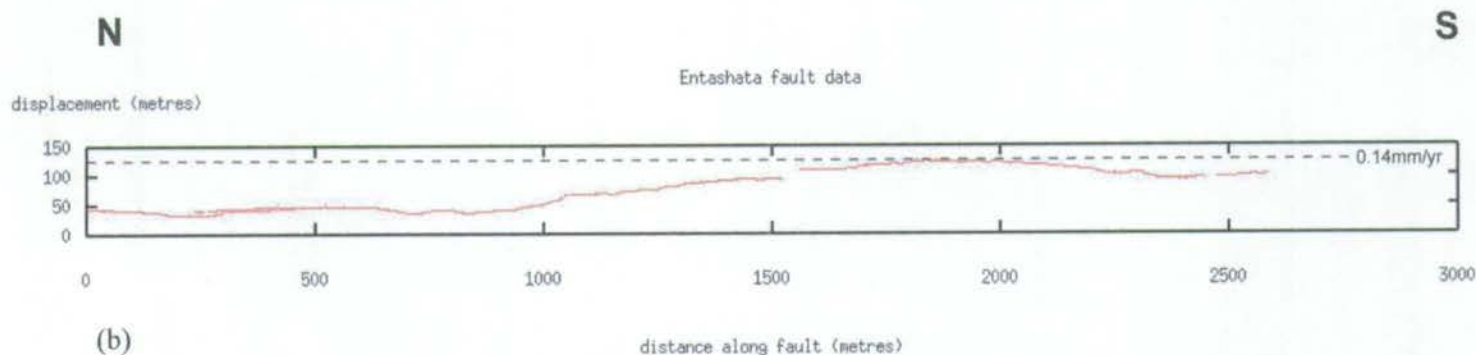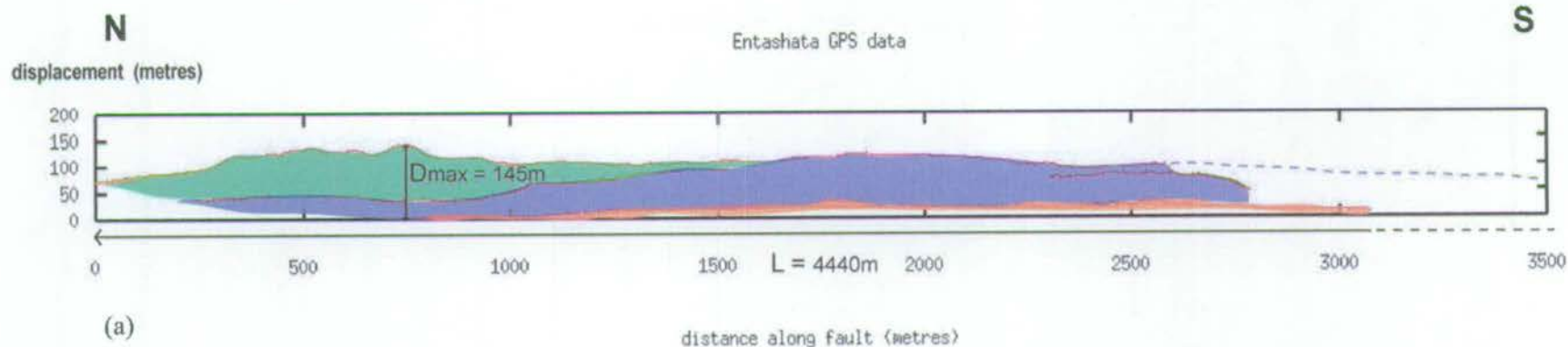
Figure 5.32 (a) Displacement-length profile along the Entashata fault at 0.360±0.001Ma, modified from figure 5.20 to show the location of Dmax. Fault length was measured from georeferenced Landsat 7 satellite images. (b) Plot of displacement accrued along the Entashata fault between 1.478±0.003Ma and 0.360±0.001Ma. The maximum displacement rate during this period, as indicated, was 0.14mmyr^{-1}.

The Porosita Hill fault curves around the eastern margin and the northern tip of the Porosita horst block, backtilting it towards the south-southwest while downthrowing the Entashata Eremit half-graben. An accurate understanding of the displacement variation along the length of this fault is restricted by the lack of basalt lava coverage. However, it is likely that the majority of displacement was localised along the central section of the fault where it reactivates the Porosita horst. Certainly, displacement is relatively limited at the northern tip of the fault, where it curves behind the Enasira block and downthrows a narrow exposure of Ol Tepesi Basalt.

Concurrently with continued displacement along pre-existing fault lines, new N-S to NNE-SSW orientated faults began to develop along the margins of the precursor Kedong Graben, partially reactivating older faults bounding the Gesumeti horst blocks. In the south of the region, a new phase of movement along the western margin of the Porosita horst cuts across the footwall of the Porosita Hill fault, acting to cut off the northern fault tip. Antithetic faulting at the same latitude formed a narrow graben feature that was later to form a section of the Kedong Graben system. Similarly, the western tip of the Entashata fault, which previously connected with the edge of Enasira horst block was dissected by a second narrow graben feature that resulted from movement along the eastern margin of the horst. Hence, at this time, the incipient Kedong Graben was composed of two independent graben segments associated with the pre-existing Gesumeti Trachyte horst blocks and produced by deformation along the block margins. This fault configuration produced a flow conduit that allowed the Barajai Trachyte lava to flow southwards from the Footwall Fault Zone into the Ol Tepesi Basin. Displacement-length profiles along the incipient Porosita and Enasira faults at 0.360 ± 0.001Ma are replotted in figures 5.33a and 5.34a respectively. At this stage, the d/L ratios of the Porosita and Enasira faults were 0.10 ± 0.05 and 0.13 ± 0.06 respectively. Note that these values are for 'newly-formed' segments of the faults that cut through the Limuru Trachyte Formation, rather than the reactivated sections bounding the margins of the Gesumeti Trachyte horst blocks. Footwall uplift is poorly constrained along the Gesumeti horsts between 1.478 ± 0.003Ma and 0.360 ± 0.001Ma and, furthermore, since much of the cumulative displacement along these blocks was accrued during the phase of activity between 2.100 ± 0.007Ma and 2.009 ± 0.004Ma, values of D_{max} taken at such locations provide limited insight into the growth of the Porosita and Enasira faults. Figures 5.33b and 5.34b show the displacement accrued along both faults between 1.478 ± 0.003Ma and 0.360 ± 0.001Ma. Since the hangingwall sediment thickness along these faults is unknown, vertical displacement rates and d/L ratios were calculated by assuming a footwall uplift to

hangingwall subsidence ratio of 1:2 as described in section 5.1.3. The maximum rates associated with each fault are 0.12 ± 0.06mmyr^{-1} and 0.07 ± 0.04mmyr^{-1} for the Porosita and Enasira faults respectively.

The positional data used for figures 5.33 and 5.34 are provided in Excel files Porositadldata(0.360Ma).xls and Enasiradldata(0.360Ma).xls (Appendix A).
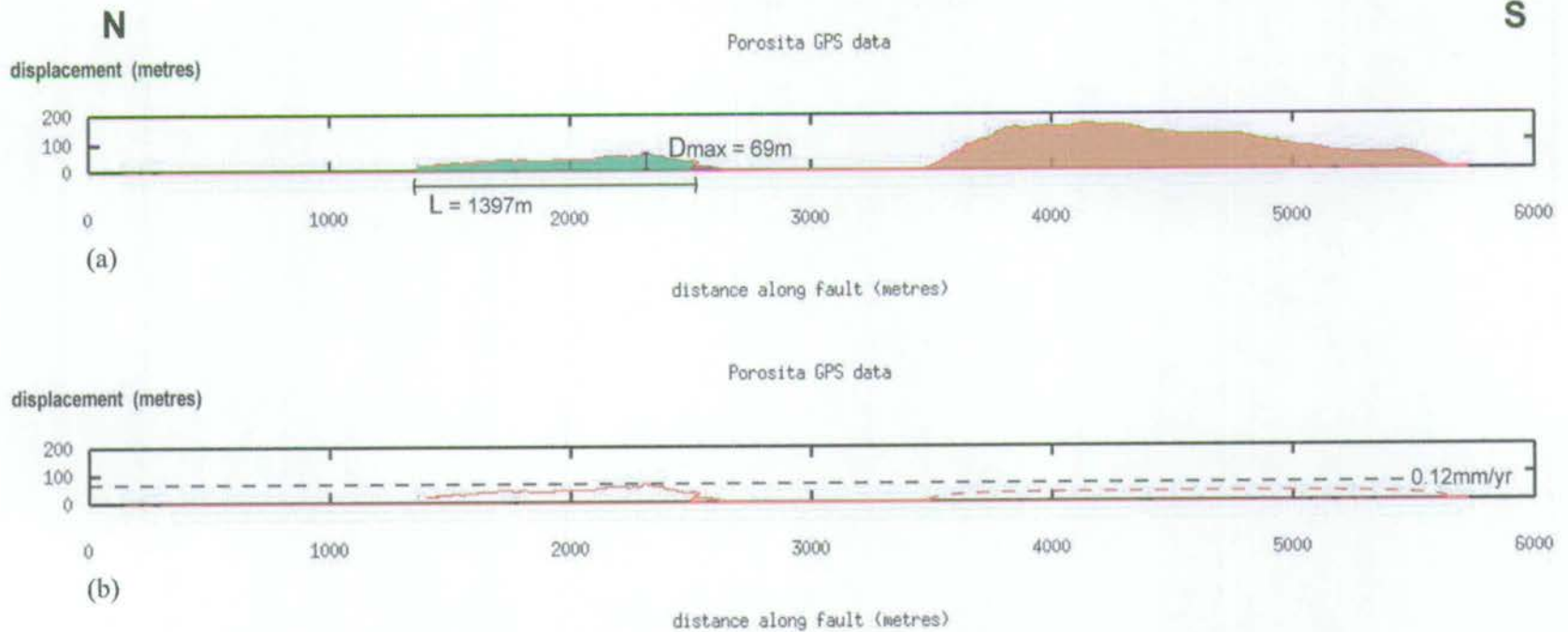
Figure 5.33 (a) Displacement-length profile along the Porosita fault at 0.360±0.001Ma. The scarp consists of two independent fault segments, one located at the intersection with the Entashata fault, at x=2300m, and the second, further to the south, resulting from a reactivation of faulting along the western margin of the Porosita Horst block. Between 1.478±0.003Ma and 0.360±0.001Ma, displacement was accrued along the segments according to the plot shown in (b) and at a maximum rate of 0.12mmyr⁻¹. Due to an absence of stratigraphic constraints, the magnitude of uplift along the Porosita horst is speculative.
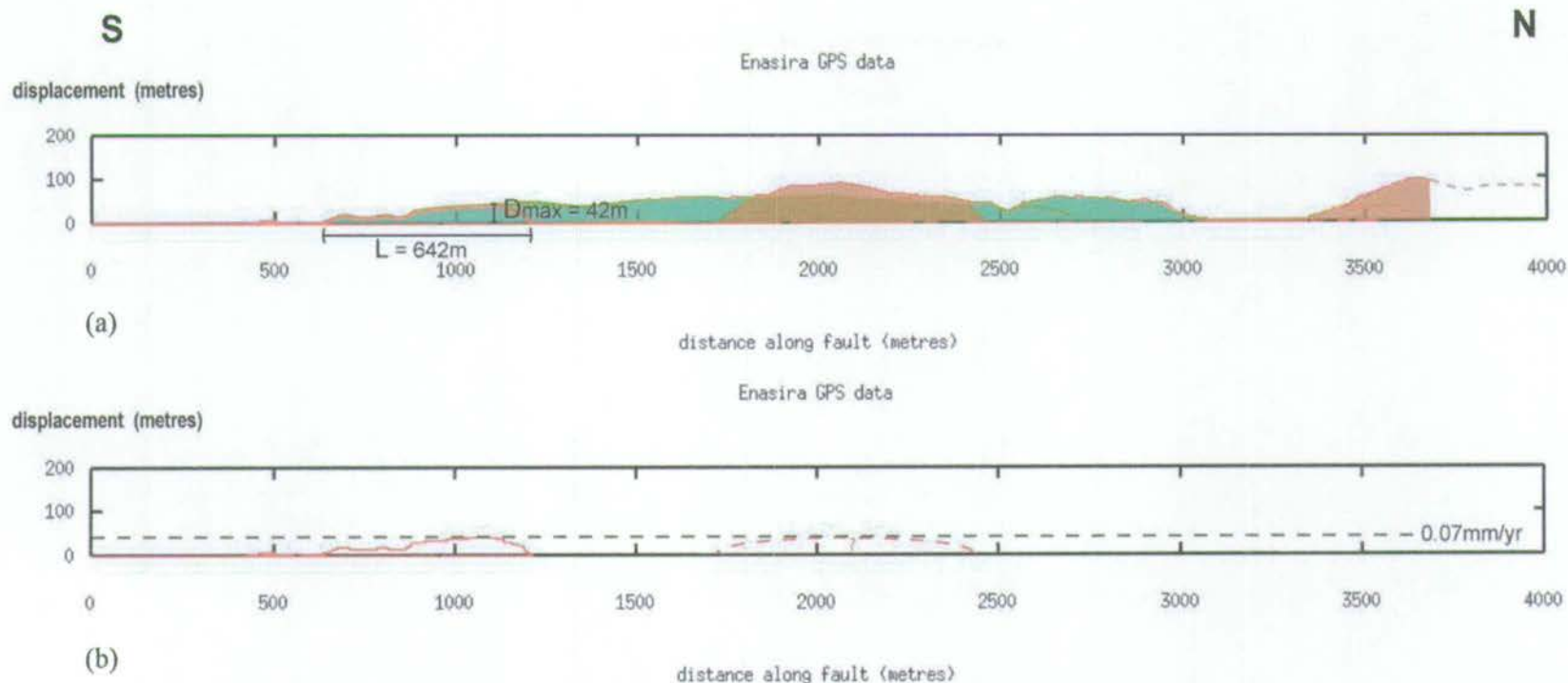
Figure 5.34 (a) Profile along the Enasira fault at 0.360±0.001Ma, modified from figure 5.9 to show the location of Dmax. The topographic low located between x=3000-3500 represents the position of deformation along the Footwall Fault Zone (FFZ) between 0.360±0.001Ma and present. (b) Plot of displacement accrued along the Enasira fault between 1.478±0.003Ma and 0.360±0.001Ma, showing that the maximum displacement rate during this period was 0.07mmyr^{-1}. Displacement was accumulated along two distinct segments, one between x=600-1200 and the other along the pre-existing Gesumeti Trachyte horst (between x=1750 and x=2450). Other areas of the scarp shown in (a) result from earlier movement along the northern tip of the Porosita Hill fault. Relative uplift of the Gesumeti Trachyte block during this period is speculative.

In the west of the area, the Taritik fault and other faults in the footwall to the Enasira fault that cut Limuru Trachyte lavas, remained active until 0.360±0.001Ma at the latest, since they do not displace the Barajai Trachyte flow. The southern tip of the Ndepen fault, close to where it was later cross-cut by movement on the Footwall Fault Zone (FFZ), was blanketed by a 10m-thick flow of Barajai Trachyte and has since remained inactive. A displacement-length profile for this fault is plotted in figure 5.35 (see file Ndependldata(0.360Ma).xls, Appendix A, for the data used in this plot). The d/L ratio and maximum displacement rate on the Ndepen fault are 0.07±0.04 and 0.02±0.01mmyr^{-1}, respectively.

At 0.360±0.001Ma, Barajai Trachyte flowed into the South Kedong region. The lavas, as suggested in section 2.4.3j, were likely to have been sourced from the precursor Mount Suswa volcano. Utilising pre-existing topographic lows in the fault hangingwalls, the trachyte flowed from the north along the base of the Taritik scarp, turning sharply eastward as it was diverted along the Footwall Fault Zone, before exiting into the South Kedong Graben and flowing southward, around both sides of the Porosita horst block, onto the Ol Tepesi Plain.

e) 0.360±0.001Ma – Recent

Following deposition of the Barajai Trachyte, faulting continued in a NNE-SSW orientation and had the affect of linking pre-existing segments together to form the 18km-long Kedong Graben structure. Uplift along the Enasira fault induced formation of the E-W orientated Footwall Fault Zone in order to accommodate strain at the tips of two neighbouring fault segments (figure 5.36). Figure 5.37 shows a displacement-length profile along the southern footwall fault. The maximum rate of displacement along this fault (0.28±0.03mmyr^{-1}) is located immediately to the west (at x=160m) of the point of intersection with the Enasira fault. The displacement data used to construct figure 5.37 are given in Appendix A as file FFZdisp.xls.

The southern section of the Enasira fault now appears to be in the process of hard linkage, as the entrance to the FFZ is currently raised relative to the floor of the Kedong Graben and has been partially cross-cut by the growing southern tip of the northern Enasira fault segment. This observation explains the slightly lower maximum displacement rate shown in figure 5.37, as compared with figure 5.38b (see below). A cumulative displacement-length profile for the current Enasira fault (d/L ~0.01) is replotted in figure 5.38a. For the reasons given in section

5.2.7e, the position of D_{max} is located along the section of the fault that dissects the Limuru Trachytes and therefore represents the location of maximum displacement accumulated on the Enasira fault between 0.360±0.001Ma and present. The raw positional data used for producing this plot are given in Excel file Enasiradldata(present).xls (see Appendix A). Displacement accrued on the fault between 0.360±0.001Ma and present is shown in figure 5.38b. The maximum displacement rate, located at the intersection of the Enasira fault with the southern wall of the Footwall Fault Zone (x=3290m on the plot) is 0.32±0.03mmyr^{-1}. The lateral propagation rate of the Enasira fault tip, between 0.360±0.001Ma and present, was determined by measurement of the horizontal distance between upoint001 and qpoint001 (figure 5.38a). This length defines the section of the scarp exposed as a result of movement along the fault since 0.360±0.001Ma and gives a rate of 1.33mmyr^{-1}. The raw displacement data used to construct figure 5.38 are provided in file Enasiradisp(0.360Ma-present).xls (Appendix A).

Antithetic movement along the Porosita scarp was less continuous and substantial than that along the Enasira scarp. A consequence of this is that the Kedong Graben has a 'half-graben like' morphology north of where the Porosita fault tips out at x=150m in figure 5.39a. The d/L ratio of the Porosita scarp, as shown on the fault displacement-length profile of figure 5.39a, is 0.03±0.01 (data for the plot is given in file Porosita+Entashatadldata(present).xls, Appendix A). Between 0.360±0.001Ma and present, the majority of displacement was accumulated close to the intersection of the Entashata and Porosita faults (figure 5.39b). The calculated fault displacement rate at this location, as indicated in figure 5.39b, was 0.25±0.03mmyr^{-1}. The displacement data for the plot shown in figure 5.39b is given in Excel file Porositadisp(0.360Ma-present).xls (Appendix A).
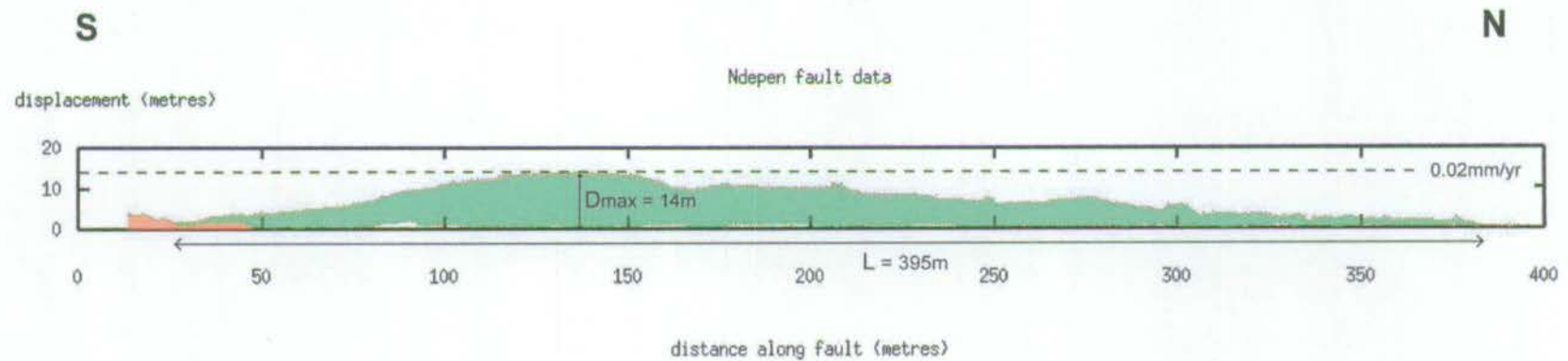
Figure 5.35 Displacement-length profile along the Ndepen fault at 0.360±0.001Ma. This is a small-scale structure, located to the west of the Enasira fault (see figure 5.31), that cuts Limuru Trachyte but is partially buried under the Barajai Trachyte flow (between x=0-50m), indicating that it became inactive by 0.360±0.001Ma. The corresponding maximum displacement rate between 2.009±0.004Ma and 0.360±0.001Ma was 0.02mmyr^{-1}, as indicated.
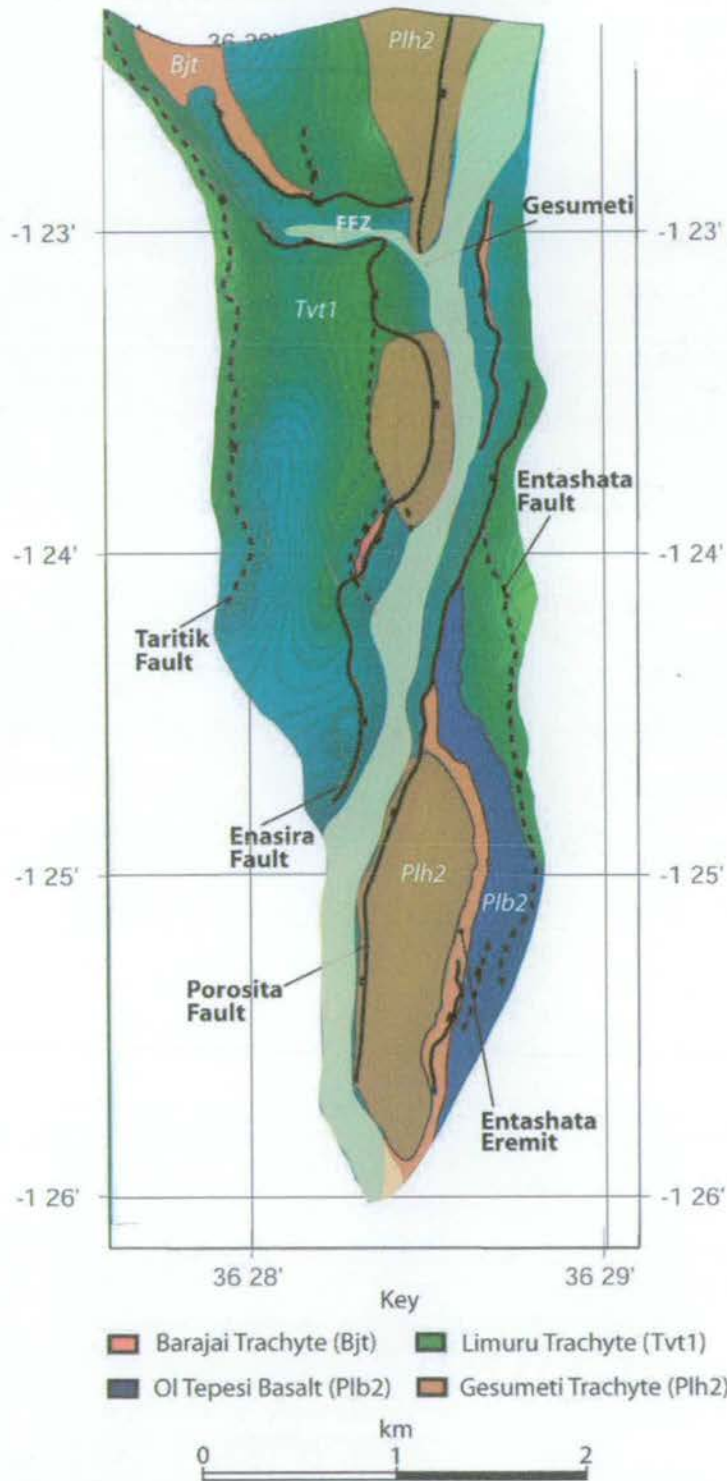
Figure 5.36 Geological map of the South Kedong region at present, modified from figure 5.7. Continued faulting between 0.360±0.001Ma and present resulted in linkage of segments along the Porosita and Enasira faults, causing the floor of the Kedong Graben to be downthrown. Initiation of E-W orientated faulting between segments of the Enasira fault resulted in formation of the FFZ.

E   Footwall Fault Zone (south) GPS data   **W**

displacement (metres)

distance along fault (metres)
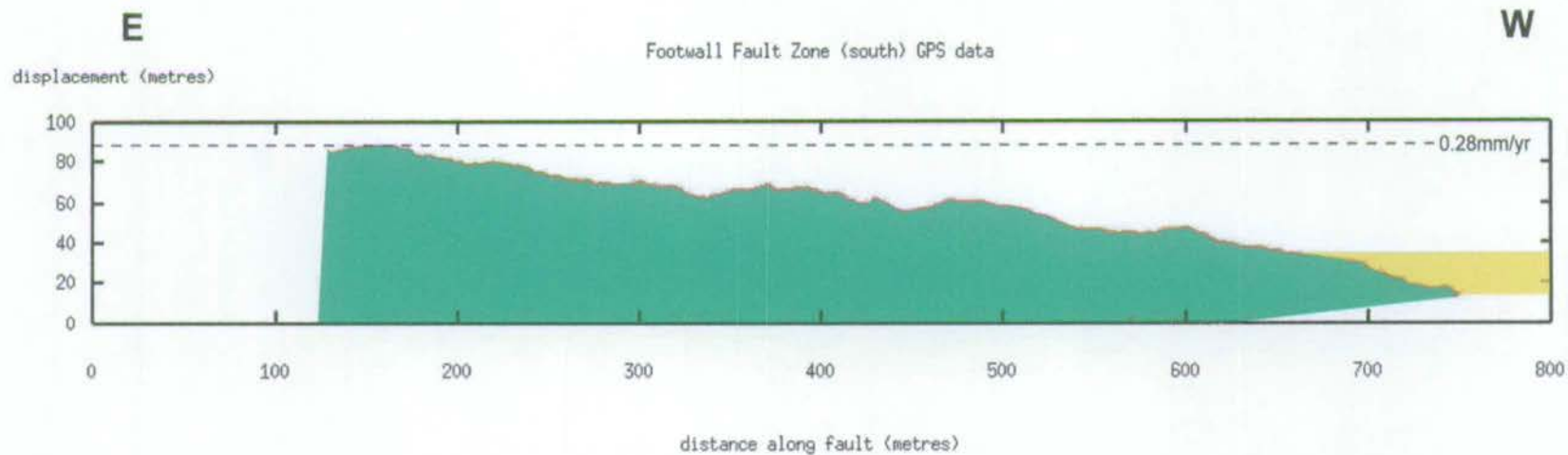
Figure 5.37 Displacement-length profile along the southern wall of the Footwall Fault Zone (FFZ), modified from figure 5.12 to show fault displacement rates for the period 0.360±0.001Ma to present. The maximum displacement rate of 0.28mmyr[-1] is located close to the position of intersection with the Enasira fault, at x=160m.
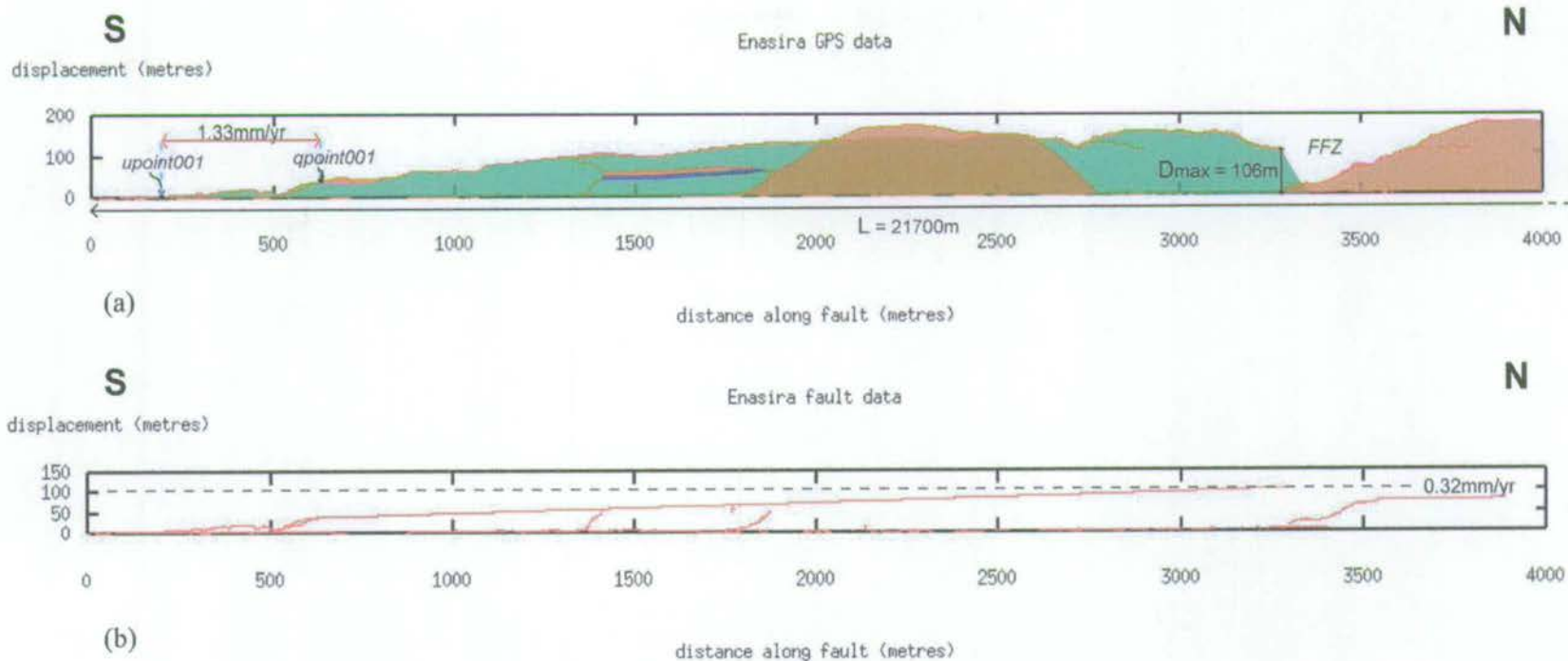
Figure 5.38 (a) Displacement-length profile along the Enasira fault, modified from figure 5.8 to show principal fault dimensions. Fault length was measured from georeferenced Landsat 7 satellite images. Also shown is the fault tip propagation rate between 0.360±0.001Ma and present, indicated by the horizontal red arrow on the left side of the plot. (b) Plot of displacement accrued along the Enasira fault between 0.360±0.001Ma and present. The maximum displacement rate of 0.32mmyr^{-1} is located at the position of intersection between the Enasira and southern footwall faults, as indicated.
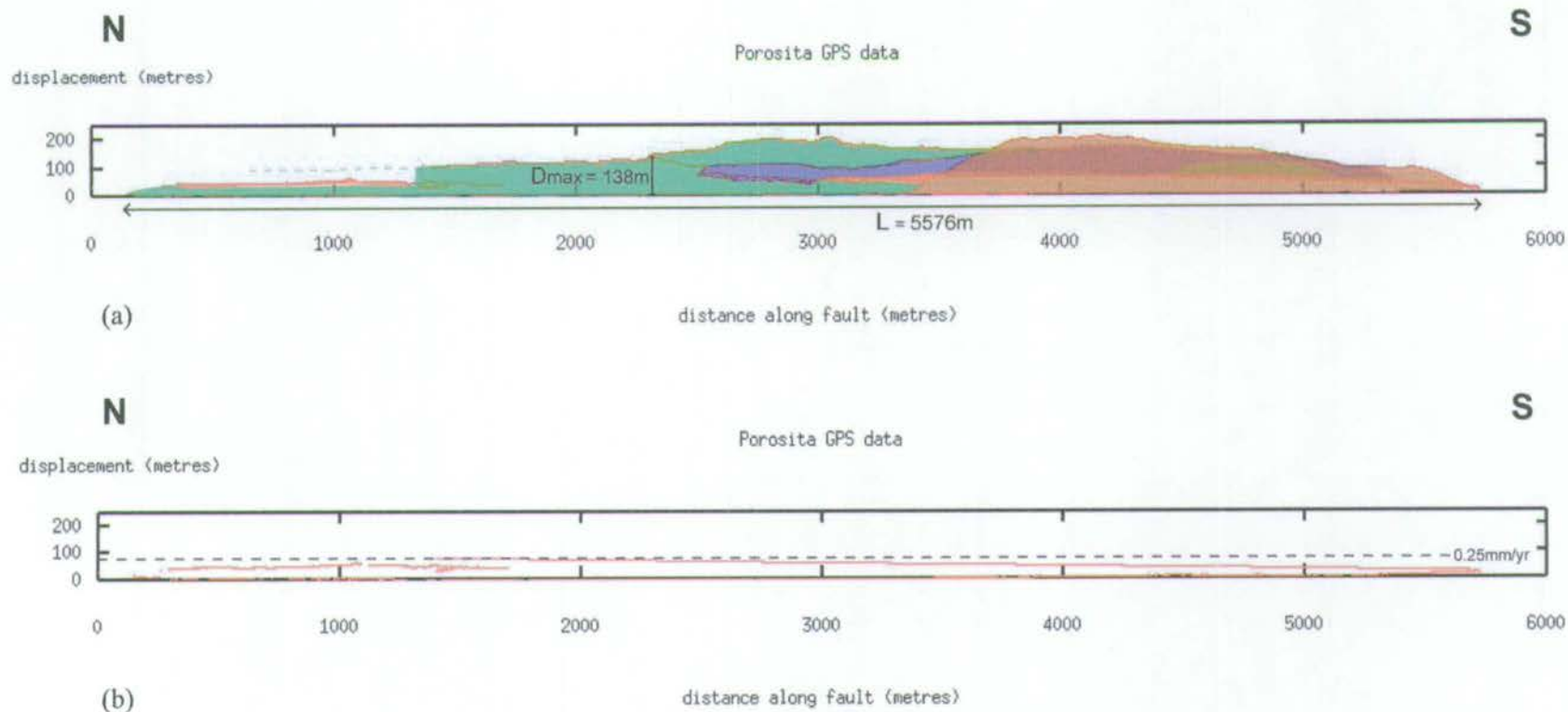
Figure 5.39 (a) Profile along the current Porosita fault, modified from figure 5.10 to show values of fault length and Dmax. (b) Plot of displacement accrued along the Porosita scarp between 0.360±0.001Ma and present. As illustrated, the maximum displacement rate during this period (0.25mmyr^{-1}) was located close the position of intersection of the Entashata and Porosita faults.

5.3 The Esiteti Region

The precise Geodetic coordinates of the GPS positional points referred to in this section are included in Appendix A and can be found in Microsoft Excel file Esiteti.xls. Positional data used to construct the fault displacement-length plots are provided in Excel file Esitetidldata.xls.

5.3.1 Reconstruction at 0.493±0.001Ma

Tilting and faulting of the Olorgesailie Lake sediments, described in section 4.4.2, allows a tight constraint to be placed on the most recent period of fault activity along the Esiteti scarp. The Olorgesailie Prehistoric Site occupies a position on the immediate footwall to the Esiteti fault, at its southernmost tip (figure 5.40a and 5.41). The sediments in this area and further to the east along the Ol Keju Nyiro river have been described in detail by previous workers (Shackleton, 1955; Baker, 1958; Baker and Mitchell, 1976; Isaac, 1978) and can be considered to be the type-locality for the Olorgesailie Formation (see section 4.4.2). Single-crystal ^{40}Ar/^{39}Ar radiometric analyses undertaken on feldspars isolated from tuff, ash and pumice within the sediments have constrained the age of the formation to between 0.992±0.039Ma and 0.493±0.001Ma (Deino and Potts, 1990).

It is generally acknowledged that the majority of fault displacement affecting the Olorgesailie Formation occurred after sediment deposition (Shackleton, 1955; Isaac, 1978). Member 14 of the formation (0.493±0.001Ma) can be identified in both the footwall (Legemunge Plain deposits) and hangingwall (Ol Tepesi Plain deposits) of the Esiteti fault and therefore must pre-date fault movement. Further, post-tectonic, deposition, in the form of the Oltepesi Beds, continued in the hangingwall to the Esiteti fault until 0.215±0.007Ma (Deino and Potts, 1990).

Other regions where the Lacustrine sediments are present can be clearly seen on satellite images as patchy white exposures, located, in the most part, to the south and east of the Esiteti horst (figure 5.40a). The small outlier in the immediate hangingwall to the Esiteti fault (see figure 5.40a) is likely to be an area of sediment that was originally connected to the deposits on the footwall of the Esiteti scarp, but which has since been downthrown and isolated by recent fault movements. As described in section 4.4.2, it is difficult to be certain as to how the small

hangingwall exposure correlates with the type section at the Prehistoric Site. Assuming the youngest members of the Olorgesailie Formation are exposed in the hangingwall locality, offsets across the fault suggest that a significant amount of displacement accumulated along the central section of the Esiteti scarp between 0.493±0.001Ma and 0.215±0.007Ma.

Construction of datum

The friable nature of the Olorgesailie Formation sediments means that they have suffered from considerable erosion and are not well preserved on the footwall to the Esiteti fault. This factor, and the lack of correlation between sedimentary sequences in the different parts of the Esiteti region, makes it difficult to use these rocks as a datum for reconstructing fault growth. However, the spatial distribution of sediments relative to the footwall block and the conformable contact between the diatomites and Plateau Trachytes at the tip of the central Esiteti fault segment provide an age constraint, even if the absolute displacements of the Olorgesailie Formation sediments are difficult to establish.

Using the satellite image in figure 5.40a, it is possible to see a narrow strip of Olorgesailie Formation sediments flooring a 'piggy-back' graben on the back of the main Esiteti fault block. This area lies immediately to the south-west of the patch of sediments at the segment tip and was presumably linked to them prior to uplift along the Esiteti fault. It is likely that the initial areal extent of the sediment on the back of the Esiteti footwall block was relatively large. However, it is clear that recent uplift and erosion along the Esiteti fault have significantly reduced this coverage, such that sediments are now confined to topographic lows and narrow fault graben. Using the assumed pre-existing sedimentary coverage shown in figure 5.40b, it is possible to extrapolate the position of the sediment blanket from the tip of the fault segment on figure 5.42 to cover the section of the fault composed of Plateau Trachytes. Similarly, the patterns of erosion at the southern tip of the Esiteti fault (as described by Shackleton (1955) and Isaac (1978)) suggest that Olorgesailie Formation sediments initially blanketed the crest of the footwall block from the southern fault tip to a distance of approximately x=1450m on figure 5.42. There is little direct evidence from satellite images for any sediment having covered the large central section of the scarp cutting the Limuru Trachytes. If any sediment existed here, it must have since been entirely removed by erosion. However, this seems unlikely since no

erosional remnants of the Olorgesailie Formation were found anywhere along the crest of the Limuru Trachyte block during fieldwork.

Using the above information, it was possible to calculate a minimum fault displacement for the period between 0.493 ± 0.001Ma and 0.215 ± 0.007Ma by restoring GPS datapoints collected along the fault tips back to the level of the cutoff between the hangingwall fill and the footwall scarp. Along the northern section of the scarp, which cuts through flat-lying Plateau Trachytes, this involved taking the arithmetic mean of all GPS displacement values between two points on the flat section of the scarp at $x = 6840$m (tpoint004) and $x = 7200$m (tpoint005) (figure 5.41) and using that average (~35m) to produce a horizontal construction line (figure 5.42). Subsequently, all displacement values recorded along the Esiteti crestal traverses were reduced by 35m, including the extreme southern tip of the fault, to give the plot shown in figure 5.43. This plot shows the South Esiteti fault as composed of two independent fault segments separated by a topographic low which, between 0.992 ± 0.039Ma and 0.493 ± 0.001Ma, remained as a fixed site of Olorgesailie Formation sedimentation.

Key
■ Plateau Trachyte (Plh3)   ■ Ol Tepesi Benmoreite (Plb2)   ■ Ol Keju Nero Basalt (Plb1)   ■ Orthophyre Trachyte
■ Limuru Trachyte (Tvt1)   □ Olorgesailie Formation sediments
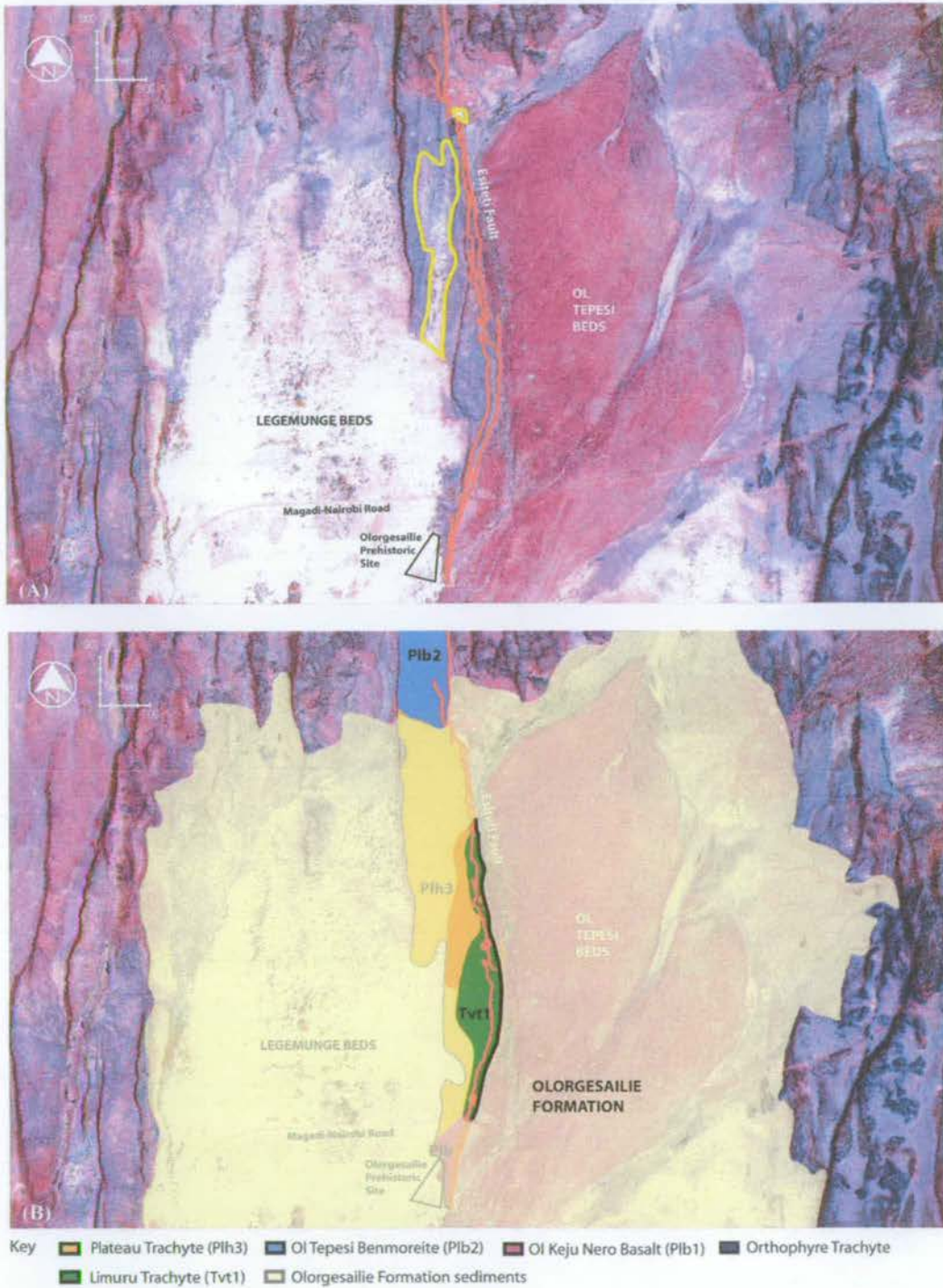
Figure 5.40 (a) Landsat 7 satellite image of the Esiteti region, modified from figure 4.23 to show exposures of Olorgesailie Formation sediments (enclosed by solid yellow lines) in close proximity to the northern section of the measured Esiteti fault (indicated by red lines). Black polygon indicates the location of the Olorgesailie Prehistoric Site. (b) Satellite image overlain with coloured ornament showing the geology and structure of the Esiteti region between 0.992±0.039Ma and 0.493±0.001Ma, when the area was masked by Olorgesailie Formation sedimentation.
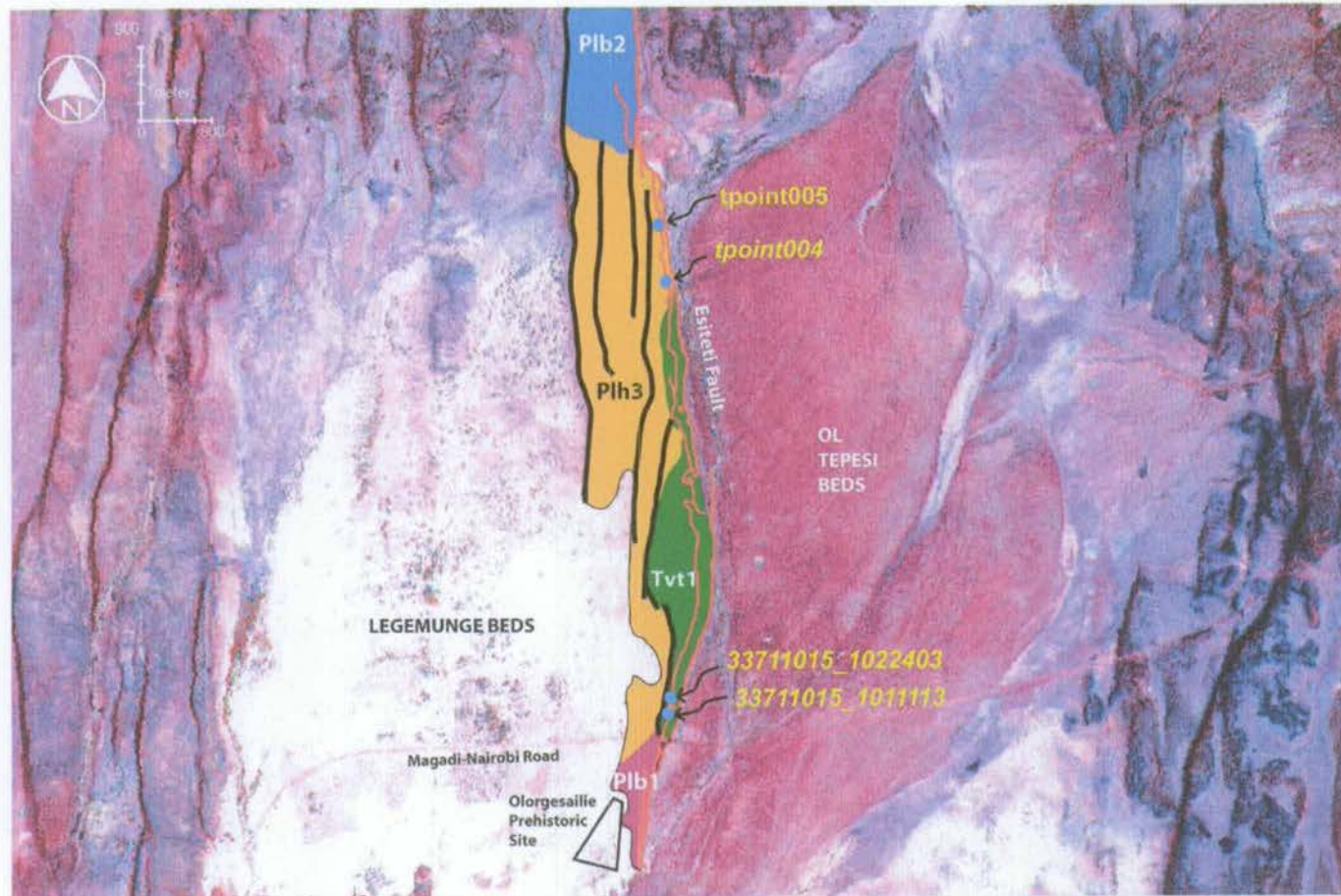
Figure 5.41 Geological map of the Esiteti region, modified from figure 4.23b to show the location GPS points described in section 5.3

S

N

Esiteti fault data

displacement (metres)

tpoint004   tpoint005

distance along fault (metres)
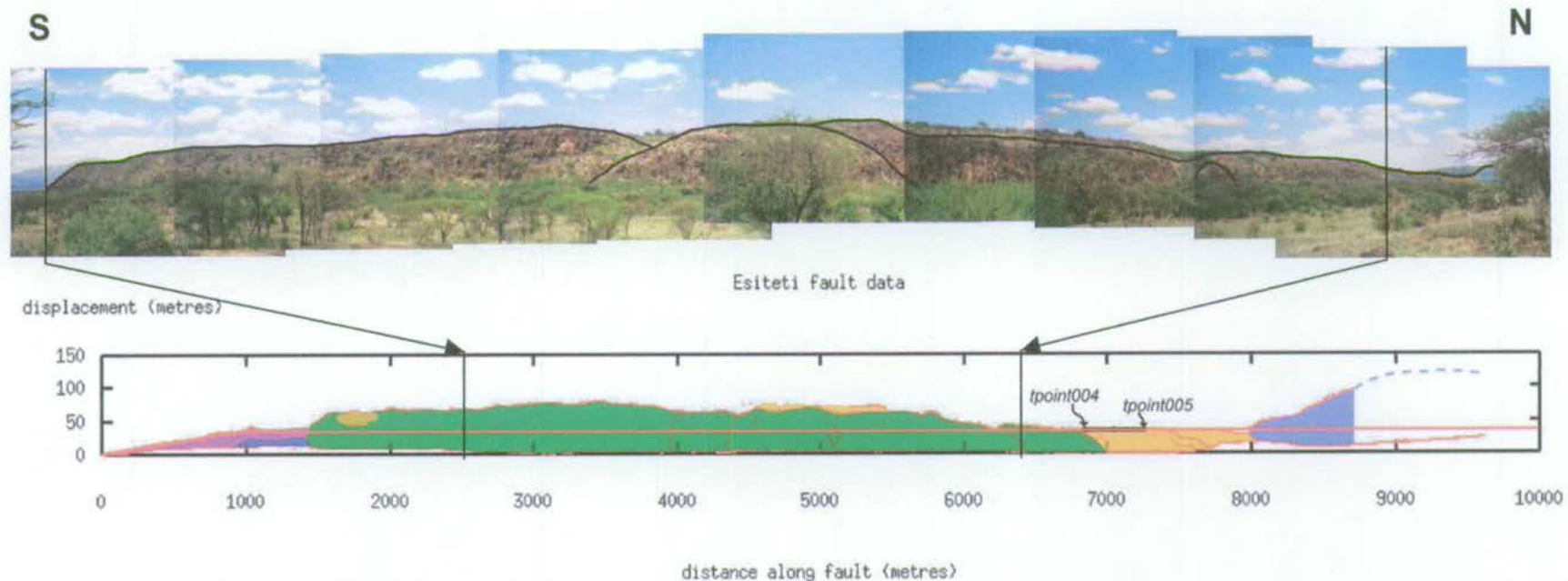
Figure 5.42 Photomontage (above) and displacement-length profile along strike of the Esiteti fault (below) as modified from figure 4.24. Solid black line linking tpoint004 with tpoint005 indicates length along which GPS data collected on the fault crestal traverse were averaged to calculate a control point for the datum surface (shown by the solid red line) used in the reconstruction of the Esiteti fault at 0.493±0.001Ma.

S

N

Esiteti GPS data

displacement (metres)

distance along fault (metres)
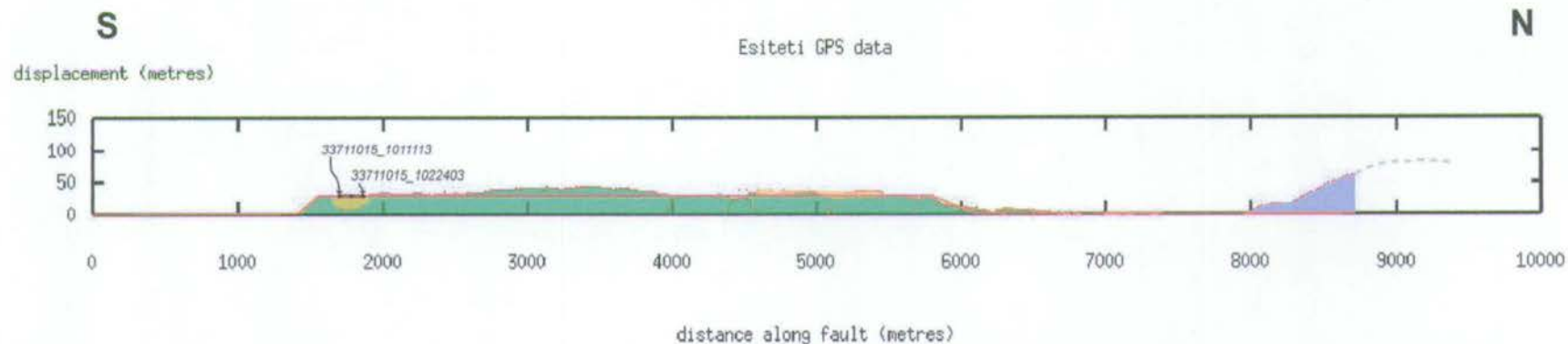
Figure 5.43 Displacement-length profile along the Esiteti fault at 0.493±0.001Ma. At this time, the scarp consisted of two independent fault segments (of Benmoreite (pale blue) and Limuru Trachyte (dark green)) separated by a topographic low, which was the site of Olorgesailie Formation sedimentation between 0.992±0.039Ma and 0.493±0.001Ma. The most southerly of the two Plateau Trachyte exposures located at the crest of the Limuru Trachyte block (marked in orange) was used to construct the datum surface (shown by the solid red line) used for reconstruction of the Esiteti fault at 1.128±0.007Ma, as discussed in section 5.3.2.

5.3.2 Reconstruction at 1.128±0.007Ma

The distribution of Plateau Trachyte lavas across the Esiteti region allows for another reconstruction to be generated, representing an earlier phase of fault growth. As discussed in section 4.4.2, the Plateau Trachytes are encountered in three locations along the crest of the Esiteti scarp. The primary exposure is located at the northern tip of the southern fault segment, where the fault dissects two conformable flows between x=6844m and x=8000m on figure 5.42. As discussed in section 3.3.12, the upper of these two flows has been dated to 1.128±0.007Ma. Elsewhere there is also a narrow facing of trachyte attached to the southern end of the main Limuru Trachyte block (between x=1690m and x=1870m on figure 5.42) and a thin mantle of lava along the crest of the scarp between x=4450m and x=5090m.

As with previous fault restorations, the upper surface of the Plateau Trachyte is assumed to have acted as an equipotential during lava eruption. The uniform thickness of the two flows dissected by the northern section of the fault suggests that the lavas were erupted onto a reasonably horizontal surface. Since the upper flow can be followed onto the crest of the Limuru Trachyte horst it is likely that this, rather than the lower flow, makes up the Plateau Trachyte exposures mantling the southern end of the scarp, even though, in practice, the flow onlap contact is difficult to follow in the field. This assumption is essential for the following restoration.

As can be seen from figure 5.42, the small Plateau Trachyte exposures mantling the main Limuru Trachyte fault block at the centre of the southern Esiteti fault segment currently have experienced larger amounts of displacement than the lava located further to the north. The most plausible explanation for this observation is differential uplift caused by movement along both the central section of the Esiteti scarp and along the smaller, antithetic faults located immediately to the west (figure 5.41).

Construction of datum

Reconstructing movement along the central Limuru Trachyte block was achieved by adjusting the heights of the GPS positional data such that the upper surface of the Plateau Trachyte lava exposures were allowed to lie along a horizontal datum. This datum, which represents the palaeo-groundsurface immediately following lava eruption, corresponds to the construction line

used in section 5.3.1. Of the two Plateau Trachyte exposures blanketing the central Limuru Trachyte block, the most southerly, between x = 1690m (autopoint 33711015_1011113) and x = 1870m (autopoint 33711015_1022403), (figure 5.41 and 5.43) is most well constrained by GPS data. The average displacement value of 245 datapoints, collected along the upper surface of the southern exposure, was calculated and used as a control point for a horizontal construction line (figure 5.43). The height difference between the construction line and the datum (29m) represents the a mount o f differential u plift a long t he L imuru T rachyte b lock. H ence, f or t he purposes of this reconstruction, all GPS heights along the crest of the scarp, between x=1550m, at the southern end of the Limuru Trachyte block and x =5780m, where the displacement decreases at the convergence point of the Esiteti scarp and an antithetic scarp located directly to the west, were lowered by 29m (see figure 5.43). A displacement-length plot for the Esiteti fault at 1.128±0.007Ma is shown in figure 5.44. At this time the Limuru Trachyte block had a much flatter, trapeszoidal-shaped, displacement-length profile, which was partially overlapped by Plateau Trachyte lava.

Figure 5.44 Displacement-length profile along the Esiteti fault at 1.128±0.007Ma, immediately following deposition of the Plateau Trachyte lavas. The red line indicates the position of the Plateau Trachyte datum or 'paleo-groundsurface' at this time, taken along the upper surface of the Plateau Trachyte flow.

5.3.3 Geological history of the Esiteti Region

a) 1.995±0.004Ma - 1.128±0.007Ma

The earliest stage in the geological history of the Esiteti region brackets the period of eruption and deformation of the Limuru Trachyte and Ol Tepesi Benmoreite lavas. An $^{40}Ar/^{39}Ar$ date taken from one of the upper Limuru Trachyte flows indicates that deposition of this formation had ceased by 1.995±0.004Ma. Early deformation and uplift along the Limuru Trachyte block at the centre of the profile shown in figure 5.42 is therefore constrained to between 1.995±0.004Ma and the time of deposition of the Orthophyre Trachyte at the southern end of the block (dated at 1.654±0.006Ma).

The Ol Tepesi Benmoreite was the product of localised volcanism at the northern end of the South Esiteti fault. This volcanic activity, which may have occurred contemporaneously with early faulting of the Limuru Trachytes in the south, took place at 1.856±0.010Ma. Hence, early activity along the large Benmoreite block shown in figure 5.42, is constrained between 1.856±0.010Ma and the time of eruption of the Plateau Trachytes (1.128±0.007Ma), which onlap the southern tip of the block.

Figures 5.45 and 5.46 show displacement-length profiles for the Limuru Trachyte and Benmoreite blocks at 1.654±0.006Ma and 1.128±0.007Ma respectively. Locations of maximum displacement (D_{max}) for each fault segment are as indicated on the profiles and have values of 52m for the Limuru Trachyte block and 96m for the measured section of the Benmoreite block. The d/L ratios for these blocks are 0.02±0.01 and 0.06±0.03 respectively. Using a footwall uplift to hangingwall subsidence ratio of 1:2 to calculate total displacements, displacement rates at the position of D_{max} are 0.27±0.14mmyr^{-1} and 0.30±0.15mmyr^{-1} for the Benmoreite and Limuru Trachyte blocks respectively.

Subsequent to the initial period of deformation, another phase of volcanism saw deposition of Ol Keju Nero Basalt at the southern end of the Esiteti fault. This was followed, at 1.128±0.007Ma, by deposition of the Plateau Trachyte flows, which flooded the pre-existing fault blocks and partially buried the crest of the Limuru Trachyte horst (figure 5.47).
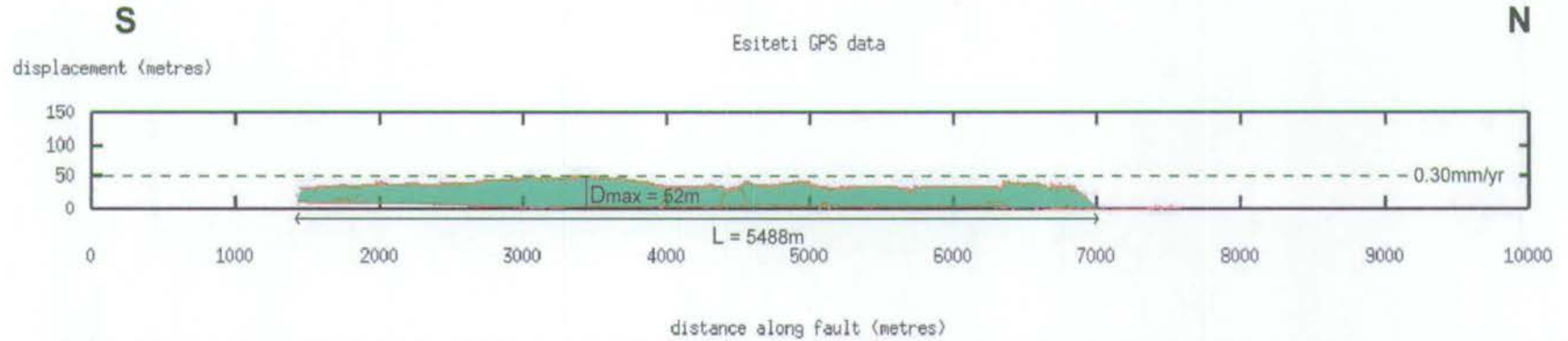
Figure 5.45 Displacement-length profile along the Limuru Trachyte fault segment at 1.654±0.006Ma, immediately prior to eruption of the Orthophyre Trachyte.
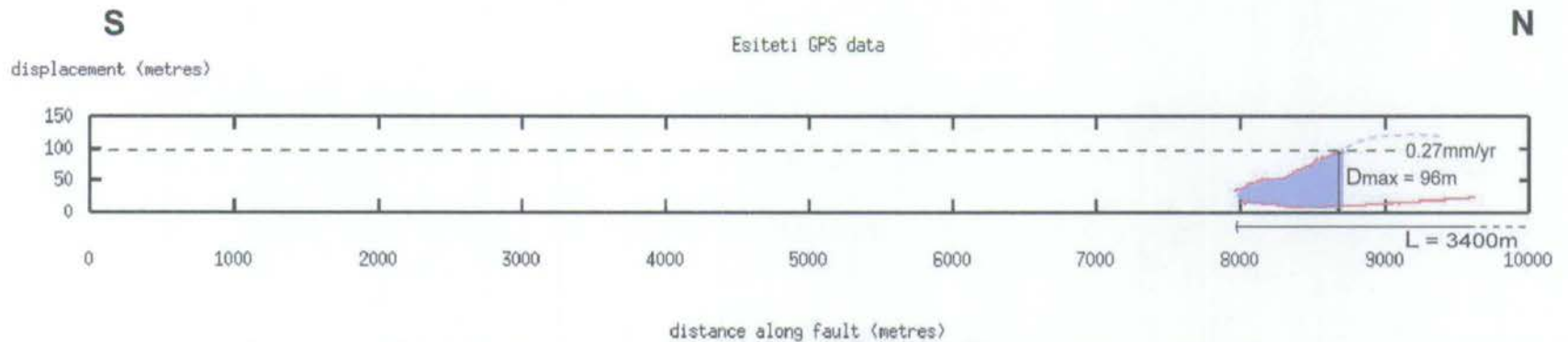
Figure 5.46 Displacement-length profile along the southern section of the Benmoreite horst block at 1.128±0.007Ma, prior to eruption of the Plateau Trachyte lavas. Fault length was measured from georeferenced Landsat7 satellite images.

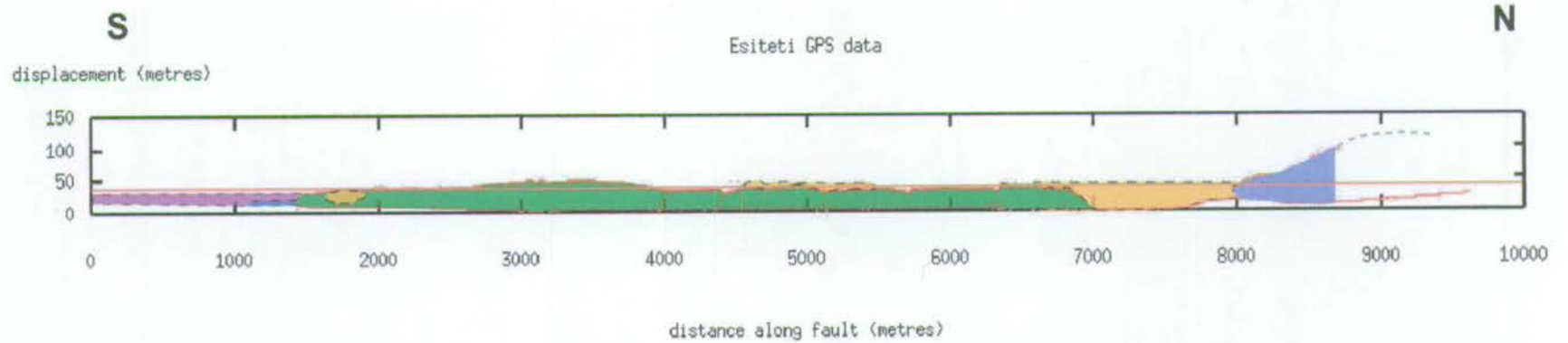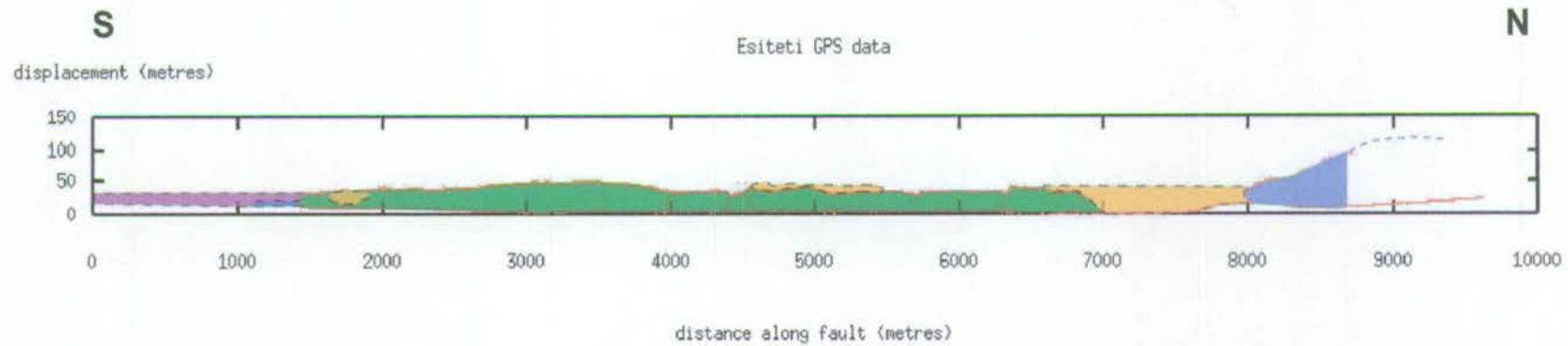**Figure 5.47 Profile along the Esiteti fault at 1.128±0.007Ma, immediately following eruption of the Plateau Trachyte lavas.**

b) 1.128±0.007Ma - 0.992±0.039Ma

Following eruption of the Plateau Trachytes, a second period of tectonic activity uplifted both sides of the Limuru Trachyte block, creating obvious Plateau Trachyte lava facings at the scarp crest. The displacement-length profile for the South Esiteti fault is replotted in figure 5.48a. Figure 5.48b shows the displacement accrued along the fault between 1.128±0.007Ma and 0.992±0.039Ma. The maximum displacement rate along the Limuru Trachyte block during this period was 0.43±0.25mmyr^{-1}.

c) 0.992±0.039Ma – 0.215±0.007Ma

Between 0.992±0.039Ma and 0.493±0.001Ma the area covering the Ol Tepesi and Legemunge Plains was the location of Lake Olorgesailie and its surrounding floodplain. Lacustrine deposits were laid down in the topographic low area between the Limuru Trachyte and Benmoreite segments of the Esiteti fault during this period.

The youngest sediments of the Olorgesailie Formation (member 14) were deposited by 0.493±0.001Ma, prior to a further period of movement along the Esiteti fault. This latest phase of activity occurred along, at least, the 9km length of the measured section of the South Esiteti fault and hard-linked the Limuru Trachyte and Benmoreite fault blocks (figure 5.49a). Olorgesailie Formation sediments on the footwall to the Esiteti fault became uplifted to form the Legemunge Plain, while those in the hangingwall to the east were downthrown and buried by the tuffaceous gravels of the Oltepesi Beds at 0.215±0.007Ma.

The nature of fault activity, if any, between 0.215±0.007Ma and present is unknown due to a lack of dateable rocks younger than the Oltepesi Beds. Assuming all the current displacement along the Esiteti fault accumulated prior to 0.215±0.007Ma, then the maximum fault displacement rate between 0.493±0.001Ma and 0.215±0.007Ma would have been 0.23±0.11mmyr^{-1} (figure 5.49b). This value is calculated by assuming a value of 60m to represent the thickness of sediments in the hangingwall to the Esiteti fault (taken from studies by Shackleton (1955) and Bye *et al.* (1987) which suggest that the Olorgesailie Formation is 50-60m in thickness).

A displacement-length profile for the present-day South Esiteti fault is shown in figure 5.49a. Taking hangingwall sediments into account, the d/L value for this scarp is 0.02±0.01.
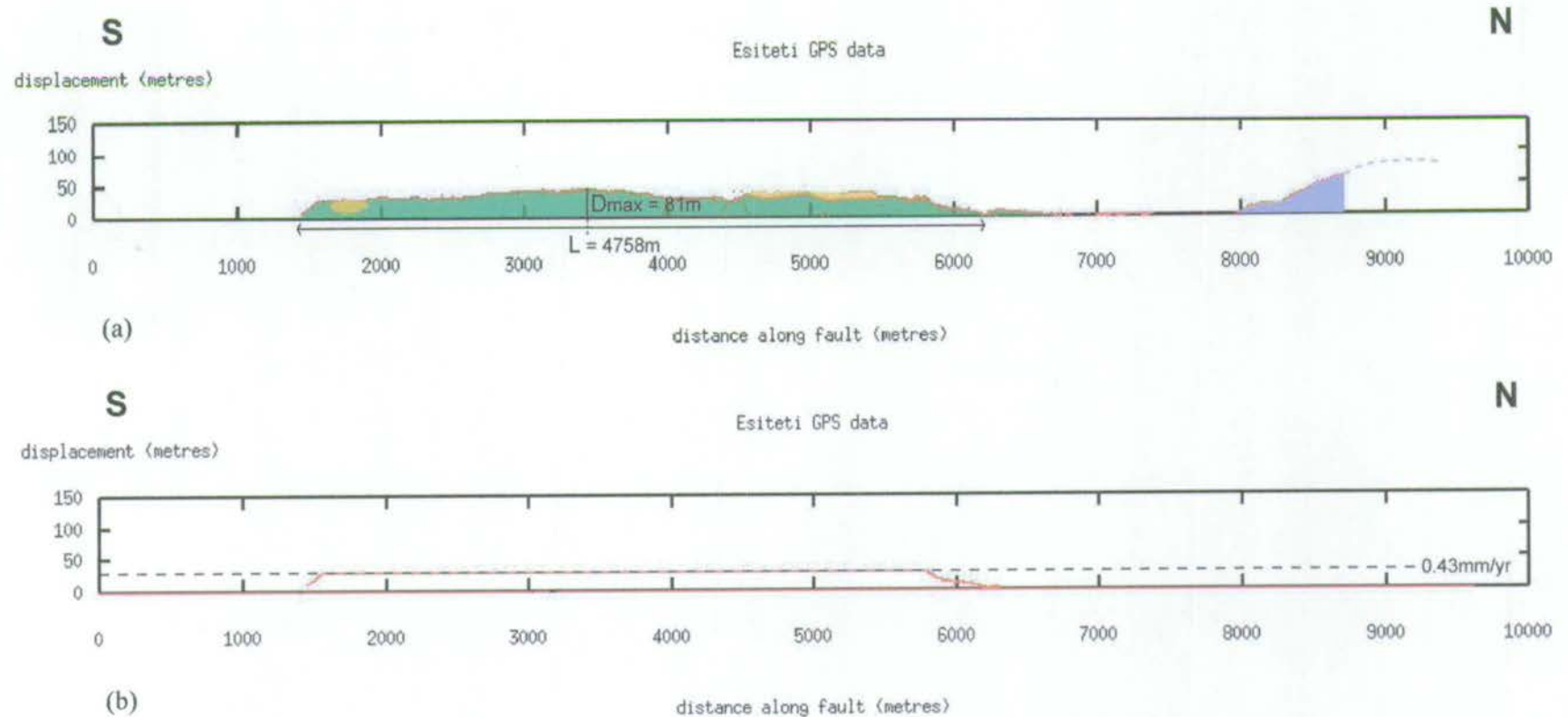
Figure 5.48 Restoration of the Esiteti fault between 1.128±0.007Ma and 0.992±0.039Ma. (a) Displacement-length profile at 0.992±0.039Ma, as replotted from figure 5.43 to show fault dimensions. Note that since the datum for this plot is the upper surface of the unfaulted Plateau Trachytes, the value of Dmax incorporates displacement accumulated before (see figure 5.45) and after Plateau Trachyte eruption. (b) Displacement accrued along the Esiteti fault between 1.128±0.007Ma and 0.992±0.039Ma, showing the maximum uplift rate along the Limuru Trachyte block as 0.43mmyr^{-1}.
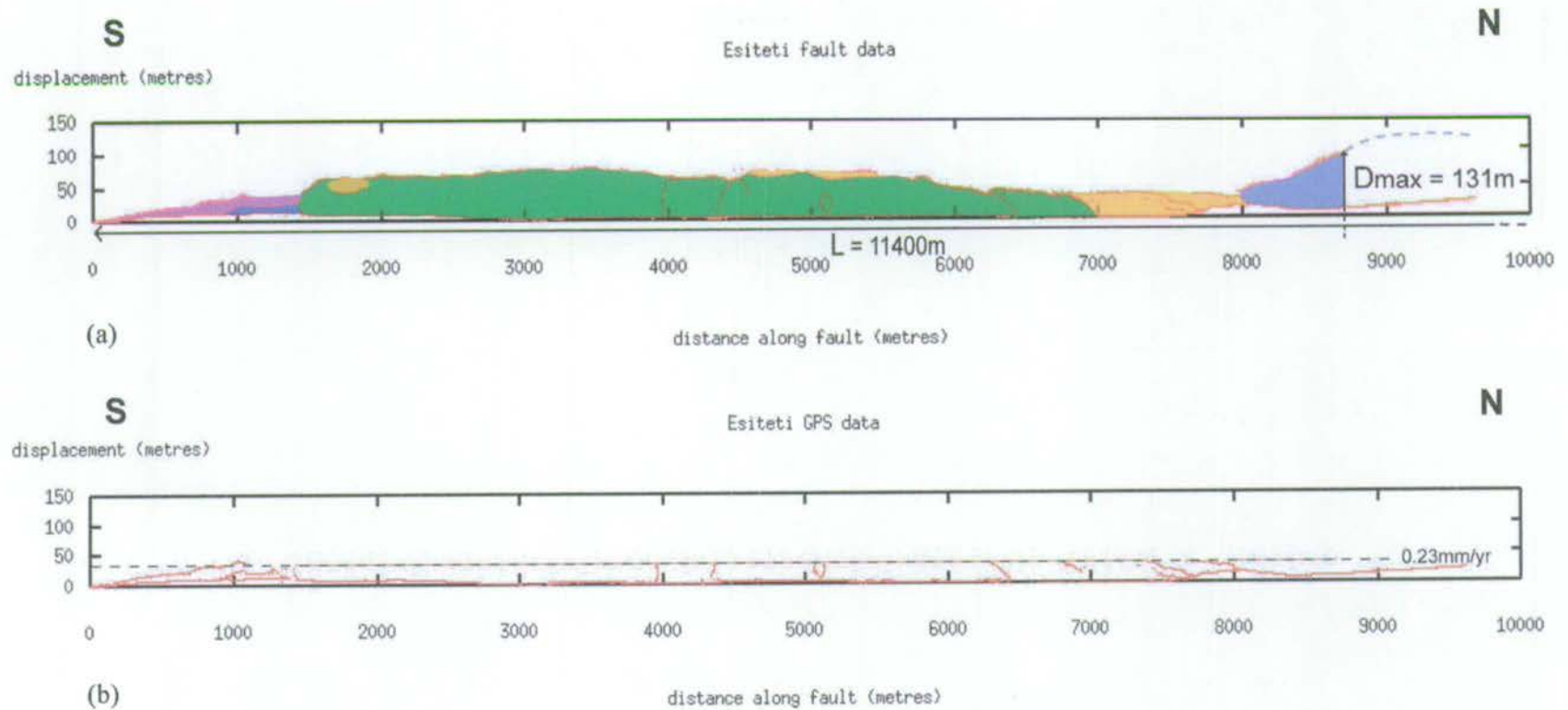
Figure 5.49 Restoration of the Esiteti fault between 0.493±0.001Ma and present. (a) Fault displacement-length profile at present, modified from figure 5.42 to show fault dimensions. Value of Dmax incorporates displacement accumulated along the Ol Tepesi Benmoreite block before and after Plateau Trachyte eruption (c.f. figure 5.48). Fault length was measured from georeferenced Landsat 7 satellite images. (b) Plot of displacement accrued along the Esiteti fault between 0.493±0.001Ma and present.

5.4 The Ilainymok Region

The Geodetic coordinates of the raw GPS data collected along the Ilainymok fault, and referred to in the following text, are included in Appendix A, within Microsoft Excel file Ilainymok.xls. Data from the East Ilainymok fault are located in file Ilainymokeast.xls. Positional data used to construct the displacement-length plots for the Ilainymok and East Ilainymok faults are provided in Excel files Ilainymokdldata.xls and Ilainymokeastdldata.xls respectively, also as part of Appendix A.

5.4.1 Reconstruction at 0.937±0.004Ma

The approach to making a restoration of displacements along the Ilainymok fault (figure 5.50) is similar to the methods described in the previous sections. As discussed in section 4.5.2, the Ilainymok fault has a gentle, bell-shaped profile, with a maximum displacement located at a distance of 1318m along the measured GPS profile (figure 5.51). By using the surface of the Upper Magadi Trachyte flow as a palaeo-datum it is possible to restore the fault displacement between 0.937±0.004Ma and present. Assuming the Upper Magadi Trachyte surface behaved as an equipotential during lava eruption and flowed passively into localised topographic lows, an accurate representation of fault topography at 0.937±0.004Ma can be reconstructed by restoring GPS elevations collected along the surface of the flow back to the horizontal. This is a reasonable assumption since there is little regional-scale tilting of the landsurface, unlike in the Kedong area.

Key ▪ Lower Magadi Trachyte flow □ Upper Magadi Trachyte flow
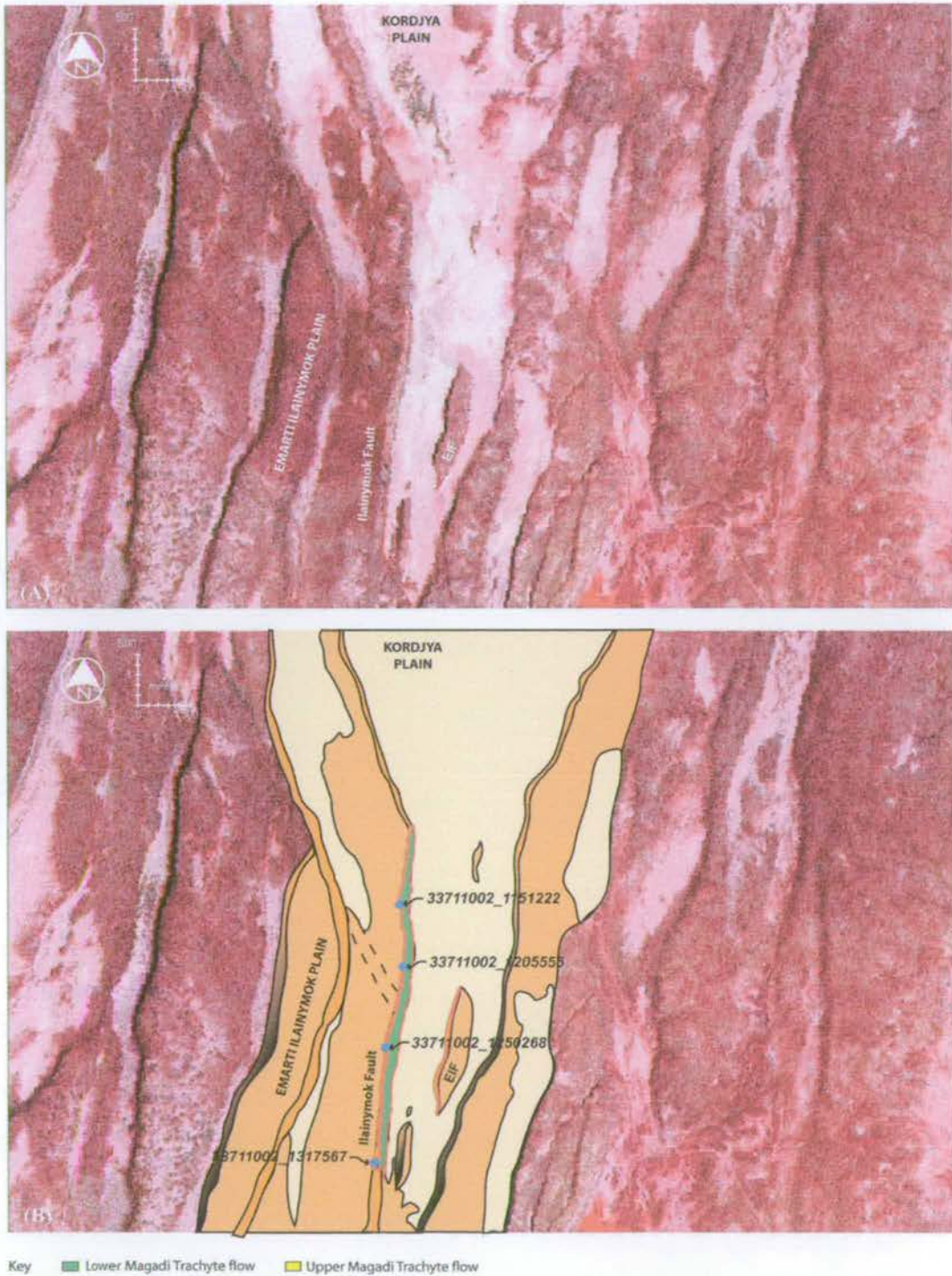
Figure 5.50 (a) Landsat 7 satellite image of the Ilainymok region, showing locations of the Ilainymok fault and East Ilainymok fault (EIF). (b) Structural map, modified from figure 4.27, showing the locations of GPS points discussed in the text (indicated by pale blue points).
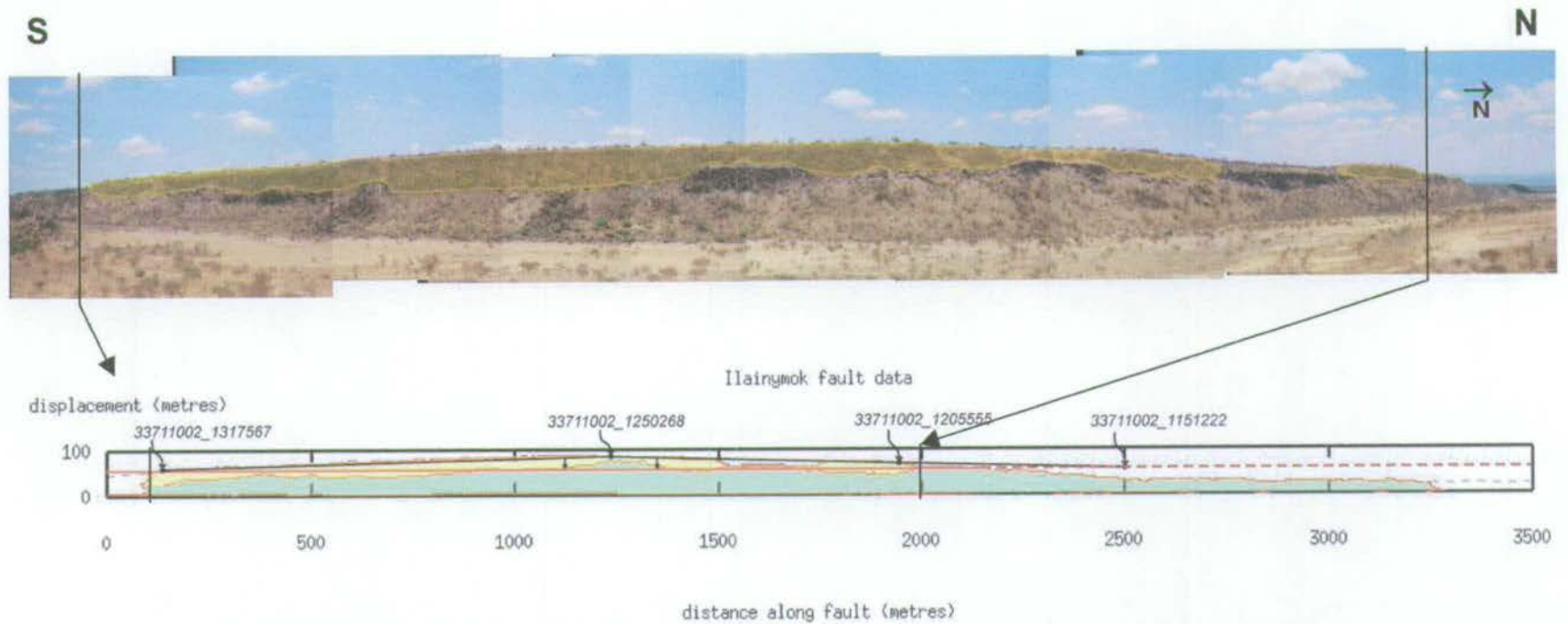
Figure 5.51 Photomontage (above) and displacement-length profile (below) along the strike of the Ilainymok fault, as modified from figure 4.28. Points annotated on the displacement-length profile represent control points used to define construction lines (indicated by solid black lines) that are required to rotate crestal GPS points back to the datum surface (indicated by the red line). The datum is shown dashed where it is extrapolated beyond the northern limit of Upper Magadi Trachyte exposure.

Construction of datum

In order to restore the surface of the Upper Magadi Trachyte flow back to the horizontal it was necessary to select a simple geometrical operation that would account for the positions of all the GPS datapoints. At the southernmost end of the profile (figure 5.51), displacements increase approximately linearly from 53m at x=100m (autopoint: 33711002_1317567) to 85m at x=1320m (autopoint: 33711002_1250268). With these as reference points it was possible to restore the intervening GPS data back to the horizontal by performing a rotation about a pivot fixed at autopoint [33711002_1317567] using the following equation:

$$H(x)_{0.937} = H(x)-[(L(x)-L(33711002\_1317567))\cdot\tan\theta_{10}] \tag{5.24}$$

$$\text{And} \quad \tan\theta_{10} = [H(33711002\_1250268)-H(33711002\_1317567)]/[L(33711002\_1250268)-L(33711002\_1317567)] \tag{5.25}$$

Where: $H(x)_{0.937}$ is the elevation at point x at 0.937 ± 0.004Ma, $H(x)$ is the present elevation at point x, $H(33711002\_1250268)$ is the elevation at autopoint $33711002\_1250268$, $H(33711002\_1317567)$ is the elevation at autopoint $33711002\_1317567$, $L(x)$ is the latitude of point x, $L(33711002\_1250268)$ is the latitude at autopoint $33711002\_1250268$ and $L(33711002\_1317567)$ is the latitude at $33711002\_1317567$.

A similar technique was adopted for the northern section of the measured scarp, though this section was slightly more complicated as a result of the intermittent nature of the upper flow exposure in this area (figure 5.51). Ignoring the short wavelength displacement undulations (discussed in section 4.5.2), this section of the scarp shows a steady decrease in displacement from 85m at x=1320m to 29m at x=2500m (autopoint: 33711002_1151222). North of this point, cumulative fault displacement remains fairly constant. Since a major premise of the reconstruction is the use of the upper flow surface as a datum, in places where no flow actually exists it is necessary to 'extrapolate' the position of the flow towards the north to provide an 'imaginary' datum surface. GPS data along this section of the scarp were therefore restored in two stages. Initially, a construction line was generated between two known points on the surface of the upper flow, one at x=1320m (autopoint 33711002_1250268) and the other towards the

northern limit of flow exposure at x=1950m (autopoint: 33711002_1205555). The slope of this line is given by:

$$\tan\theta_{11} = [H(33711002\_1250268)-H(33711002\_1205555)]/[L(33711002\_1205555)-L(33711002\_1250268)]$$ (5.26)

Where: $\tan\theta_{11}$ is the slope of the construction line, H(33711002_1250268) is the elevation at autopoint 33711002_1250268, H(33711002_1205555) is the elevation at autopoint 33711002_1205555, L(33711002_1250268) is the latitude at autopoint 33711002_1250268 and L(33711002_1205555) is the latitude at autopoint 33711002_1205555.

Secondly, using an identical slope, the construction line was extrapolated to x=2500m. It was then possible to restore GPS points at the crest of the scarp and along the inter-flow palaeosol between x=1320m and x=2500m back to the horizontal with the aid of equation (5.27):

$$H(x)_{0.937}= H(x)-[(L(33711002\_1151222)-L(x))\cdot\tan\theta_{11}]$$ (5.27)

Where: $H(x)_{0.937}$ is the elevation at point x at 0.937±0.004Ma, H(x) is the elevation at point x, L(x) is the latitude of point x, L(33711002_1151222) is the latitude at autopoint 33711002_1151222

To the north of x=2500m, the GPS points were maintained in their original positions.

Figure 5.52 shows a displacement-length plot for the pre-cursor Ilainymok fault at 0.937±0.004Ma. This diagram clearly illustrates the undulating upper surface of the Lower Magadi Trachyte flow that resulted from movement along an early, precursor, fault train.

Ilainymok fault data

displacement (metres)

distance along fault (metres)
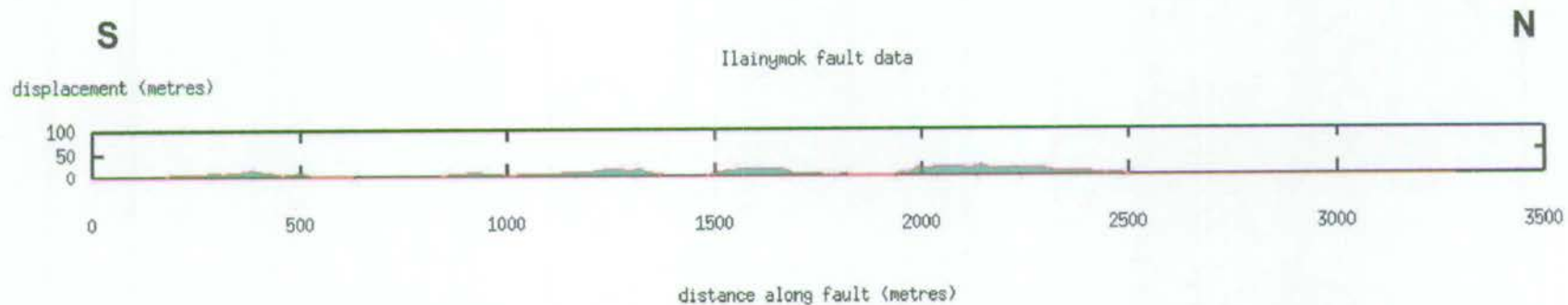
Figure 5.52 Displacement-length profile along the Ilainymok fault at 0.937±0.004Ma. This plot illustrates the undulating fault-generated topography present immediately prior to eruption of the Upper Magadi Trachyte flow.

5.4.2 Geological History of the Ilainymok Region

a) 1.121 ± 0.003Ma – 0.937 ± 0.004Ma

The earliest significant event to affect the Ilainymok region was the eruption of the Lower Magadi Trachyte flow at 1.121 ± 0.003Ma. As discussed above, this flow was subsequently dissected by a train of small, roughly bell-shaped fault blocks, each ~200-500m in length. A displacement-length profile along the blocks illustrates the undulating nature of the topography at this time (figure 5.53). The d/L ratios for these small scarps varied between 0.07 ± 0.04 and 0.13 ± 0.07 and time-averaged displacement rates for this period were a maximum of 0.23 ± 0.11mmyr^{-1}.

By 0.937 ± 0.004Ma, the Ilainymok region was flooded by the Upper Magadi Trachyte flow and many of the early fault blocks were buried under the incoming lava (see figure 5.54). However, pre-existing fault-generated topography influenced flow pathways and, towards the northern end of the fault, the lava was baffled by pre-existing fault blocks.

b) 0.937 ± 0.004Ma – Recent

Following eruption of the Upper Magadi Trachyte flow, renewed movement along the pre-existing fault train resulted in a relatively large increase in the dimensions of the Ilainymok fault. Figure 5.55a shows a current displacement-length profile along the fault and indicates the position of D_{max}. As well as linking the precursor fault segments, it can be seen from the profile that the latest phase of tectonic activity dramatically increased both the fault displacement and length. Using a combination of satellite data and the profile shown in figure 5.55a, the d/L ratio for the present-day Ilainymok fault is 0.02 ± 0.01. A plot of displacement accrued along the Ilainymok fault between 0.937 ± 0.004Ma and present is shown in figure 5.55b. Maximum displacements (61m at D_{max}) are associated with the central and southern sections of the fault and decrease to a relatively constant value of 25-30m further to the north. Since the thickness of the hangingwall sedimentary wedge is unknown, displacement rates along this fault were calculated by assuming a footwall uplift to hangingwall subsidence ratio of 1:2, which gives a value of 0.13 ± 0.06mmyr^{-1} at the position of D_{max}.

The antithetic East Ilainymok fault became active following eruption of the Upper Magadi Trachyte flow at 0.937±0.004Ma and developed the bell-shaped displacement-length profile shown in figure 5.56. The d/L ratio for this fault is 0.04±0.02. Assuming a footwall uplift to hangingwall subsidence ratio of 1:2, the maximum vertical displacement rate along the East Ilainymok fault was 0.07±0.03mmyr^{-1}.

S   N

Ilainymok fault data

displacement (metres)
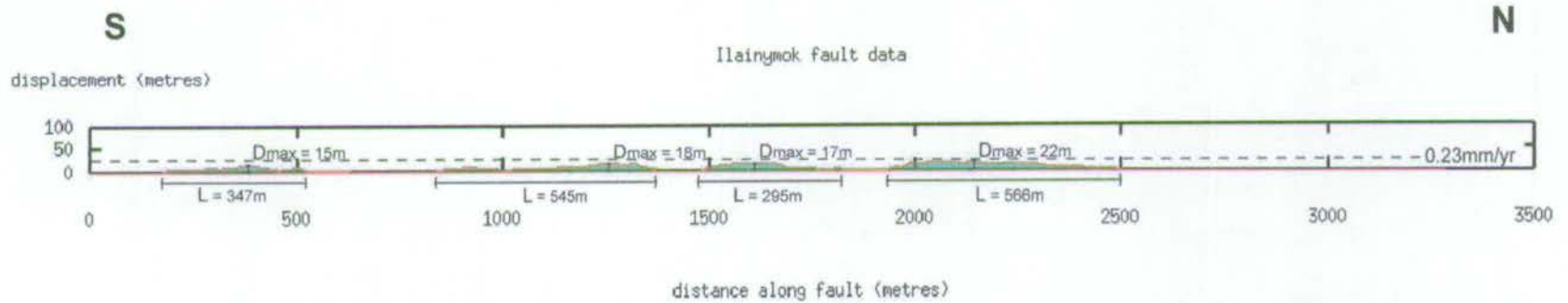
Figure 5.53 Displacement-length profile along the Ilainymok fault at 0.937±0.004Ma, modified from figure 5.52 to show the dimensions of fault blocks comprising the precursor fault train. The maximum displacement rate, between 1.121±0.003Ma and 0.937±0.004Ma, as determined from the largest block in the train, is 0.23mmyr⁻¹.

S   N

Ilainymok fault data

displacement (metres)
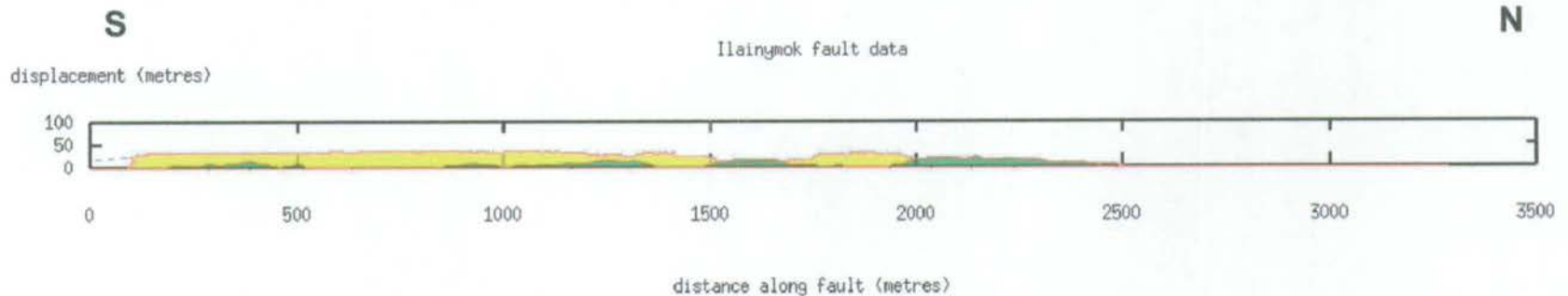
Figure 5.54 Displacement-length profile along the Ilainymok fault immediately following eruption of the Upper Magadi Trachyte flow at 1.121±0.003Ma.
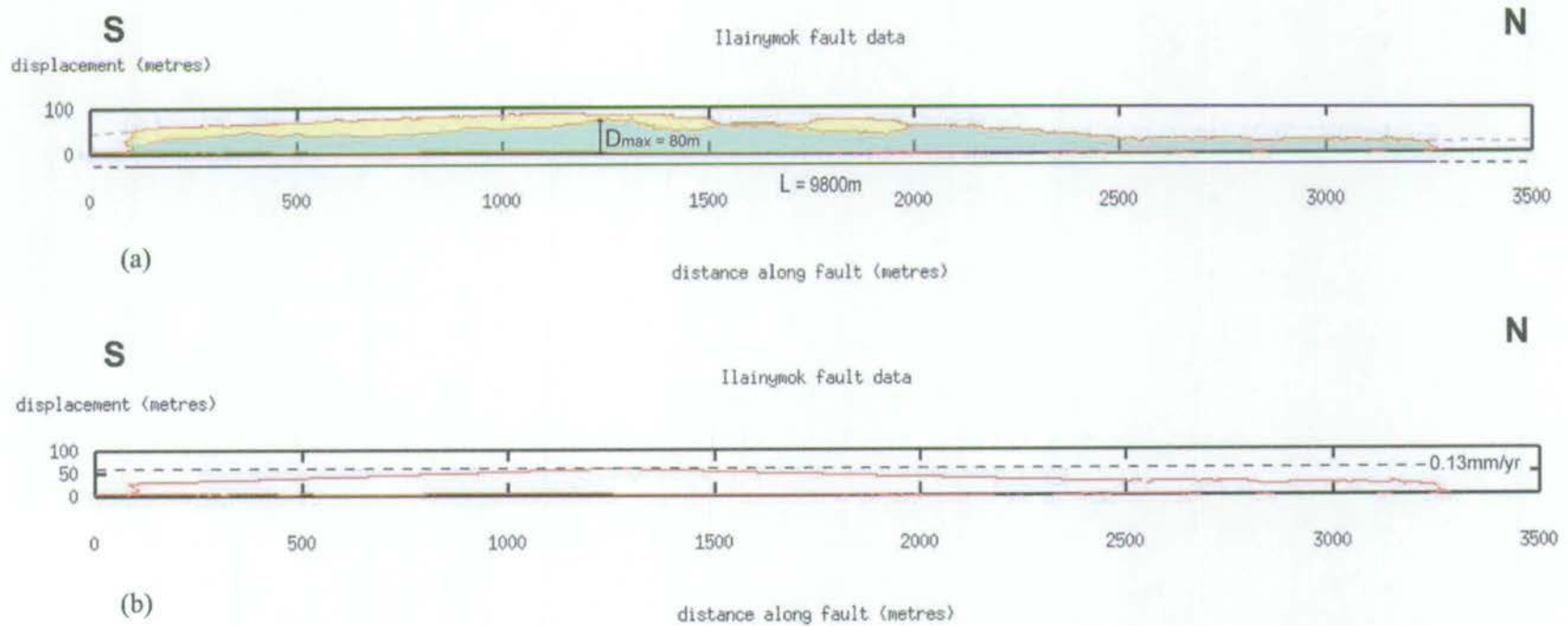
Figure 5.55 Restoration of the Ilainymok fault between 0.937±0.004Ma and present. (a) Displacement-length profile along the fault at present, modified from figure 5.51 to show fault dimensions. Fault length information was measured from georeferenced Landsat 7 satellite images. (b) Plot of displacement accrued on the Ilainymok fault between 0.937±0.004Ma and present. The maximum displacement rate during this period was 0.13mmyr⁻¹, located at a position of x=1320m.
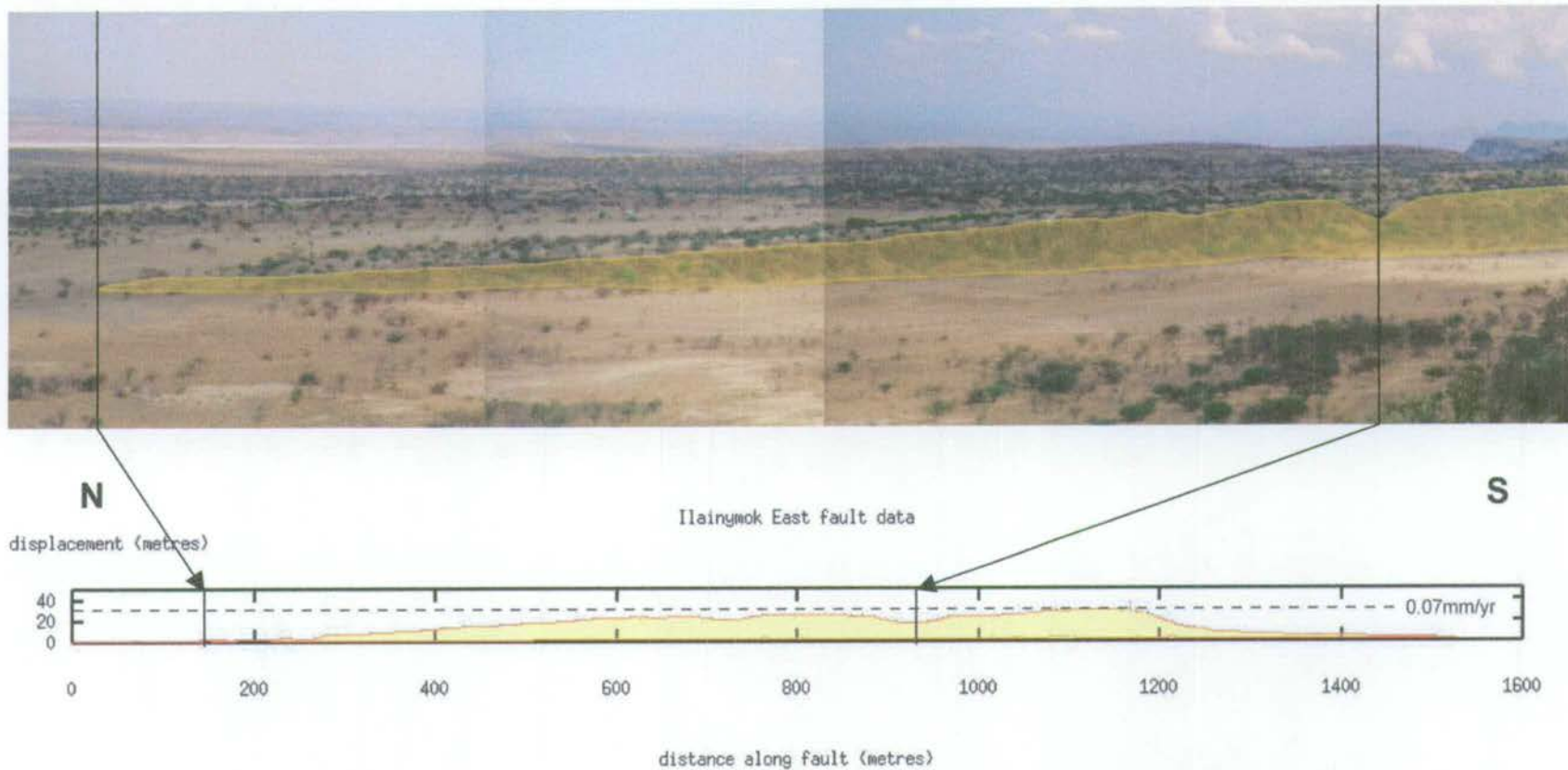
Figure 5.56 Photomontage (above) and displacement-length profile (below) along the East Ilainymok fault. The maximum verical displacement rate is calculated for the period between 0.937±0.004Ma and present.

5.5 The Olooltepes Region

The precise Geodetic coordinates of the GPS positional points referred to in this section are included in Appendix A and can be found in Microsoft Excel file Olooltepes.xls. Adjusted positional data used to construct the fault displacement-length plots are provided in file Olooltepesdldata.xls.

5.5.1 Reconstruction at 1.116±0.002Ma

The ~10m thick Plateau Trachyte lava flow that onlaps the northern tip of the Ileek Pusi horst (figure 5.57, 5.58 and 5.59) provides a useful marker horizon for reconstruction of the Olooltepes scarp at 1.116±0.002Ma. As with the Ilainymok fault restoration, this trachyte flow is assumed to have acted as an equipotential. The reasonably uniform flow thickness at the northern tip of Ileek Pusi suggests that the lava was erupted onto a reasonably horizontal surface at this location. It is therefore possible to reconstruct fault movements between 1.116±0.002Ma and recent by using the onlapping flow as a palaeo-datum. A slight variation to the method used in section 5.4.1 was that the lower, rather than the upper, surface of the flow was selected as the datum horizon, since in this case the basal flow contact was well constrained by GPS data. The other advantage of using the lower contact is that it represents an accurate definition of the ground surface immediately prior to lava eruption.

Construction of datum

It was possible to calculate a minimum fault displacement for the past 1.116±0.002Ma by restoring GPS datapoints collected along the lower surface of the onlapping Magadi Trachyte flow back to the level of the cutoff between the hangingwall fill and the footwall block. This involved taking the arithmetic mean of all GPS displacement values recorded at the base of the onlapping flow (between gpoint001 and gpoint003) and using that average (~59m) to produce a horizontal construction line (figure 5.59). Subsequently, all displacement values recorded along the base of the Magadi Trachyte flow were reduced by 59m, while every point on the upper surface of the lava was set to zero. As described in section 4.6.2, the crest of the Ileek Pusi horst gradually loses displacement from north to south, largely as a result of the fault movement

localised a t the n orthern t ip o f t he h orst d uring t he l ast 1 .116±0.002Myr. G PS d isplacement values collected on the northernmost crest of the Ileek Pusi horst were also reduced by 59m, as were four of the interpolated values measured towards the northernmost end of the Ileek Pusi crest from a 1:50,000 scale topographic map of the Olooltepes region. The result of these restorations is the plot shown in figure 5.60. This diagram shows the situation at 1.116±0.002Ma, immediately prior to eruption of the onlapping Plateau Trachyte flow (Olooltepes flow 2). Restoration of GPS and map data has given the Ileek Pusi horst a flatter, more symmetric profile and has removed the southward tilt along the crest of the block.
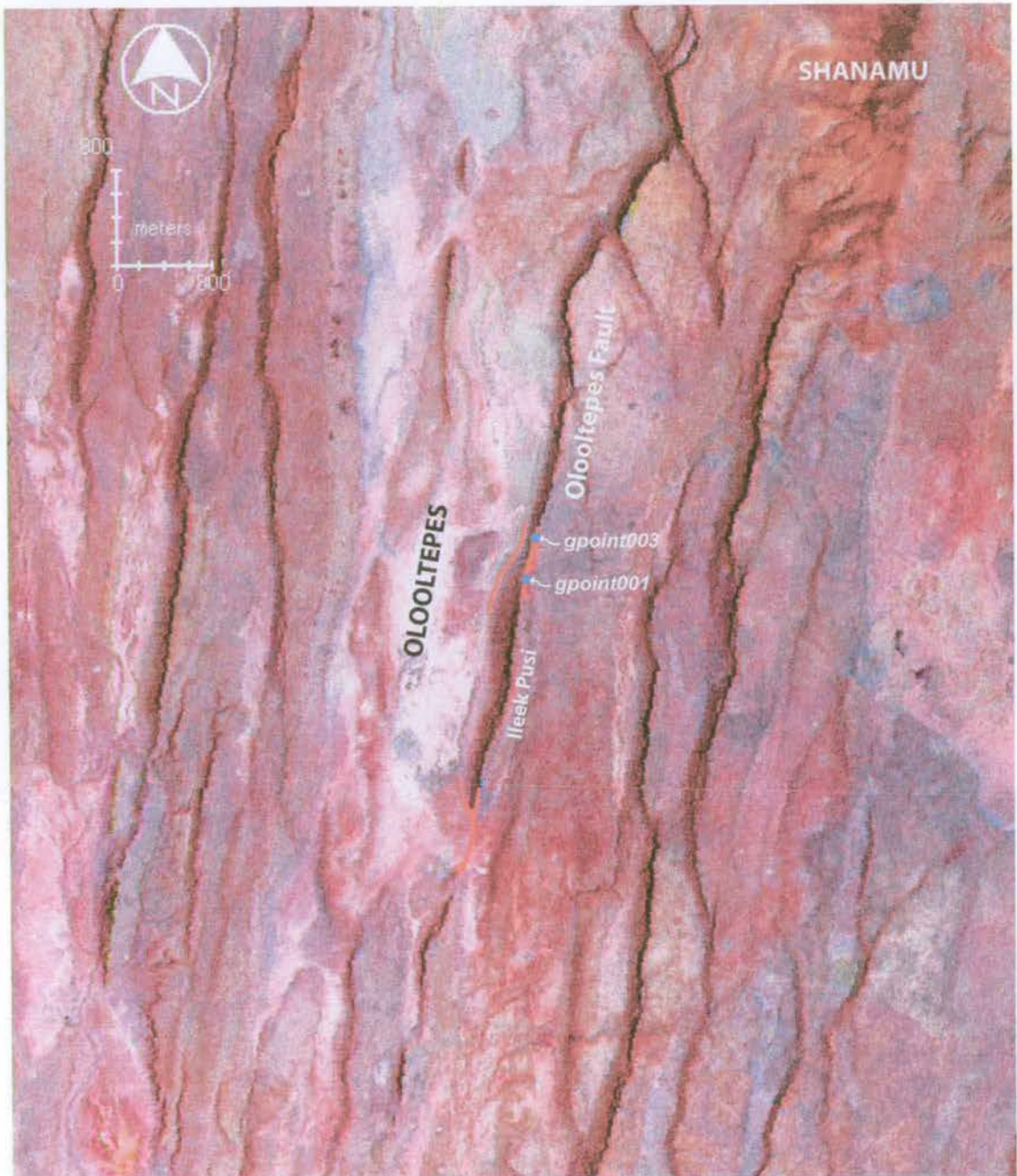
Figure 5.57 Landsat 7 satellite image of the Olooltepes region, modified from figure 4.31 to show the locations of GPS control points (indicated in pale blue) used in the fault restoration described in section 5.5.1.
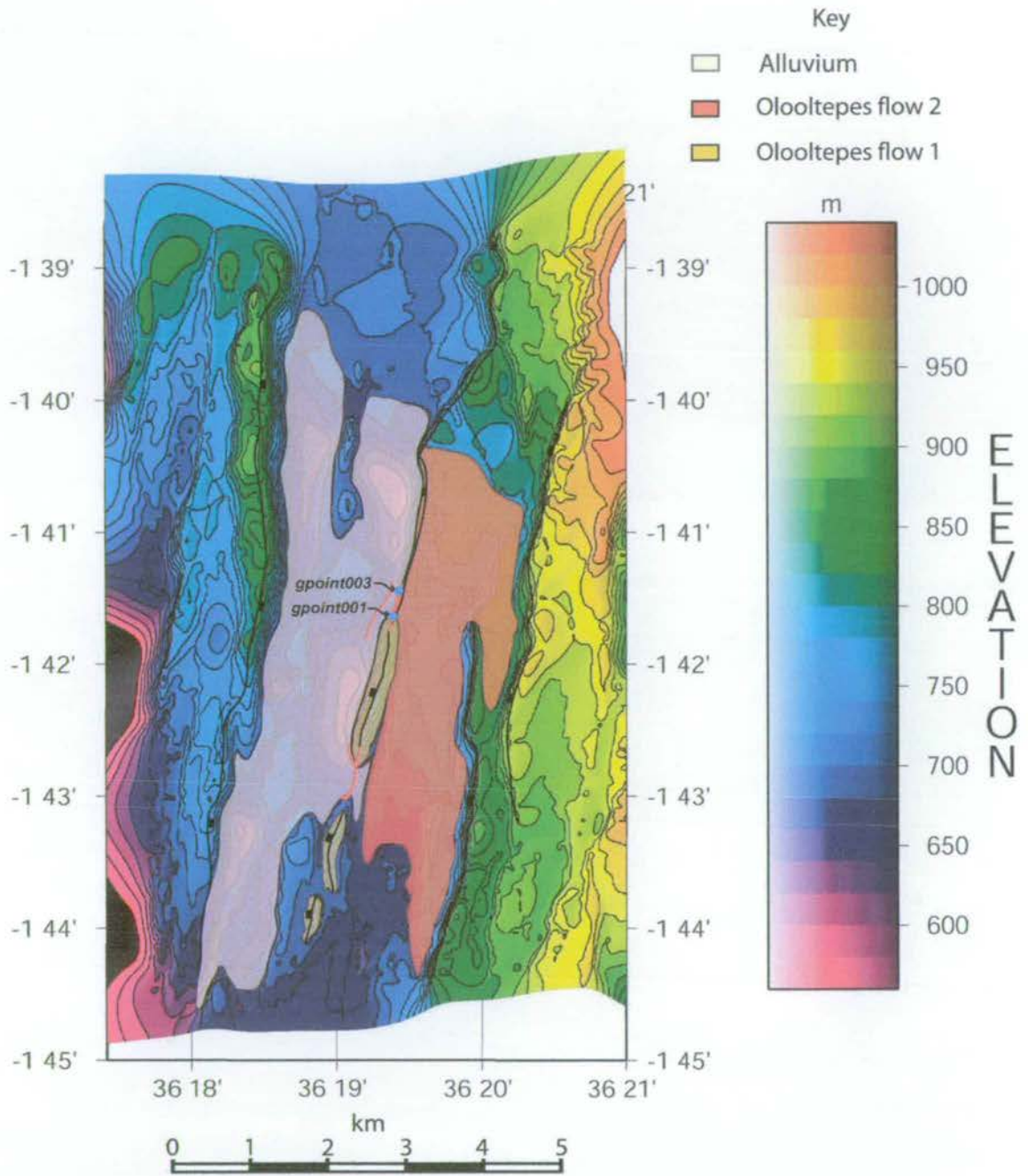
Figure 5.58 Topographic plot of the Olooltepes region, as redrawn from figure 4.32. This GMT-based plot has been partially overlain by transparencies illustrating local geology. Also shown are the locations of GPS control points displayed in figure 5.57.
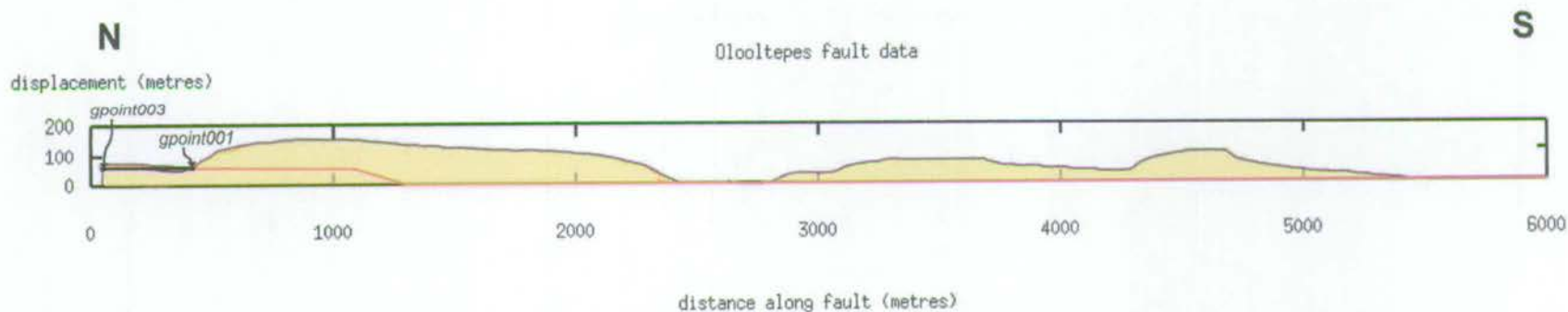
Figure 5.59 Displacement-length profile along the Olooltepes fault, redrawn from figure 4.33. Solid black line linking gpoint001 with gpoint003 indicates length along which GPS data, collected on the fault crestal traverse, were averaged to calculate a control point for the datum surface (shown by the solid red line) used in the reconstruction of the Olooltepes fault at 1.116±0.002Ma.
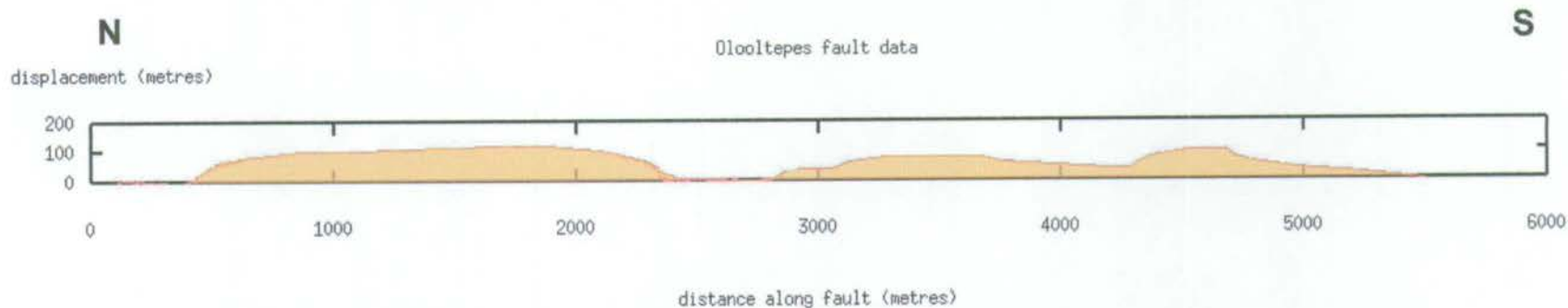
Figure 5.60 Displacement-length profile along the Olooltepes fault at 1.116±0.002Ma. Obvious from this plot are the independent horst blocks of the pre-cursor fault train.

5.5.2 Geological History of the Olooltepes Region

a) 1.134±0.002Ma-1.116±0.002Ma

By 1.134±0.002Ma, regional volcanism had resulted in eruption of the older of the two Magadi Trachyte flows that were sampled in the Olooltepes region. Immediately subsequent to deposition, the lava was intensely faulted to create the ~10km long train of horst blocks north of Lake Magadi, the most northerly of which is the Ileek Pusi horst. As can be seen from the displacement-length profile replotted in figure 5.61, the horsts are characteristically ~1-2km in length, with a minimum of ~100m of vertical displacement, giving a d/L ratio of ~0.07-0.11 (after the thickness of hangingwall sediments has been taken into account). The rate of uplift of these horst blocks was rapid, with a maximum of 12.20±5.90mmyr^{-1} at the position of D_{max1} marked on figure 5.61.

At 1.116±0.002Ma, the northern tip of the Ileek Pusi horst was onlapped by the ~10m thick Olooltepes flow 2.

b) 1.116±0.002Ma-Recent

The most recent phase of tectonic activity to affect the Olooltepes region occurred subsequent to deposition of Olooltepes flow 2 and resulted in uplift of the northern tip of the Ileek Pusi horst. Active faulting occurred to the north of ~x = 1.5km on the displacement-length profile shown in figure 5.62a and created an ~20km long, flat, continuous, fault scarp along the western side of Mount Shanamu (see figure 5.57 for detail). A plot showing the displacement accrued on the most southerly part of this active section of the scarp is shown in figure 5.62b. Assuming a footwall uplift to hangingwall subsidence ratio of 1:2, the maximum displacement rate for the period 1.116±0.002Ma-recent was some 0.11±0.05mmyr^{-1}. Taking the length of the fault from satellite data, the current d/L ratio for the Olooltepes fault is 0.02±0.01.
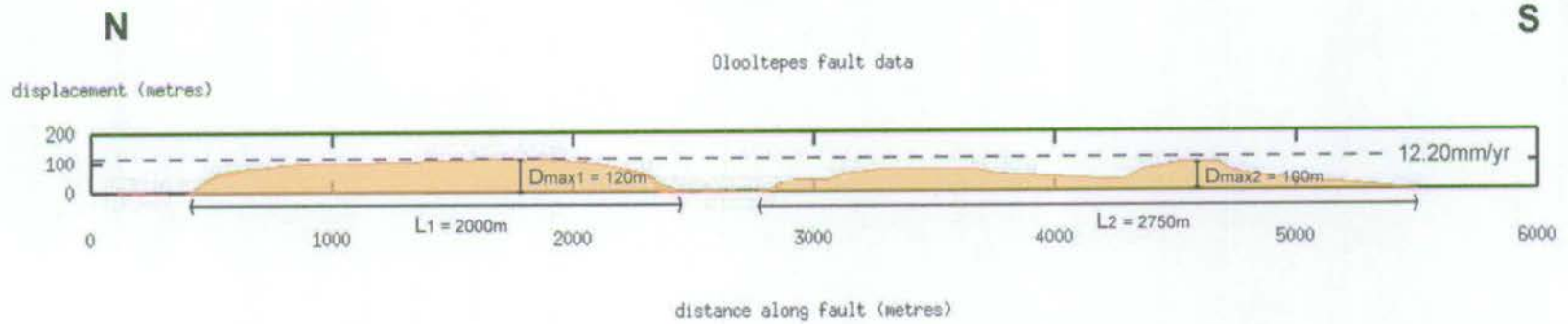
Figure 5.61 Displacement-length plot along the Olooltepes fault at 1.116±0.002Ma, modified from figure 5.60 to show the dimensions of the pre-existing horst blocks. The maximum displacement rate associated with the northernmost horst (Ileek Pusi) is 12.20mmyr[-1], as indicated.
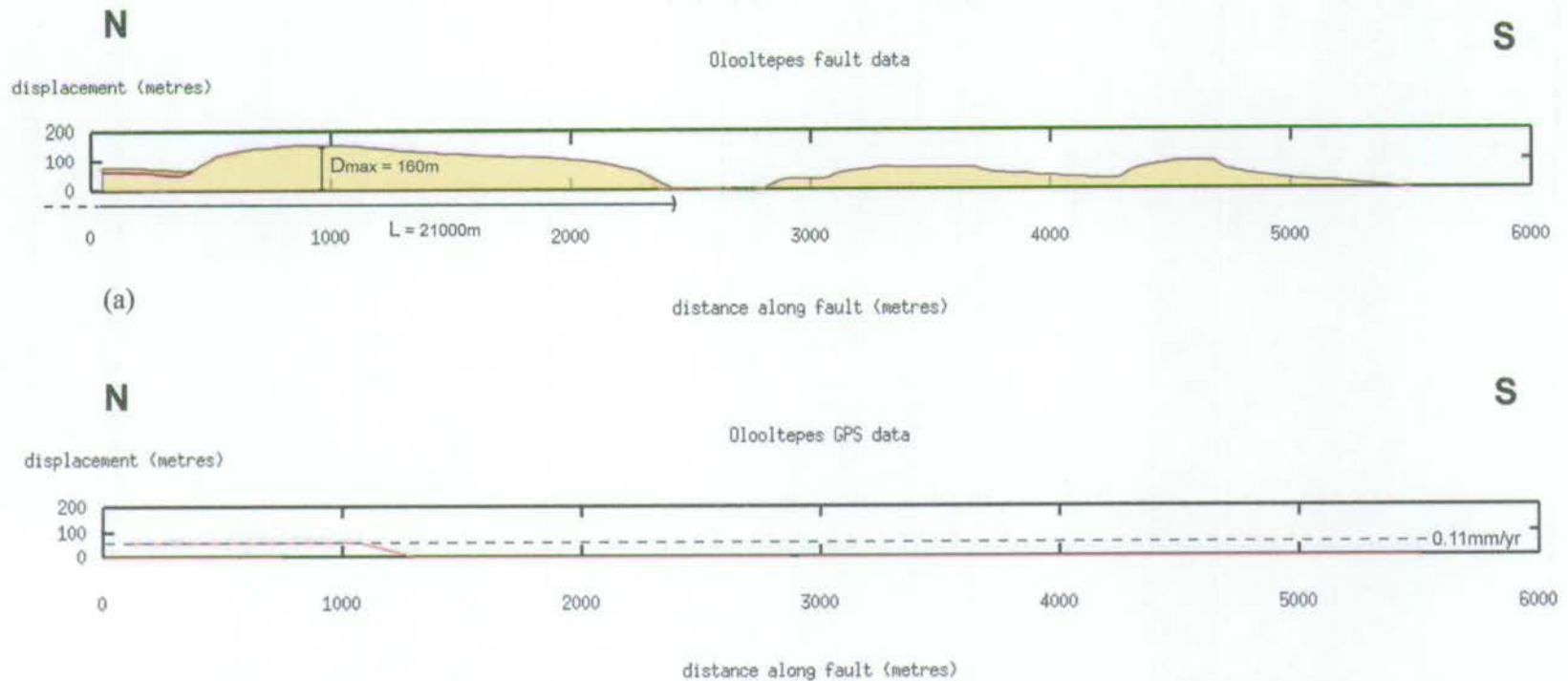
Figure 5.62 Reconstruction of the Olooltepes fault between 1.116±0.002Ma and present. (a) Displacement-length plot modified from figure 5.59 to show fault dimensions. Fault length information was taken from georeferenced Landsat 7 satellite data. (b) Plot of displacement accrued along the Olooltepes fault between 1.116±0.002Ma and present. During this period the northern tip of the Ileek Pusi horst was uplifted at a rate of 0.11mmyr⁻¹.

5.6 Summary

In order to make an accurate spatio-temporal reconstruction of fault growth it is necessary to have a detailed knowledge of fault structural morphology and the relationship between the fault and its associated rock stratigraphy. This chapter combines highly accurate morpho-structural GPS data collected from four localities in the South Kenya Rift with a suite of new lava ages determined from $^{40}Ar/^{39}Ar$ radiometric analyses, to produce a series of detailed fault restorations. The evolution of each fault scarp is presented as a sequence of along-strike displacement-length profiles and, where lava coverage is adequate, as GMT-based structural maps. To undertake each fault reconstruction it was necessary to establish a datum horizon to which the GPS positional data could be adjusted, rotated or translated accordingly. Such an horizon was generally modelled on a lava flow or some other feature that could be assumed to reflect an equipotential surface.

For each fieldarea there is a discussion of structural fault information such as fault dimensions (comprising maximum displacement (D_{max}) and length values), fault displacement rates and, for the Enasira scarp, a fault tip-propagation rate. Fault dimensions and displacement rate data are summarised in table 5.1, accompanied by the associated data errors.

The aim of the following chapter is to assimilate the data of table 5.1 into the pre-existing knowledge base to produce a number of fault growth trends that can be evaluated with respect to the large-scale development of the South Kenya Rift and further considered within the wider context of established numerical and analytical extensional fault models.

Location	Min. disp. during time interval (m)[1]	Disp. error (m)[2]	Sediment thickness	1/2 sediment thickness	Compound disp. error (m)[3]	Est. total displacement[4]	Lava flow ages (ka)	Error in age (ka)	Time interval (ka)	Compound age error (ka)[5]	Disp. rate at Dmax (mmyr⁻¹)	Error in disp. rate at Dmax (mmyr⁻¹)[6]	Est. cum. disp. at end interval (m)[7]	Cum. disp. error (m)[8]	Fault length (m)	Error in length (m)	Dmax/L	Error in Dmax/L
KEDONG																		
Gesumeti	274	27	300	150	152	420	2100	7	91	8	4.70	1.70	420	152	3500	350	0.12	0.05
Trachyte	239	24	300	150	152	390	2009	4			4.30	1.70	390	152	1200	120	0.32	0.13
Horsts (2.100-2.009Ma)	224	22	300	150	152	370					4.10	1.70	370	152	3000	300	0.12	0.05
Entashata (2.009-1.478Ma)	118	8 2	50	25	26	140	2009 1478	4 3	531	5	0.27	0.05	140	26	2200	220	0.07	0.01
Entashata (1.478-0.360Ma)	126	2	50	25	25	150	1478 360	3 1	1118	3	0.14	0.02	170	36	4400	440	0.04	0.01
Porosita (1.478-0.360Ma)	69	2	140	70	70	140	1478 360	3 1	1118	3	0.12	0.06	140	70	1400	140	0.10	0.05
Enasira (1.478-0.360Ma)	42	2	80	40	40	80	1478 360	3 1	1118	3	0.07	0.04	80	40	640	64	0.13	0.06
Porosita (0.360Ma-Present)	80	<0.1	20	10	10	90	360 0	1 0	360	1	0.25	0.03	150	71	5600	560	0.03	0.01
Enasira (0.360Ma-Present)	106	<0.1	20	10	10	120	360 0	1 0	360	1	0.32	0.03	120	10	21700	2170	0.01	0.00
Footwall fault (south) (0.360Ma-Present)	90	<0.1	20	10	10	100	360 0	1 0	360	1	0.28	0.03						
Ndepen (2.009-0.360Ma)	14	<0.1	30	15	15	30	2009 360	4 1	1649	4	0.02	0.01	30	15	400	40	0.07	0.04

Table 5.1 Summary of dimensions and vertical displacement rates for faults surveyed in the South Kedong region. [1]Minimum displacement accrued on the fault in the given time interval. [2]Errors in displacement as calculated for each fault reconstruction. [3]Compound error in displacement calculated by combining individual errors from each fault reconstruction. [4]Estimated total displacement (=minimum displacement + 1/2 sediment thickness) in the given time interval. [5]Compound age error for the given time interval calculated by combining individual errors for each lava flow. [6]Error in vertical displacement rate calculated by combining compound displacement and age errors. [7]Estimated cumulative fault displacement accumulated by the end of the given time interval. [8]Errors in cumulative fault displacement.

Location	Min. disp. during time interval (m)[1]	Disp. error (m)[2]	Geological Error	1/2 sediment thickness	Compound disp. error (m)[3]	Est. total displacement[4]	Lava flow ages (ka)	Error in age (ka)	Time interval (ka)	Compound age error (ka)[5]	Disp. rate at Dmax (mmyr[-1])	Error in disp. rate at Dmax (mmyr[-1])[6]	Est. cum. disp. at end interval (m)[7]	Cum. disp. error (m)[8]	Fault length (m)	Error in length (m)	Dmax/L	Error in Dmax/L
ESITETI																		
Benmoreite segment (1.856-1.128Ma)	96	<0.1	200	100	100	200	1856 1128	10 7	728	12	0.27	0.13	200	100	3400	340	0.06	0.03
Limuru Trachyte seg. (1.995-1.654Ma)	52	<0.1	100	50	50	100	1995 1654	4 6	341	7	0.30	0.15	100	50	5500	550	0.02	0.01
Limuru Trachyte seg. (1.128-0.992Ma)	29	1 1	60	30	30	60	1128 992	7 39	136	40	0.43	0.25	160	58	4800	480	0.03	0.01
Linked Esiteti fault (0.493-0.215Ma)	35	1	60	30	30	70	493 215	1 7	278	7	0.23	0.10	260	104	11400	1140	0.02	0.01
ILAINYMOK																		
Ilainymok segments (1.121-0.937Ma)	22 15 18 17	3 3 3 3	40 40 40 40	20 20 20 20	20 20 20 20	40 30 40 40	1121 937	3 4	184	5	0.23 0.19 0.21 0.20	0.11 0.13 0.10 0.10	40 30 40 40	20 20 20 20	560.0 350.0 550.0 300.0	56 35 55 30	0.07 0.10 0.07 0.13	0.04 0.07 0.04 0.07
Ilainymok (0.937Ma-Present)	61	<0.1	120	60	60	120	937 0	4 0	937	4	0.13	0.06	160	63	9800.0	980	0.02	0.01
East Ilainymok (0.937Ma-Present)	32	<0.1	60	30	30	60	937 0	4 0	937	4	0.07	0.03	60	30	1500.0	150	0.04	0.02
OLOOLTEPES																		
Olooltepes horsts (1.134-1.116Ma)	119 99	6 6	200 200	100 100	100 100	220 200	1134 1116	2 2	18	3	12.20 11.10	5.90 5.80	220 200	100 100	2000.0 2700.0	200 270	0.11 0.07	0.05 0.04
Olooltepes (1.116Ma-Present)	59	<0.1	120	60	60	120	1116 0	2 0	1116	2	0.11	0.05	320	112	21000.0	2100	0.02	0.01

Table 5.1 (continued) Summary of dimensions and displacement rates for faults surveyed in the Esiteti, Ilainymok and Olooltepes regions.

Chapter 6: Discussion

6.1 Introduction

The main purpose of this chapter is to use the collected field data to elucidate the principal fault growth trends in the South Kenya Rift. These trends will be compared with observations described from other field areas and subsurface datasets (see chapters 1 and 2) to produce a synthesis of kilometre-scale normal faulting that is applicable to volcanic rift settings. The observed spatial and temporal variations in fault growth rates will initially be discussed with respect to existing models of fault array growth and fault network development. Features of the Kenyan faults that cannot be explained by the application of these idealised models will then be explained through consideration of complicating factors such as oblique rifting, variations in rheology and changes in both regional (far-field) and local strain rates.

6.2 Synthesis of faulting within the South Kenya Rift

6.2.1 Introduction

Table 5.1 summarises the principal characteristics of faults surveyed during the course of this study, including the dimensions and growth rates as determined from the structural restorations described in Chapter 5. Fault displacement rates are similar to those calculated by Baker *et al.* (1988), in which they describe young, minor faults of the rift floor with rates of 0.1-0.2mmyr^{-1}.

As mentioned in section 5.1.7, it is important to recognise that any calculation of fault displacement rates is dependent on the temporal resolution of the volcanic record. Given the episodic nature of volcanic activity, calculated growth rates are time-averaged over the time interval between eruption of volcanic marker horizons using:

Average vertical displacement rate = <u>(vertical offset in stratigraphy across the fault)</u>　　(6.1)

(time interval)

If, in reality, faulting is highly episodic and is characterised by periods of very rapid growth on a time-scale shorter than the 'volcanic time interval', then the actual vertical displacement rate may be significantly underestimated as a result of averaging displacement rates over long time intervals – i.e. these rate values will represent minima.

Figure 6.1 shows fault growth rates plotted against the length of time interval over which the rates are averaged. The best-fit curve to these data is shown in black and indicates that there is a strong relationship between the calculated displacement rates and the associated time interval. However, a plot of fault displacement against the time interval over which the displacement was accrued (figure 6.2) also indicates that the largest amounts of vertical displacement were generally accumulated during the shortest time intervals. This observation implies that truly high fault displacement rates must have occurred during some of the shortest time intervals and may reflect the fact that fault displacements were accrued more rapidly during periods of increased volcanic activity (characterised by narrower intervals between lava eruptions). However, these observations cannot discount the possibility that over longer time intervals fault growth occurred through a sequence of rapid growth intervals (at similar rates to those recorded during the shorter time intervals) interspersed with periods of relative quiescence. Unfortunately this is an inherent limitation of this dataset.

Although the lavas used in the fault reconstructions described in this study represent useful, and in many cases, areally extensive, marker horizons, there is a lack of temporal constraint between the volcanic episodes. The documented fault growth rates therefore represent a set of 'baseline' values for growth along the scarp. In order to constrain fault growth at a greater temporal resolution, it would be necessary to extend this study by using another technique, perhaps through cosmogenic analysis of footwall rocks. Such a study would require intensive sampling of a selected number of well-exposed fault scarps that have been unaffected by significant erosion or temporary burial since their uplift. Work would be restricted to gaining a further, more detailed, understanding of fault development along a limited number of scarps, using a similar method to that used by Jackson *et al.* (2002b) in their analysis of reverse fault

development and fault tip propagation in Otago, New Zealand. During that detailed study, 11 samples were collected over a 600m distance along the crest of a fault-generated anticline ridge, at its northern tip. The rate of crestal uplift along the ridge was subsequently calculated through the determination of cosmogenic [10]Be exposure ages. Use of such a technique in Kenya would be complimentary to the current study since it would offer improved temporal resolution along faults where areally extensive lavas have already allowed for good spacial control.

The fault data shown in table 5.1 have been plotted graphically in figures 6.3 and 6.4, and will be discussed further in sections 6.2.2 to 6.2.5. Note that fault displacements and time-averaged displacement rate values referred to in the text include an estimate of hangingwall sediment thickness and are not the 'minimum' values shown in the fault displacement-length profiles of the previous chapter or in figures 6.5-6.9.
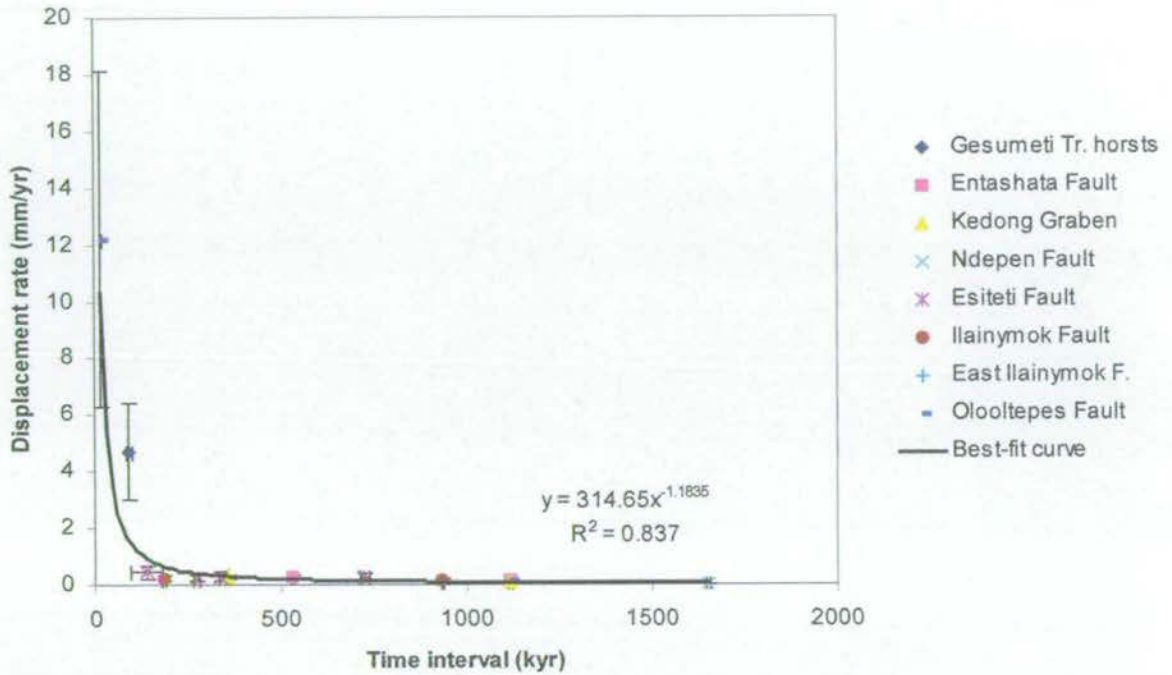
Figure 6.1 Plot of fault displacement rate versus time interval over which the rates are calculated. Solid black line indicates the best fit to the entire fault dataset.
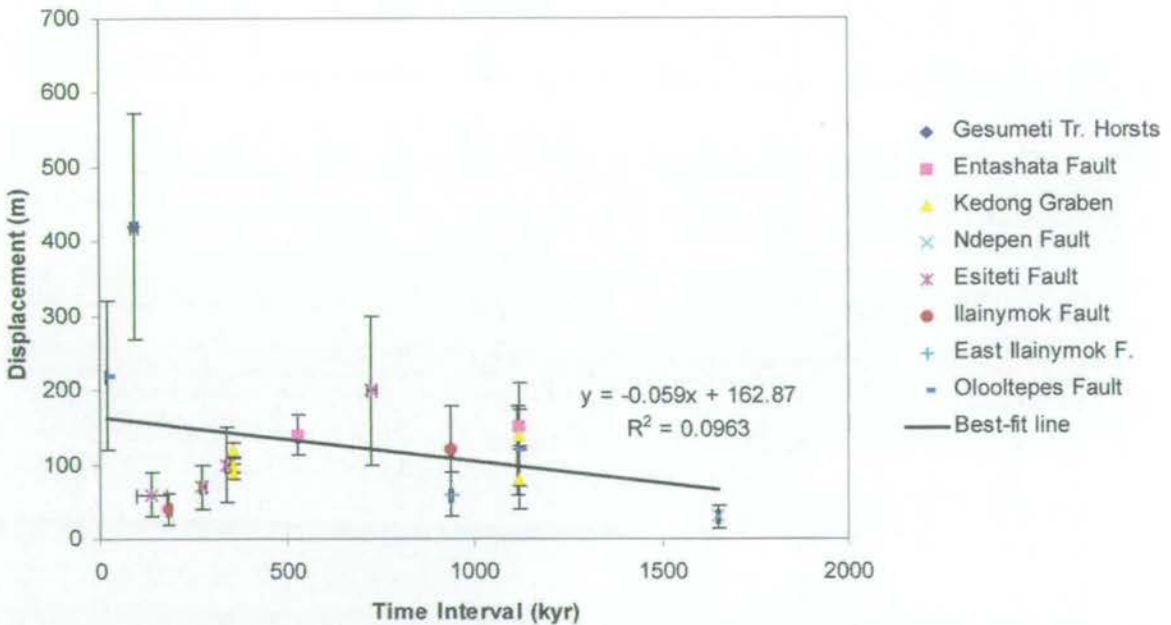
Figure 6.2 Plot of fault displacement versus time interval between eruption of lavas displaced by faulting. Solid black line indicates the best fit to the entire fault dataset.
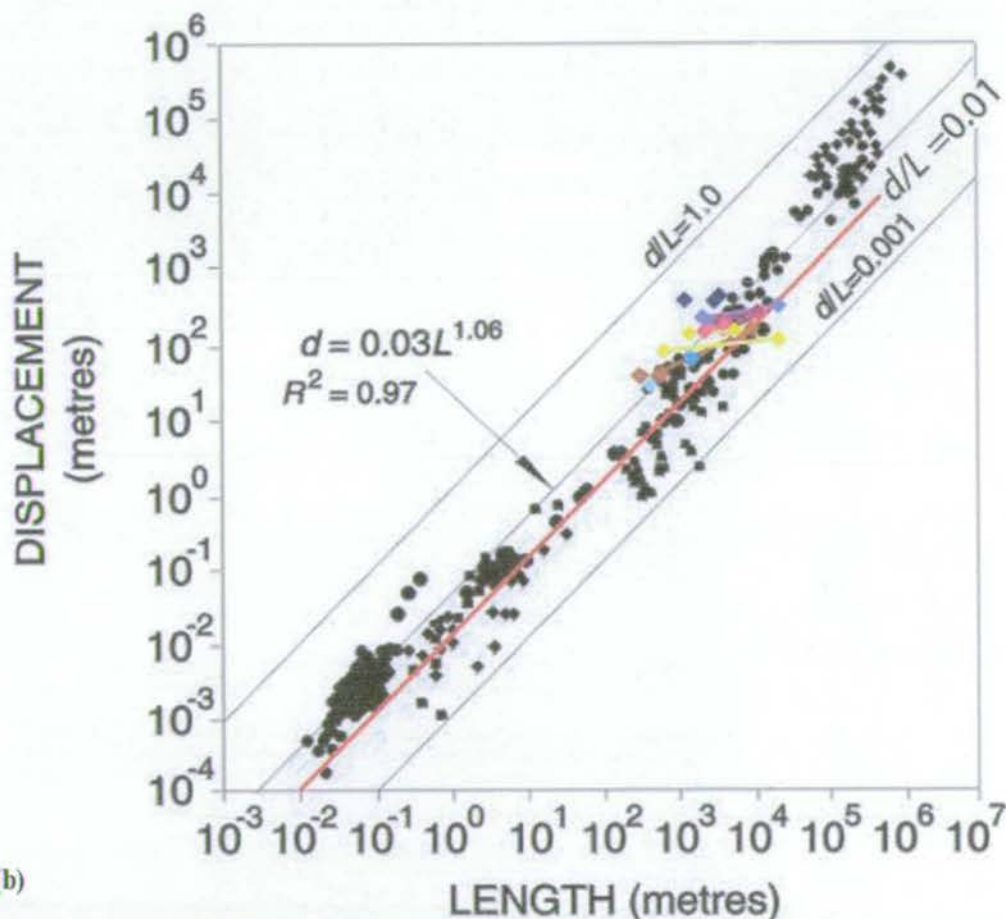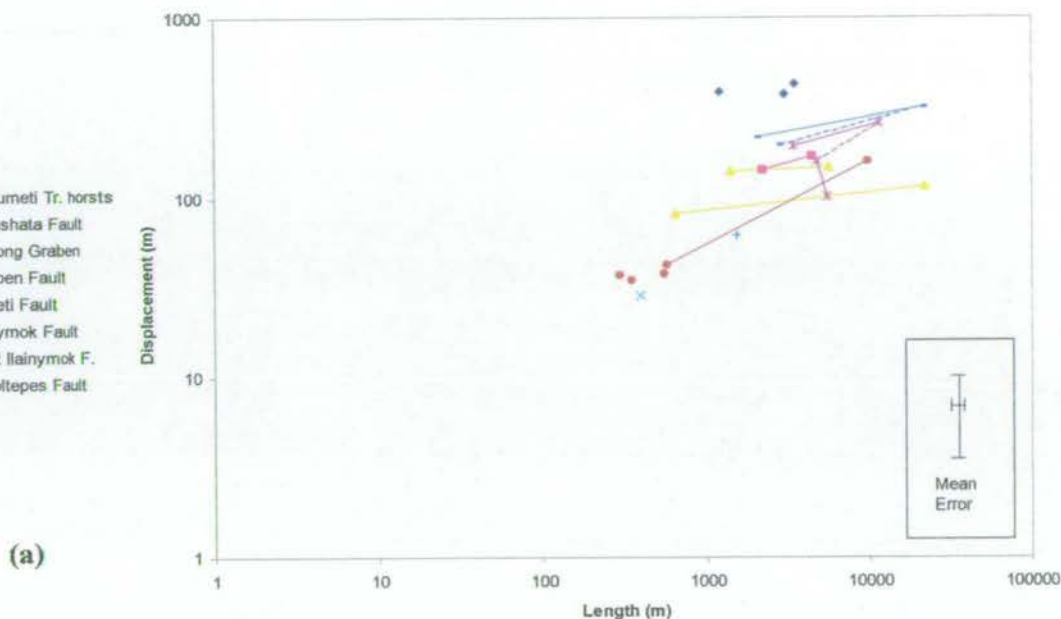
Figure 6.3 (a) Data from the South Kenya Rift shown on a log-log plot of maximum displacement versus length (see section 5.1.7 for details of errors). (b) Kenyan fault data on a log-log plot of maximum displacement versus length for various published fault populations (modified from Morewood and Roberts, 2002). In both diagrams, lines connect points from the same fault dataset.
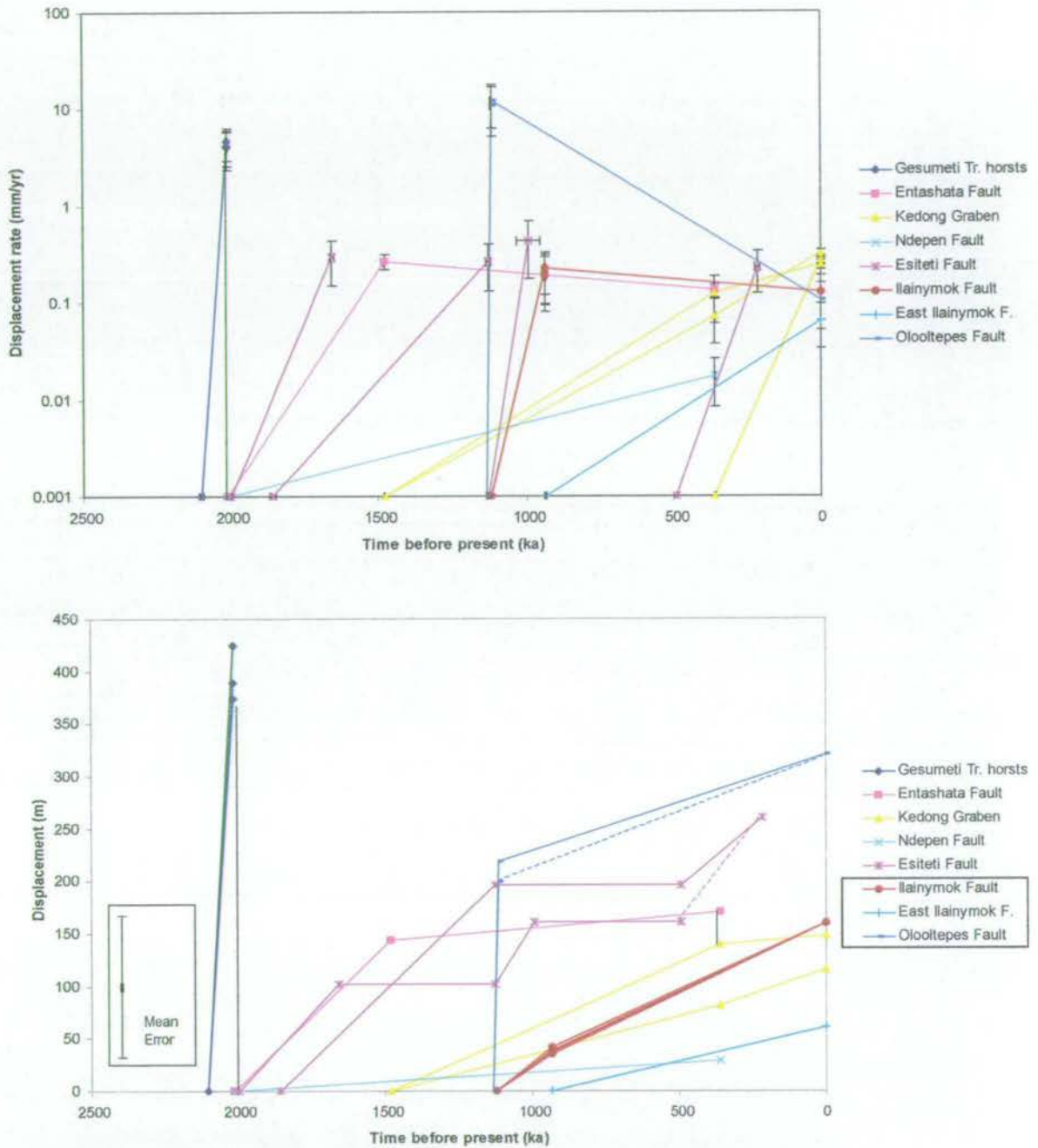
Figure 6.4 Graphs showing the evolution of Kenyan faulting: (a) plot of vertical displacement rate versus time, (b) cumulative fault displacement versus time. Coloured lines connect points from each fault dataset. The convergence of lines within a dataset indicates a period of fault linkage; dashed lines are shown where one segment (dashed) carried significantly less displacement than its neighbour (solid), prior to linkage. Black dotted lines indicate proposed periods of strain transfer between fault sets. Section of key enclosed by the rectangle indicates faults located at the axis of the rift.

6.2.2 The South Kedong Region

Displacement-length profiles along the Enasira and Porosita faults (figures 5.38a and 5.39a respectively) show that the maximum displacements (D_{max}) associated with each fault are currently located at the crest of Gesumeti Trachyte fault segments. The entire displacement on these segments was accrued at a maximum rate of 4.70 ± 1.70mmyr^{-1} during the 91kyr period immediately following deposition of the Gesumeti Trachyte Formation (figure 6.4). By 2.009 ± 0.004Ma, growth along this narrow train of horsts had ceased.

Subsequent to deposition of the Limuru Trachytes at 2.009 ± 0.004Ma, local strain became distributed over a relatively large region as a result of the nucleation of several curved faults, such as the Ndepen, Entashata, Taritik and Porosita Hill faults, that varied in orientation between N-S and NW-SE. The majority of these scarps displaced the upper surface of the Limuru Trachyte Formation, though the southern section of the Porosita Hill fault also reactivated the eastern margin of the southernmost Gesumeti Trachyte horst block. It is unclear as to whether these faults nucleated within the Limuru Trachytes or represent older structures reactivated from depth. The latter scenario may be true for the largest faults (Entashata and Taritik) but seems unlikely for the Ndepen fault, which is too small to cross the ~200m thickness of the Limuru Trachyte Formation.

The well-constrained Ndepen and Entashata fault scarps show somewhat different growth histories. Both appear to have nucleated at 2.009 ± 0.004Ma, immediately subsequent to deposition of the Limuru Trachyte lavas, and both ceased activity by 0.360 ± 0.001Ma, when most local deformation was transferred to the margins of the Kedong Graben. The Ndepen fault displayed a low growth rate (0.02 ± 0.01mmyr^{-1}) during this period and remained as a small structure, accumulating only ~30m of displacement over the entirety of its growth history. By contrast, the Entashata fault grew relatively quickly for the first 0.531 ± 0.005Ma, at a rate of 0.27 ± 0.05mmyr^{-1}, and then slowed to 0.14 ± 0.02mmyr^{-1} until its death at 0.360 ± 0.001Ma. The scarp showed a progressive increase in length from 2200m to 4400m over the 1.118 ± 0.003Ma period of fault activity. During this time, the location of maximum displacement migrated towards the south as the fault propagated laterally. However, the overall cumulative displacement on the fault remained relatively unchanged (figure 6.5).

N   S

Entashata GPS data

displacement (metres)

distance along fault (metres)
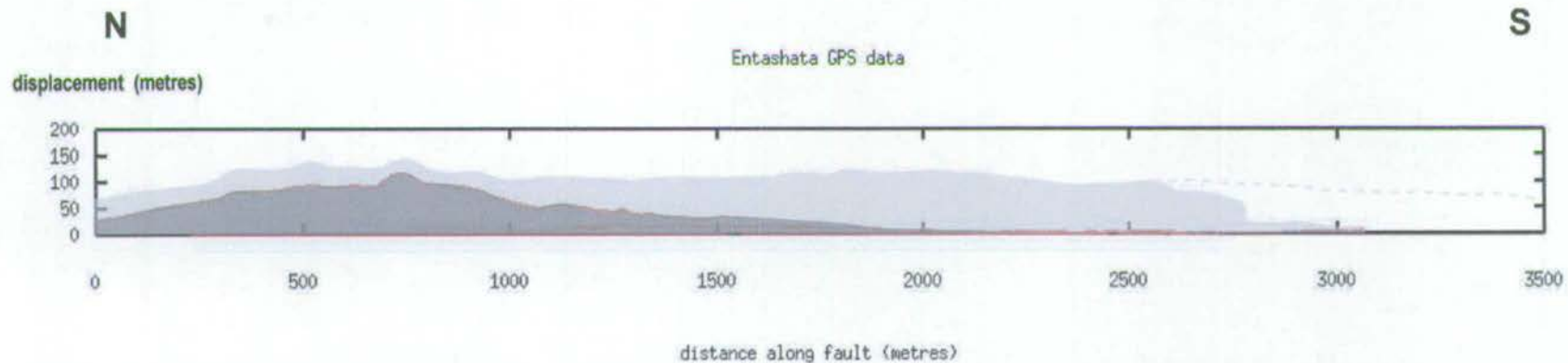
Figure 6.5 Displacement accumulation profile for the Entashata fault between 2.009±0.004Ma and 0.360±0.001Ma. Region shown in dark grey represents the section of scarp uplifted between 2.009±0.004Ma and 1.478±0.003Ma. Light-grey area shows the fault morphology at 0.360±0.001Ma.

Between 0.360±0.001Ma and present, fault growth occurred predominantly through fault segment linkage. By 0.360±0.001Ma, deformation in the South Kedong region had been transferred onto the N-S orientated Enasira and Porosita faults, which, by cross-cutting the NW-SE trending Entashata and Porosita Hill faults, eventually developed into the boundary faults of the Kedong Graben. The Enasira fault evolved from the linkage of a number of separate segments, the most southerly of which was 640m in length, to become the 21km long structure that bounds the entire western margin of the Kedong Graben. Similarly, the Porosita fault lengthened through the linkage of two short fault segments (d/L ~0.10) to form a single scarp, 5600m in length, along the eastern wall of the Graben. Growth of the present-day Kedong Graben occurred at a time-averaged rate of 0.32 ± 0.03mmyr^{-1} and 0.25 ± 0.03mmyr^{-1} (along the Enasira and Porosita faults respectively), which was relatively fast as compared with previous movements along the Entashata fault. Southward propagation of the Enasira fault tip between 0.360±0.001Ma and present occurred at a rate of 1.33mmyr^{-1}.

The overall trend in fault growth in the South Kedong region is of the initial rapid development of bell-shaped horst blocks with high d/L ratios (~0.10) that eventually evolved, through the linkage of pre-existing fault blocks, into long fault structures with low d/L values (~0.01-0.03). Plots of temporal displacement accumulation along the Kedong Graben-bounding faults are shown in figure 6.6. As can be seen from figure 6.4, growth rates are highly variable, with faults moving rapidly at first, then slowing and ceasing activity for a period of time before, in some cases, being reactivated at a later stage.
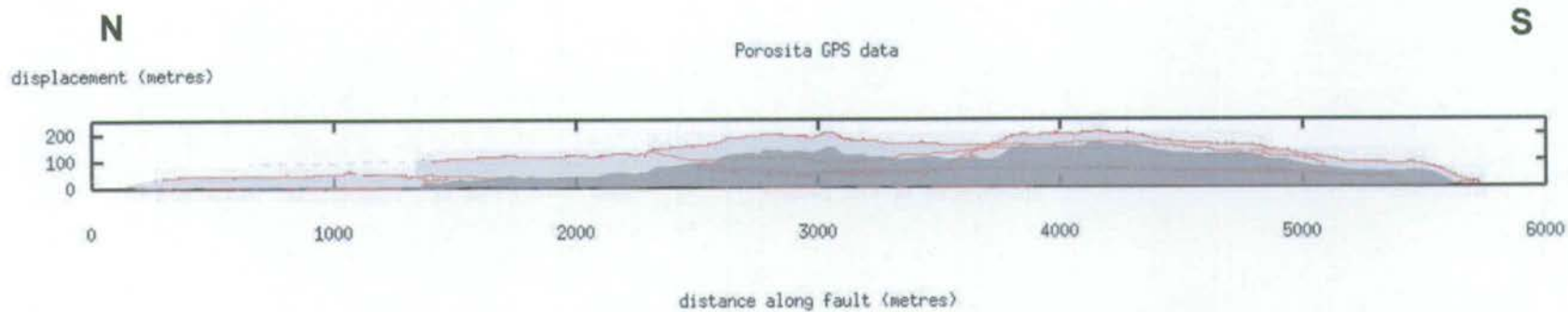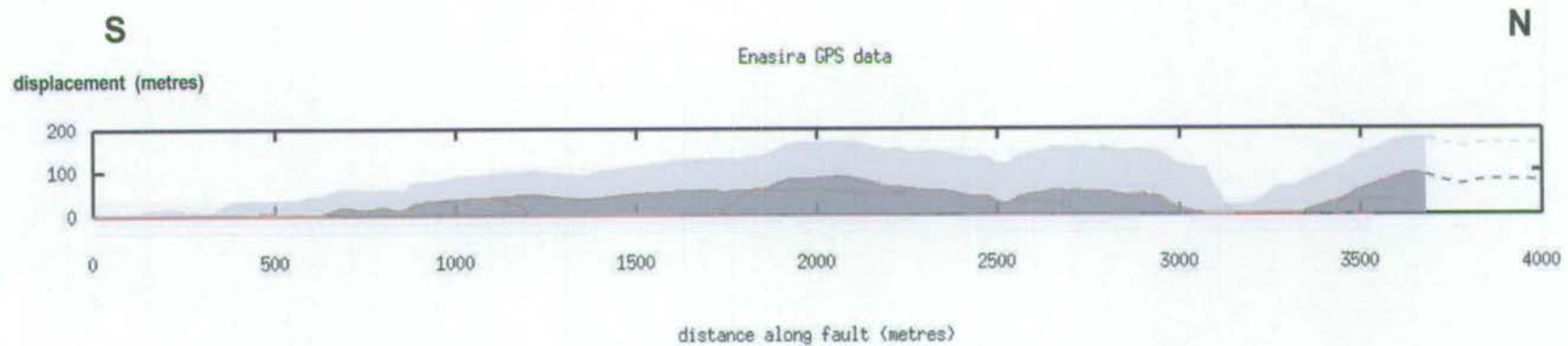
Figure 6.6 Displacement accumulation profile along (a) the Enasira fault and (b) the Porosita fault. In each plot the present-day displacement profiles are indicated in pale grey while those in dark grey represent the fault backstripped to 0.360±0.001Ma.

6.2.3 The Esiteti Region

The southern section of the Esiteti fault shows a pattern of development characterised by episodes of rapid fault growth that were interspersed with relatively long periods of quiescence. Vertical displacement on this scarp was accrued along two independent fault segments that, in time, linked to form a single structure with a low displacement-length ratio.

The position of D_{max} was established early in the history of the South Esiteti fault due to growth of the Ol Tepesi Benmoreite horst. To some extent this occurred coincidentally with development of a separate fault segment that uplifted the Limuru Trachytes further to the south. Both fault blocks had very similar rates of displacement (0.27 ± 0.13mmyr^{-1} and 0.30 ± 0.15mmyr^{-1} for the benmoreite and trachyte horsts respectively), though the benmoreite block accumulated a larger amount of displacement by virtue of a longer period of growth. A second phase of activity, between 1.128 ± 0.007Ma and 0.992 ± 0.039Ma, caused further uplift of the Limuru Trachyte horst at a rate of 0.43 ± 0.25mmyr^{-1}, increasing the estimated cumulative displacement along this section of the precursor Esiteti fault to 160m. Linkage of the fault segments occurred between 0.493 ± 0.001Ma and 0.215 ± 0.007Ma, and resulted in a further 70m of uplift along the Esiteti fault such that the cumulative displacement by 0.215 ± 0.007Ma at D_{max} was 260m. Further inactivity, between 0.215 ± 0.007Ma and present, may represent another period of quiescence or, alternatively, fault death. As can be seen from figure 6.3 and 6.7, the early fault blocks had relatively large d/L values (e.g. 0.06 ± 0.03 for the benmoreite block) that decreased to a value of 0.02 ± 0.01 as a consequence of segment linkage.

The above growth trend, of fault segment growth followed by linkage, is somewhat similar to that displayed by the bounding faults of the Kedong Graben. However, in the case of the Esiteti fault the initial displacement rate is an order of magnitude lower than that calculated for growth of the Gesumeti Trachyte horst blocks.

S   Esiteti GPS data   **N**

displacement (metres)
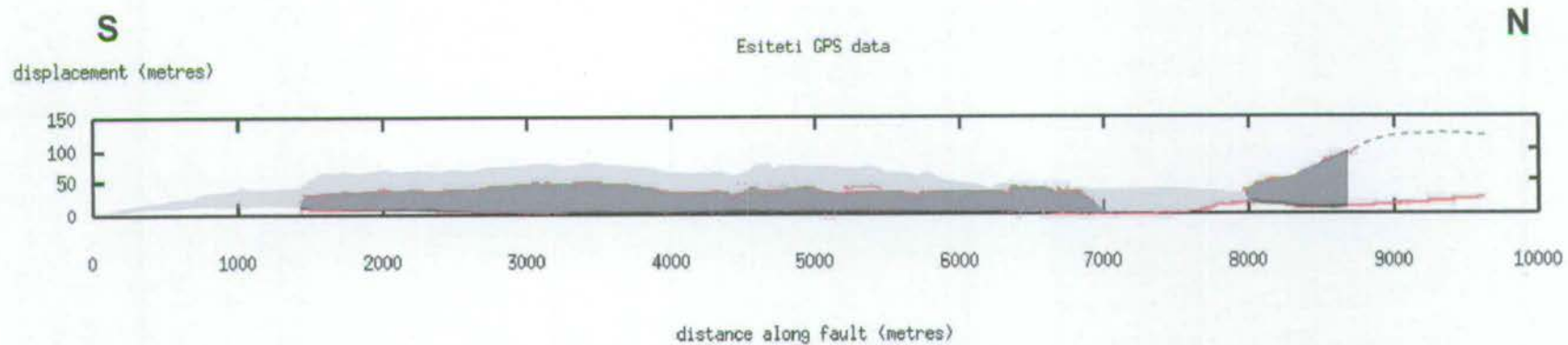
Figure 6.7 Displacement accumulation profile along the Esiteti Fault. Pale grey region represents the present-day displacement distribution along the fault scarp, while that shown in dark grey is the fault as backstripped to 1.128±0.007Ma.

6.2.4 The Ilainymok Region

Initial growth of the Ilainymok fault took place between 1.121±0.003Ma and 0.937±0.004Ma, at a maximum rate of 0.23±0.11mmyr^{-1} and resulted in formation of four small, N-S orientated fault blocks, each with 30-40m of vertical displacement and d/L ratios of 0.07-0.13 (figures 6.3 and 6.4). Between 0.937±0.004Ma and present, these early blocks linked to form a long, through-going fault (d/L of 0.02±0.01) that follows a N-S trend in the south, while in the north curves sharply towards the northwest (see figure 5.50 and 6.8). Though the maximum displacement rate slowed to 0.13±0.06mmyr^{-1} during this period, a further 120m vertical displacement was accrued on the fault at the position of D_{max}.

6.2.5 The Olooltepes Region

The growth pattern of the Olooltepes fault mirrors that of scarps studied elsewhere in the South Kenya Rift. Early fault development consisted of very rapid (up to 12.20±5.90mmyr^{-1}) uplift of three, N-S trending, independent horst blocks that were characterised by relatively large d/L values. During this initial 0.018±0.003Ma period of fault growth, the Ileek Pusi horst accrued some 220m of displacement at D_{max}. From 1.116±0.002Ma until present, faulting continued immediately to the north of the Ileek Pusi horst at a much-reduced rate of 0.11±0.05mmyr^{-1}. This period of deformation resulted in uplift of a scarp with 120m of vertical displacement and dramatically increased the total length of the fault to some 20km. Rotation of the northern tip of the Ileek Pusi horst increased the displacement at D_{max} to 160m (figure 6.9).

Unlike the other scarps surveyed in this study, the presence of seismicity (Ibs-von Seht *et al.*, 2001) along the Olooltepes fault provides direct evidence that this structure is currently active. The NNE-SSW linear swarm of microseismicity that was recorded in May 1998 opened an 15cm wide tension gash that connects the southern tip of the Ileek Pusi horst to the tip of the neighbouring fault segment. It appears that the train of horsts lying directly to the south of Ileek Pusi may be in the process of linkage.

S   Ilainymok fault data   N

displacement (metres)

100
50
0

0   500   1000   1500   2000   2500   3000   3500

distance along fault (metres)
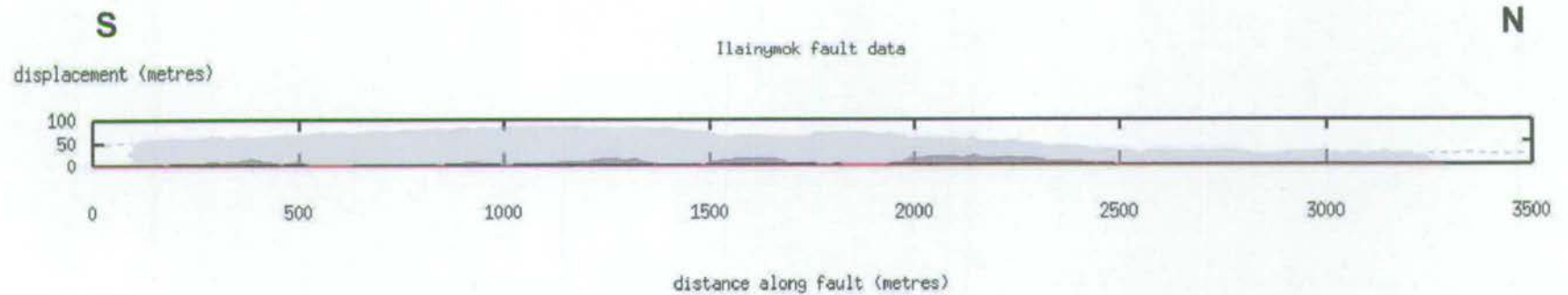
Figure 6.8 Displacement accumulation profile along the Ilainymok fault. Present-day along strike profile is shown in pale grey; dark grey regions indicate displacement backstripped to 0.937±0.004Ma.

N   Olooltepes fault data   S

displacement (metres)

200
100
0

0   1000   2000   3000   4000   5000   6000

distance along fault (metres)
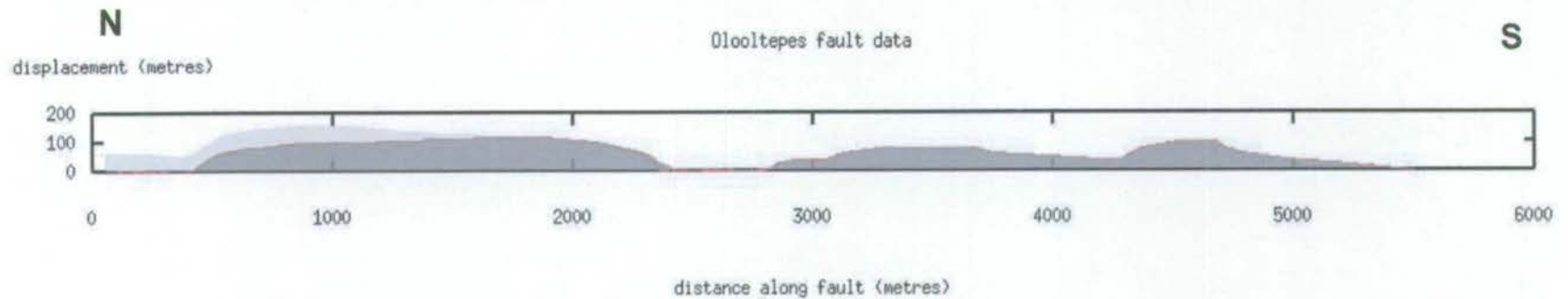
Figure 6.9 Displacement accumulation profile along the Olooltepes fault. Dark grey area shows the fault morphology at 1.116±0.002Ma. Uplift at the northern end of the profile between 1.116±0.002Ma and present is represented by the pale grey region.

6.3 Lateral fault-growth model

The faults documented in this study display a number of strong similarities. All initially consist of several small, independent segments (ranging in length from ~300m to ~5km) that have relatively high d/L values. In some cases (illustrated by the faults of the South Kedong and the Olooltepes regions) these segments are characterised by high vertical displacement rates. With time, in many cases, there is a dramatic increase in fault length as a result of lateral linkage between the early fault segments (see for example figure 6.6a, 6.7, 6.8 and 6.9). However, in the majority of cases there appears to be little interaction between the segments prior to linkage. In the context of previous work, this observation resembles studies of the Canyonlands fault-array of SE Utah (Cartwright *et al.*, 1995, 1996) and of fault development in central Greece (Morewood and Roberts, 1999, 2002). These authors find that fault length is established early, as a result of segment linkage, and remains relatively constant through time, while displacement is accumulated throughout the remainder of the fault growth history. This is in contrast to models that describe fault segment interaction prior to hard-linkage (Peacock and Sanderson, 1991; Childs *et al.*, 1995; Nicol *et al.*, 1996; Willemse *et al.*, 1996; Gupta and Scholz, 2000). Faults showing evidence for such interaction have been described in previous field studies and are typically characterised by a steepening of displacement gradients at the interacting fault tips and d/L ratios above those expected for isolated faults (e.g. Peacock and Sanderson, 1991; Contreras *et al.*, 2000).

The main characteristics of fault array evolution as a result of the two contrasting models of fault growth are summarised in Cowie *et al.* (2000) (figure 6.10). As can be seen from figure 6.3, though fault development within the South Kenya Rift partially follows the model of early linkage, there is little evidence of a re-equilibration or recovery phase as suggested in the graph shown on the upper right-hand side of figure 6.10. These faults are therefore 'under-displaced' relative to the idealised linear displacement-length scaling relationship ($d=\gamma L$) of Cowie and Scholz (1992) and retain a relatively 'flat' displacement profile (figure 6.10).

Although there is a relative paucity of hangingwall data in the current study, the reconstructions of the Entashata and Porosita Hill faults, between 1.478 ± 0.003Ma and 0.360 ± 0.001Ma, indicate a fault footwall to hangingwall ratio of 1:1.4, which is substantially lower than the value of 1:6

observed from neotectonic studies (e.g. Stein and Barrientos, 1985). A ratio of approximately 1:1.4 to 1:2 can also account for observed displacements along the Enasira Fault between 0.360±0.001Ma and present. During this period, footwall uplift at the intersection with the Footwall Fault Zone is calculated to be some 35m relative to the Barajai Trachyte datum (see table in section 5.2.1c), while the remaining fault displacement must result from ~60m of hangingwall subsidence. Although these are minimum displacements (since the hangingwall stratigraphy is not visible), the alluvium in the hangingwall to the Enasira Fault is probably no more than a thin veneer (since bedrock exposures are common along the FFZ) and certainly cannot be thick enough (~200m) to accord with a footwall uplift:hangingwall subsidence ratio of 1:6. This evidence further supports the notion that the faults of the South Kenya Rift are relatively long, flat structures that are under-displaced when compared to the displacement-length scaling relationship based on the global fault dataset (see figures 6.3 and 6.10).

The faults of the South Kenya Rift are also characterised by a distinctive, serrated, morphology that results from the early fault segments retaining their original identities, rather than experiencing fault segment interaction prior to linkage. McLeod *et al.* (2000), have similarly described a serrated fault morphology along the crest of the linked Strathspey-Brent-Statfjord fault array, Northern North Sea, which is also underdisplaced with respect to its length. They suggest that the lack of late-stage re-equilibration may reflect the immaturity of a fault system that was 'switched off' while in the process of linkage. In the case of the present study, it may be that given more time those faults that are still active (e.g. Olooltepes) will re-equilibrate according to the model of early linkage.

Only in one case, the Enasira fault, is there direct evidence for segment growth and interaction prior to linkage of the fault array. Between 0.360±0.001Ma and present, the southern segment of the Enasira fault develops a distinctive, skewed displacement profile as a result of interaction with the neighbouring segment to the north. Development of the Footwall Fault Zone, during this period, results from a significant steepening of displacement gradients at the tips of the interacting fault segments (see figure 6.6a). Although the Limuru Trachyte block of the Esiteti fault shows an increase in displacement between 1.128±0.007Ma and 0.992±0.039Ma, the segment retains a relatively symmetric displacement-length profile and shows little evidence for interaction with the neighbouring benmoreite block (figure 6.7).

The general fault growth trends displayed by scarps within the South Kenya Rift are summarised in figure 6.11.
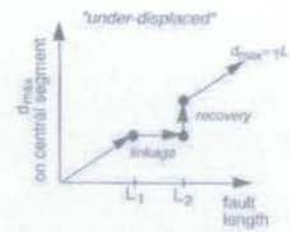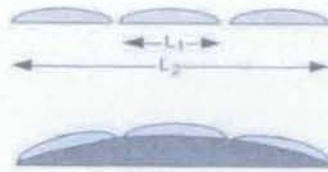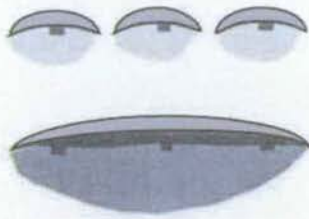
Figure 6.10 Diagram showing the two end-member models of normal fault growth (modified after Cowie *et al.*, 2000). Left-hand side: plan view of faults and associated basins. Centre: displacement-length profile along the faults. Right-hand side: maximum displacement on the central segment plotted as a function of fault length. Case 1: Early linkage – fault segments link without any prior interaction to form a single, through-going fault. The fault displacement profile re-equilibrates following segment linkage. Case 2: Late linkage – Interaction between fault segments occurs prior to linkage, causing an increase in displacement on the central fault segment without significant length change. Increased fault tip gradients can result in formation of footwall fault zones (FFZ) as a mechanism of strain release at segment boundaries. The FFZ's become inactive with time as the segments eventually link to produce a through-going fault.
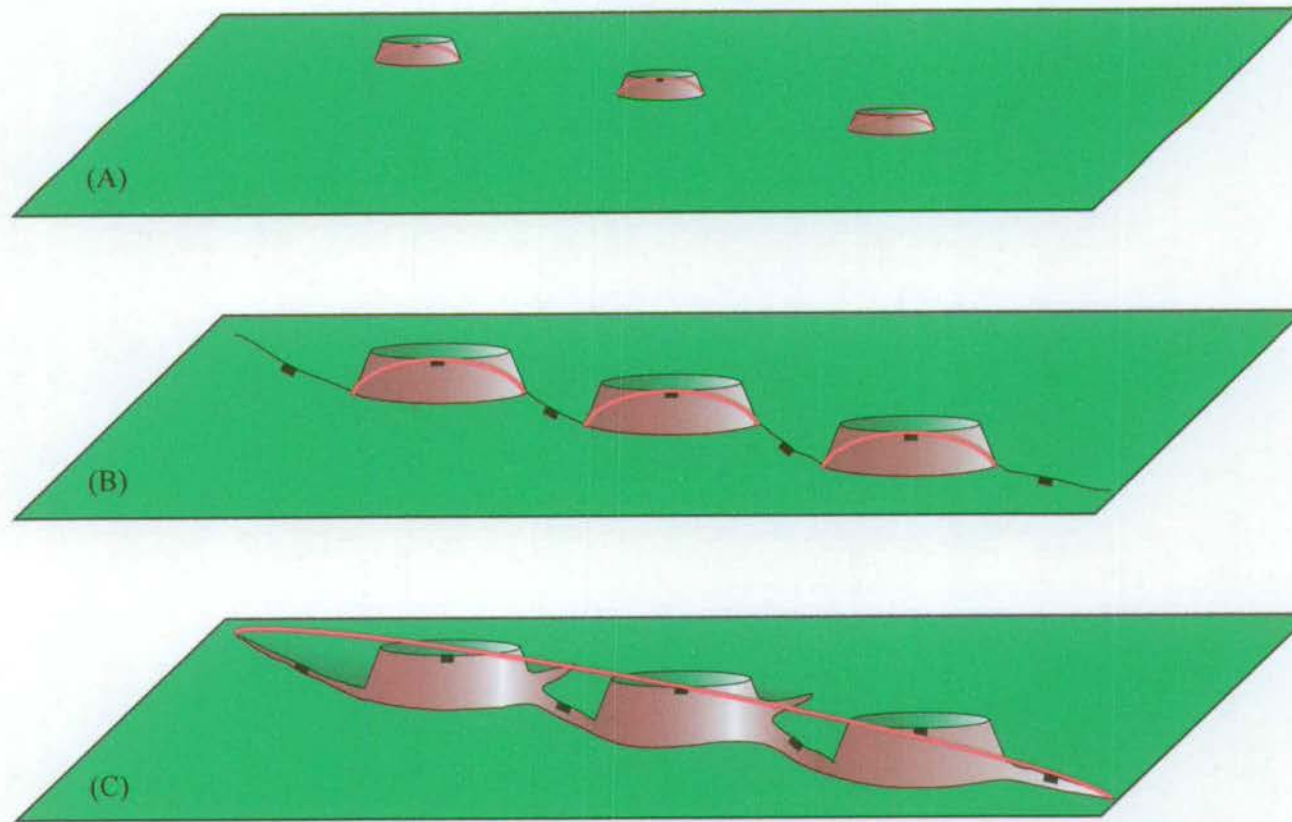
Figure 6.11 Summary diagrams showing the evolution of a kilometre-scale extensional fault within the Kenya Rift. Initial fault development is by the self-similar growth of independent segments, (A) and (B), prior to a phase of lateral fault linkage (C). Segments often form as curved horst blocks that are characterised by rapid uplift rates. Red curves indicate the average displacement-length profile at each stage of fault development. The locations of footwall cross-faults, associated with segment linkage and accommodating differential along-strike strain, are also shown in (C)

6.4 Fault network development

6.4.1 Introduction

A number of studies, including the numerical modelling of Cowie *et al.* (1995, 2000); Gupta *et al.* (1998) and analytical work of McLeod *et al.* (2000, 2002); Young *et al.* (2001); Meyer *et al.* (2002) and Gawthorpe *et al.* (2003) have attempted to characterise the progressive development of extensional fault networks, in both two and three dimensions. At present there are essentially two end-member models of rift development. The numerical modelling of Cowie *et al.* (1995, 2000) suggests that, during rift initiation, strain is taken up on a set of diffuse, isolated faults. A number of these faults, which are optimally located with respect to neighbouring structures, experience enhanced growth and lateral fault linkage according to the model proposed by Cowie (1998). Eventually, strain becomes progressively localised onto a limited number of long, through-going faults at the expense of smaller, less optimally orientated structures, which become inactive (figure 1.9).

The second end-member model of fault network development also predicts a progressive localisation of faulting. However, where it differs is in the size distribution of the fault population during nucleation. Nicol *et al.* (1997); Meyer *et al.* (2002) and Walsh *et al.* (2003) suggest that fault lengths and displacement rates are established early in a rift episode and are generally constant through time, with larger faults moving faster than smaller ones. This latter model suggests that once the initial length has been established, each fault grows primarily by progressive accumulation of displacement rather than through linkage of pre-existing fault segments.

6.4.2 Small-scale fault localisation – The South Kedong Region

The large aerial extent of lava coverage in the South Kedong region affords the opportunity to study the development of a normal fault network in two-dimensions. Fault growth in this area can be subdivided into three distinct episodes of activity that overlap in both time and space (figure 6.12).

i)   Rapid development of north-south trending bell-shaped horst blocks, that subsequently are partially buried under a ~230m thick layer of trachyte lava. The crests of the pre-existing horst blocks protrude through the upper surface of the lava.

ii)   Across the South Kedong region, deformation is taken up on a network of discrete N-S to NW-SE orientated faults, including the Entashata, Ndepen and Taritik faults.

iii) Strain becomes progressively transferred onto the N-S trending Enasira and Porosita fault scarps that bound the Kedong Graben. These long structures (the Enasira scarp is 21km in length) form as a result of linkage between pre-existing fault segments. As a result of this period of fault development, the pre-existing scarps were cross-cut, uplifted and in some cases rotated on the back of the later faults (e.g. the Ndepen fault on the footwall to the Enasira fault) (see figure 4.17). The fault displacement rate during this period was significantly higher than during the fault growth described in ii) (figure 6.4).

The most recent phase of fault activity in the South Kedong region (point iii) bears a striking similarity to the model of strain localisation described by Cowie *et al.* (2000), in which deformation becomes progressively localised onto a few through-going faults as a result of fault segment linkage. There is, however, still controversy in the scientific literature as to the precise nature of fault growth at depth. Walsh *et al.* (2003) argue that the majority of studies which model fault evolution in terms of lateral growth, interaction and linkage of pre-existing fault segments only consider fault development from a two-dimensional perspective. In their model, based on 3D subsurface data, they suggest that the segments of a fault array, observed in 2D, may link into a single fault plane out of the plane of inspection and hence may be kinematically interrelated from inception. They suggest that, in reality, the three-dimensional fault structure cannot be fully deduced from a field-based study or from 2D numerical modelling. Evidence from a cluster of microseismicity recorded under the train of the Olooltepes horst blocks at the centre of the South Kenya Rift suggests that this argument may be correct (Ibs-von Seht *et al.*, 2001). The seismic activity defines a continuous fault plane, at least 10km in length, that directly underlies the surface train, and indicates that these apparently independent fault segments are indeed linked at depth (see section 6.6 for a further discussion).

Figure 6.12 Landsat 7 satellite image of the South Kedong region, overlain by lines to show the principal phases of fault development. Pale blue lines: N-S to NW-SE trending faults that were active between 2.009±0.004Ma and 0.360±0.001Ma. Curved orange and white lines: faults active between 0.360±0.001Ma and present; orange lines demarcate the margins of the Footwall Fault Zone (FFZ) that formed in association with the N-S trending Kedong Graben (indicated by the solid white lines in the centre of the image). Dashed oblique line at the left-hand side of the image indicates the margin of the Esageri-Esakut Platform, as shown on figure 6.13.

6.4.3 Large-scale fault localisation – The South Kenya Rift

The graph of displacement rate against time, plotted in figure 6.4, shows a general migration of fault activity towards the centre of the rift over the last ~2Myr. Faults in the South Kedong region, located at the eastern margin of the rift, show the highest rates of displacement early in their history and then subsequently slow with time. (The acceleration of fault activity during the late-stage formation of the Kedong Graben is a local effect related to initiation of the Suswa volcano, and will be discussed further in section 6.7). By 1.116 ± 0.002Ma, the highest rate of fault growth is located on the Olooltepes fault, at the core of the rift, while, at the same time, activity on the Entashata fault, in the South Kedong region, continues to decrease. Microseismic activity, recorded over a eight-month period in 1998, indicates that the Olooltepes fault is still currently active, while there is little evidence for much deformation further towards the rift margins (Ibs-von Seht *et al.*, 2001). However, evidence from the Ilainymok and Esiteti faults is more inconclusive.

6.5 Affect of basement heterogeneities on rift development

6.5.1 Introduction

As described in section 2.2.2, the crustal basement underlying the Kenya Rift is traversed by several discrete NW-SE-trending basement lineaments that were inherited from the Proterozoic orogenesis of the East African continental crust. Such lineaments are orientated obliquely to the E-W direction of regional extension and appear to influence fault geometries in the overlying lava pile. As a result, where the regional N-S orientated faults interact with these lineaments they are often seen to curve into an oblique trend that mirrors the underlying basement structure (e.g. Le Turdu *et al.*, 1999). Two of the faulted regions described in this study, South Kedong and Ilainymok, show evidence for possible fault interaction with basement lineaments.

6.5.2 The South Kedong Region

Immediately to the south of the South Kedong region, topographic relief decreases as the steep-sided fault-generated topography of the Esageri-Esakut platform opens out onto the Ol Tepesi Plain (figure 6.12 and 6.13). Although not bound by a continuous fault system, the southern margin of the Esakut Platform has a NW-SE orientation that is distinct from the regional N-S fault trend (figure 6.13). It seems that the orientation of this platform margin may be controlled by a NW-SE-trending lineament in the underlying crustal basement. Structural maps and satellite images of the Olorgesailie-Kedong region show that fault lines often curve into a NW-SE orientation as they approach the edge of the Esageri-Esakut Platform from the north (figure 6.12 and 6.13).

In the South Kedong region, the variation between N-S and NW-SE orientated faulting, both temporally and spatially, is likely to reflect the competing influences of E-W regional extension versus localised deformation generated by an inferred NW-SE trending basement lineament.

Many of the unusual fault geometries recognised in regions of oblique rifting have been recreated with the aid of analogue modelling (Withjack and Jamison, 1986; Tron and Brun, 1991; McClay and White, 1995; Clifton and Schlische, 2001; McClay *et al.*, 2002). Most methods use scaled sandbox models in which a layer of a medium such as sand, clay or silicone is extended above of a deformable rubber sheet (Withjack and Jamison, 1986; McClay and White, 1995; Clifton *et al.*, 2000; Clifton and Schlische, 2001; McClay *et al.*, 2002). The acute angle between the rift axis and the direction of extension, α, is varied such that it is possible to reconstruct fault geometries in both orthogonal ($\alpha = 90°$) and oblique ($\alpha < 90°$) rift environments. McClay and White (1995) and McClay *et al.* (2002) have demonstrated that both orthogonal and oblique rifts are characterised by segmented border faults parallel to the rift axes and by smaller, intrarift faults that are subperpendicular to the direction of extension. Hence rift morphology is strongly influenced by the value of α, as shown in figure 6.14. Clifton and Schlische (2001) have studied the temporal evolution of border fault and intra-rift fault populations in oblique rift zones by progressively extending a layer of wet clay above a latex sheet. They show that for moderately oblique rifting ($\alpha = 60°$), which is similar to the

orientation of basement heterogeneities relative to the regional extension direction of the South Kenya Rift, faults initially nucleate as diffuse clusters and then evolve through rapid tip propagation and linkage. As rifting progresses, deformation becomes concentrated onto the largest faults, and the nucleation of new faults is inhibited.

Applying the results of analytical modelling to the South Kedong region suggests that both the N-S faults, orientated perpendicular to regional extension, and the curved N-S to NW-SE trending faults developed through similar mechanisms of fault propagation, linkage and strain localisation. As described in the fault synthesis given in section 6.2.2, the early, curved N-S to NW-SE-trending fault set consists of a relatively diffuse network of faults that dissect the surface of the Limuru Trachyte Formation. The curved nature of the faults can be regarded as a direct response to oblique rifting associated with the postulated underlying basement lineament. Hence, the faults, or sections of faults, that are orientated directly N-S, form in response to E-W regional extension across the rift valley, whereas the NW-SE-orientated structures represent sections of the segmented 'border' faults, as described from analogue modelling experiments. As extension progressed across the South Kedong region, strain gradually became localised onto a few through-going faults in each fault sub-population through a process of fault propagation and linkage. In this way, as deformation became localised along the margins of the Kedong Graben, through the linkage of N-S orientated fault segments, the locus of active NW-SE faulting was forced towards the south as pre-existing NW-SE-trending structures were progressively cross-cut and uplifted (see also section 6.7).
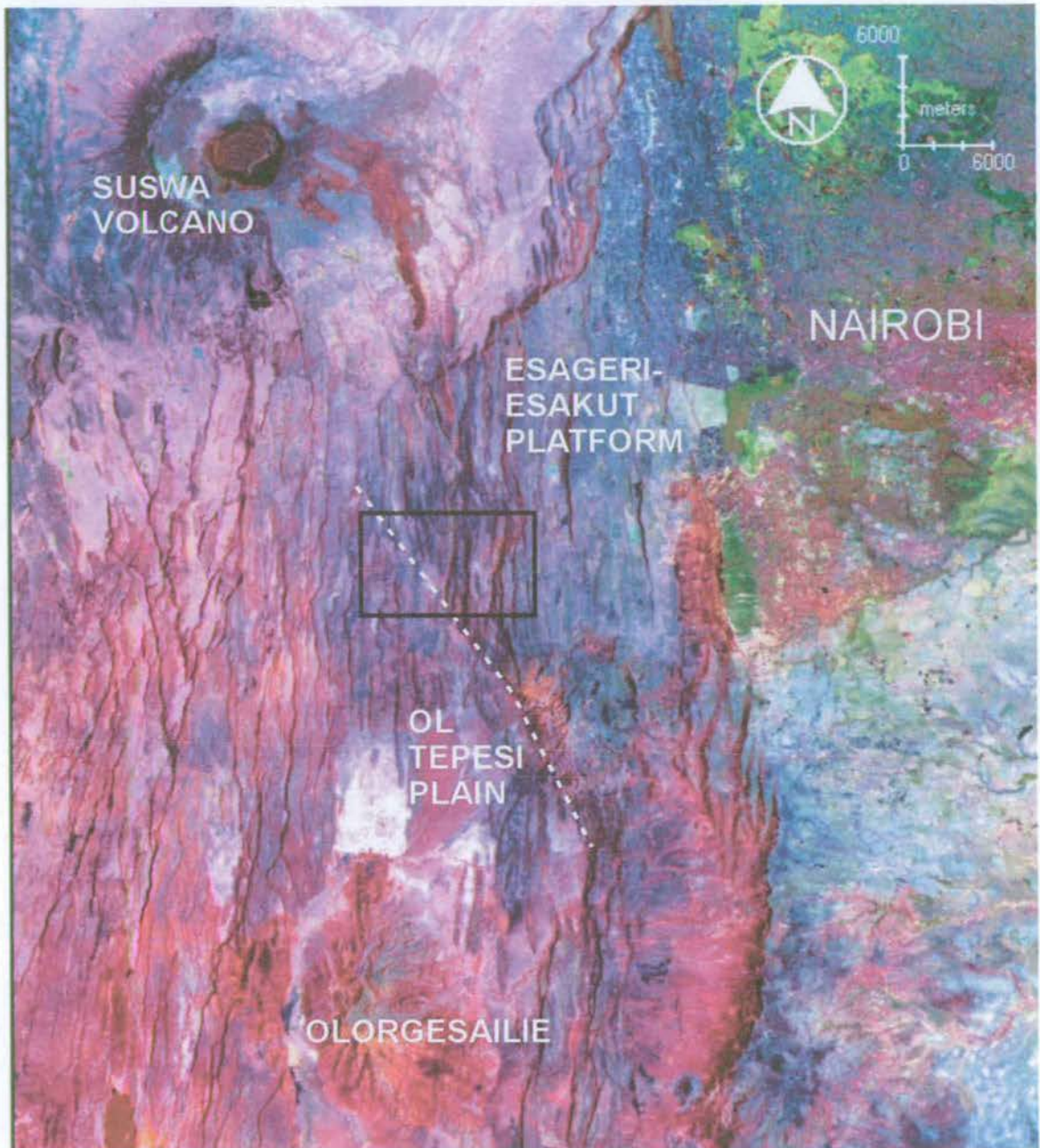
Figure 6.13 Satellite image along the eastern margin of the South Kenya Rift, annotated to show the major features of interest. Oblique dashed line indicates the southern margin of the Esageri-Esakut Platform. Black rectangle shows the location of figure 6.12.
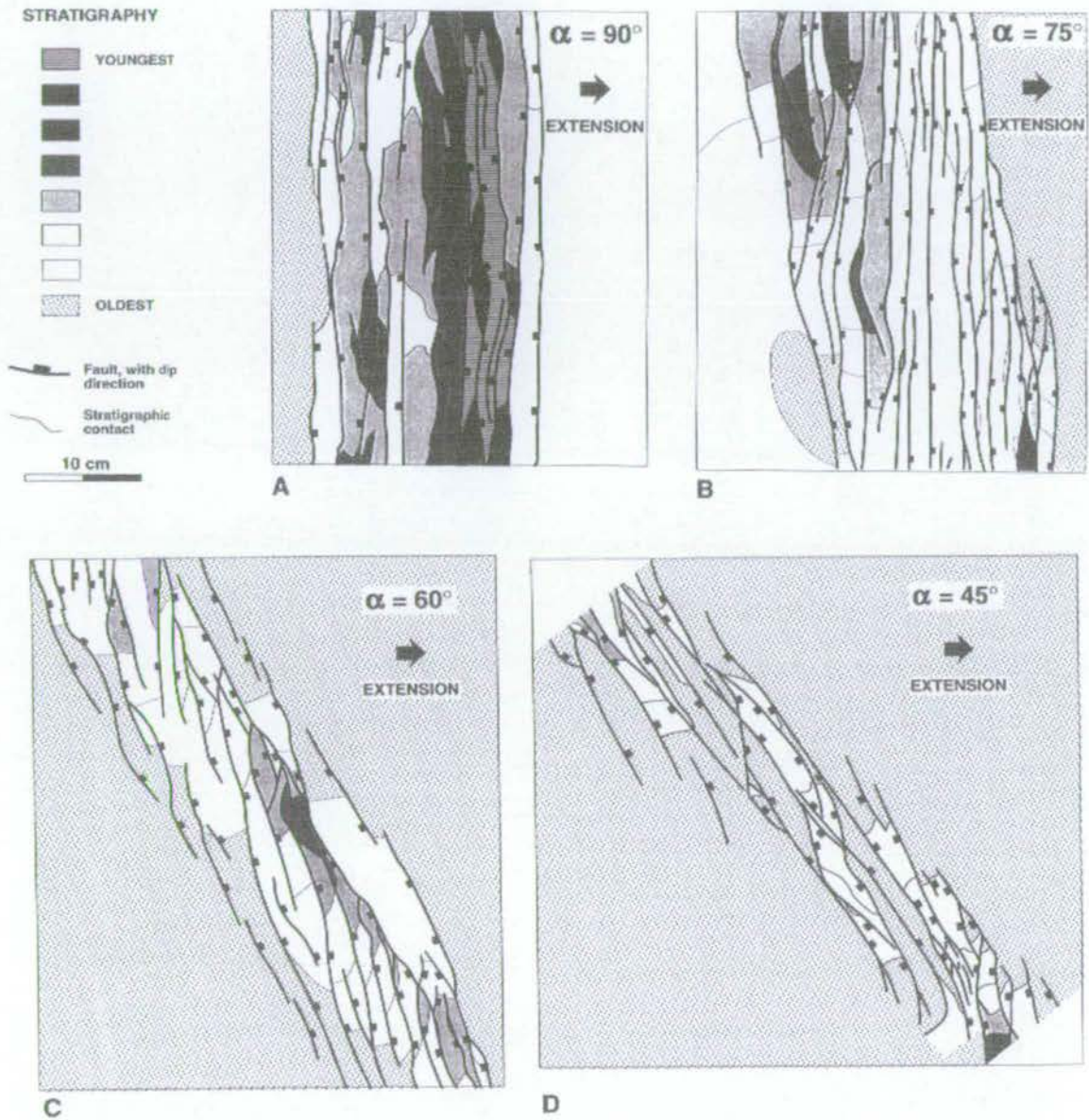
Figure 6.14 Interpreted drawings made from analogue modelling of rift development. (A) Orthogonal extension, α = 90°. (B) Slightly oblique extension, α = 75°. (C) Moderately oblique extension, α = 60°. (D) Oblique extension, α = 45° (from McClay and White, 1995).

6.5.3 The Ilainymok Region

As described in section 6.2.4, the Ilainymok fault is somewhat unusual due to its curved morphology in plan view (figures 6.15 and 6.16). The Ilainymok region represents a section of the Magadi Transverse Zone (MTZ), which is an area characterised by curved fault-lines that are believed to form in response to interaction with a basement lineament (see figure 2.7). Development of the Ilainymok fault is characterised by linkage of a train of four discrete fault segments to form a continuous scarp, some ~10km in length, that has a N-S orientation in the south but which gradually curves towards the north-west along its northern section. As with fault evolution in the Kedong region, the curved nature of the Ilainymok fault is thought to result from interaction with an underlying basement lineament.

The displacement-length profile along the Ilainymok fault, shown in figure 6.17, has a 'flat triangular-shaped' appearance along its central and southern sections. The present location of D_{max}, at the apex of this 'triangular' profile, is also the location of a ~6m offset in the footwall stratigraphy, which is downthrown towards the north. It appears that this offset may result from movement along an incipient fault plane that dissects a tip propagation fold ahead of a NW-SE-trending fault located immediately to the west of the Ilainymok scarp. The Ilainymok fault therefore provides a cross-section through the fault-tip propagation fold, which may, with time, evolve into a mature, north-east dipping normal fault with a NW-SE strike (see figure 6.17). Similar structural morphologies, associated with the development of a propagating normal fault from a breached fault tip fold, have been identified in the Gulf of Suez region by Gawthorpe *et al.* (1997).
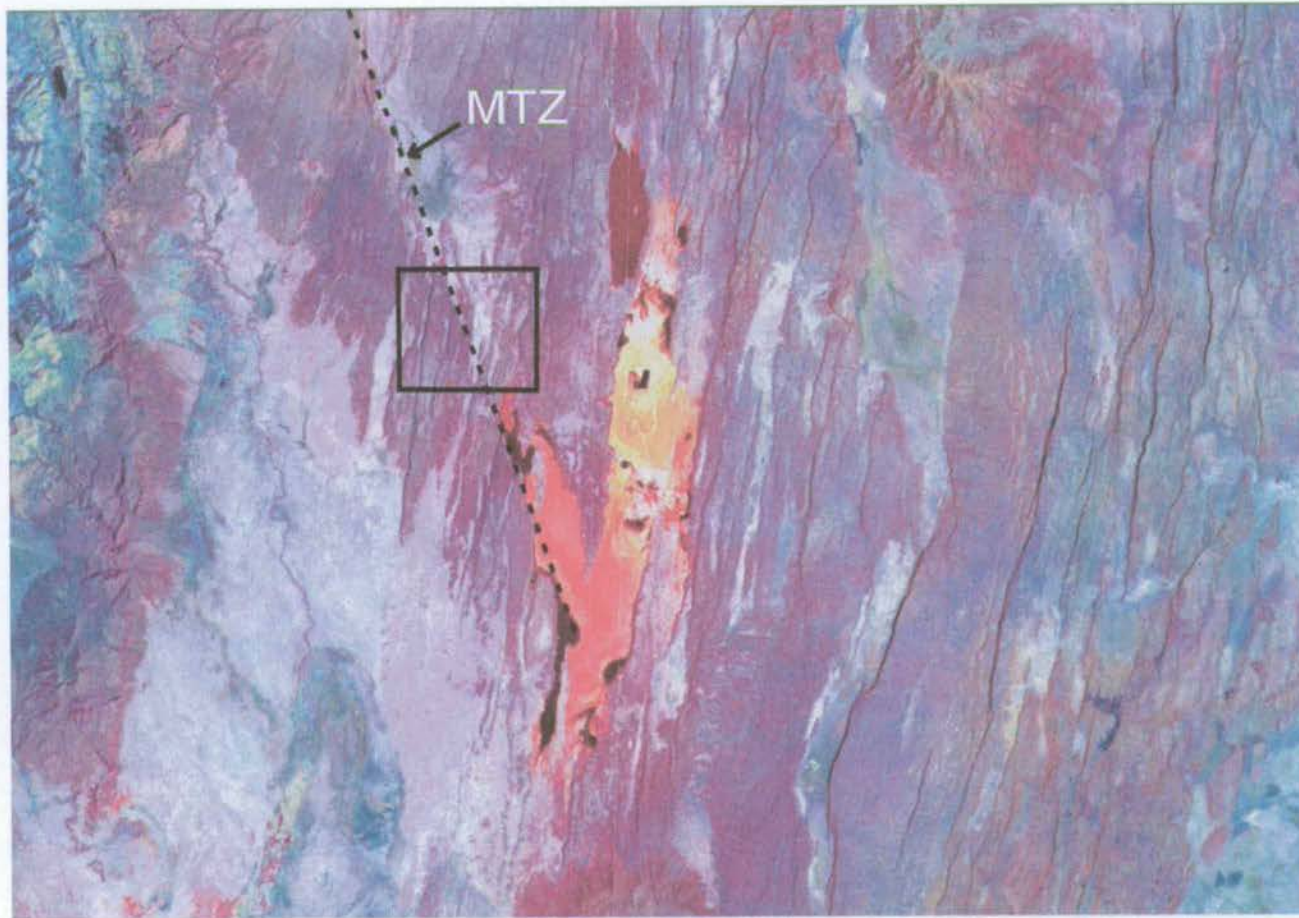
Figure 6.15 Satellite image of the Lake Magadi region, located at the centre of the South Kenya Rift. Oblique dashed line indicates the position of the Magadi Transverse Zone (MTZ). Black rectangle shows the location of the Ilainymok region (see figure 6.16).
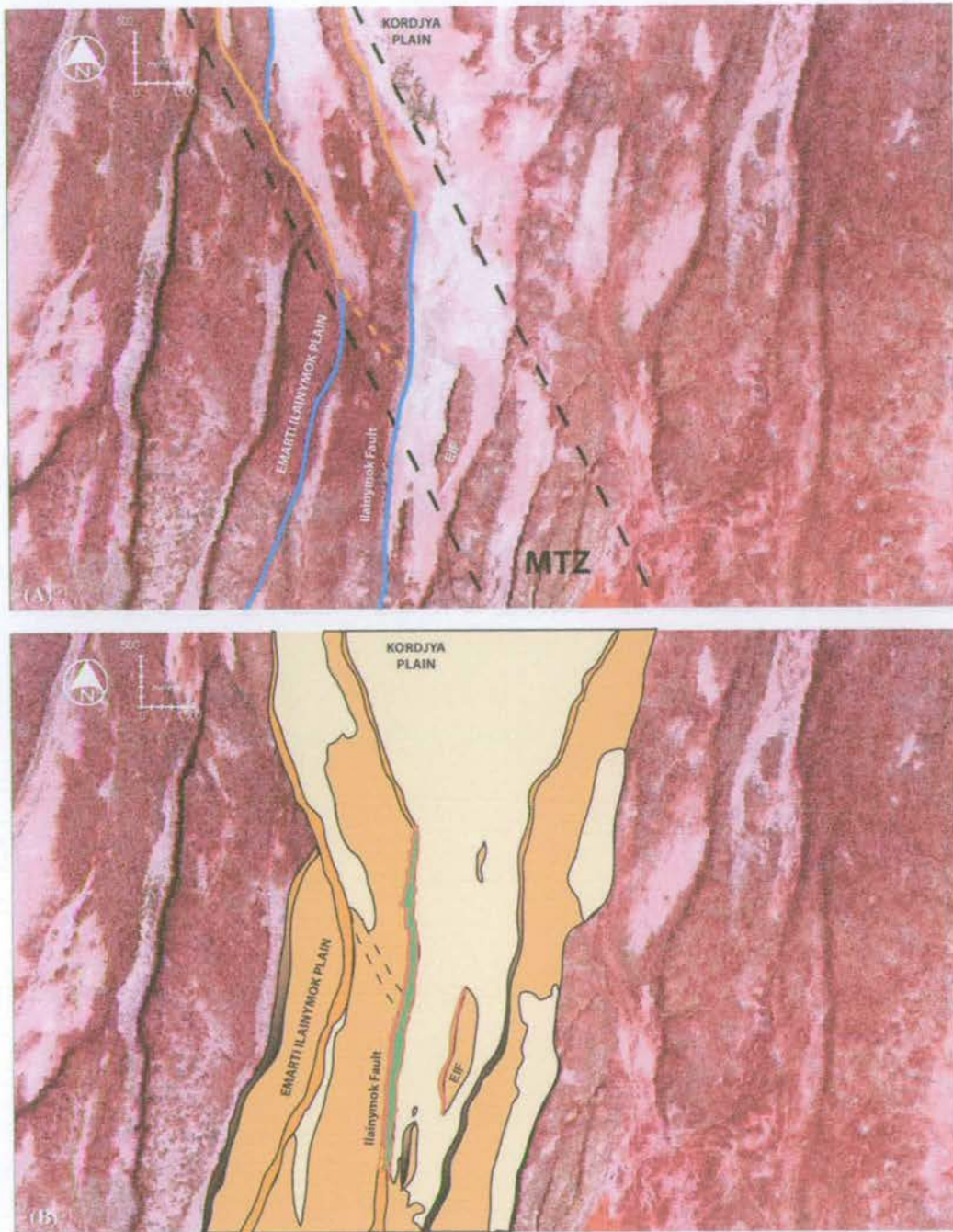
Figure 6.16 (a) Satellite image of the Ilainymok region, showing the major structural trends. N-S orientated fault scarps (shown in pale blue) result from pure E-W extension, whereas those trending NW-SE (shown in orange) form part of the Magadi Transverse Zone (demarcated with dashed black lines), which is thought to reflect fault interaction with an obliquely orientated basement lineament. The dashed orange line located immediately to the west of the Ilainymok fault represents the crest of a propagation fold at the tip of the neighbouring NW-SE orientated fault scarp. (b) Structural map of the Ilainymok region, redrawn from figure 5.46. Dashed black lines indicated the location of the fault-tip propagation fold.
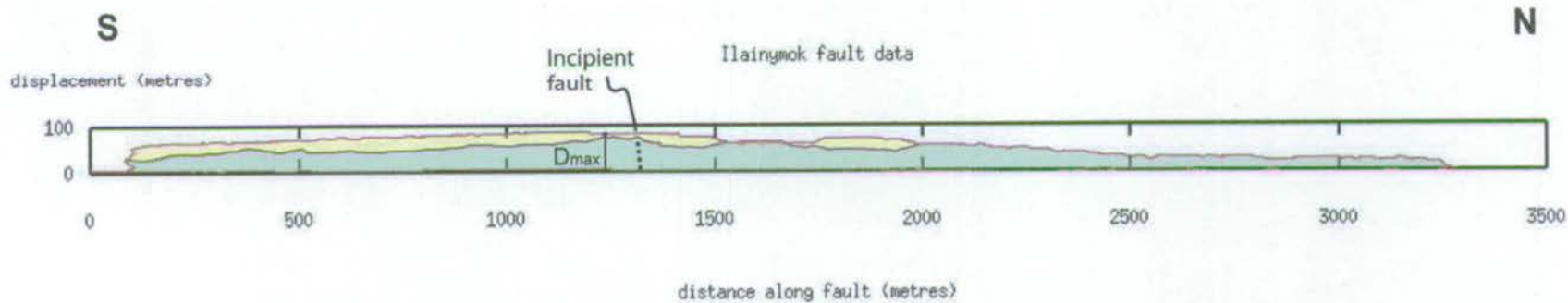
Figure 6.17 Displacement-length profile along the Ilainymok fault showing the location of an incipient, NW-SE orientated fault plane propagating from the northwest.

6.6 Mechanisms of fault growth and rift development

6.6.1. Strain localisation models

Observed fluctuations in fault growth rates cannot be explained through the application of strain localisation models, such as those of Cowie *et al.* (1995, 2000) or Gupta *et al.* (1998), since they predict either a systematic increase, or decrease, in fault growth rates through time, depending on the location of the fault within the network. According to such models, faults that are optimally orientated with respect to neighbouring structures experience enhanced growth rates due to fault interaction. This occurs at the expense of other, more isolated faults that become increasingly inactive (see section 1.2.5) until, eventually, all the strain across the deforming region becomes localised onto one or two through-going faults (figure 1.9). Therefore, depending on its relative location, any particular fault within the South Kenya Rift should either experience a gradual increase, or decrease, in vertical displacement rates through time. This means that the episodic nature of fault growth in this study cannot be justified through the simplistic application of a strain localisation model. Even for those structures that show progressively smaller displacement rates through time, such as the Olooltepes or South Kedong faults, the high initial growth rates ($\sim$12mmyr^{-1} for the Olooltepes fault) must eventually become accommodated onto larger structures, with even higher displacement rates, during strain localisation. Although there is a lack of displacement data from the largest faults in the South Kenya Rift, it seems unlikely that any fault moved, with any consistency, at such high displacement rates. Baker *et al.* (1988) assume an average extension rate across the Kenya Rift of 3mmyr^{-1} based on 20km of horizontal extension having occurred over the past 7Myr. Best-fit plate models indicate that the total extension rate across both arms of the East African Rift, as averaged over the past 3Myr, is 4-5mmyr^{-1} (Jestin *et al.*, 1994; Foster and Jackson, 1998). Hence, rapid rates of fault uplift could not have been sustained for long periods.

6.6.2 The influence of tectono-magmatic cycles

Fault growth along the floor of the South Kenya Rift appears to be highly episodic in nature. As described in section 6.2, many of the surveyed faults are characterised by periods of rapid growth, usually associated with the earliest stages of fault development, interspersed with

phases of much slower growth or even fault quiescence. The rapid spatial and temporal variations in fault growth rate across the South Kenya Rift cannot be explained by changes in regional strain rate since such variations should influence all faults equally, irrespective of their location. Rate variability must instead be a response to localised, and transient, perturbations in the strain field. Figure 6.4 shows that the highest fault displacement rates are associated with periods of rift volcanism. The episodes of most rapid fault activity, represented by uplift of the Gesumeti Trachyte horst blocks between 2.100±0.007Ma and 2.009±0.004Ma and the Olooltepes horsts between 1.134±0.002Ma and 1.116±0.002Ma, occur immediately subsequent to eruption of the Gesumeti Trachyte and Plateau Trachyte formations, respectively. Given their respective thicknesses, these lavas represent the products of substantial pulses of volcanic activity. It is probably no coincidence that the highest vertical displacement rates are characteristic of the earliest stages of fault-segment development since the structures are nucleating within hot, weak, volcanic rocks at a time when rift magmatism is still prevalent. As volcanic activity begins to wane, fault growth rates similarly decrease. This provides an explanation for the observation that the highest displacement rates are associated with the smallest time intervals between volcanic marker horizons.

Tectono-magmatic cycling, both within rift provinces and along oceanic ridges, is commonly discussed in the scientific literature (e.g. Baker *et al.*, 1988; MacGregor *et al.*, 1998; Navin *et al.*, 1998; Sinha *et al.*, 1998). The general principle is that rifts experience pulses of intense magmatic activity and volcanic accretion, interspersed with periods of tectonic activity and fault development. The ages of volcanic formations, relative to the timing of rift subsidence, has been used by Baker *et al.* (1988) to suggest the presence of tectono-magmatic cycling within the Kenya Rift. Evidence from the current study supports the principle of tectono-magmatic cycling and, in addition, suggests that most displacement is accumulated during the initial period of each tectonic phase.

6.6.3 The influence of mechanical layer thickness

An alternative explanation for the variable fault growth rates, which may also account for the 'under-displaced' nature of the Kenyan faults relative to the idealised fault-scaling relationship (d=γL; see figure 6.10), involves consideration of fault dimensions with respect to the elastic thickness of the crust. Cowie *et al.* (2000) and Cowie and Roberts (2001) speculate that a

temporal change in fault behaviour may be anticipated to occur once the entire thickness of the brittle (seismogenic) layer has been breached, since this will limit the down-dip width of the fault and force it to propagate laterally. Other studies suggest that fault segment length may be limited by the effective elastic thickness of the crust (T_e), which is closely approximated by the seismogenic thickness (T_{seis}) (Jackson and White, 1989; Scholz and Contreras, 1998; Ebinger *et al.*, 1999). This hypothesis can be tested along the Olooltepes fault, at the centre of the Kenya Rift, since the presence of seismicity provides information about the fault at depth (see also section 6.4.2). As described in section 2.4.5, a swarm of shallow microseismic activity, ranging in magnitude from 1.5 to 3.7 and located some 10km north of Lake Magadi, was recorded over a four-week period in May 1998. The swarm, which was limited to the upper 9km of the crust, defined a NNE-SSW trending, planar, structure lying directly beneath the train of the Olooltepes horst blocks, suggesting that the blocks link into a single fault at depth (figure 6.18). If T_e is approximately equal to T_{seis}, then according to Jackson and White (1989) and Ebinger *et al.* (1999), the maximum fault segment length in this region should be ~9km. However, given that maximum earthquake rupture-length scales with the thickness of the strong upper crust (Das and Scholz, 1983) and that the maximum earthquake magnitude (3.7) is too small to rupture a 9km crustal thickness, T_e must be thinner than T_{seis} in this region. If this is the case, the 2-3km length of the Olooltepes horst blocks may represent the maximum possible fault segment length that could be supported by the crust at the centre of the rift, as governed by the effective elastic thickness. Note that since T_e is thinner than T_{seis}, even though the crust behaves in a brittle fashion to a depth of 9km, the wavelength of the supported topography is limited to a few kilometres. The obvious change in fault morphology from short, bell-shaped segments, with high d/L values, to a long, 'under-displaced', linked fault with a much lower d/L ratio, might then occur as the fault begins to impinge on the base of the elastic crust (figure 6.19). According to this model, small faults nucleating within the brittle upper crust, defined by T_e, would begin to accrue displacement rapidly, as a result of localised earthquake activity, until they interact with the base of the brittle crust. At this point, fault growth in the down-dip direction becomes restricted and strain is transferred laterally within the brittle layer. Since the total strain across the deforming region must stay at a constant, as the fault length increases the accumulated displacement decreases. This may also account for the large reduction in vertical displacement rates associated with some faults during and after segment linkage. During periods of seismic activity, such as in May 1998, earthquakes nucleating on one section of the fault trigger other events along strike, such that a swarm of activity migrates along the faultline. Following this

pattern, the 1998 earthquake swarm migrated northwards along the Olooltepes fault at a rate of 0.3km/day. A consequence of this process is to 'smear' strain laterally and cause a long section of the fault to be uniformly uplifted by a small amount. As a result, faults grow as long, flat, structures that are under-displaced with respect to displacement-scaling relationships and have vertical displacement rates that decrease with time (figure 6.19).

The relative ease with which strain can be laterally transferred probably reflects the lack of asperities to lateral fault growth within what is a uniformly bedded series of horizontal lava flows. In such a lithological environment, horizontal asperities, such as boundaries between lava beds, are expected to be far more of an important obstruction to fault growth. A number of previous studies have described the influence of horizontal layering on the growth of normal faults (Muraoka and Kamata, 1983; Dawers *et al.*, 1993; Mansfield and Cartwright, 1996; Nicol *et al.*, 1996). In their study of faulting within the Volcanic Tablelands, California, Dawers *et al.* (1993) recognise two distinct patterns of along-strike displacement distributions: elliptical (for faults less than 200m in length) and flat-topped (for faults greater than 600m in length) (see figure 1.2). The characteristic flat-topped morphology of the largest fault set bears a remarkable similarity to the long, flat faults that cut the floor of the South Kenya Rift. In the case of the Volcanic Tablelands, the observed change in the characteristic displacement-length profile is believed to relate to the size at which the fault is able to break through the brittle host rock (the Bishop Tuff ash flow sheet) and begin to interact with the underlying poorly consolidated alluvium, ash and lacustrine sediments. Accordingly, the small faults have an elliptical-shaped displacement length profile because they are contained entirely within the tuff sheet and hence propagate as circular cracks. Flat-topped profiles are generated when the faults become large enough to break through the base of the brittle sheet and are then restricted to propagate laterally by the underlying lithology.

The importance of mechanical layer thickness in controlling fault development is likely to be important at all scales where there are large vertical contrasts in rheology within a sequence of horizontally bedded rocks (see Wilkins and Gross, 2002). The relevance of the seismogenic thickness or effective elastic thickness may, therefore, be overstated and the apparent change in fault morphology with length may instead reflect another rheological contrast at depth, such as that between 'brittle' volcanic stratigraphy and 'ductile' lacustrine or alluvial beds.
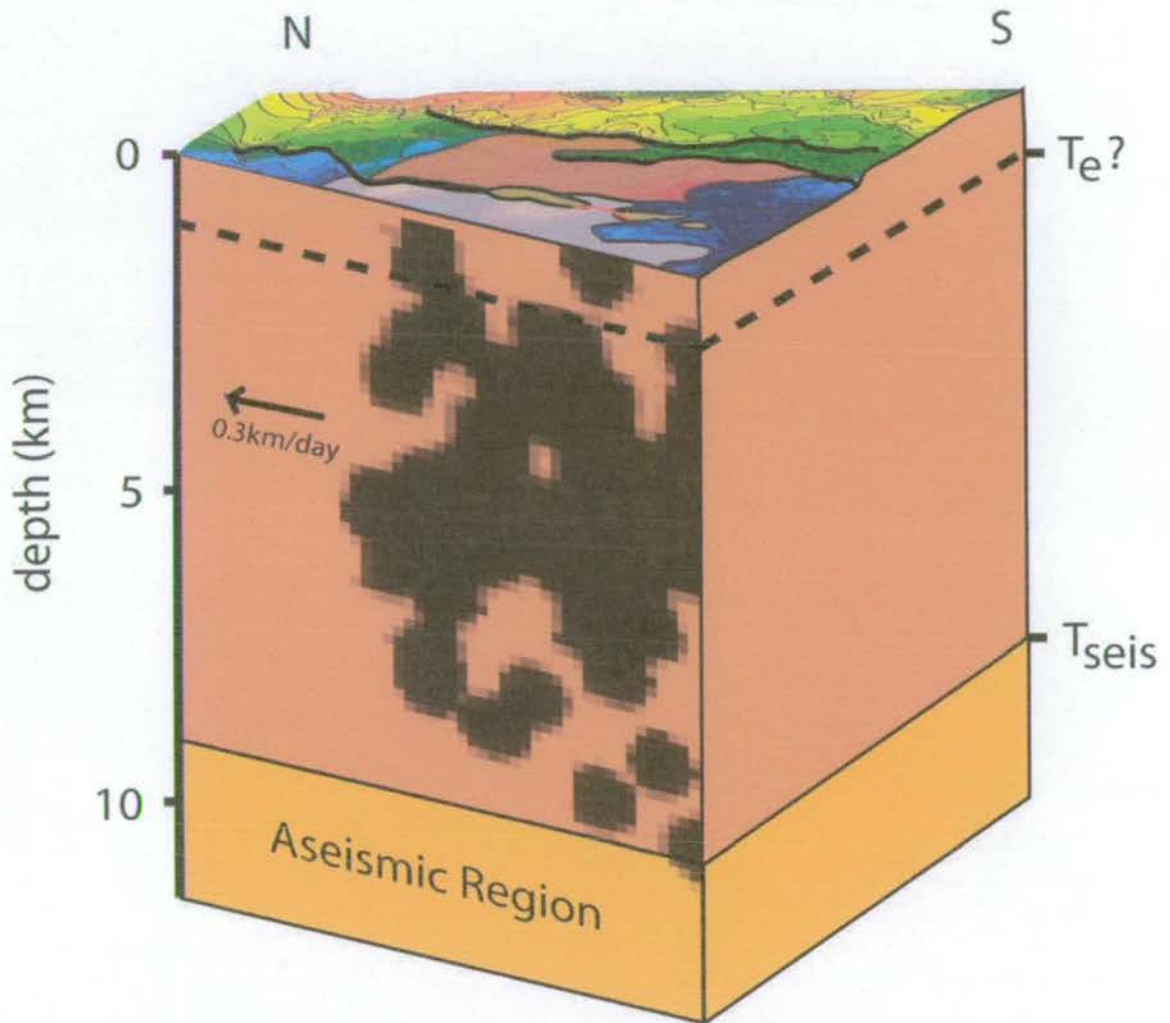
Figure 6.18 True-scale block diagram to illustrate the relationship between surface fault patterns and underlying upper crustal structure as revealed by seismic activity in the Olooltepes region. The hypocentre depths of a swarm of microseismic earthquakes, recorded in May 1998 by Ibs-von Seht *et al.* (2001), is scaled to surface topography and pasted to the surface of the block, which is orientated along strike of the swarm (014 NNE). The events lay directly beneath the surface expression of the Olooltepes fault and resulted in the formation of a tension gash linking two of the horst blocks, as shown by the red line. The arrow indicates the migration direction of the earthquake events as they moved towards the NNE at a rate of 0.3kmday^{-1}. The maximum depth of the microseismic swarm is ~9km, beneath which is interpreted to be a ductile layer that may represent a magma body (Ibs-von Seht *et al.*, 2001).
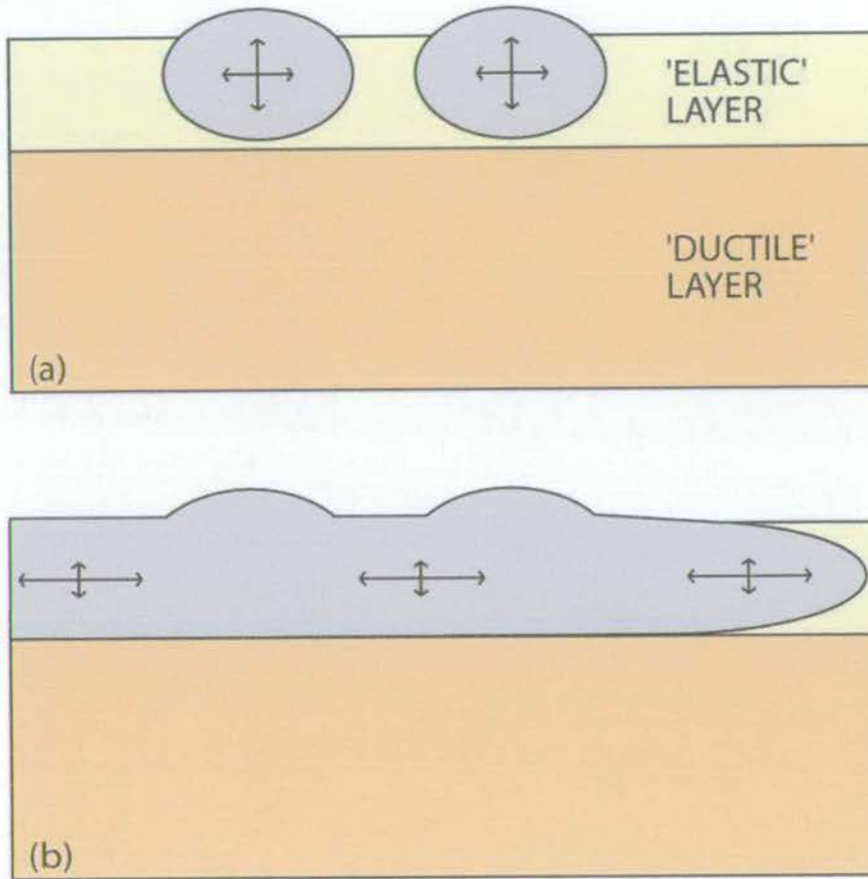
Figure 6.19 Idealised model of extensional fault development in the elastic upper crust at the centre of the South Kenya Rift. (a) Faults nucleate within the strong upper crust and begin to grow self-similarly as a result of repeated earthquake events. This period is characterised by high vertical displacement rates. (b) As the fault begins to interact with the base of the elastic/brittle layer its vertical growth becomes restricted and strain is taken up laterally in the form of segment linkage and fault propagation. Deformation effectively becomes 'smeared-out' along strike and hence vertical displacement rates are much reduced. In both diagrams, arrows show relative proportions of vertical and horizontal deformation.

6.7 Growth of the Kedong Graben

The most recent period of activity in the South Kedong region, between 0.360±0.001Ma and present, resulted in rapid development of the ~250m wide Kedong Graben structure. During this period, the graben flanks were uplifted by a total of ~100m as a result of movement on the graben-bounding faults (Enasira and Porosita). As previously discussed, faulting along the margins of the Kedong Graben involved linkage between the pre-existing, but inactive, N-S trending Gesumeti Trachyte horst blocks. Development of the through-going N-S faults involved dissection and uplift of the pre-existing NW-SE trending structures as a result of reactivation along the Gesumeti Trachyte horsts.

The youngest lava to have been cross-cut by growth of the Kedong Graben is the Barajai Trachyte, which, with an age of 0.360±0.001Ma, is believed to represent one of the earliest lavas to have been sourced from Mount Suswa (Baker *et al.*, 1988). It is therefore possible that the Kedong region experienced a perturbation in the local strain rate as a result of volcanism associated with Mount Suswa.

Faulting along the Kedong Graben may have initiated as a result of magmatic dyke injections beneath the Esageri-Esakut Platform that were sourced from the Suswa volcano. Tectonic deformation associated with magmatic activity has been described from a number of volcanic provinces, such as Iceland, Afar and Hawaii (Pollard *et al.*, 1983; Rubin and Pollard, 1988; Rubin, 1992; Clifton *et al.*, 2002; Bull *et al.*, 2003). Rubin and Pollard (1988) and Rubin (1992) model surface displacements resulting from individual dyke intrusion events in Northern Iceland. They suggest that movement on graben-bounding faults can be induced by dyke emplacement and, in particular, that significant faulting and subsidence would be expected to occur ahead of a laterally propagating dyke or dyke swarm. Bull *et al.* (2003) have applied these models of instantaneous dyke injection to the development of Icelandic normal faults over a geological timescale. They describe how, over a 2-3ky period, 25-30m of subsidence was rapidly accumulated on a single normal fault, at the northern end of Lake Thingvallavatn, in response to dyke emplacement associated with the formation of a nearby volcanic cone.

The timing of formation of the Kedong Graben is consistent with development of Mount Suswa, some 25km to the north, and with the eruption of Barajai Trachyte lavas. It is likely that the

latest stage in the evolution of the South Kedong Graben was dominated by faulting that was associated with dyke intrusion under the moderation of the regional E-W strain field, as has been suggested for the development of certain Icelandic faults (Bull *et al.*, 2003). Hence, while the localisation of strain onto the Kedong Graben was governed by regional extension, the process was considerably accelerated by local magmatic activity and dyke emplacement. Assuming the amount of displacement along the graben reflects the width of the magma intrusion, then the ~100m of subsidence at the southern end of the Kedong Graben reflects emplacement of a 100m thick dyke, or set of dykes (Rubin, 1992; Bull *et al.*, 2003). Such an intrusion would account for the increase in displacement rates in the South Kedong region between 0.360±0.001Ma and present.

6.8 Conclusions

- Kilometre-scale faulting across the floor of the South Kenya Rift occurs in two distinct stages (figure 6.20):

  i)   Self-similar growth of 'bell-shaped' fault segments that develop a large amount of displacement in a short period of time (e.g. 18kyr for the Olooltepes horsts). These segments are commonly observed as distinctive 2-3km-long horst blocks with displacement to length (d/L) ratios of 0.06-0.10.

  ii) Development of long, 'flat', faults characterised by low d/L values (~0.01-0.02) as a result of linkage between the pre-existing fault segments. Linkage occurs early in fault development, without any intervening period of fault segment interaction. The only exception to this is along the southern section of the Enasira fault, in the South Kedong region, where interaction between neighbouring faults, prior to linkage, resulted in an increase in fault tip gradients and formation of a zone of footwall faulting.

  Hangingwall data, where available, suggest that the ratio of footwall uplift to hangingwall subsidence is approximately 1:1.4 to 1:2 for long-term faulting (over a timescale of several hundred kyr) in the South Kenya Rift.
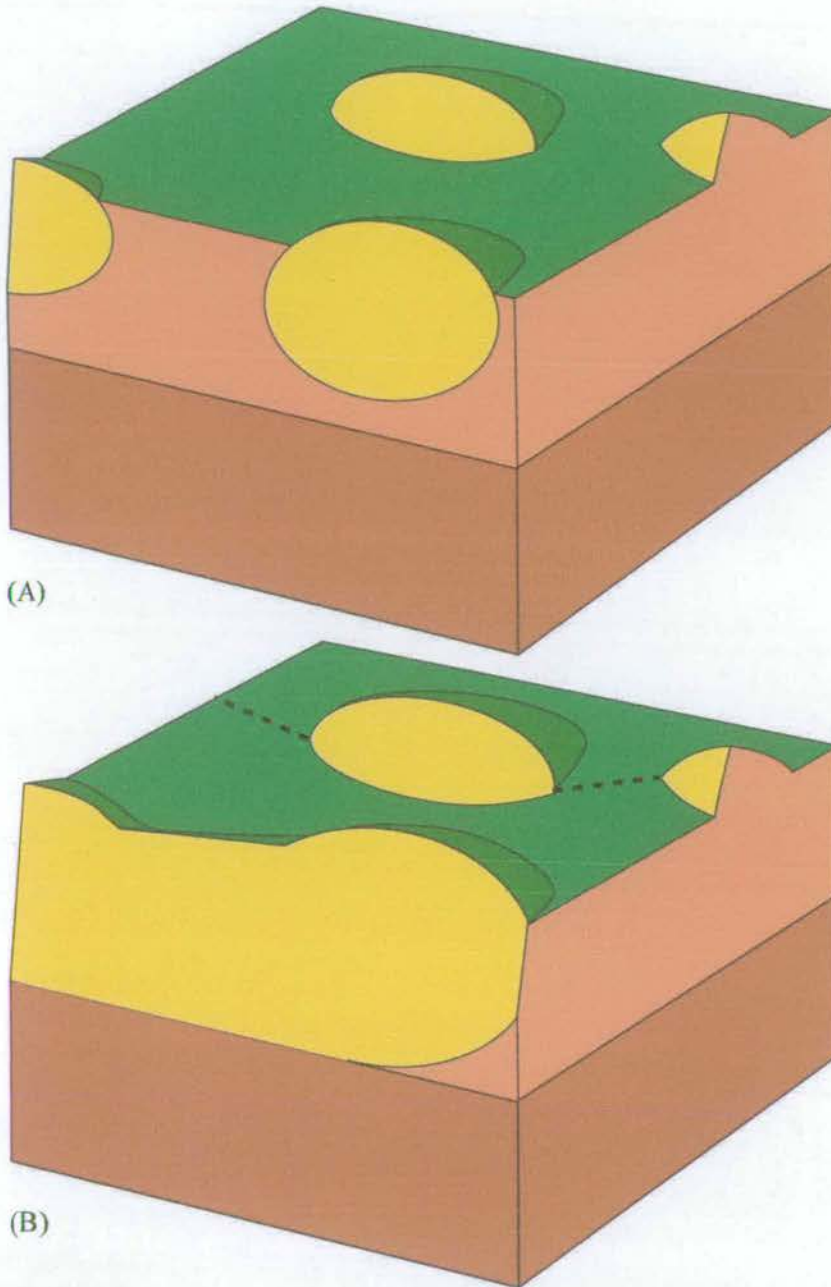
Figure 6.20 Schematic block diagrams showing the spatial and temporal evolution of kilometre-scale faulting in the South Kenya Rift. (A) Faults initiate as small (2-3km long) bell-shaped segments as a result of rapid (up to 12mmyr⁻¹) self-similar growth within the brittle, upper mechanical layer of the rift-floor stratigraphy. (B) With continued growth, the faults begin to interact with rheological contrasts at depth (either within the volcanic pile or at the base of the effective elastic thickness (Te)) and are constrained to propagate laterally. At this time, vertical displacement rates and d/L ratios are much reduced (to values of 0.1-0.3mmyr⁻¹ and ~0.01 respectively) as strain is transferred along strike and the fault preferentially increases in length.

- In the case of the South Kedong and Olooltepes regions, fault displacement rates are high during fault initiation (up to 12mmyr^{-1}), but then either slow with time or show episodes of activity, interspersed with periods of quiescence. Where rates decrease with time (to values of 0.1-0.3mmyr^{-1}), the decrease often occurs during, and after, fault segment linkage.

- Early linkage between fault segments may be a reflection of down-dip interaction with vertical strength contrasts in the volcanic lava pile or, on a more fundamental scale, the base of the effective elastic thickness (T_e). As small fault segments become large enough to interact with the base of the mechanical layer in which they are developing, they begin to transfer strain along strike. This allows deformation to become 'smeared' along a relatively long section of fault and is a possible explanation for the decrease in fault displacement rates with time (figure 6.20).

- Large displacement rates on faults located at the centre of the rift, at the same time as lower rates on faults located towards the rift margins, suggests that there may be a progressive migration of strain towards the centre of the rift with time. This is supported by observations of neotectonic activity (Ibs-von Seht *et al.*, 2001), which indicate that most microseismic events are currently located at the rift centre.

- Fault development is likely to be influenced by the effects of magmatism within the rift. Phases of increased volcanic activity, during tectono-magmatic cycling, may cause a transient increase in the local strain rate that would produce large initial fault displacement rates after eruption of volcanic material. These rates would then decrease with time, as volcanism waned. On a smaller scale, increased fault subsidence may also be affected by dyke emplacement. In this way, subsidence along the margins of the Kedong Graben, between 0.360±0.001Ma and present, is likely to have been influenced by dyke injection associated with the growth and development of Mount Suswa.

- Regions in which faults show dramatic variations in strike, such as the Magadi Transverse Zone (MTZ) and along the southern margin of the Esageri-Esakut Platform, are likely to be affected by interaction with major basement heterogenities aligned obliquely to the principal E-W extension direction.

References

Ackermann, R.V. and Schlische, R.W., 1997
    Anticlustering of small normal faults around larger faults
    Geology, **25**, 1127-1130

Ackermann, R.V., Schlische, R.W. and Withjack, M.O., 2001
    The geometric and statistical evolution of normal fault systems: an experimental study of the
    effects of mechanical layer thickness on scaling laws
    Journal of Structural Geology, **23**, 1803-1819

Anders, M.H. and Schlische, R.W., 1994
    Overlapping Faults, Intrabasin Highs, and the Growth of Normal Faults
    Journal of Geology, **102**,165-180

Atmaoui, N. and Hollnack, D., 2003
    Neotectonics and extension direction of the Southern Kenya Rift, Lake Magadi area
    Tectonophysics, **364**, 71-83

Baker, B.H., 1958
    Geology of the Magadi Area
    *Geological Survey of Kenya Report No.***42**

Baker, B.H., 1963
    Geology of the Area South of Magadi
    Geological Survey of Kenya Report No. **61**

Baker, B.H., 1986
    Tectonics and volcanism of the southern Kenya Rift Valley and its influence on rift
    sedimentation
    In: Frostick, L.E., Renaut, R.W., Reid, I. and Tiercelin, J.J. (eds.), *Sedimentation in the
    African Rifts.* Geological Society Special Publication No. **25**, 45-57

Baker, B.H., Crossley, R. and Goles, G.G., 1978

Tectonic and magmatic evolution of the southern part of the Kenya rift valley

In: *Neumann, E.R. and Ramberg, I.B. (eds.),* Petrology and Geochemistry of Continental Rifts. *D. Reidel, Dordrecht, 29-50*

Baker, B.H. and Mitchell, J.G., 1976

Volcanic stratigraphy and geochronology of the Kedong-Olorgesailie area and the evolution of the South Kenya rift valley.

Journal of the Geological Society of London, **132**, 467-484

Baker, B.H., Mitchell, J.G. and Williams, L.A.J., 1988

Stratigraphy, geochronology and volcano-tectonic evolution of the Kedong-Naivasha-Kinangop region, Gregory Rift Valley, Kenya

Journal of the Geological Society of London, **145**, 107-116

Baker, B.H. and Wohlenberg, J., 1971

Structure and evolution of the Kenya Rift Valley

Nature, **229**, 538-542

Barrientos, S.E., Stein, R.S. and Ward, S.N., 1987

Comparison of the 1959 Hebgen Lake, Montana and the 1983 Borah Peak, Idaho, earthquakes from geodetic observations

Bulletin of the Seismological Society of America, **77**, 784-808

Birt, C.S., Maguire, P.K.H., Khan, M.A., Thybo, H., Keller, G.R. and Patel, J., 1997

The influence of pre-existing structures on the evolution of the southern Kenya Rift Valley – evidence from seismic and gravity studies

Tectonophysics, **278**, 211-242

Bosworth, W., 1985

Geometry of propagating continental rifts

Nature, **316**, 625-627

Brunner Mond, 2001
>
> Magadi Soda Company
>
> <Available at http://www.brunnermond.com/magadi/> [accessed on 05/2001]

Bull, J.M., Minshull, T.A., Mitchell, N.C., Thors, K., Dix, J.K. and Best, A.I., 2003
>
> Fault and magmatic interaction within Iceland's western rift over the last 9 kyr
>
> *Geophysical Journal International*, **154**, F1-F8

Bye, B.A., Brown, F.H., Cerling, T.E. and McDougall, I., 1987
>
> Increased age estimate for the Lower Palaeolithic hominid site at Olorgesailie, Kenya
>
> *Nature*, **329**, 237-239

Byrne, G.F., Jacob, A.W.B., Mechie, J. and Dindi, E., 1997
>
> Seismic structure of the upper mantle beneath the southern Kenya Rift from wide-angle data
>
> *Tectonophysics*, **278**, 243-260

Cartwright, J.A., Mansfield, C. and Trudgill, B., 1996
>
> The growth of faults by segment linkage.
>
> *In:* Buchanan, P.G. and Nieuwland, D.A. (eds.), *Modern Developments in Structural Interpretation, Validation and Modelling.* Geological Society Special Publication No. **99**, 163-177

Cartwright, J.A., Trudgill, B.D. and Mansfield, C.S., 1995
>
> Fault growth by segment linkage: an explanation for scatter in maximum displacement and trace length data from the Canyonlands Grabens of SE Utah.
>
> *Journal of Structural Geology*, **17**, 1319-1326

Chambers, L.M., 2000
>
> Age and duration of the British Tertiary Igneous Province: implications for the development of the ancestral Iceland Plume
>
> *Thesis, Ph.D., University of Edinburgh (unpubl.).*

Childs, C., Watterson, J. and Walsh, J.J., 1995

Fault overlap zones within developing normal fault systems.
Journal of the Geological Society of London, **152**, 535-549

Childs, C., Watterson, J. and Walsh, J.J., 1996
A model for the structure and development of fault zones.
Journal of the Geological Society of London, **153**, 337-340

Cladouhos, T.T. and Marrett, R., 1996
Are fault growth and linkage models consistent with power-law distributions of fault lengths?
Journal of Structural Geology, **18**, 281-293

Clifton, A.E. and Schlische, R.W., 2001
Nucleation, growth and linkage of faults in oblique rift zones: Results from experimental clay models and implications for maximum fault size
Geology, **29**, 455-458

Clifton, A.E., Schlische, R.W., Withjack, M.O. and Ackermann, R.V., 2000
Influence of rift obliquity on fault-population systematics: Results of experimental clay models
Journal of Structural Geology, **22**, 1491-1509

Clifton, A.E., Sigmundsson, F., Feigl, K.L., Gudmundsson, G. and Árnadóttir, Th., 2002
Surface effects of faulting and deformation resulting from magma accumulation at the Hengill triple junction, SW Iceland, 1994-1998
Journal of Volcanology and Geothermal Research, **115**, 233-255

Contreras, J., Anders, M.H. and Scholz, C.H., 2000
Growth of a normal fault system: observations from the Lake Malawi basin of the east African rift.
Journal of Structural Geology, **22**, 159-168

Cowie, P.A., 1998

A healing-reloading feedback control on the growth rate of seismogenic faults

Journal of Structural Geology, **20**, 1075-1087

Cowie, P.A., Gupta, S. and Dawers, N.H., 2000

Implications of fault array evolution for synrift depocentre development: insights from a numerical fault growth model

Basin Research, **12**, 241-261

Cowie, P.A. and Roberts, G.P., 2001

Constraining slip rates and spacings for active normal faults

Journal of Structural Geology, **23**, 1901-1915

Cowie, P.A. and Scholz, C.H., 1992a

Physical explanation for the displacement length relationship of faults using a post-yield fracture-mechanics model.

Journal of Structural Geology, **14**, 1133-1148

Cowie, P.A. and Scholz, C.H., 1992b

Displacement length scaling relationship for faults – data synthesis and discussion.

Journal of Structural Geology, **14**, 1149-1156

Cowie, P.A., Sornette, D. and Vanneste, C., 1995

Multifractal scaling properties of a growing fault population.

Geophysical Journal International, **122**, 457-469

Cowie, P.A., Vanneste, C. and Sornette, D., 1993

Statistical physics model for the spatio-temporal evolution of faults.

Journal of Geophysical Research, **98**, 21809-21821

Crossley, R., 1976

Structure, stratigraphy and volcanism in the Nguruman Escarpment area of the western side of the Kenya Rift Valley.

Thesis, Ph.D., University of Lancaster (unpubl.).

Crossley, R., 1979

The Cenozoic stratigraphy and structure of the western part of the Rift Valley in southern Kenya.

Journal of the Geological Society of London, **136**, 393-405

Das, S. and Scholz, C.H., 1983

Why large earthquakes do not nucleate at shallow depths

Nature, **305**, 145-148

Davies, S.J., Dawers, N.H., McLeod, A.E. and Underhill, J.R., 2000

The structural and sedimentological evolution of early synrift successions: the Middle Jurassic Tarbert Formation, North Sea

Basin Research, **12**, 343-365

Dawers, N.H. and Anders, M.H., 1995

Displacement-length scaling and fault linkage

Journal of Structural Geology, **17**, 607-614

Dawers, N.H., Anders, M.H. and Scholz, C.H., 1993

Growth of normal faults – displacement-length scaling

Geology, **21**, 1107-1110

Dawers, N.H. and Underhill, J.R., 2000

The role of fault interaction and linkage in controlling synrift stratigraphic sequences: Late Jurassic, Statfjord East area, northern North Sea

American Association of Petroleum Geologists Bulletin, **84**, 45-64

Deino, A. and Potts, R., 1990

Single-Crystal $^{40}Ar/^{39}Ar$ Dating of the Olorgesailie Formation, Southern Kenya Rift

Journal of Geophysical Research, **95**, 8453-8470

Destro, N., 1995

Release fault: a variety of cross fault in linked extensional fault systems, in the Sergipe-Alagoas Basin, NE Brazil.

Journal of Structural Geology, **17**, 615-629

Destro, N., Szatmari, P., Alkmim, F.F. and Magnavita, L.P., 2003

Release faults, associated structures, and their control on petroleum trends in the Reconcavo Rift, northeast Brazil

American Association of Petroleum Geologists Bulletin, **87**, 1123-1144

Ebinger, C.J., Jackson, J.A., Foster, A.N. and Hayward, N.J., 1999

Extensional basin geometry and the elastic lithosphere

Philosophical Transactions of the Royal Society of London, **A357**, 741-765

Elliot, D., 1976

The energy balance and deformation mechanisms of thrust sheets.

Philosophical Transactions of the Royal Society of London, **A283**, 289-312

England, P., 1983

Constraints on extension of continental lithosphere.

Journal of Geophysical Research, **88**, 1145-1152

Evernden, J.F. and Curtis, G.H., 1965

Potassium-argon dating of Late Cenozoic rocks in East Africa and Italy.

Current Anthropology, **6**, 343-385

Fairhead, J.D., 1976

The structure of the lithosphere beneath the Eastern rift, East Africa, deduced from gravity studies.

Tectonophysics, **30**, 269-298

Fairhead, J.D., Mitchell, J.G. and Williams, L.A.J., 1972

New K/Ar Determinations on Rift Volcanics of S.Kenya and their Bearing on Age of Rift Faulting.

Nature Physical Science, **238**, 66-69

Ferrill, D.A., Stamatakos, J.R. and Sims, D., 1999

Normal fault corrugation: implications for growth and seismicity of active normal faults

Journal of Structural Geology, **21**, 1027-1038

Foster, A.N. and Jackson, J.A., 1998

Source parameters of large African earthquakes: implications for crustal rheology and regional kinematics

Geophysical Journal International, **134**, 422-448

Gawthorpe, R.L., Jackson, C.A.-L., Young, M.J., Sharp, I.R., Moustafa, A.R. and Leppard, C.W., 2003

Normal fault growth, displacement localisation and the evolution of normal fault populations: the Hammam Faraun fault block, Suez rift, Egypt.

Journal of Structural Geology, **25**, 883-895

Gawthorpe, R.L., Sharp, I.R., Underhill, J.R. and Gupta, S., 1997

Linked sequence stratigraphic and structural evolution of propagating normal faults

Geology, **25**, 795-798

Geophysical Equipment Facility (Natural Environment Research Council), 2004

Leica System 530

<Available at http://www.glg.ed.ac.uk/gep/> [accessed on 12/05/04]

Gillespie, P.A., Walsh, J.J. and Watterson, J., 1992

Limitations of dimension and displacement data from single faults and the consequences for data-analysis and interpretation.

Journal of Structural Geology, **14**,1157-1172

Gilpin, R.E. and Dawers, N.H., 2001

Interactions between normal fault growth and drainage development; insights from the Volcanic Tableland, Owen's Valley, California

Annual Meeting Expanded Abstracts - American Association of Petroleum Geologists, **6**, 72

Gloaguen, R., 2000

Mid-Ocean Ridges and Continental Rifts. Compared Geometries. Surface deformation analysis using 3D imagery.

Thesis, Ph.D., University of Brest (unpubl.).

Gregg, T.K.P. and Fink, J.H., 2000

A laboratory investigation into the effects of slope on lava flow morphology

Journal of Volcanology and Geothermal Research, **96**, 145-159

Grimaud, P., Richert, J.P., Rolet, J., Tiercelin, J.J., Xavier, J.P., Morley, C.K., Coussement, C., Karanja, S.W., Renaut, R.W., Guérin, G., Le Turdu, C. and Michel-Noël, G., 1994

Fault geometry and extension mechanisms in the Central Kenya Rift, East Africa. A 3D remote sensing approach

Bulletin des Centres de Recherches Exploration-Production Elf Aquitaine, **18**, 59-92

Gupta, A. and Scholz, C.H., 2000

A model of normal fault interaction based on observations and theory

Journal of Structural Geology, **22**, 865-879

Gupta, S., Commins, D., Phillips, W.M. and Cartwright, J.A., 2003

Constraining rates of normal fault growth using in situ cosmogenic surface exposure dating of relict fluvial landforms, Canyonlands Graben, Utah

2003 Annual Meeting Abstracts - American Association of Petroleum Geologists, **12**, A68-69

Gupta, S., Cowie, P.A., Dawers, N.H. and Underhill, J.R., 1998

A mechanism to explain rift-basin subsidence and stratigraphic patterns through fault-array evolution

Geology, **26**, 595-598

Gupta, S., Underhill, J.R., Sharp, I.R. and Gawthorpe, R.L., 1999
Role of fault interactions in controlling synrift sediment dispersal patterns: Miocene, Abu Alaqa Group, Suez Rift, Egypt
Basin Research, **11**, 167-189

Harford, C.L., Pringle, M.S., Sparks, R.S.J. and Young, S.R., 2002
The volcanic evolution of Montserrat using ^{40}Ar/^{39}Ar geochronology
In: Druitt, T.H. and Kokelaar, B.P. (eds.) *The eruption of the Soufriere Hills Volcano, Montserrat, from 1995 to 1999.* Geological Society of London, Memoirs, **21**, 93-113

Hayward, N.J. and Ebinger, C.J., 1996
Variations in the along-axis segmentation of the Afar Rift system
Tectonics, *15*, 244-257

Hollnack, D and Stangl, R., 1998
The seismicity related to the southern part of the Kenya Rift
Journal of African Earth Sciences, **26**, 477-495

Huggins, P., Watterson, J., Walsh, J.J. and Childs, C., 1995
Relay zone geometry and displacement transfer between normal faults recorded in coal-mine plans
Journal of Structural Geology, **17**, 1741-1755.

Ibs-von Seht, M., Blumenstein, S., Wagner, R., Hollnack, D. and Wohlenberg, J., 2001
Seismicity, seismotectonics and crustal structure of the southern Kenya Rift – new data from the Lake Magadi area.
Geophysical Journal International, **146**, 1-20.

Incorporated Research Institutions for Seismology (IRIS), 2003
SeismiQuery – Event Query: IRIS
<Available at http://www.iris.edu/SeismiQuery/events.htm> [accessed on 07/08/2003]

Isaac, G. Ll., 1978

The Olorgesailie Formation: Stratigraphy, tectonics and the palaeogeographic context of the Middle Pleistocene archaeological sites
In: Bishop, W.W., (ed) *Geological Background to Fossil Man*. Scottish Academic Press, Edinburgh, pp. 173-206

Jackson, C.A.-L., Gawthorpe, R.L. and Sharp, I.R., 2002a
Growth and linkage of the East Tanka fault zone, Suez rift: structural style and syn-rift stratigraphic response.
Journal of the Geological Society of London, **159**, 175-187

Jackson, J.A., Norris, R. and Youngson, J., 1996
The structural evolution of active fault and fold systems in central Otago, New Zealand: evidence revealed by drainage patterns
Journal of Structural Geology, **18**, 217-234

Jackson, J.A. and White, N.J., 1989
Normal faulting in the upper continental crust: observations from regions of active extension
Journal of Structural Geology, **11**, 15-36

Jackson, J., Ritz, J-F., Siame, L., Raisbeck, G., Yiou, F., Norris, R., Youngson, J. and Bennett, E., 2002b
Fault growth and landscape development rates in Otago, New Zealand, using in situ cosmogenic ^{10}Be
Earth and Planetary Science Letters, **195**, 185-193

Jestin, F., Huchon, P. and Gaulier, J.M., 1994
The Somalia plate and the East African Rift System: present-day kinematics
Geophysical Journal International, **116**, 637-654

King, B.C., 1978
Structural and volcanic evolution of the Gregory Rift Valley
In: Bishop, W.W., (ed) *Geological Background to Fossil Man*. Scottish Academic Press, Edinburgh, pp. 29-54

Larsen, P.H., 1988

> Relay structures in a Lower Permian basement-involved extension system, East Greenland.
> *Journal of Structural Geology*, **10**, 3-8

Leakey, L.S.B., 1974

> *By the Evidence: Memoir 1932-1951*. New York and London: Harcourt, Brace and Jovanovich.

Leica Geosystems AG, 1999

> *Introduction to GPS (Global Positioning System)*. Version 1.0. Heerbrugg, Switzerland.

le Roex, A.P., Späth, A. and Zartman, R.E., 2001

> Lithospheric thickness beneath the southern Kenya Rift: implications from basalt geochemistry.
> *Contributions to Mineralogy and Petrology*, **142**, 89-106

Le Turdu, C., Coussement, C., Tiercelin, J.J., Renaut, R.W., Rolet, J., Richert, J.P. and Coquelet, D., 1995

> Rift basin structure and depositional patterns interpreted using a 3D remote sensing approach: The Baringo and Borgoria Basins, Central Kenya Rift, East Africa.
> *Bulletin des Centres de Recherches Exploration-Production Elf Aquitaine*, **19**, 1-37

Le Turdu, C., Tiercelin, J.J., Richert, J.P., Rolet, J., Xavier, J.P., Renaut, R.W., Lezzar, K.E. and Coussement, C., 1999

> Influence of pre-existing oblique discontinuities on the geometry and evolution of extensional fault patterns; evidence from the Kenya Rift using SPOT imagery.
> *In:* Morley, C.K. (ed.), *Geoscience of Rift Systems – Evolution of East Africa*, AAPG Studies in Geology **44**, 173-191

Lin, J. and Parmentier, E.M., 1990

> A finite-amplitude necking model of rifting in brittle lithosphere.
> *Journal of Geophysical Research*, **95**, 4909-4923

MacGregor, L.M., Constable, S.C. and Sinha, M.C., 1998
The RAMESSES experiment; III, Controlled-source electromagnetic sounding of the Reykjanes Ridge at 57 degrees 45'N
Geophysical Journal International, **135**, 773-789

Mansfield, C.S. and Cartwright, J.A., 1996
High resolution fault displacement mapping from three-dimensional seismic data: Evidence for dip linkage during fault growth.
Journal of Structural Geology, **18**, 249-263

Mansfield, C.S. and Cartwright, J.A., 2001
Fault growth by linkage: observations and implications from analogue models.
Journal of Structural Geology, **23**, 745-763

Marrett, R. and Allmendinger, R.W., 1991
Estimations of strain due to brittle faulting – sampling of fault populations.
Journal of Structural Geology, **13**, 735-738

McClay, K.R., Dooley, T., Whitehouse, P. and Mills, M., 2002
4-D evolution of rift systems: Insights from scaled physical models
American Association of Petroleum Geologists Bulletin, **86**, 935-959

McClay, K.R. and White, M.J., 1995
Analogue modelling of orthogonal and oblique rifting.
Marine and Petroleum Geology, **12**, 137-151

McKenzie D., 1978
Some remarks on the development of sedimentary basins.
Earth and Planetary Science Letters, **40**, 25-32

McLeod, A.E., Dawers, N.H. and Underhill, J.R., 2000
The propagation and linkage of normal faults: insights from the Strathspey-Brent-Statfjord fault array, northern North Sea
Basin Research, **12**, 263-284

McLeod, A.E., Underhill, J.R., Davies, S.J. and Dawers, N.H., 2002
The influence of fault array evolution on synrift sedimentation patterns: Controls on deposition in the Strathspey-Brent-Statfjord half graben, northern North Sea.
American Association of Petroleum Geologists Bulletin, **86**, 1061-1093

Meyer, V., Nicol, A., Childs, C., Walsh, J.J. and Watterson, J., 2002
Progressive localisation of strain during the evolution of a normal fault system in the Timor Sea.
Journal of Structural Geology, **24**, 1215-1231

Miller, J.A., 1967
Problems of dating East African Tertiary and Quaternary volcanics by the potassium-argon method.
In: Bishop, W.W. and Clark, J.D., (eds.) *Background to Evolution in Africa.* Chicago University Press, Chicago, pp. 259-272.

Morewood, N.C. and Roberts, G.P., 1999
Lateral propagation of the surface trace of the South Alkyonides normal fault segment, central Greece: its impact on models of fault growth and displacement-length relationships.
Journal of Structural Geology, **21**, 635-652

Morewood, N.C. and Roberts, G.P., 2002
Surface observations of active normal fault propagation: implications for growth
Journal of the Geological Society of London, **159**, 263-272

Morley, C.K., Nelson, R.A., Patton, T.L. and Munn, S.G., 1990
Transfer zones in the East African Rift system and their relevance to hydrocarbon exploration in rifts.
American Association of Petroleum Geologists Bulletin, **74**, 1234-1253.

Morley, C.K., Ngenoh, D.K. and Ego, J.K., 1999
Introduction to the East African Rift System.
In: Morley C.K. (ed) *Geoscience of Rift Systems – Evolution of East Africa,* AAPG Studies in Geology No. **44**, 1-19

Morley, C.K., 1999a
Basin Evolution Trends in East Africa
In: Morley C.K. (ed) *Geoscience of Rift Systems – Evolution of East Africa,* AAPG Studies in Geology No. **44**, 131-150

Morley, C.K., 1999b
Aspects of Transfer Zone Geometry and Evolution in East African Rifts
In: Morley C.K. (ed.) *Geoscience of Rift Systems – Evolution of East Africa,* AAPG Studies in Geology No. **44**, 161-171

Morley, C.K., 1999c
Influence of Preexisting Fabrics on Rift Structure
In: Morley C.K. (ed.) *Geoscience of Rift Systems – Evolution of East Africa*, AAPG Studies in Geology No. **44**, 151-160

Muraoka, H. and Kamata, H., 1983
Displacement distribution along minor fault traces
Journal of Structural Geology, **5**, 483-495

National Geographic and ESRI, 2002
MapMachine
<Available at http://plasma.nationalgeographic.com/mapmachine/> [accessed on 01/2002]

National Imagery and Mapping Agency (NIMA), 2002

> 2.2.2 - Geographic Translator
>
> <Available at http://164.214.2.59/GandG/geotrans/geotrans.html> [accessed on 08/2002]

Navin, D.A., Peirce, C. and Sinha, M.C., 1998

> The RAMESSES experiment; II, Evidence for accumulated melt beneath a slow spreading
> ridge from wide-angle refraction and multichannel reflection seismic profiles
> *Geophysical Journal International*, **135**, 746-772

Nicol, A., Walsh, J.J., Watterson, J. and Underhill, J.R., 1997

> Displacement rates of normal faults
> *Nature*, **390**, 157-159

Nicol, A., Watterson, J., Walsh, J.J. and Childs, C., 1996

> The shapes, major axis orientations and displacement patterns of fault surfaces
> *Journal of Structural Geology*, **18**, 235-248

Peacock, D.C.P. and Sanderson, D.J., 1991

> Displacements, segment linkage and relay ramps in normal fault zones.
> *Journal of Structural Geology*, **13**, 721-733

Peacock, D.C.P. and Sanderson, D.J., 1994

> Geometry and development of relay ramps in normal-fault systems
> *American Association of Petroleum Geologists Bulletin*, **78**, 147-165

Pollard, D.D., Delaney, P.T., Duffield, W.A., Endo, E.T. and Okamura, A.T., 1983

> Surface deformation in volcanic rift zones
> *Tectonophysics*, **94**, 541-584

Prodehl, C., Ritter, J.R.R., Mechie, J., Keller, G.R., Khan, M.A., Jacob, B., Fuchs, K.,
Nyambok, I.O., Obel, J.D. and Riaroh, D., 1997

> The KRISP 94 lithospheric investigation of southern Kenya - the experiments and
> their main results

Tectonophysics, **278**, 121-147

Ramsey, J.G. and Huber, M.I., 1987

The techniques of modern structural geology, Volume 2, Folds and fractures.
London Academic Press, 700p.

Rosendahl, B.R., Reynolds, D.J., Lorber, P.M., Burgess, C.F., McGill, J., Scott, D., Lambiase, J.J. and Derksen, S.J., 1986

Structural expressions of rifting; lessons from Lake Tanganyika, Africa
In: Frostick, L.E., Renaut, R.W., Reid, I. and Tiercelin, J.J. (eds) 1986, *Sedimentation in the African Rifts*, Geological Society Special Publication No. **25**, 29-43

Rubin, A.M., 1992

Dike-induced faulting and graben subsidence in volcanic rift zones
Journal of Geophysical Research, **97**, 1839-1858

Rubin, A.M. and Pollard, D.D., 1988

Dike-induced faulting in rift zones of Iceland and Afar
Geology, **16**, 413-417

Schlische, R.W., 1995

Geometry and origin of fault-related folds in extensional settings
American Association of Petroleum Geologists Bulletin, **79**, 1661-1678

Schlische, R.W., Young, S.S., Ackermann, R.V. and Gupta, A., 1996

Geometry and scaling relations of a population of very small rift-related normal faults
Geology, **24**, 683-686

Scholz, C.H. and Contreras, J.C., 1998

Mechanics of continental rift architecture
Geology, **26**, 967-970

Shackleton, R.M., 1955

Pleistocene movements in the Gregory Rift Valley
Geologische Rundschau, **43**, 257-263

Shackleton, R.M., 1978
Geological map of the Olorgesailie Formation
In: Bishop, W.W., (ed) *Geological Background to Fossil Man.* Scottish Academic Press,
Edinburgh, p.172

Sharp, I.R., Gawthorpe, R.L., Underhill, J.R. and Gupta, S., 2000
Fault-propagation folding in extensional settings: Examples of structural style and synrift
sedimentary response from the Suez rift, Sinai, Egypt
Geological Society of America Bulletin, **112**, 1877-1899

Simiyu, S.M. and Keller, G.R., 1998
Upper crustal structure in the vicinity of Lake Magadi in the Kenya Rift Valley
region
Journal of African Earth Sciences, **27**, 359-371

Sinha, M.C., Constable, S.C., Peirce, C., White, A., Heinson, G., MacGregor, L.M. and Navin,
D.A., 1998
Magmatic processes at slow spreading ridges; implications of the RAMESSES experiment at
57 degrees 45'N on the Mid-Atlantic Ridge
Geophysical Journal International, **135**, 731-745

Smith, M. and Mosley, P., 1993
Crustal Heterogeneity and Basement Influence on the development of the Kenya Rift, East
Africa.
Tectonics, **12**, 591-606

Sornette, D., Davy, P. and Sornette, A., 1990
Growth of fractal fault patterns.
Physical Review Letters, **65**, 2266-2269

Stein, R.S. and Barrientos, S., 1985

High-angle normal faulting in the intermountain seismic belt: geodetic investigation of the 1983 Borah Peak, Idaho, earthquake

Journal of Geophysical Research, **90**, 11355-11366

Swain, C.J., 1992

The Kenya Rift axial gravity high: a re-interpretation.

Tectonophysics, **204**, 49-70

Temperley, B.N., 1966

The faced scarp structure and the age of the Kenya Rift Valley.

Overseas Geology and Mineral Resources, **10**, 11-29

Tron, V., and Brun, J.P., 1991

Experiments on oblique rifting in brittle-ductile systems

Tectonophysics, **188**, 71-84

Trudgill, B. and Cartwright, J., 1994

Relay-ramp forms and normal-fault linkages, Canyonlands national-park, Utah

Geological Society of America Bulletin, **106**, 1143-1157

Upton, B.G.J., 1996

Volcanoes and their products

In: Duff, P. McL. D., (ed) *Holmes' Principles of Physical Geology*. Chapman and Hall, London, pp 207-258

Walsh, J.J., Bailey, W.R., Childs, C., Nicol, A. and Bonson C.G., 2003

Formation of segmented normal faults: a 3-D perspective.

Journal of Structural Geology, **25**, 1251-1262

Walsh, J.J. and Watterson, J., 1987

Distributions of cumulative displacement and seismic slip on a single normal-fault surface.

Journal of Structural Geology, **9**, 1039-1046

Walsh, J.J. and Watterson, J., 1988
   Analysis of the relationship between displacements and dimensions of faults
   Journal of Structural Geology, **10**, 239-247

Watterson, J., 1986
   Fault dimensions, displacements and growth
   Pure and Applied Geophysics, **124**, 365-373

Wessel, P., and Smith, W.H.F., 1998
   New, improved version of Generic Mapping Tools released
   EOS Transactions of the American Geophysical Union, **79**, 579

Wessel, P., and Smith, W.H.F., 2003
   The Generic Mapping Tools v3.4.3
   <Available at http://gmt.soest.hawaii.edu/> [accessed on 02/2003]

Wilkins, S.J. and Gross, M.R., 2002
   Normal fault growth in layered rocks at Split Mountain, Utah: influence of mechanical
   stratigraphy on dip linkage, fault restriction and fault scaling
   Journal of Structural Geology, **24**, 1413-1429

Willemse, E.J.M., 1997
   Segmented normal faults: Correspondence between three dimensional mechanical models
   and field data
   Journal of Geophysical Research, **102**, 675-692

Willemse, E.J.M., Pollard, D.D. and Aydin, A., 1996
   Three-dimensional analyses of slip distributions on normal fault arrays with consequences
   for fault scaling
   Journal of Structural Geology, **18**, 295-309

Withjack, M.O. and Jamison, W.R., 1986

Deformation produced by oblique rifting

Tectonophysics, **126**, 99-124

Wojtal, S.F., 1994

Fault scaling laws and the temporal evolution of fault systems

Journal of Structural Geology, **16**, 603-612

Young, M.J., Gawthorpe, R.L. and Hardy, S., 2001

Growth and linkage of a segmented normal fault zone; the Late Jurassic Murchison-Statfjord

North Fault, northern North Sea

Journal of Structural Geology, **23**, 1933-1952

Young, P.A.V., Maguire, P.K.H., Laffoley, d'A. and Evans, J.R., 1991

Implications of the distribution of seismicity near Lake Bogoria in the Kenya Rift

Geophysical Journal International, **105**, 665-674

Appendices

A.1 Introduction

Appendices are available in electronic format on the compact disk attached to the inside back cover of this thesis. Differential GPS and $^{40}Ar/^{39}Ar$ geochronological data have been collated in a series of Microsoft Excel spreadsheet files and can be found in the following folders:

\Appendix A

    \South Kedong

        \Enasira.xls

        \Enasiradisp(0.360Ma-present).xls

        \Enasiradldata(0.360Ma).xls

        \Enasiradldata(present).xls

        \Entashata.xls

        \Entashatadisp(1.478-0.360Ma).xls

        \Entashatadldata(0.360Ma).xls

        \Entashatadldata(1.478Ma).xls

        \FFZ.xls

        \FFZdisp.xls

        \Ndependldata(0.360Ma).xls

        \Porosita.xls

        \Porosita+Enasiradldata(2.009Ma).xls

        \Porosita+Entashatadldata(present).xls

        \Porositadisp(0.360Ma-present).xls

        \Porositadldata(0.360Ma).xls

    \Esiteti

        \Esiteti.xls

        \Esitetidldata.xls

    \Ilainymok

        \Ilainymok.xls

\Ilainymokdldata.xls

\Ilainymokeast.xls

\Appendix A

\Ilainymok

\Ilainymokeastdldata.xls

\Olooltepes

\Olooltepes.xls

\Olooltepesdldata.xls

\Appendix B

\Ihdata.xls

A.2 Appendix A

Appendix A is an electronic folder comprising 4 subfolders, each containing differential GPS data collected from the four fieldareas described in the main body of the thesis, namely; South Kedong, Esiteti, Ilainymok and Olooltepes.

A.2.1 South Kedong

This folder contains 16 Excel files of GPS data recorded from fault scarps in the South Kedong region. Note that all displacements refer to 'minimum' displacements.

a) Enasira.xls

This file contains the raw GPS data recorded as latitude, longitude and ellipsoidal elevation along the Enasira fault. Also included are columns of data calculated for the fault reconstructions described in chapter 5 such as the restored GPS elevations at 0.360 ± 0.001Ma and 1.478 ± 0.003Ma and the intermediate data required to undertake those calculations.

b) Enasiradisp(0.360Ma-present).xls

This file provides data regarding the displacement accumulated along the Enasira fault between 0.360 ± 0.001Ma and present and the associated minimum displacement rates during the same period.

c) Enasiradldata(0.360Ma).xls

This provides the along-strike displacement-length data for the Enasira fault as backstripped to 0.360 ± 0.001Ma.

d) Enasiradldata(present).xls

This file provides the along-strike displacement-length data for the present-day Enasira fault scarp.

e) Entashata.xls

This file contains the raw GPS data recorded as latitude, longitude and ellipsoidal elevation along the Entashata fault. Also included are columns of data calculated for the fault reconstructions described in chapter 5 such as the restored GPS elevations at 0.360 ± 0.001 Ma and 1.478 ± 0.003 Ma and the intermediate data required to undertake those calculations, such as elevations along the Barajai Trachyte reference datum.

f) Entashatadisp(1.478-0.360Ma).xls

This file provides data regarding the displacement accumulated along the Entashata fault between 1.478 ± 0.003 Ma and 0.360 ± 0.001 Ma and the associated minimum displacement rates during the same period.

g) Entashatadldata(0.360Ma).xls

This provides the along-strike displacement-length data for the Entashata fault as backstripped to 0.360 ± 0.001 Ma.

h) Entashatadldata(1.478Ma).xls

This file provides the along-strike displacement-length data for the Entashata fault as backstripped to 1.478 ± 0.003 Ma.

i) FFZ.xls

This file contains the raw GPS data recorded as latitude, longitude and ellipsoidal elevation along the Footwall Fault Zone (FFZ). Also included are columns of data calculated for the fault

reconstructions described in chapter 5 such as the restored GPS elevations at 0.360±0.001Ma and the intermediate data required to undertake those calculations, such as elevations along the Barajai Trachyte reference datum.

j)   FFZdisp.xls

This file provides data regarding the displacement accumulated along the Footwall Fault Zone (FFZ) between 0.360±0.001Ma and present and the associated minimum displacement rates during the same period.

k)   Ndependldata(0.360Ma).xls

This provides the along-strike displacement-length data for the present-day Entashata fault and a calculation of minimum vertical displacement rates between 0.360±0.001Ma and present.

l)   Porosita.xls

This file contains the raw GPS data recorded as latitude, longitude and ellipsoidal elevation along the Porosita fault. Also included are columns of data calculated for the fault reconstructions described in chapter 5 such as the restored GPS elevations at 0.360±0.001Ma and 1.478±0.003Ma and the intermediate data required to undertake those calculations, such as elevations along the Barajai Trachyte reference datum.

m) Porosita+Enasiradldata(2.009Ma).xls

This file provides along-strike displacement-length data for the train of Gesumeti Trachyte horst blocks as backstripped to 2.009±0.004Ma and a calculation of minimum vertical displacement rates between 2.100±0.007Ma and 2.009±0.004Ma.

n)   Porosita+Entashatadldata(present).xls

This provides the combined along-strike displacement-length data for the present-day Porosita and Entashata fault scarps.

o) Porositadisp(0.360Ma-present).xls

This file provides data regarding the minimum displacement accumulated along the Porosita fault from 0.360±0.001Ma to present and the associated displacement rates during the same period.

p) Porositadldata(0.360Ma).xls

This provides the along-strike displacement-length data for the Porosita fault as backstripped to 0.360±0.001Ma.

A.2.2 Esiteti

This folder contains two Excel files of GPS data recorded from the Esiteti fault. Note that all displacements refer to 'minimum' displacements.

a) Esiteti.xls

This file contains the raw GPS data recorded as latitude, longitude and ellipsoidal elevation along the Esiteti fault.

b) Esitetidldata.xls

This file provides along-strike displacement-length data for the present-day Esiteti fault and as backstripped to 1.654±0.006Ma, 1.128±0.007Ma, 0.992±0.039Ma and 0.215±0.007Ma. Also included is the minimum displacement accumulated in the intervening periods and the associated vertical displacement rates.

A.2.3 Ilainymok

This folder contains four Excel files of GPS data recorded from fault scarps in the Ilainymok region. Note that all displacements refer to 'minimum' displacements.

a)   Ilainymok.xls

This file contains the raw GPS data recorded as latitude, longitude and ellipsoidal elevation along the Ilainymok fault.

b)   Ilainymokdldata.xls

This file provides along-strike displacement-length data for the present-day Ilainymok fault and as backstripped to 0.937±0.004Ma. Also included is the minimum displacement accumulated from 1.121±0.003Ma to 0.937±0.004Ma and 0.937±0.004Ma to the present-day, together with the associated vertical displacement rates.

c)   Ilainymokeast.xls

This file contains the raw GPS data recorded as latitude, longitude and ellipsoidal elevation along the East Ilainymok fault.

d)   Ilainymokeastdldata.xls

This file provides the along-strike displacement-length data for the present-day East Ilainymok fault scarp and the minimum vertical displacement rates between 0.937±0.004Ma and present.

A.2.4 Olooltepes

This folder contains two Excel files of GPS data recorded from the Olooltepes fault. Note that all displacements refer to 'minimum' displacements.

a) Olooltepes.xls

This file contains the raw GPS data recorded as latitude, longitude and ellipsoidal elevation along the Olooltepes fault.

b) Olooltepesdldata.xls

This file provides along-strike displacement-length data for the present-day Olooltepes fault and as backstripped to 1.116±0.002Ma. Also included is the minimum displacement accumulated from 1.134±0.002Ma to 1.116±0.002Ma and 1.116±0.002Ma to the present-day, together with the associated vertical displacement rates.

A.3 Appendix B

Appendix B is an electronic folder containing one Microsoft Excel file: Ihdata.xls. This file contains data from the incremental (step) heating analyses of rock samples from the South Kenya Rift. The numbered samples are indexed in table 3.2.